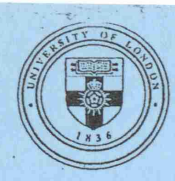

REFERENCE ONLY

UNIVERSITY OF LONDON THESIS

Degree PhD Year 2006 Name of Author RHODES K.S.

COPYRIGHT

This is a thesis accepted for a Higher Degree of the University of London. It is an unpublished typescript and the copyright is held by the author. All persons consulting the thesis must read and abide by the Copyright Declaration below.

COPYRIGHT DECLARATION

I recognise that the copyright of the above-described thesis rests with the author and that no quotation from it or information derived from it may be published without the prior written consent of the author.

LOANS

Theses may not be lent to individuals, but the Senate House Library may lend a copy to approved libraries within the United Kingdom, for consultation solely on the premises of those libraries. Application should be made to: Inter-Library Loans, Senate House Library, Senate House, Malet Street, London WC1E 7HU.

REPRODUCTION

University of London theses may not be reproduced without explicit written permission from the Senate House Library. Enquiries should be addressed to the Theses Section of the Library. Regulations concerning reproduction vary according to the date of acceptance of the thesis and are listed below as guidelines.

A. Before 1962. Permission granted only upon the prior written consent of the author. (The Senate House Library will provide addresses where possible).

B. 1962 - 1974. In many cases the author has agreed to permit copying upon completion of a Copyright Declaration.

C. 1975 - 1988. Most theses may be copied upon completion of a Copyright Declaration.

D. 1989 onwards. Most theses may be copied.

This thesis comes within category D.

☑ This copy has been deposited in the Library of UCL

☐ This copy has been deposited in the Senate House Library, Senate House, Malet Street, London WC1E 7HU.

The Measurement of Arterial Blood Flow from Dynamic Digital X-ray Images

Kawaldeep Singh Rhode

A thesis submitted in partial fulfillment of the requirements for the degree of Doctor of Philosophy of the University of London

December 2005

Academic Division of Surgical and Interventional Sciences,
University College London, The Royal Free Hospital,
Rowland Hill Street, London NW3 2PF, UK.

UMI Number: U593145

All rights reserved

INFORMATION TO ALL USERS
The quality of this reproduction is dependent upon the quality of the copy submitted.

In the unlikely event that the author did not send a complete manuscript
and there are missing pages, these will be noted. Also, if material had to be removed,
a note will indicate the deletion.

UMI U593145
Published by ProQuest LLC 2013. Copyright in the Dissertation held by the Author.
Microform Edition © ProQuest LLC.
All rights reserved. This work is protected against
unauthorized copying under Title 17, United States Code.

ProQuest LLC
789 East Eisenhower Parkway
P.O. Box 1346
Ann Arbor, MI 48106-1346

Abstract

This thesis contributes to knowledge by describing three new methods to measure volumetric blood flow waveforms from dynamic digital x-ray images of arteries following the injection of iodine-based contrast material.

Three novel approaches were developed to overcome the main limitation of image noise sensitivity of the leading existing methods. The first method was a variation of the concentration-distance curve correlation approach and was termed the *polynomial approximation algorithm* (PA algorithm). This method modeled concentration-distance curves using polynomial functions prior to determining the optimal shifts between adjacent curves. The second method used a blood flow waveform shape model based on principal component analysis to constrain the blood flow estimates determined by the concentration-distance curve correlation approach. This was termed the *model based algorithm* (MB algorithm). The third method computed blood flow by performing a weighted average of optical flow estimates along the target vessel with weighting based on the magnitude of the spatial derivative of contrast material concentration. This was termed the *weighted optical flow algorithm* (OP algorithm).

The properties of the OP algorithm were initially investigated using a computer simulation of pulsatile blood flow. Following this, all three algorithms were validated using dynamic x-ray images of progressively more challenging simulated arterial vessels that formed part of a pulsatile blood flow circuit. The x-ray angiographic image data were analysed using a newly developed integrated software package. Flow waveforms were extracted using all three algorithms and compared to simultaneous *gold standard* recordings from an electromagnetic flow meter (EMF) for a range of different flow rates.

The results from the flow circuit experiments showed that the MB and OP algorithms produced flow measurements with low measurement variability and high measurement linearity when compared to EMF values. Furthermore, these algorithms out-performed the basic concentration-distance correlation method and were more robust to image noise and reducing vessel segment length. The PA algorithm showed only minor improvements in performance over the basic approach.

Acknowledgements

Foremost, I would like to thank my supervisors, Alexander Seifalian and David Hawkes, for their encouragement and support. It was a pleasure to continue the work for which they had laid the foundations. I thank Graeme Taylor for providing the initial encouragement for me to embark on the course of study for a PhD. As my BSc project supervisor, he kindled my interest in research.

I would like to acknowledge the Stanley Thomas Johnson Foundation for the generous funding of the research contained in this thesis.

I am very grateful to Tryphon Lambrou, Sean Goldner, and Gareth Ennew for their assistance during the flow circuit experiments. I would like to thank the members of the radiography department at the Royal Free Hospital for teaching me how to use the x-ray equipment. I thank Cliff Ruff for having the patience to explain to me the mathematics of principal component analysis.

I would like to thank Colin Renshaw who provided me with computer support. By his skill I was able to get the old version of SARA working on outdated computer hardware. He also helped to recover the source code for the old software that saved me many months during my re-implementation.

I am grateful to Adam Chandler and Marc Miquel for the proof reading of my thesis. I am also grateful to Derek Hill and Reza Razavi for giving me the final push to complete the writing of my thesis.

I must thank my parents for their moral and financial support while I was a PhD student. Finally, I thank my wife and my son for providing the driving force during the writing of my thesis.

Contents

List of Figures

List of Tables

List of Abbreviations

1D	one-dimensional
2D	two-dimensional
3D	three-dimensional
CISG	Computational Imaging Science Group
CPU	compliant polyurethane
DSA	digital subtraction angiography
EMF	electromagnetic flow meter
LAO	left anterior oblique
MB	model based (algorithm)
MRI	magnetic resonance imaging
ORG	original (algorithm)
PA	polynomial approximation (algorithm)
PC	principal component
PCA	principal component analysis
PCS	principal component score
PI	pulsatility index
PMCC	product moment correlation coefficient
PTFE	polytetrafluoroethene
RAM	random access memory
RAO	right anterior oblique
SARA	System for Angiographic Reconstruction and Analysis
SD	standard deviation
TDP	transverse density profile

Chapter 1

Introduction

The work described in this thesis concerns the measurement of volumetric blood flow from dynamic digital x-ray images of the passage of iodine based contrast material through a target artery. In this chapter I will describe the clinical motivation behind the work, discuss other non x-ray based methods that are available for volumetric arterial blood flow measurement, and describe the structure of the thesis.

1.1 Clinical Motivation

The use of catheter based procedures to assist in the diagnosis of and to treat cardiovascular disease has significantly increased since Seldinger introduced his technique for catheterisation using a needle, a guide wire, and a catheter [Seldinger 1953]. Vascular anatomy can be visualised using the Seldinger technique to introduce radio-opaque iodine based contrast material into a target vessel while imaging with x-ray radiation. This technique, known as *x-ray angiography* has become the gold standard method for the assessment of vascular disease. The procedure is carried out in the *catheterisation laboratory*, which houses the facilities required, including the x-ray

system, and is ubiquitous in hospitals. Modern x-ray systems detect the x-ray radiation that has penetrated the patient using fluoroscopy detectors such as image intensifiers, or more recently, flat panel detectors [Beutel 2000 & Bushberg 2002]. With fluoroscopic detectors it is possible to view the dynamic passage of contrast material through a target vessel. These images can be stored digitally on computers so that they can be recalled and processed in a number of useful ways. Subtraction of images acquired prior to the arrival of the contrast material in the target vessel from subsequent images is called *digital subtraction angiography* (DSA) [Katzen 1995]. DSA images remove unwanted background information and thereby increase the conspicuity of the vascular structures (see figure 1.1). X-ray angiography images are routinely used to assess the severity of occlusive arterial disease, especially coronary artery disease. Furthermore, x-ray fluoroscopic imaging has become the leading method to guide catheter based interventional procedures. Examples of these procedures include percutaneous transluminal coronary angioplasty, vascular stent deployment, embolization of cerebral vascular aneurysms, and embolization of cerebral aterio-venous malformations [Arjomand 2003 & Byrne 1996]. Catheter based interventions have the advantage that they are minimally invasive leading to less patient morbidity when compared to their open surgical counterparts. Furthermore, they also have similar success rates and result in shorter duration of patient hospitalization and therefore often have a cost benefit. However, the assessment of x-ray angiographic images is usually qualitative and the quantitative information available in these images is seldom used [Nissen 1999]. Blood flow is an example of this quantitative information and measurement of flow will provide an objective assessment of the haemodynamic impact of the example interventional procedures mentioned earlier. Monitoring of pre-, intra-, and

(a)

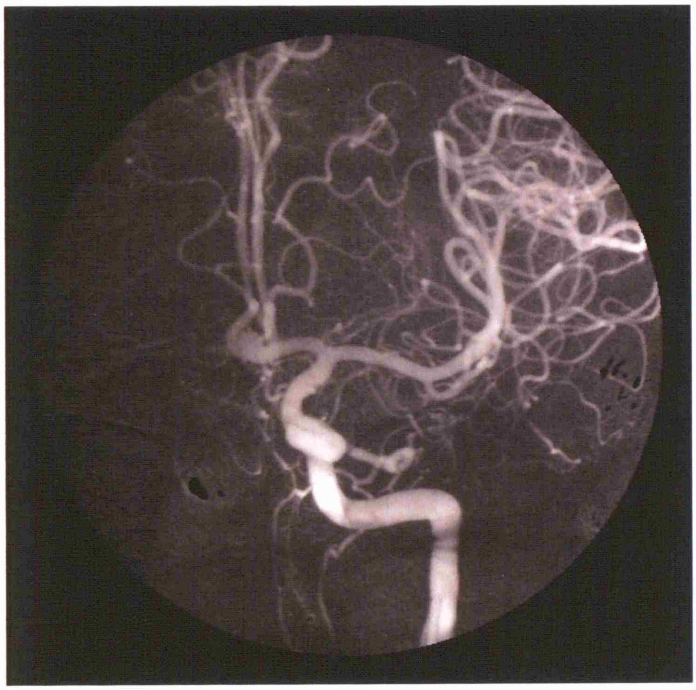

(b)

Figure 1.1: (a) An example of a cerebral x-ray angiogram. Contrast material was injected into the left internal carotid artery and the cerebral vessels on the left side of the circle of Willis can be seen. (b) DSA image showing how image subtraction improves vessel conspicuity.

post-procedural blood flow in the arteries targeted by the interventions could be useful for diagnosis, treatment planning, treatment monitoring, and determination of prognosis. This provides the clinical motivation for the work carried out in this thesis. The development of an algorithm that could measure volumetric blood flow using the x-ray images that were routinely acquired during the interventional procedures would not impose a radiation dose penalty or extend procedure duration but would provide potentially useful objective information.

1.2 Non X-ray Methods to Measure Volumetric Arterial Blood Flow

The non x-ray based methods that are available for the measurement of volumetric blood flow can be divided into the three categories of invasive, minimally invasive and non-invasive methods. Invasive methods include the use of flow probes such as the electromagnetic flow meter (EMF) [Nichols 1997] and the transit-time flow meter [Beldi 2000]. Both of these devices are highly accurate but require direct placement of a probe on the target artery. This limits their use to open surgical procedures. The use of intra-arterial Doppler catheters is a minimally invasive technique that is often used to assess haemodynamic function of the coronary arteries [Wilson 1987]. The catheter is inserted into the target artery and the flow velocity is measured before and after administration of a pharmacological agent that induces hyperaemia. The ratio of the hyperaemic to basal velocity is the coronary flow reserve and provides an objective measure of vascular function. Although intra-arterial Doppler catheters can measure flow velocity, they cannot measure volumetric flow and the required vessel cross-sectional area must computed separately. Duplex ultrasound provides a

non-invasive method to measure volumetric blood flow [Evans 1989]. This combines Doppler ultrasound with B-mode ultrasound imaging. Doppler ultrasound can be used to measure flow velocity and B-mode ultrasound imaging can be used to assess vessel diameter. Magnetic resonance imaging (MRI) is another non-invasive method that can measure volumetric blood flow [Gatehouse 2005]. Both Duplex ultrasound and MRI can be used in the cardiovascular interventional setting. For example, transoesophageal ultrasound is used to guide the placement of closure devices for atrial and ventricular septal defects. Also, the use of MRI for cardiovascular procedure guidance is in rapid development [Razavi 2003]. However, although both Duplex ultrasound and MRI can be used for peripheral and cerebral vascular flow measurement, the measurement of coronary blood flow is still a challenge for these methods due to the rapid motion of the coronary arteries during the cardiac cycle. Compared to the methods mentioned in this section, the use of x-ray angiography for flow measurement has several advantages. X-ray imaging is the most commonly used imaging modality for catheter based cardiovascular procedures so that the images that are routinely acquired can be used for flow measurement without an increase in radiation dose and procedure duration or the requirement of any additional equipment. Furthermore, the high temporal and spatial resolutions of x-ray imaging make this modality suitable for coronary artery flow measurement.

1.3 Structure of Thesis

Chapter 2 presents a review of x-ray angiographic techniques to measure blood flow. The techniques were divided into five categories:

1. Indicator dilution techniques.
2. Techniques based on the measurement of the concentration-time curves at two sites along a target vessel.
3. Techniques based on the measurement of the concentration-distance-time curves.
4. First pass distribution analysis techniques.
5. Techniques based on the computation of optical flow.

The methodology is explained for each of the five categories and results of exemplar studies were given. The relative advantages and disadvantages of the different methods contained within these categories were discussed. Particular attention was given to the categories of concentration-distance-time curve techniques and optical flow techniques since two of the leading existing methods were found within these categories: the concentration-distance curve correlation approach and a differential optical flow approach. These were extended to produce three novel algorithms that are described in chapters 3 and 4.

Chapter 3 presents two new algorithms for the measurement of x-ray angiographic flow based on the concentration-distance curve correlation approach. The first algorithm, termed the *polynomial approximation algorithm* (PA algorithm), was a variation on the basic approach that used polynomial functions to model the concentration-distance curves prior to assessing the correlation between successive curves. The second algorithm, termed the *model based algorithm* (MB algorithm), constrained flow

measurement by the concentration-distance curve correlation method using a mathematical model of flow waveform shape. The choice of modeling technique was made by reviewing the methods that have been used to mathematically characterize the shape of blood flow waveforms in arteries. The techniques of Laplace transform analysis and principal component analysis (PCA) were discussed in terms of their relative advantages and disadvantages. PCA was chosen as the technique to be used in this thesis for waveform shape modeling. The methodology for the formation of the shape model using PCA and the integration of this shape model into the concentration-distance curve correlation method is described.

Chapter 4 presents the third novel algorithm developed in this thesis. The methodology for this *weighted optical flow* (OP) algorithm is described showing how blood flow velocity was estimated using a weighted average of optical flow estimates along a target vessel segment with weighting based on the magnitude of the spatial derivative of contrast material concentration.

Chapter 5 details the validation of the OP algorithm using a computer simulation of pulsatile blood flow. The computer simulation and the underlying flow model on which it was based are described. Two simulation studies were carried out to assess the performance of the OP algorithm while varying the site of contrast material injection, the target vessel segment length, the noise in the synthetic image data, and the mean flow rate.

Chapter 6 describes the validation of the MB, OP and PA algorithms using a pulsatile flow circuit. Details of the flow circuit are given along with a description of the four different types of simulated vessel that were used. It is shown how a waveform shape

model was constructed using many sample EMF recording collected under a variety of flow conditions. The experimental protocol for the pulsatile flow experiments is given along with the details of the image acquisition and analysis software that were developed for this thesis. The results of flow measurement for the different simulated vessels by the MB, OP, and PA algorithms were compared to the true values recorded by the EMF. Also these algorithms were compared to the basic concentration-distance curve correlation method, termed the *original algorithm* (ORG algorithm). The effects of varying image noise and vessel segment length were also investigated separately.

Chapter 7 has concluding remarks with particular attention to the suitability of the newly developed algorithms for clinical flow measurement and suggestion of future work.

Chapter 2

Review of X-Ray Angiographic Techniques to Measure Blood Flow

2.1 Introduction

A plethora of techniques have been reported for the quantitative determination of blood flow from dynamic x-ray angiographic images following the injection of iodine-based contrast material into a target vessel. A thorough review of these techniques was recently carried out by Shpilfoygel *et al.* [Shpilfoygel 2000]. In this chapter I will describe the principles behind these techniques and discuss their relative advantages and disadvantages. I have divided the techniques into the following five categories:

1. Indicator dilution techniques.
2. Techniques based on the measurement of the variation of iodine concentration as a function of time (concentration-time curves) at 2 sites along the target vessel.

3. Techniques based on the measurement of the variation of iodine concentration as a function of distance along the target vessel and of time (concentration-distance-time curves).
4. First pass distribution analysis techniques.
5. Techniques based on optical flow.

2.2 Indicator Dilution Techniques

Indicator dilution, or Stewart-Hamilton techniques are the earliest group of techniques that have been applied to quantify blood flow from x-ray angiographic images. Stewart first suggested the use of indicator dilution to measure blood flow [Stewart 1894, Stewart 1897] and Hamilton was the first to apply this in the case of bolus injection [Hamilton 1928, Hamilton 1932].

These techniques use the principle that the area under an indicator density versus time curve will be directly proportional to the quantity of indicator injected and inversely proportional to flow. For angiographic applications, the iodine-based contrast material is used as the indicator. In the case of bolus injection, the volume flow rate Q can be calculated by

$$Q = \frac{M}{\int C dt} \tag{2.1}$$

where Q = volume flow rate

M = total mass of contrast material injected

C = concentration of contrast material at sampling point

t = time.

This method can be used to measure both absolute and relative flow. In order to measure absolute flow, the relationship between image density and contrast material concentration must be determined, a process known as x-ray calibration or iodine calibration. Relative flow in two arteries, or successively in the same artery, can be determined using identical injection protocols without the need for the calibration. The technique can also be used under the condition of prolonged constant rate injection using a modified version of Eq. 2.1.

The indicator dilution technique has seen widespread early use for blood flow measurement. Exemplar reports include those from Hilal *et al.*. They used the technique to initially measure flow in the femoral arteries of dogs [Hilal 1966a] and then in human carotid arteries [Hilal 1966b]. Mygind *et al.* [Mygind 1995] reported the most recent use of this technique. They evaluated the technique using a constant flow circuit. They compared their obtained flow values with those using fluid collection. The regression equation was $Q_{dilution} = 0.94 \times Q_{true} - 16$ ml/min, and the product moment correlation coefficient (PMCC) was PMCC = 0.94, n = 8. The range of flow values measured was between 600 to 1980 ml/min. Iodine calibration was carried out by imaging vessels with known concentrations of iodine in order to relate image density to contrast material concentration.

The use of indicator dilution theory for angiographic flow measurement is limited under physiological conditions due to the following disadvantages:

1. The technique cannot measure instantaneous flow but only average flow. It is therefore not possible to detect reverse flow. Moreover, the technique assumes constant flow conditions whereas arterial flow is pulsatile under physiological conditions. Experiments with constant flow phantoms invariably report encouraging results whereas in-vivo results are invariably poor.
2. For absolute measurement of flow in a single artery, accurate iodine calibration must be performed and the total amount of contrast material injected must be known precisely.
3. For computation of relative blood flow, repeated injection of contrast material is required.
4. Complete mixing of the contrast material with blood is assumed. However, physiologically, contrast material replaces blood and can then stream along small parts of the arterial cross-section and settle due to the effects of gravity.
5. The application of indicator dilution theory to x-ray angiographic flow measurement may not be mathematically valid. Doriot *et al.* [Doroit 1997] investigated the application of indicator dilution theory to blood flow measurement by considering a simple model. They conclude that the application of this theory is *"incorrect for most flow systems when the detector used to record the curve c(t) is of the 'trans-illumination' type, as is the case for instance in dye dilution methods and in many angiographic or CT techniques"*.

2.3 Concentration-time Curve Analysis at 2 Sites

The measurement of the time taken for contrast material to pass between two points, the transport time, can be used to calculate blood flow velocity if the vessel segment length between these points is known. Together with vessel cross-sectional area, this can then be used to compute volumetric flow by the following equation

$$Q = vA = \frac{L}{T} \times A \tag{2.2}$$

where Q = volumetric blood flow

v = blood flow velocity

A = cross-sectional area of blood vessel

L = distance between measuring sites

T = transport time.

The transport time can be computed by finding the bolus arrival time from the concentration-time curves at the two measurement sites. There have been many criteria suggested for determining the bolus arrival time including:

1. Time of peak [Forbes 1985].
2. Time of half-peak [Silverman 1977].
3. Time of percentage of peak [Mygind 1995].
4. Time of centre of gravity [Rutishauser 1967 & Kruger 1983].
5. Time of leading edge [Crepeau 1973].

Of the many proposed algorithms based on determination of the bolus arrival time, those that use a criterion based on a single feature or a small part of the

concentration-time curve tend to perform poorly when compared to those that use one based on a larger part or the entire curve. For example, one of the more successful methods of measuring the transport time is that employed by Bursch *et al.*. The peak of the concentration-time curve is identified, and the area under the curve up to this point is calculated. A square wave of the same height and the same area is then placed with its right-hand edge coinciding with the peak of the curve. The left-hand edge of the square wave is taken as the arrival time for each curve. This method uses all the data from the first part of the curve. Although identification of the peak of the curve is required, circumstances where the peak is difficult to define produce only a small error in the calculated arrival time. This method was used to measure blood flow in swine iliac arteries [Bursch 1981] and in major human arteries [Bursch 1983 & Bursch 1985].

Another method is to cross-correlate concentration-time curves [Rosen 1973 & Silverman 1977]. This method avoids the determination of the bolus arrival time and uses the entire concentration-time curve. In this method two concentration-time curves are compared for agreement. The first curve is shifted relative to the second along the time axis until there is maximum cross-correlation. At this point, there is maximal agreement between the two curves and the time shift is taken as the bolus transport time. This method has shown improved accuracy over the methods that determine the bolus arrival time.

Limited improvement in the determination of the bolus transport time has been achieved by modeling the concentration-time curves using either gamma variate curves [Thompson 1964, Starmer 1970, & Bateman 1984] or by using polynomial curves [Kwan 1986] in order to overcome noise.

The techniques based on the measurement of the concentration-time curves at 2 sites have the following limitations:

1. Determination of the bolus arrival time in a consistent manor is difficult. This difficulty is reflected by the many possible criteria that have been suggested to accomplish this. If the shape of the concentration-time curve remains unchanged along the target vessel then consistent determination of the arrival time would be possible. This would only occur under the conditions of zero diffusion and plug flow, conditions that are not seen physiologically. In fact, the shape of the concentration-time curve changes along the vessel segment due to diffusion, convective dispersion under laminar flow conditions, and due to the variable mixing of contrast material with blood. Measurements of bolus arrival time using the peak or leading edge of the concentration-time curves will overestimate velocity since these parts of the bolus move faster than the average velocity under laminar flow conditions.
2. These techniques cannot measure instantaneous flow but only average flow. Also, it is not possible to measure reverse flow.
3. Although the techniques are more successful at measuring pulsatile flow than those based on indicator dilution theory, experiments under constant flow conditions invariably produce better results than those under pulsatile conditions.

2.4 Concentration-distance-time Curve Techniques

The use of contrast material concentration-time curves at only two measurement sites results in the loss of information that is present in dynamic angiographic images about

the propagation of the bolus along the target vessel. In order to preserve this information, the contrast material concentration can be considered as a function of distance along the target vessel as well as a function of time. This leads to a group of algorithms that operate on the resultant concentration-distance-time curves.

2.4.1 Tracking Features of the Concentration-distance Curve

Parker *et al.* [Parker 1985] tracked the leading edge of the bolus in successive concentration-distance curves to derive velocity. The velocity was computed by multiplying the distance between successive locations of the leading edge by the imaging frame rate. They validated their approach using a flow phantom and then used the technique to measure flow in the human coronary circulation. The main disadvantage of this technique is that it considerably overestimates the true velocity. In conditions of laminar flow, the leading edge of the bolus will be traveling in the centre of the vessel due to convective dispersion. In this region of the vessel, the velocity is twice the average velocity. Therefore, methods that track the leading edge will overestimate the true mean velocity by up to a factor of two.

Instead of using the leading edge, Guggenheim *et al.* [Guggenheim 1992 & Guggenheim 1994] applied a threshold to the concentration-distance curve computed as a percentage of the maximum concentration achieved by the curve. They then compute the velocity by measuring the distance between the threshold points on successive concentration-distance curves separated in time by 1 cardiac cycle. For application to a constant flow rate phantom, they used a threshold value of 50% and showed that x-ray flow measurements agreed with true flow as measured by fluid collection with ±10%

accuracy. For measurements on human left anterior descending coronary arteries, they used a threshold value of 30%. The concentration-distance curves were computed after reconstructing the coronary artery tree using biplane imaging. The measured flow values for 12 patients were compared to simultaneous measurements made by thermodilution in the great cardiac vein. They reported the regression equation $Q_{angio} = 0.83 \times Q_{thermo} + 16.1$ ml/min, and a correlation coefficient of PMCC = 0.87, n = 29. Doriot *et al.* [Doriot 1995] later determined the optimal threshold value to be 50% by computer simulation of flow in the coronary circulation and Dorsaz *et al.* [Dorsaz 1997] employed the technique to measure coronary flow in 22 patients. X-ray flow measurements were compared with those made by intracoronary Doppler velocity measurements and the reported error was 11% with a correlation coefficient of PMCC = 0.81, n = 32. The results from this method are encouraging. One limitation is the use of an empirically determined threshold value that may not apply under all flow conditions. Also by using concentration-distance curves separated by 1 cardiac cycle, the method is limited to measuring average flow and not instantaneous flow.

Shaw *et al.* [Shaw 1986] constructed a special contrast material injector that was capable of pulsed injection of contrast material at frequencies up to 15 Hz. This allowed the rapid introduction of multiple boluses into a target vessel. They used a flow phantom consisting of a plastic tube bent in a circular path. Dynamic x-ray images were acquired of the phantom and concentration-distance-time curves computed. Each bolus produced a peak in the concentration-distance curve and the position of these peaks was determined automatically. The velocity was calculated by measuring the average distance between the boluses and multiplying by the pulsing frequency. The measured

velocities were corrected by subtracting the flow introduced by the injection itself and compared to the true values as measured by fluid collection. The range of velocities measured was 80 to 600 mm/sec. The correlation coefficient was PMCC = 0.997, n = 11. A single experiment was also conducted using pulsatile flow of frequency 1 Hz generated using a pulsatile pump. However, the true velocity was not measured by a reference technique and the accuracy of this method cannot be known in pulsatile conditions. The limitations of this method are:

1. Pulsed injection of contrast material is required with accurately known pulsing frequency. Power injectors are not usually able to offer this feature and a specially modified injector is required.
2. The pulsing frequency needs to be adjusted according to the flow conditions in order to ensure adequate separation of boluses over the vessel segment being imaged. Therefore, in conditions of pulsatile flow it may not be possible to measure bolus separation accurately with a single pulsing frequency.
3. Detection of flow reversal is not possible.

2.4.2 Tracking Iso-concentration Contours

Colchester *et al.* [Colchester 1983] proposed a new way of representing dynamic angiographic data. They used a parametric image in which the x-axis represents time, the y-axis is the distance along the target vessel, and the image grey value is the concentration of contrast material in the blood vessel at position (x,y). An example of the parametric image representation of dynamic angiographic data is shown in figure 2.1.

Colchester *et al.* estimated bolus velocity by measuring the gradient of iso-concentration contours in the parametric image. This was performed by manually marking tangents to the iso-concentration contours using a computer display and light pen. They used the algorithm to measure blood flow in the cerebral circulation and in a pulsatile flow phantom [Colchester 1983, Colchester 1984, & Colchester 1986]. An advantage of this technique is that it can measure both instantaneous and reverse flow. A major disadvantage is that the interactive approach was time-consuming. Also, the method produces multiple velocity estimates for each time frame at different distances along the vessel segment. Colchester *et al.* simply averaged these estimates.

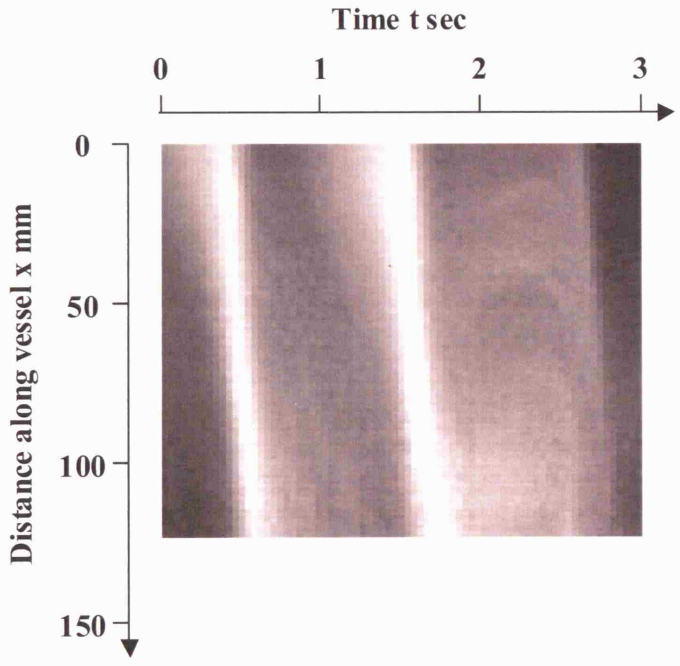

Figure 2.1: An example of a parametric image. This was formed from dynamic x-ray images acquired during the injection of contrast material into a 6 mm silicone tube that formed part of a pulsatile flow circuit. The mean flow rate was 338 ml/min.

du Boulay *et al.* [du Boulay 1986] reported an automated method to measure the gradient of the iso-concentration contours removing the user interaction previously required. Unfortunately, they did not detail the technique. They applied the technique to a pulsatile flow phantom using instantaneous flow rates of 30 to 400 ml/min. The results showed good visual comparison with simultaneous measurements made using an EMF and the errors were reported to be within 10%.

Wicks [Wicks 1989] detailed a fully automated approach to the measurement of blood flow velocity using the iso-concentration contour approach. He computed the velocity using a circular gradient operator. Furthermore, the problem of obtaining multiple velocity estimates as a function of distance along a vessel segment was overcome by performing a weighted average with weighting based on the magnitude of the operator. Brunt *et al.* [Brunt 1992a & Brunt 1992b] applied this technique to a pulsatile flow phantom, and to a human carotid artery. The phantom results showed close agreement with EMF recordings for flow rates below 400 ml/min but underestimation of higher flow rates. They note that the technique is limited by the requirement of high contrast material concentration gradients along the vessel segment.

2.4.3 Tracking of Bolus Mass

Swanson *et al.* [Swanson 1986] suggested a method for determining velocity by tracking a constant mass of contrast material between successive angiographic images. The concentration-distance curve is integrated over a fixed length of the imaged vessel segment in the first angiographic image. This integral will be proportional to the mass of contrast material present in the chosen length. The integral is then computed for the

same length but as a function of distance along the vessel segment moving from the proximal to the distal end in the next angiographic image. The metric used for determining bolus velocity is the difference of the integral computed for the first image and the next image, or the bolus mass difference. The distance when the bolus mass difference is minimum is equal to the distance traveled by the bolus. The velocity can then be computed using the time between the two images. This algorithm was validated by measuring the flow in the femoral artery of dogs. There was good agreement with simultaneous measurements made using an EMF.

The advantages of the bolus mass tracking algorithm are that it can measure instantaneous pulsatile flow with the ability to deal with flow reversal. A disadvantage of the approach was found by Seifalian *et al.* [Seifalian 1989 & Seifalian 1993] . They investigated the bolus mass tracking algorithm proposed by Swanson *et al.* using a computer simulation of pulsatile blood flow. They demonstrated that the algorithm produced accurate results for low flow rates but failed under high flow conditions. This result can be explained in two ways. Firstly, there is a limit to the maximum velocity that can be measured which depends on the length chosen for integrating the concentration-distance curves. Secondly, this length must be reduced to measure higher velocities, which increases the likelihood of finding incorrect velocity estimates.

Shpilfoygel *et al.* [Shpilfoygel 1999] presented a modified technique based on the approach of Swanson *et al.*. They computed the bolus mass difference as a function of distance along a pair of concentration-distance curves but did not fix the length over which the bolus mass is computed. Instead this was allowed to vary from the maximum value (total length of the vessel segment) to a predefined minimum value. This allowed

a higher limit to the maximum measurable velocity, a limitation in the original method by Swanson *et al.*. They also fitted a straight line to the bolus mass difference data and determined the zero-crossing point to calculate bolus velocity. This technique was evaluated using simulated angiograms and a constant flow phantom. For the phantom study the range of velocities measured was 190 to 500 mm/sec and the error in velocity measurement was –7.1% (underestimation) when compared to fluid collection. The advantage of this technique over the approach of Swanson *et al.* is that it can be used to measure high flow rates. In fact, the technique can be used to extrapolate velocities in cases where the bolus has almost completely passed through the target vessel segment.

2.4.4 Using Correlation Between Successive Concentration-distance-time Curves

The concept of deriving blood flow velocity by shifting adjacent concentration-distance curves until there is a "best match" was first suggested by Swanson *et al.* [Swanson 1988]. Unfortunately, they did not define their "best match" criterion. Whether this was bolus mass difference, as used in their previous work [Swanson 1986], or another new criterion is not clear. They employed their technique to quantify pulsatile instantaneous and mean flow in coronary artery bypass grafts of 5 dogs. They reported very good agreement of both instantaneous and mean flow rates with simultaneous measurements made by an EMF. The correlation coefficient for mean flow rates, ranging from 18 to 130 ml/min, was PMCC = 0.91, n = 17. Unfortunately, the method was not validated for higher flow rates.

Seifalian *et al.* [Seifalian 1989] were the first to detail a technique to measure blood flow velocity by shifting adjacent concentration-distance curves until a "best match" was obtained. They defined the "best match" as the shift that minimised the mean sum of squared differences between curves. This shift was then multiplied by the image acquisition frame rate to derive instantaneous blood flow velocity. They validated the technique using a computer simulation [Hawkes 1988] of pulsatile blood flow. The simulated mean velocities ranged from 30 to 360 mm/sec (corresponding to mean flow rates from 51 to 610 ml/min for a 6 mm diameter vessel). There was very good agreement between the estimated velocities and the known true velocities from the computer simulation using a variety of contrast material injection profiles. The correlation coefficient for mean velocities was PMCC = 0.995, n = 64, with a mean error of 2.37 (underestimation) ± 10.3 (1SD) mm/sec. The authors also computed the velocities using the bolus mass tracking approach of Swanson *et al.* and reported a correlation coefficient of PMCC = 0.735, n = 64, and mean error of 48.6 ± 66.2 mm/sec. They further validated the technique for smaller vessels of 2 and 4 mm diameter and reported very good agreement with the known velocities. They concluded that their concentration-distance curve technique was more robust than the bolus mass tracking approach and was capable of accurately measuring blood flow velocities over the range of clinically observed velocities and vessel diameters. Furthermore, the algorithm was shown to produce velocity estimates that were independent of the contrast injection profile.

Seifalian *et al.* [Seifalian 1991] carried out further validation of the concentration-distance curve correlation approach using a pulsatile flow phantom. They

compared velocities estimated using the angiographic method to simultaneous measurements made using an EMF. Three different mean velocities were used ranging from 147.2 to 733.0 mm/sec. The measured instantaneous velocities showed good agreement with the EMF. However, peak velocities were overestimated for lower flow rates and then underestimated for higher flow rates. The effect of varying the site of contrast material injection and the length of the vessel segment were also investigated. The technique was robust when varying the site of injection but progressively failed when the vessel segment length was reduced from 200 to 20 mm. The technique was also applied to the femoral artery of a patient before and after percutaneous transluminal angioplasty demonstrating the restoration of the normal biphasic flow waveform after the procedure.

The technique was later combined with three-dimensional (3D) vascular reconstruction from biplane angiographic images and densitometric vessel cross-sectional area measurement to compute absolute volumetric blood flow in flow phantoms and the carotid arteries of patients undergoing carotid artery endarterectomy [Hawkes 1992, Seifalian 1992, Seifalian 1993, Hawkes 1994, & Seifalian 1996].

Hoffman *et al.* [Hoffman 1990 & Hoffman 1991] independently devised the concentration-distance curve correlation approach to determine blood flow velocity. They used the minimum root mean squared difference between adjacent concentration-distance curves to define the "best match" and subsequently to determine blood flow velocity. They validated the method using a pulsatile flow phantom for mean flow rates ranging from 210 to 600 ml/min in a 6.7 mm diameter vessel. They

reported the root mean squared difference between measured flow rates and those of an EMF of 174 ml/min for instantaneous flow and 48 ml/min for average flow.

Holdsworth *et al.* [Holdworth 1999] combined the concentration-distance curve correlation approach with the pulsed contrast material injection technique first suggested by Shaw *et al.* [Shaw 1986]. They constructed a pulsed injector capable of delivering boluses at a maximum frequency of 30 Hz. When compared with the injector used by Shaw *et al.*, their injector produced more discrete boluses. They validated their technique using a flow phantom with both constant and pulsatile flow conditions. For constant flow rates between 300 and 1800 ml/min the accuracy was reported within 11% of EMF values. For pulsatile flow rates, the accuracy of instantaneous flow measurements was reported within 8%.

Out of all the angiographic flow measurements techniques described so far in this review, the concentration-distance curve correlation approach is the most successful for the measurement of instantaneous pulsatile flow. The technique can measure flow over the range of clinically observed flow rates and can also deal with flow reversal. It seems to be robust under conditions of different injection profile and has the additional advantage of being computational inexpensive. However, there are two disadvantages. Firstly, there is an upper limit to the maximum velocity that can be measured. This depends on the vessel length over which the concentration-distance curves are computed and the minimum overlap between adjacent curves that is allowed for matching. Secondly, investigators have consistently reported that the algorithm overestimates peak velocities in flow phantom experiments. This has been partially explained by the streaming of contrast material along the centre of the target vessel.

Shpilfoygel *et al.* [Shpilfoygel 1998 & Shpilfoygel 1999] modified the concentration-distance curve correlation technique by fitting a parabola to the profile of root mean squared differences between consecutive curves. They then used the minimum of this parabola to find the optimal displacement of the contrast material. They evaluated this technique using simulated angiograms and a constant flow circuit. Compared with the basic method used by Seifalian *et al.* and Hoffman *et al.* the modified technique showed a lower mean error in flow measurement of –16.5% (underestimation) compared to –18.8% and lower variability in measurement. Shpilfoygel *et al.* suggested that the curve fitting approach could be used to extrapolate velocity measurements to overcome the upper limit of measurable velocity imposed by the concentration-distance curve correlation approach. However, such extrapolation was found to be unreliable from experiments conducted using their flow phantom data.

2.5 First Pass Distribution Analysis Techniques

This group of techniques can be applied to the measurement of blood flow in arteries that supply a well defined perfusion bed. By applying the conservation of mass principal to the injected contrast material, the equation derived from first pass distribution analysis (FPDA) to measure blood flow is

$$\overline{Q} = \frac{\Delta V}{C \Delta t} \tag{2.3}$$

where $\overline{Q}$ = average volumetric flow in the target vessel in time period Δt

ΔV = change in contrast material volume in the perfusion bed

C = average input contrast material volume concentration.

The FPDA technique has been applied using two methods. The first method, known as the videodensitometric method, uses Eq. 2.3 directly. In this method, contrast material is injected as a rate above the peak expected flow rate so that it replaces blood. Then the input concentration of contrast material, C, is assumed to be constant and equal to that of the injected contrast material. The change in contrast material volume, ΔV, in the perfusion bed is determined by the difference in the integrated image intensity over a region covering the perfusion volume, and by a calibration that relates intensity to contrast volume. The second method, known as the entrance vessel method, uses a modified version of Eq. 2.3. In this method, the requirement for iodine calibration is removed and the requirement for determining the input concentration of iodine is also removed. This is achieved by measuring the integrated intensity signal for both the perfusion volume and for a known volume of the target vessel as a function of time. If the time interval between image acquisitions, Δt, is short then the FPDA technique can be used to measure instantaneous flow rate which can be averaged over a cardiac cycle to yield mean flow rate.

Marinus *et al.* [Marinus 1990] used the entrance vessel method to measure blood flow in a 4 mm diameter coronary artery phantom. They compared calculated flow measurements to those made by an EMF. For constant flow between 90 and 420 ml/min, the correlation coefficient was PMCC = 0.993, n = 45, and the regression line was $Q_{FPDA} = 0.92Q_{TRUE} + 0.19$ ml/min. For pulsatile flow conditions, PMCC = 0.982. They also used the technique to measure blood flow in the left main coronary artery of one patient and in the bypass graft of another patient. Although there was no gold

standard for comparison, multiple measurements showed that the technique was reproducible.

Hangiandreou *et al.* [Hangiandreou 1991] applied the videodensitometric method to both phantom and in-vivo flow measurement. In flow phantom experiments with constant flow rates from 30.0 to 252.7 ml/min, there was very good agreement between angiographic flow measurements and those made using fluid collection. The correlation coefficient was PMCC = 0.993, n = 24, and the slope of the regression line was $Q_{FPDA} = 1.054Q_{TRUE}$. For the in-vivo experiments, flow measurements were made on the perfused circumflex artery of 3 dogs. Angiographic flow rates were compared to those measured with an EMF. Although there was good correlation, the results from 2 dogs produced a 16% underestimation. This underestimation was thought to be caused by video camera lag in the imaging chain.

Molloi *et al.* [Molloi 1993] overcame the camera lag problem by using a charge-coupled device video camera. Furthermore, they noted that the FPDA techniques were sensitive to image subtraction artifacts and to the non-linearities due to scatter and veiling glare. They used a dual energy x-ray system to minimize subtraction artifacts and corrected for scatter and veiling glare. They compared both the videodensitometric and the entrance vessel methods by measuring flow in a pulsatile flow phantom. The mean flow rate was varied between 30 and 150 ml/min and the measured flow rates were compared to measurements made with an intra-arterial Doppler flow catheter. The regression line was $Q_{FPDA} = 1.14Q_{TRUE} - 0.12$ ml/min for the entrance vessel methods, and $Q_{FPDA} = 1.12Q_{TRUE} - 0.23$ ml/min for the videodensitometric method. The correlation coefficient was better for the entrance vessel method (PMCC = 0.99, n = 16)

than for the videodensitometric method (PMCC = 0.95, n = 16) and there was less variation for the entrance level method. Using a conventional x-ray system (i.e. without dual energy capability) Ersahin *et al.* [Ersahin 1995] later applied the two methods to the measurement of flow in the internal carotid artery of rabbits. Molloi *et al.* subsequently applied the videodensitometirc method to the coronary arteries of swine [Molloi 1996, Molloi 1998 & Molloi 2004]. The results from the animal experiments demonstrated very good agreement with recordings from a transit-time ultrasound flow probe.

First pass distribution analysis techniques have produced very promising results for the measurement of blood flow. These techniques have several advantages. Firstly, they are able to successfully measure pulsatile flow. Secondly, for the videodensitometric method, there is no need to quantify vessel cross-sectional area and absolute flow can be measured directly. Finally, the techniques have been successfully demonstrated on clinically important arterial circulations, such as the coronary and the cerebral circulation. However, these techniques have the following limitations:

1. Flow measurements are restricted to circulations that fit the model of having a single supply vessel and a well defined perfusion volume that can be imaged entirely in the x-ray field of view.
2. It is assumed that the contrast material does not exit the perfusion volume while flow measurements are being made. Therefore, measurements can only be made if the contrast material persists in the perfusion volume for a sufficient time.
3. For both the videodensitometric and entrance vessel methods, the flow measurements are very susceptible to artifacts in the imaging and pre-processing

stages, e.g. video camera lag, motion artifacts during image subtraction, and scatter and veiling glare. Although investigators have overcome these problems, the solutions either require specialized hardware, such as dual energy x-ray systems, or additional calibration stages, e.g. for scatter and veiling glare correction.

4. For the videodensitometric method, the average input iodine concentration is usually taken as the concentration of the injected contrast material. This can only be true if the contrast material completely displaces blood on injection. This requires high injection rates that will alter the underlying flow. Furthermore, this method requires the additional step of accurate iodine calibration.
5. For the entrance vessel technique, the accurate determination of the volume of part of the entrance vessel is required.

2.6 Optical Flow Techniques

If a moving scene is captured by as a series of time-ordered images, these images will contain the projected motion of the objects in the scene. The estimated two-dimensional (2D) motion of these objects in the images is termed the optical flow field or the image velocity field. Techniques to determine optical flow were first developed to study the motion of objects for computer vision applications [Horn *et al.* 1981]. Beauchemin *et al.* have presented a review of these techniques [Beauchemin 1995]. They divide the techniques into three categories:

1. Intensity-based differential methods.
2. Frequency-based filtering methods.
3. Correlation-based methods.

The first of these techniques calculates the optical flow by the computation of the temporal and spatial derivatives of image intensity. The second uses orientation sensitive filters in the Fourier domain to compute the optical flow. The final group of techniques computes image velocity by matching small image regions between consecutive images in the sequence. Beauchemin *et al.* discuss the relative advantages and limitations of each approach and conclude that the best choice of technique is largely dependent on the nature of the image motion and on image quality. Jahne [Jahne 1997] also presents a detailed description of optical flow computation techniques. As well as a thorough mathematical basis for each of the techniques, he also presents an analysis of errors due to noise, unsteady motion, motion discontinuity, and illumination change.

For application to dynamic x-ray angiographic images, investigators have attempted to compute optical flow in order to infer information about the motion of contrast material and thus the underlying blood flow. Most of the published work regarding optical flow computation from angiographic images is either based on the optical flow constraint equation or the equation of continuity for fluid flow.

2.6.1 The Optical Flow Constraint Equation and the Equation of Continuity for Fluid Flow

Let $I(x,y,t)$ represent the image brightness for the image region at location (x,y) at time t. The image region is displaced by δx in the x direction and by δy in the y direction in a short time δt. If the brightness of this region does not change in the time δt then

$$I(x,y,t) = I(x+\delta x, y+\delta y, t+\delta t)\,. \tag{2.4}$$

Expanding the right-hand side by a Taylor series gives

$$I(x,y,t) = I(x,y,t) + \delta x\frac{\partial I}{\partial x} + \delta y\frac{\partial I}{\partial y} + \delta t\frac{\partial I}{\partial t} + O^2 \tag{2.5}$$

where O^2 represents the second and higher order terms, which are assumed to be small. Neglecting these terms, subtracting $I(x,y,t)$ from both sides, and dividing by δt gives

$$\frac{\delta x}{\delta t}\frac{\partial I}{\partial x} + \frac{\delta y}{\delta t}\frac{\partial I}{\partial y} + \frac{\partial I}{\partial t} = 0\,. \tag{2.6}$$

Now

$$\frac{\delta x}{\delta t} = u \text{ and } \frac{\delta y}{\delta t} = v \tag{2.7}$$

where u and v are the components of velocity in the x and y directions, respectively. Therefore, Eq. 2.6 can be written as

$$(I_x, I_y)\bullet(u,v) = -I_t \tag{2.8}$$

where I_x, I_y, and I_t are the partial derivatives of I with respect to x, y, and t, respectively. Eq. 2.8 is known as the optical flow constraint equation.

The continuity equation used in fluid dynamics is

$$\frac{\partial \rho}{\partial t} + \nabla\bullet(\vec{v}\rho) = D\nabla\rho\,. \tag{2.9}$$

This expresses the conservation of mass for a fluid of density ρ moving with velocity $\vec{v}$ and with diffusion coefficient D. Using certain assumptions, Eq. 2.9 can be reduced to the optical flow constraint equation. Firstly, under the assumption of zero diffusion,

$$\frac{\partial \rho}{\partial t} + \nabla \bullet (\vec{v}\rho) = 0. \tag{2.10}$$

Now

$$\frac{\partial \rho}{\partial t} + \nabla \bullet (\vec{v}\rho) = \frac{\partial \rho}{\partial t} + \vec{v} \bullet \nabla \rho + \rho \nabla \bullet \vec{v} = 0. \tag{2.11}$$

If we assume that the divergence of the velocity field, $\nabla \bullet \vec{v}$, is negligible in a local region, then

$$\frac{\partial \rho}{\partial t} + \vec{v} \bullet \nabla \rho = 0. \tag{2.12}$$

For logarithmically subtracted angiographic images, the fluid density can be replaced by the image intensity, I, of the contrast material,

$$\frac{\partial I}{\partial t} + \vec{v} \bullet \nabla I = 0. \tag{2.13}$$

For the 2D case, Eq. 2.13 can be written as Eq. 2.8, the optical flow constraint equation. The relationship between the continuity equation and the optical flow constraint equation is important because it demonstrates some of the conditions under which the optical flow constraint equation will be valid when applied to angiographic images. These are when there is zero diffusion of contrast material ($D = 0$ in Eq. 2.9) and when there is no spatial variation of contrast material velocity in a local region ($\nabla \bullet \vec{v} = 0$ in

Eq. 2.11). Fitzpatrick [FitzPatrick 1985] demonstrated this relationship and investigated the agreement between velocity field measurements computed using the optical flow constraint equation and the equation of continuity using synthetic test pattern image sequences. He concluded that the differences between the two methods could be significant.

2.6.2 Techniques Based on the Optical Flow Constraint Equation

When the optical flow constraint equation is applied in the 2D case, the resulting velocity maps can be useful for studying flow patterns. For angiographic images this quantification could highlight regions of disturbed flow, which have been implicated in the development of pathologies such as atherscelerotic plaques and arterial aneurysms. The evolution of flow patterns during interventional procedures to treat these pathologies may be related to clinical outcome and reoccurrence.

If the temporal and spatial derivatives are estimated from an image sequence, the optical flow constraint equation constrains the image velocity along a line of points. An exact solution for the velocity components cannot be determined since this is a single linear equation with two unknowns. Therefore, determination of the 2D optical flow requires at least one other constraint to be imposed. Horn *et al.* [Horn 1981] were the first to present a computational scheme for the calculation of 2D optical flow. They imposed a smoothness constraint on the optical flow field by assuming that field changes smoothly over a local region. This produced a formulization that was solved using an iterative approach. They tested the algorithm on synthetic test pattern image sequences and report errors between 7 and 10% for the calculation of velocity vectors. It was noted

that larger errors were obtained in regions where the spatial gradient was small and when there was greater noise in the image intensity values.

Cornelius *et al.* [Cornelius 1986] were the first to apply 2D optical flow determination to x-ray angiographic images. They used an approach similar to Horn *et al.* but allowed velocities to change abruptly across boundaries in the image and also allowed the image brightness to vary. They evaluated their approach using synthetic test pattern image sequences and one angiographic sequence of a beating dog heart. The approach was not used to explicitly compute blood flow velocity but did in fact illustrate endocardial wall motion with limited success.

Mongrain *et al.* [Mongrain 1991] computed 2D optical flow from both computer simulated angiographic sequences and dynamic coronary artery angiograms. Instead of using a smoothness constraint on the velocity field, they constrained the optical flow using the 2D form of the Navier-Stokes equations. They reported a 5-10% error for velocity determination in the computer simulations and demonstrated the expected parabolic velocity profile in coronary artery images.

Amini *et al.* [Amini 1993 & Amini 1994] presented a formulization for 2D optical flow computation that was based on expressing the velocity field as a "stream function" that strictly enforced the divergence constraint. They tested their method using computer simulated images but did not evaluate the accuracy of the results quantitatively.

Reduction of the optical flow constraint equation to the one-dimensional (1D) form has been used with greater success for velocity determination in blood vessels than application of the 2D form. Efron *et al.* [Efron 1978] used the 1D form of the optical

flow constraint equation by constraining motion to be only parallel to the target vessel centreline. This gives the velocity, u, in the direction of the centreline, x, as

$$u = -\frac{\frac{\partial I}{\partial t}}{\frac{\partial I}{\partial x}}. \tag{2.14}$$

They could have applied this equation to lines parallel to the target vessel centreline but instead they chose to use the integrated image intensity perpendicular to vessel centreline, I_Σ, so that

$$u = -\frac{\frac{\partial I_\Sigma}{\partial t}}{\frac{\partial I_\Sigma}{\partial x}}. \tag{2.15}$$

They validated the technique using both constant and pulsatile flow in a vascular phantom, and in the descending aorta of dogs and humans. X-ray acquisition was performed at 60 frames per second and the resultant cine film was digitized for analysis. They obtained the concentration-time curves for 4 regions of interest separated by 4 mm along the target vessel. These were then used as adjacent pairs to determine both the temporal and spatial intensity gradients by the method of finite differences. Instantaneous velocity was then calculated using Eq. 2.15 and the 4 velocities combined to give an average velocity for each time point. For the constant flow experiments, true velocity ranged from 80 to 800 mm/sec as determined by fluid collection. Although the time-averaged computed velocities showed good agreement with the true velocity values (PMCC = 0.99, n = 6) there was significant variation of measured velocity as the contrast material bolus passed through the target vessel. Measurements on the leading

edge produced overestimates and those on the trailing edge produced underestimates. These results can be explained by the convective dispersion of the bolus in conditions of laminar flow. The results from the pulsatile flow experiments showed greater variation, as did those from the in-vivo studies. However, the pulsatile velocity waveforms extracted from the in-vivo data were plausible aortic waveforms.

Imbert *et al.* [Imbert 1995a, Imbert 1995b, & Imbert 1997] applied the 1D form of the optical flow constraint equation to compute velocities for computer simulated dynamic angiograms of normal and stenotic vessels, and dynamic angiograms of the femoral artery of a patient. Starting with Eq. 2.14, they imposed the additional constraint that the 2D distribution of velocity perpendicular to the vessel centreline is parabolic. This assumption is valid if the flow within the vessel is laminar. They replaced u by a parabolic function to give

$$u_{\max}\left(1-\frac{(y-y_0)^2}{R^2}\right)=-\frac{\frac{\partial I}{\partial t}}{\frac{\partial I}{\partial x}} \tag{2.16}$$

where $u_{\max}$ is the maximum velocity, y_0 is the vessel centreline position, y is the perpendicular distance from the vessel centreline, and R is the vessel radius. Once the temporal and spatial derivatives were determined from the image data, Eq. 2.16 produced a set of over determined linear equations that were solved by least squares fitting. Parameters derived were y_0, R, and $u_{\max}$. For the simulation study, synthetic angiograms were produced by modeling laminar blood flow with a constant contrast material injection rate. The vessel was parallel to the imaging plane. Synthetic angiograms were generated of 1 normal vessel (7 mm diameter) and 2 stenotic vessels

with 20% and 40% stenoses and the mean velocity was set to 50 mm/sec. Results showed that there was no measurable error in y_0, the percentage error in R was –0.72 to –11.69%, and the percentage error in u_{max} was –2.29 to 0.18%. For the femoral artery study, the percentage error in y_o was 0.4%, the percentage error in R was 6.6%, and the percentage error in u_{max} was –10.2%. The calculated values were compared to values derived by manual measurements made from the angiographic image sequence. This method has the advantage that it can simultaneously compute peak velocity and vessel radius, parameters that can be used to assess stenosis severity. One disadvantage is the assumption of laminar flow in the formulization. It is known that the in-vivo radial velocity profile in arteries varies between the extremes of plug and laminar flow [Nichols 1997]. The study was limited in several ways. Firstly, the performance of the algorithm was not tested under pulsatile flow condition in the computer simulation study. Although conditions were pulsatile for the in-vivo study, only one pair of rapidly acquired images was used for analysis. The x-ray calculated velocity was compared to manual measurements made on the leading edge, an approach that leads to large errors. Furthermore, the performance of the algorithm for a range of mean flow values was not evaluated but only a single flow rate was used. The authors note that their technique was limited by the requirement of sufficient temporal and spatial gradients of image intensity. It seems that they limited their measurements to the leading edge of the bolus, which will result in overestimation of velocity.

2.6.3 Techniques Based on the Equation of Continuity for Fluid Flow

Close *et al.* [Close 1992] used the integrated 1D form of the continuity equation (Eq. 2.9) in a discretized form to compute volumetric blood flow as

$$Q = -\frac{\sum_{x=x_1}^{x=x_2}[I_\Sigma(x,t_2) - I_\Sigma(x,t_1)]}{\sum_{t=t_1}^{t=t_2}\left[\frac{I_\Sigma(x_2,t)}{A(x_2)} - \frac{I_\Sigma(x_1,t)}{A(x_1)}\right]} \tag{2.17}$$

where x_1 and x_2 are two sites along the target vessel, t_1 and t_2 are two image acquisition times, and A is vessel cross-sectional area. The assumptions of plug flow and zero diffusion were made in the derivation. The algorithm was tested using dynamic x-ray images of a constant flow phantom and of a human internal carotid artery. The flow phantom results showed large variation in flow measurements as the contrast material bolus passed through the target vessel. Measurements made on the leading edge overestimated the flow and those made on the trailing edge underestimated flow. Mean internal carotid artery flow measurements were reported and good agreement between calculations made using three angiographic views was used to conclude that the technique was repeatable. Unfortunately, Eq. 2.17 can be shown to be an expression of the Stewart-Hamilton equation, and therefore, this technique will suffer from the limitations of indicator dilution methods.

Huang *et al.* [Huang 1997a] demonstrated the derivation of a 1D equation for determination of contrast material bolus velocity from the equation of continuity. Under the assumption of zero diffusion, they expressed bolus velocity as

$$u = -\frac{\dfrac{\partial I_\Sigma}{\partial t}}{\dfrac{\partial I_\Sigma}{\partial x}} - I_\Sigma \frac{\dfrac{\partial u}{\partial x}}{\dfrac{\partial I_\Sigma}{\partial x}}. \tag{2.18}$$

It can be seen from this equation that the bolus velocity depends not only on the temporal and spatial derivatives of integrated image intensity but also on the spatial derivative of velocity itself. This equation can be written as

$$u = u_D + \Delta u \tag{2.19}$$

where Δu is the error term between the measurable derivative velocity, u_D, and the true bolus velocity, u. The authors considered two cases for which Δu could be determined. Firstly, if the spatial derivative of velocity is zero, as in the case of plug flow, then Eq. 2.18 reduces to Eq. 2.15, i.e. the method used by Efron *et al.*. Secondly, they considered the motion of the bolus leading edge under the conditions of laminar flow and showed that Eq. 2.19 could be written as

$$u = u_D - \frac{I_\Sigma}{2} \cdot \frac{\dfrac{\partial u_D}{\partial x}}{\dfrac{\partial I_\Sigma}{\partial x}}. \tag{2.20}$$

It can be seen that in this case the error term is dependent on the spatial variation of the derivative velocity, u_D. They validated their approach using a constant flow phantom with three vessel diameters of 2.12, 3.18 and 4.76 mm and vessel lengths between 140 and 160 mm. The flow rates were varied between 60 and 720 ml/min giving a velocity range of 56.0 to 1983 mm/sec. The contrast material injection was performed by a power injector at a constant rate that was varied according to the blood flow rate. The

image acquisition was carried out with three different views to allow 3D reconstruction of the simulated vessels. The image data was represented as a temporal sequence of concentration-distance curves. Temporal and spatial derivatives were calculated from these curves and used to find the bolus velocity both with and without the error term, Δu. Measurements were restricted to the leading edge of the bolus. The results were presented graphically showing the variation of measured velocity with distance along the leading edge of the bolus, and the measured flow velocity against the true flow velocity. It was found that the measured velocity was a function of the distance along the leading edge of the bolus. Velocity estimates at the tip of the leading edge were higher than those obtained behind the leading edge. This would be expected in the case of convective dispersion of the bolus under conditions of laminar flow. For illustration, five equally spaced points were chosen along the leading edge for measurement. The central point was then chosen to compare measured velocity with true average velocity. In general, the measured velocity was found to be between the true average velocity and the true peak velocity. The calculated velocities were consistently higher than the true velocities by 10-50%. Application of the correction term did not seem to affect velocity estimates for the smallest diameter vessel. However, the uncorrected velocity estimates were visually better than the corrected velocity estimates for the larger vessels when compared to the true average velocity. Critical points to note from this study are:

1. There was no attempt to present summary statistics for the results and no statistical comparisons were made between the measured velocities and the true velocity. Also it would have been interesting to quantify the difference between using the uncorrected velocity and the corrected velocity estimates.

2. The theory presented is only applicable along the bolus leading edge and measurements were restricted to this region. Therefore, much of the information in the angiographic images was not used for velocity estimation. For comparison with true mean velocity, only a single central point was chosen along the bolus leading edge to derive computed velocities.
3. The flow conditions were constant and the contrast material injection was also at a constant rate. This will make much of the contrast material concentration signal homogeneous, producing small temporal and spatial gradients. The authors reported that measurements behind the leading edge of the bolus were prone to large errors. The choice of flow conditions and contrast injection protocol may explain this.
4. Contrast material injection was sometimes carried out while flow was arrested for measurement of slow velocities. Although this is possible with a blood flow circuit, it is highly non-physiological.
5. It was not stated how the true velocity values were obtained. However, this is most likely to have occurred by fluid collection. During x-ray measurements, there will be instantaneous changes to the base-line flow due to the injection of contrast material. These changes are difficult to measure if fluid collection is the gold standard against which x-ray measurements are compared. In order to minimize this problem the authors have placed the injection catheter 60 cm upstream from the imaging site. This distance is extremely large compared to typical distances used in practical angiography.
6. The authors have not considered how flow reversal might affect the measured velocity estimates. Flow reversal is found in many arteries in the human circulation,

such as the femoral arteries, and detection of reverse flow is sometimes pathologically significant.

In a further study [Huang 1997b], the authors confirmed their flow phantom experiment results using a mathematical model of the dispersion of contrast material in a fluid flowing in a circular tube under the conditions of constant laminar flow. They conclude from these simulations that their derivative technique can successfully measure the bolus transport velocity and that this velocity varies from the peak of the fluid velocity at the tip of the leading edge of the bolus to the true average fluid velocity at the bolus peak. However, they state that measurements at the bolus peak produce velocity estimates that are prone to error, presumably due to the homogeneous nature of the bolus concentration in this region.

Sarry *et al.* [Sarry 1997] used the 1D form of the equation of continuity in their approach to compute flow velocity for dynamic angiographic images. This equation was stated as

$$\frac{\partial}{\partial x}(uI_{\Sigma})(x,t)+\frac{\partial I_{\Sigma}}{\partial t}(x,t)=0 \tag{2.21}$$

where $u(x,t)$ is the blood flow velocity and $I_{\Sigma}(x,t)$ is the contrast material density, both as a function of distance along the target vessel, x, and of time, t. They used the parametric image representation of angiographic data. They presented a technique that computes an estimate for the contrast material density function using an initial estimate of the velocity function. This estimate is then compared to the actual density function and the velocity function is refined iteratively until there is convergence. They initially tested the algorithm on synthetic parametric images. They simulated pulsatile flow

through a 60 mm length of vessel of cross-sectional area 10 mm^2. The flow waveform was triangular and the injection waveform was a ramp. They also simulated a stenotic vessel by uniformly decreasing the vessel area to 3 mm^2 (70% stenosis) and then uniformly increasing it back to 10 mm^2. The results quoted the relative error in velocity estimation for the normal vessel to be within 5% except for a few locations in the spatiotemporal plane. The results for the percentage stenosis were between 69.9 and 70.0%. They tested immunity towards noise by adding 7, 10, and 14% zero mean Gaussian distributed noise to the parametric image of the stenotic vessel. The calculated percentage stenosis ranged from 70.3% for least noise to 71.8% for maximum noise. The algorithm was also tested on a coronary angiogram of patient with angina. Biplane images were acquired and 3D reconstruction was performed of the coronary vasculature. Blood velocity was measured in the left circumflex artery for both basal and hyperaemic flows to determine coronary flow reserve. Measurements were compared with those made simultaneously by an intra-arterial Doppler catheter. The mean difference between x-ray and Doppler velocities was 2 mm/sec (overestimation) for the basal flow and –17 mm/sec for the hyperaemic flow. The 95% limits of agreement for the basal flow were –114 to 118 mm/sec and –168 to 135 mm/sec for the hyperaemic flow. This technique has the unique feature that it can compute the velocity distribution as a function of both time and distance along the vessel. Therefore, it is well suited to the assessment of vessel stenosis. Disadvantages include the sensitivity of the iterative approach to dicretization of the spatiotemporal intensity data, leading to a requirement for both high spatial and temporal resolution. Furthermore, the iterative approach can become unstable when spatiotemporal gradients are small. Also, reverse velocities are not permitted in the computation scheme. A further disadvantage is that

the algorithm is computationally expensive. The authors tried to address the latter two problems and presented a new computational scheme for solving Eq 2.21 [Sarry 2002]. Their new approach produced results almost identical to their previous validation study but was faster by an order or magnitude taking only "a dozen of seconds" as opposed to "a dozen of minutes".

2.7 Summary

The measurement of blood flow from dynamic angiographic images has been attempted using the plethora of methods that are outlined in this review chapter. Quantitative comparison of the methods, for example in terms of accuracy and variability, is difficult because of the different ways in which the approaches have been validated and the different ways in which experimental results have been reported. However, the relative advantages and disadvantages of the techniques are useful for assessing suitability for physiological blood flow measurement. Early techniques were based on indicator dilution theory and on the measurement of the concentration-time curve at two sites along the target vessel. Although these methods are computationally inexpensive, they are only able to measure average flow and fail under the conditions of pulsatile flow. Furthermore, the indicator dilution techniques require accurate iodine calibration. The methods based on concentration-distance-time curve analysis have shown greater success for pulsatile flow measurement. This is partly because these techniques use more of the information that is present about the bolus motion. Of these methods, both the bolus mass tracking method suggested by Swanson *et al.* and the correlation method suggested by Seifalian *et al.* have shown promising results. However, these methods have the limitation of a maximum measurable velocity. The reliable measurement of

higher flow rates requires longer segments of the target vessel for analysis. Furthermore, these techniques are sensitive to noise in the image data. Algorithms based on first pass distribution analysis have reported very successful results for the measurement of pulsatile blood flow. These techniques have the disadvantage that they are only applicable to target arteries that fit the requirements of the FPDA model. Also the methods may require accurate iodine calibration and extra image pre-processing due to sensitivity to image artifacts. Optical flow techniques are limited by the requirement of high spatiotemporal gradients and sensitivity to noise. 2D optical flow techniques are useful for assessing patterns of flow. However, these methods only show projected velocities and the true bolus velocity can only be recovered when assumptions are made about the flow profile inside the target artery, as in the work by Imbert *et al.*. 1D techniques based on computation of temporal and spatial gradients of bolus concentration, such as those proposed by Efron *et al.* and Huang *et al.*, have shown a degree of success and show better noise immunity than 2D methods due to integration of image intensity. Similarly, the indirect approach introduced by Sarry *et al.* has shown good noise immunity but is still reliant on high spatiotemporal gradients.

Two approaches have been developed further in this thesis. Chapter 3 describes how the concentration-distance curve correlation method suggested by Seifalian *et al.* has been extended in two ways. Firstly, polynomial functions have been used to model the concentration-distance curves prior to determining the optimum shift between adjacent curves. Secondly, the concentration-distance curve correlation approach has been modified by incorporating *a priori* shape information about the volumetric blood flow waveform. Chapter 4 describes how the 1D optical flow approach suggested by Efron *et*

al. has been extended by using a weighted average of velocities measured as a function of distance along the target artery.

Chapter 3

The Polynomial Approximation and Model Based Algorithms to Measure Pulsatile Blood Flow Waveforms

3.1 Introduction

None of the algorithms reviewed in chapter 2 for the measurement of pulsatile blood flow in arteries from dynamic digital x-ray images have taken into account the shape of the flow waveforms that are likely for the target vessel. At most, investigators have made assumptions about the different velocity profiles that exist radially across an arterial lumen, considering the conditions of either plug or laminar flow. With the advent of the use of Doppler ultrasound to measure blood flow in arteries [Satomura 1959], it became apparent that the shape and content of the Doppler sonogram was characteristic of the artery being investigated and the disease state of this artery. I formed the hypothesis that *a priori* knowledge of the likely shape of the blood flow waveform through a target artery could be used to improve the measurement of

blood flow through that artery using dynamic digital x-ray images. In order to test this hypothesis, a mathematical method was required to model the shape of blood flow waveforms. Section 3.2 presents a review of the techniques that have been used to characterize the shape of blood flow waveforms in arteries. By considering the relative advantages and disadvantages of these techniques, principal component analysis (PCA) was selected as the mathematical modeling method. Section 3.3 describes how a waveform shape model can be formed using PCA. Section 3.4 describes the novel model based algorithm that integrates this shape model into the concentration-distance curve correlation method of Seifalian *et al.*. This section also describes the polynomial approximation algorithm that resulted during the development of the model based approach and represents a variation of the concentration-distance curve correlation method.

3.2 Review of Methods to Characterize the Shape of Blood Flow Waveforms in Arteries

The early reports for the characterization of blood flow waveforms were based on measurements made using Doppler ultrasound [Evans 1989]. The non-invasiveness, ease of use, and relative cost effectiveness of Doppler ultrasound have made this technique the most widespread method of assessing vascular disease. The characterization of Doppler-shifted ultrasound waveforms has been the focus of much research with a view to classify vascular disease. The techniques that have been reported can be divided into two categories. Firstly, there are those that derive only one parameter from the waveform, and secondly, there are those that attempt to characterize the whole waveform. Many single parameters derived from Doppler-shifted ultrasound

waveforms have been suggested and examples of single parameters are shown in figure 3.1. Such parameters have been shown to vary between different arterial vessels and between healthy and diseased arteries. These parameters use only a limited part of the blood flow waveform and therefore have limited use in characterization of the entire waveform shape. However, two techniques that take the whole waveform into account are Laplace transform analysis and PCA. Both these techniques provide a mathematical way to describe an entire waveform by using only a few parameters.

3.2.1 Techniques Based on Laplace Transform Analysis

Skidmore *et al.* [Skidmore 1978] were the first to report the use of describing a Doppler ultrasound derived blood flow waveform in terms of its Laplace transform. They modelled the maximum frequency envelope of the Doppler signal by initially performing a Fourier transform and then calculating the equivalent Laplace transform by a curve-fitting procedure. They used the third order Laplace transform given by

$$H(S) = \frac{1}{(S^2 + 2\delta\omega_0 S + \omega_0^{\,2})(S + \gamma)} \tag{3.1}$$

where $S = j\omega$.

In their first study [Skidmore 1980a], the parameters ω_0, γ, and δ were found for waveforms recorded from the posterior tibial arteries of healthy volunteers and patients with lower limb vascular disease. It was found that these parameters had physiological significance: (1) γ was related to the degree of vasocontriction/vasodilation of the distal arterial bed; and (2) ω_0 was related to the elastic modulus of the wall of the artery under investigation. In their second study [Skidmore 1980b], they characterized the common

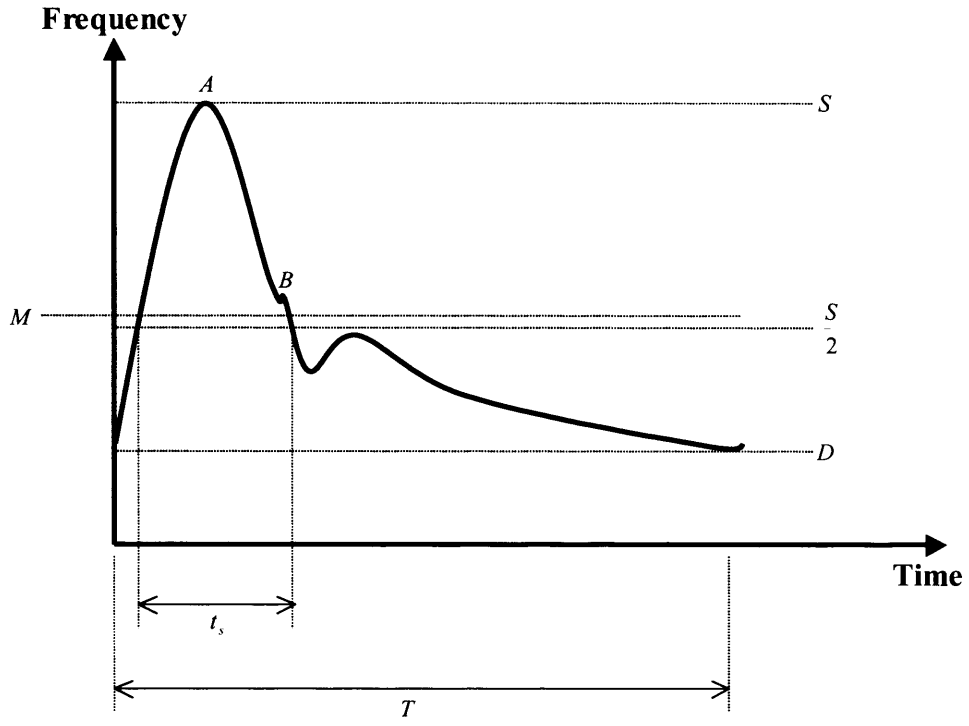

M = mean over cardiac cycle

Pulsatility Index $$PI = \frac{S - D}{M}$$

Pourcelot's Resistance Index $$RI = \frac{S - D}{S}$$

A/B Ratio $$= \frac{A}{B}$$

Height Width Index $$HWI = \frac{S - D}{M} \times \frac{T}{t_s}$$

Path Length Index $$PLI = \sum_{i=0}^{i=N-1} \sqrt{\frac{(f_{i+1} - f_i)^2}{M^2} + \frac{(t_{i+1} - t_i)^2}{T^2}}$$

where the maximum frequency envelope consists of N samples $\{f_0, f_1, ..., f_{N-1}\}$ at times $\{t_0, t_1, ..., t_{N-1}\}$.

Figure 3.1: Examples of single parameters derived from Doppler sonograms. A typical maximum frequency envelope for the common carotid artery is shown.

femoral artery waveforms of healthy volunteers and patients with vascular disease. This study confirmed the previous results and also concluded that parameter δ was associated with the degree of proximal stenosis. In the same study, the accuracy of modelling the arterial waveforms using the Laplace analysis technique was investigated by comparing the measured flow waveforms to those obtained by reconstruction using the parameters of the Laplace transform. Visual inspection of reconstructed waveforms showed good agreement with the measured waveforms. Finally, these investigators compared the use of the Laplace transform for waveform characterization of the common femoral artery to use of the pulsatility index (PI) [Skidmore 1980c]. Their results indicated several advantages of the Laplace transform analysis technique when compared to the use of PI for analysis of aortoiliac disease. These results we later confirmed in a larger study by Baird *et al.* [Baird 1980].

Johnston *et al.* [Johnston 1984] subsequently compared four methods for quantifying Doppler ultrasound waveforms. They made measurements on 232 common femoral arteries and measured the PI, height-weight index, path length index, and the δ parameter of the Laplace transform function proposed earlier by Skidmore *et al.*. They concluded that all four indices were equally capable of detecting significant aortoiliac disease. However, they stated that the PI had advantages of simplicity and ease of calculation. As well as fitting to the Laplace transform in the frequency domain they also fitted to the inverse Laplace transform in the time domain. The inverse function was given by

$$f(t) = \frac{\gamma(\alpha^2 + \beta^2)}{(\gamma - \alpha)^2 + \beta^2}\left[e^{-\gamma t} + e^{-\alpha t} \times \left(\frac{\gamma - \alpha}{\beta}\sin \beta t - \cos \beta t\right)\right] \quad (3.2)$$

where α, β, γ are the fitted parameters

and $\alpha = \omega_0 \delta$, $\beta^2 = \omega_0^2 - \alpha^2$.

These early studies into the use of Laplace transform analysis to characterize blood flow waveforms have led to others investigating its use for many different arterial vessels [Ramsay 1994, Stone 1994, Brackley 1998a, Brackley 1998b, Stone 1998, & Brackley 2000]. In general, the technique has been shown to be superior to the use of single indices in the assessment of arterial disease by Doppler ultrasound. The advantage of this technique for mathematical modelling of the blood flow waveform shape is that only 3 parameters are required to represent the shape for both the frequency domain (Eq. 3.1) and the time domain methods (Eq. 3.2). A disadvantage is that the time-varying flow is explicitly modelled using a particular function, i.e. by Eq. 3.2. It is assumed that all waveforms can be modelled by this function alone. Skidmore *et al.* demonstrated the suitability of this function by computing the reconstructed waveforms using the parameters derived from Eq. 3.1. Visual comparison of the reconstructed waveforms with the original data showed good agreement.

3.2.2 Techniques Based on Principal Component Analysis

PCA is a linear coordinate transformation that produces a new set of orthogonal axes for a data set such that the greatest variance by any projection of the data set lies along the first axis, the second greatest variance along the second axis, and so forth. It has widespread use in data analysis, such as investigation of data structure, reduction of data dimensionality, and data classification. Jackson [Jackson 1991] presents a detailed

description of the mathematical background of this technique. Subsequently in section 3.3, I show how the technique can be applied to blood flow waveform shape modelling. Using a set of waveforms as input for PCA, a model can be formed that expresses the waveform shape as a linear combination of the mean shape and a variable amount of independent modes of variation of this shape. PCA involves the eigen analysis of the input waveform data and the resulting eigenvectors represent the modes of variation, each with an associated eigenvalue that gives the relative contribution to the total variation.

Martin *et al.* [Martin 1980] compared the use of PCA with A/B ratio for characterizing vessel disease in the common carotid artery. They collected waveforms from 25 normal vessels and 18 stenotic vessels. PCA was performed on the maximum frequency envelope and each waveform was reconstructed using two eigenvectors. Both the use of PCA and A/B ratio was shown to be able to distinguish between the healthy and diseased groups. However, PCA-based classification was shown to be superior to the traditional A/B ratio parameter. Walton *et al.* [Walton 1983] demonstrated the use of PCA-based classification for patients with lower limb ischaemia. The common femoral artery waveforms of 80 patients with lower limb ischaemia were used to generate a PCA-based classification scheme. The scheme was then tested on a further 28 patients and the results compared to x-ray angiographic findings. The authors concluded that the PCA technique has improved diagnostic accuracy when compared to other methods.

Evans *et al.* [Evans 1981] compared the use of PCA, Laplace transform analysis and PI in determining degree of stenosis in canine iliac arteries. They inserted artificial stenoses of varying area reduction (0-95%) into the iliac arteries of five greyhounds.

133 Doppler waveforms were measured and subjected to the three analytical methods. It was reported that PCA was better at distinguishing stenosis than the other two techniques. Two eigenvectors were used to reconstruct the waveforms and these explained over 90% of the total variation in the population. Prytherch *et al.* [Prytherch 1982] investigated the Doppler waveforms from the iliac arteries of three dogs that had known degrees of stenosis. These waveforms were subjected to PCA and then reconstructed using the first two eigenvectors. It was demonstrated that PCA could be used to successfully classify 75% of the stenoses with the remaining 25% being classified at most one group away from the correct category. The practical components involved in an on-line system for waveform characterization and classification using PCA were discussed by Evans [Evans 1984]. Subsequently, Evans *et al.* [Evans 1985] used PCA to detect abnormal cerebral haemodynamics in neonates. The maximum frequency envelope from the Doppler sonograms of the anterior cerebral arteries of 40 normal full-term babies and 14 mature babies with intracranial pathology was extracted. PCA was shown to be significantly better at detecting abnormalities than the more widely used resistance index. Macpherson *et al.* [Macpherson 1984] made a comparison of three techniques for the analysis of Doppler ultrasound waveforms. They compared the use of PI, Laplace transform, and PCA to assess vascular disease with direct pressure measurements taken as the gold standard. Ultrasound recordings were taken from the femoral arteries of 50 patients with vascular disease. PCA yielded 32 eigenvectors but once again, only two eigenvectors were used to reconstruct the original waveforms. It was shown that PI and Laplace transform analysis performed equally when compared to the pressure measurements. However, PCA produced significantly better agreement and was more sensitive to arterial disease.

For the comparative studies mentioned, PCA seems superior to the use of single parameters and Laplace transform analysis for the identification of vascular disease. In terms of waveform shape modeling, PCA has the advantage that it does not use a predefined mathematical function for the blood flow waveform, as is the case of Laplace transform analysis. Instead, the input waveforms serve as a statistical sample to form a shape model of the statistical population. Therefore, a PCA based shape model is more flexible and able to incorporate a wider range of waveform shapes. One disadvantage is that the technique produces a large number of parameters, or specifically, modes of variation. However, often only a few eigenvectors are required to represent important features of the waveform shape. In fact, for the studies mentioned, at most two eigenvectors were retained. Therefore, PCA can enable the shape information to be represented with much reduced dimensionality. I selected PCA as the mathematical method to model blood flow waveform shape for the model based flow extraction algorithm presented in this chapter because of the flexibility that this technique offers for shape modeling.

3.3 Construction of a Blood Flow Waveform Shape Model using Principal Component Analysis

I will now detail how the blood flow waveform shape model was constructed. Consider many sample input volumetric flow waveforms, $\mathbf{P}_i$, consisting of S sample points $\{q_{i1}, q_{i2}, q_{i3}, \ldots\ldots, q_{iS}\}$. The input waveforms are averaged to produce a mean waveform shape

$$\overline{\mathbf{P}} = \frac{1}{N}\sum_{i=1}^{i=N}\mathbf{P}_i \tag{3.3}$$

where N = total number of input waveforms.

The input waveforms are then transformed by subtracting the mean waveform shape

$$\mathbf{dP}_i = \mathbf{P}_i - \overline{\mathbf{P}} = \{dq_{i1}, dq_{i2}, dq_{i3}, ..., dq_{iS}\} \text{ for } 1 \le i \le N \ . \tag{3.4}$$

The $S \times S$ covariance matrix $\mathbf{C}$ is calculated

$$C_{ij} = \frac{1}{N}\sum_{k=1}^{k=N} dq_{ki}dq_{kj} \text{ for } 1 \le i, j \le S \ . \tag{3.5}$$

Eigen analysis of this real symmetric covariance matrix yields S normalized eigenvectors $\mathbf{e}_j$ with corresponding eigenvalues λ_j, $1 \le j \le S$. The eigenvectors are sorted in order of decreasing eigenvalue. Therefore, the first eigenvector has the largest eigenvalue and the last eigenvector has the smallest eigenvalue. The results of this analysis can be interpreted in both a mathematical manner and by using the concept of shape space. Mathematically, the eigenvectors, also known as the principal components (PCs), form a basis vector set for the transformed input waveforms $\mathbf{dP}_i$. Each eigenvector accounts for one mode of variation of the mean waveform shape $\overline{\mathbf{P}}$ with variance equal to the corresponding eigenvalue. Any of the input waveforms $\mathbf{P}_i$ can now be expressed as the sum of the mean waveform shape and a linear combination of the eigenvectors

$$\mathbf{P}_i = \overline{\mathbf{P}} + \sum_{j=1}^{j=S} w_{ij}\mathbf{e}_j \tag{3.6}$$

where w_{ij} is the weighting factor for eigenvector $\mathbf{e}_j$ for waveform $\mathbf{P}_i$.

Using the concept of shape space, each of the input waveforms can be represented as a single point in a S- dimensional hyperspace or 'shape space'. The eigenvectors form the axes of this shape space. The subtraction of the mean waveform shape yields the transformed input waveforms $\mathbf{dP}_i$, which can be interpreted as moving the origin of shape space so that it is centred about the mean waveform shape. The coordinates of each of the transformed input waveforms $\mathbf{dP_i}$ are $(w_{i1}, w_{i2}, w_{i3}, ..., w_{iS})$. If it were possible to view this hyperspace it would be noted that points corresponding to the transformed input waveforms are largely distributed along the axes corresponding to the first few eigenvectors. This reflects the fact that most of the variation in the waveform shape occurs along these axes. The percentage variation $v\%_j$ attributed to eigenvector $\mathbf{e}_j$ can be calculated as

$$v\%_j = \frac{\lambda_j}{\sum_{i=1}^{i=S} \lambda_i} \times 100 \tag{3.7}$$

where λ_j is the eigenvalue associated with eigenvector $\mathbf{e}_j$.

For each input waveform $\mathbf{P}_i$ there is a set of eigenvector weighting factors $\mathbf{w}_i$. These weighting factors are known as the principal component scores (PCSs) of the waveform $\mathbf{P}_i$. The PCSs can be calculated by

$$w_{ij} = \sum_{k=1}^{k=S} e_{jk} dq_{ik} \tag{3.8}$$

where w_{ij} is the j^{th} PCS of waveform $\mathbf{P}_i$.

Each eigenvector is responsible for one mode of variation of the waveform shape. In order to investigate the effect of each mode of variation on the waveform shape, it is possible to add varying quantities of each eigenvector to the mean waveform shape. Waveform $\mathbf{P}$ can be formed by adding x standard deviations of eigenvector $\mathbf{e}_j$,

$$\mathbf{P} = \overline{\mathbf{P}} + x\sqrt{\lambda_j}\mathbf{e}_j \tag{3.9}$$

where $1 \le j \le S$.

It is possible to represent each of the input waveforms by using only the first few modes of variation. The input waveform $\mathbf{P}_i$ can be approximated by the reconstructed waveform $\mathbf{P}_i'$ using the first k modes of variation by

$$\mathbf{P}_i' = \overline{\mathbf{P}} + \sum_{j=1}^{j=k} w_{ij}\mathbf{e}_j \,. \tag{3.10}$$

As more eigenvectors are used, the reconstructed waveform will follow the original input waveform more closely. Therefore, it is possible with PCA to approximate a high dimensionality waveform shape using reduced dimensionality. Instead of using the full number of PCs, S, it is possible to use the first k PCs to represent the waveform shape. There are several methods that can be used to decide how many PCs to retain. A detailed description of these methods is presented by Jackson [Jackson 1991]. In this thesis, analysis of residuals was used to decide the number of modes of variation that could be used to represent the waveform shape information. If the input waveform $\mathbf{P}_i$ is approximated by $\mathbf{P}_i'$ using only the first k modes of variation as given in Eq. 3.10, then

$$\mathbf{P}_i = \mathbf{P}_i^{'} + \mathbf{R}_i \tag{3.11}$$

where $\mathbf{R}_i$ is the vector of residuals.

The sum of squares of the residuals is given by

$$Q_i = (\mathbf{P}_i - \mathbf{P}_i^{'})^T (\mathbf{P}_i - \mathbf{P}_i^{'}). \tag{3.12}$$

It can be shown that

$$Q_i = \sum_{j=k+1}^{j=S} w_{ij}^2 . \tag{3.13}$$

Therefore, if k out of the possible S PCs are retained then it is possible to calculate the sum of squares of the residuals Q_i for input waveform $\mathbf{P}_i$. The root mean square of the residuals is given by

$$Qrms_i = \sqrt{\frac{Q_i}{S}} . \tag{3.14}$$

The root mean square of the residuals is a measure of the error when using only k out of the possible S PCs when reconstructing the input waveforms. The error can be expressed as a percentage of the mean flow rate

$$E_i = \frac{100 Qrms_i}{\frac{1}{S}\sum_{j=1}^{j=S} dq_{ij}} . \tag{3.15}$$

The average percentage error can be calculated for all input waveforms

$$\overline{E} = \sum_{i=1}^{i=N} E_i . \tag{3.16}$$

The number of retained PCs should be enough to model the waveform signal without modelling the noise component of this signal. Eq. 3.16 can be used to decide on the number of PCs to retain once the noise level in the input signals has been determined.

3.4 The Polynomial Approximation and Model Based Algorithms for X-ray Blood Flow Measurement

I will initially describe the concentration-distance curve correlation algorithm in section 3.4.1 and show how this was modified to form the polynomial approximation algorithm. I will then show in section 3.4.2 how the PCA based waveform shape model was combined with the concentration-distance curve correlation approach to produce a novel model based algorithm for the measurement of blood flow from dynamic angiographic images.

3.4.1 Concentration-distance Curve Correlation Algorithm and The Polynomial Approximation Algorithm

The concentration of contrast material along an arterial vessel segment can be expressed as a function of distance along the vessel and of time, $\mathbf{C}(x,t)$, where x and t correspond to discrete samples of distance and time. The distance x is measured in millimetres and $0 \le x \le N$. The segment length is then $(N+1)$mm. The time t is measured in angiographic sampling intervals, or time frames, and $0 \le t \le T$. This gives rise to a series of concentration-distance curves $\mathbf{C}(x,0),\mathbf{C}(x,1),\mathbf{C}(x,2),.....,\mathbf{C}(x,T)$ where T is the last frame in the series. These concentration-distance curves can be modeled using polynomial fits to reduce the effects of noise in the measured data. The order of

the polynomial fit depends upon the length of the vessel segment. Longer segment lengths require higher order fits. For the range of vessel lengths investigated in this thesis, forth order polynomials were used. Higher order polynomials would have modeled the noise component whereas lower order polynomials would not have adequately modeled the shape of the curves. Figure 3.2 shows a series of concentration-distance curves.

If curve $\mathbf{C}(x,t)$ is shifted by s mm with respect to curve $\mathbf{C}(x,t+1)$, the cost function $\mathbf{\Psi}(s,t)$ is calculated as

$$\Psi(s,t) = \frac{1}{N-s+1}\sum_{x=0}^{x=N-s}\left(C(x,t)-C(x+s,t+1)\right)^2 \quad \text{if } s \geq 0 \tag{3.17a}$$

and $$\Psi(s,t) = \frac{1}{N+s+1}\sum_{x=0}^{x=N+s}\left(C(x-s,t)-C(x,t+1)\right)^2 \quad \text{if } s < 0. \tag{3.17b}$$

This cost function is the mean sum of squared differences between consecutive concentration-distance curves. A computed example of this function is shown in figure 3.3. The velocity, $v(t)$, in millimeters per second for shift s is given by

$$v(t) = s \times FR \tag{3.18}$$

where FR is the frame rate in frames per second.

The concentration-distance curve correlation algorithm selects the value of s for which $\mathbf{\Psi}(s,t)$ is minimum. This value, s_{opt}, is the value for which there is the "best match" in the least squares sense between consecutive concentration-distance curves. The estimated contrast medium velocity is then given by

$$v(t) = s_{opt} \times FR. \tag{3.19}$$

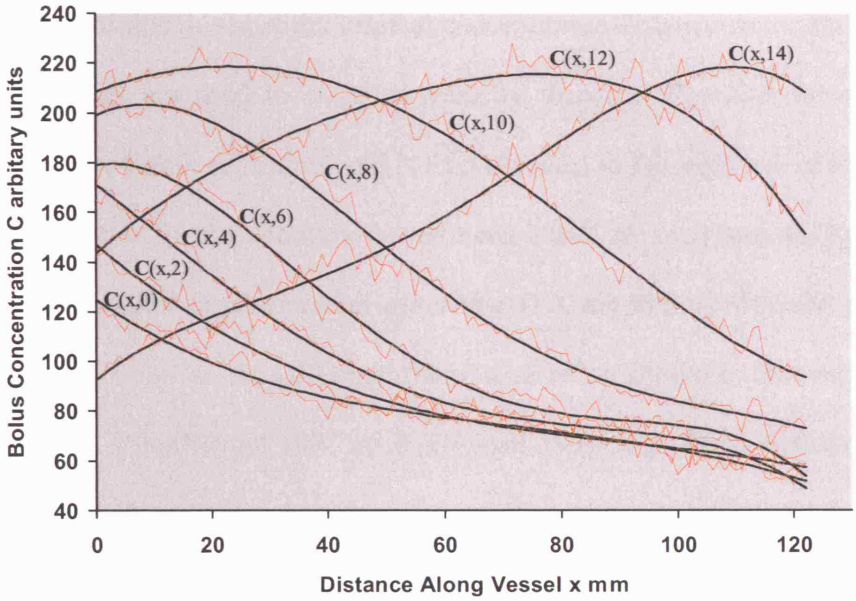

Figure 3.2: Time varying concentration-distance curves showing the passage of contrast material along a vessel. These were taken from the parametric image shown in figure 2.1. The original data are shown in red and the polynomial fitted data are shown in black.

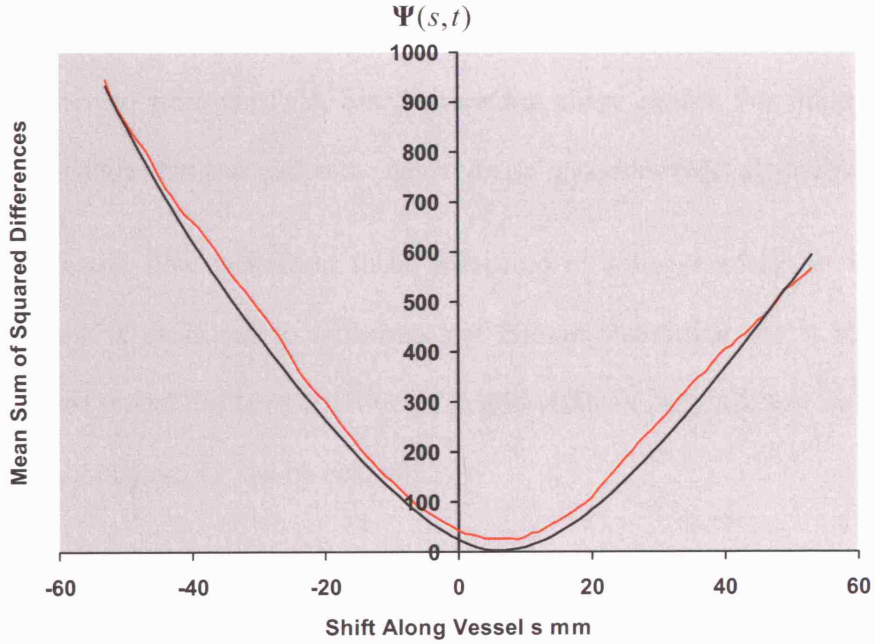

Figure 3.3: The mean sum of squared differences between consecutive concentration-distance curves as a function of shift along the vessel. The first pair of concentration-distance curves in the parametric image shown in figure 2.1 was used. The red line shows the computed function using the original data and the black line using the polynomial fitted data. The optimal shift by the original data was 9 mm and 6 mm by the polynomial data.

For the purpose of this thesis, if the original concentration-distance curve data (without polynomial fitting) are used to compute velocity then the algorithm is termed the *original algorithm* (ORG algorithm) and is then identical to the approach of Seifalian *et al.*. If the polynomial fit concentration-distance curve data are used then the algorithm is termed the *polynomial approximation algorithm* (PA algorithm). The PA algorithm forms a slight variation on the ORG algorithm, a variation similar to that suggested by Shpilfoygel *et al.* [Shpilfoygel 1998 & Shpilfoygel 1999] who fitted a parabola to the function $\Psi(s,t)$ before finding the value of s_{opt}. They reported a marginal improvement in flow measurement error compared to the ORG algorithm.

3.4.2 Novel Model Based Algorithm

The concentration-distance curve correlation algorithm was modified to include the information derived from the PCA based waveform shape model. For the purpose of this thesis, this algorithm was called the *model based algorithm* (MB algorithm).

Let the volumetric flow waveform to be measured in a target artery be $\mathbf{G}$, where volumetric flow is measured in millilitres per minute. Assuming that a blood flow waveform shape model has been constructed that includes the target artery waveform in its statistical population, $\mathbf{G}$ can be estimated by

$$\mathbf{G} \cong \overline{\mathbf{P}} + \sum_{i=1}^{i=k} w_i \mathbf{e}_i \tag{3.20}$$

where k out of the possible S PCs are used and $1 \leq k \leq S$.

The model fitting task entails selecting the values of w_i that minimize the mean value of the cost function $\Psi(s,t)$.

Stage 1:

The concentration-distance curve function $\mathbf{C}(x,t)$ will contain one or more flow cycles depending on the cardiac rate and the number of frames acquired. For the cycle for which the shape model is to be fitted, t_s is the starting frame and t_e is the end frame of the cycle. The cycle length is then given by

$$T_c = t_e - t_s + 1. \tag{3.21}$$

Initially, the waveform $\mathbf{G}$ contains S sample points. $\mathbf{G}$ is now rescaled by linear interpolation to T_c sample points to give $\mathbf{G}(t)$ where $0 \le t \le T_c - 1$.

Stage 2:

The velocity $\mathbf{v}(t)$, measured in centimetres per minute, is calculated by

$$\mathbf{v}(t) = \frac{\mathbf{G}(t)}{A} \tag{3.22}$$

where A is the vessel cross-sectional area in centimetres squared.

Stage 3:

The velocity waveform is converted into units of mm shift per frame by

$$\mathbf{s}(t) = \frac{\mathbf{v}(t)}{k \times FR} \tag{3.23}$$

where $k = 6$ is the unit conversion factor.

Stage 4:

The cost function Φ is calculated by

$$\Phi = \frac{1}{T_c} \sum_{t=t_s}^{t=t_e} \Psi(s(t - t_s), t). \tag{3.24}$$

The values of the weighting factors w_i are found which minimize the cost function Φ. This is done by the downhill simplex method [Press 1997]. Eq. 3.20 can then be used to compute the extracted volumetric waveform using these weighting factors.

3.5 Summary

The use of Doppler ultrasound to assess vascular disease has shown that the shape of the flow waveform in arteries is characteristic for different arteries and changes when there is vascular disease. I formed the hypothesis that a priori knowledge of the likely blood flow waveform shape in a target artery could be used to improve the x-ray measurement of blood flow in that artery. The experience of investigators with the characterization of flow waveforms acquired using Doppler ultrasound suggested that PCA was a useful technique for classifying vascular disease. This combined with the flexibility of PCA for shape modeling, lead me to base my waveform shape model on PCA. I have detailed how a PCA based shape model can be constructed from many sample input flow waveforms. I have also showed how the dimensionality of the model can be reduced by retaining PCs based on residual error analysis. The concentration-distance curve correlation approach of Seifalian *et al.* was presented and was termed the *original algorithm* (ORG algorithm). Modeling the concentration-distance curves by polynomials prior to computation of blood flow velocity produced a slight variation of the ORG algorithm that was termed the *polynomial approximation algorithm* (PA algorithm). The PCA based shape model was combined with the concentration-distance curve correlation approach to produce a novel model based flow extraction algorithm (MB algorithm). This algorithm uses the waveform shape model to constrain the search

for the distance shifts between consecutive concentration-distance curves. The algorithm allows only the extraction of flow waveforms that are consistent with the waveform shape model. In chapter 6 of this thesis, I detail the validation of the MB and PA algorithms using a pulsatile blood flow circuit.

Chapter 4

A Weighted Optical Flow Algorithm to Measure Pulsatile Blood Flow Waveforms

4.1 Introduction

One-dimensional optical flow techniques, as discussed in chapter 2, have shown promising results for the measurement of blood flow from dynamic angiographic images. Whether based on the optical flow constraint equation or the equation of continuity for fluid flow, the approaches have two main disadvantages. Firstly, errors in velocity measurement arise when the temporal and spatial gradients of concentration are small. In particular, large errors can occur when the spatial gradient approaches zero since these techniques require division by this quantity. Secondly, the techniques are sensitive to noise in the image data. In order to overcome the first of these two disadvantages, I hypothesized that the magnitude of the spatial derivative could be used as a confidence measure on velocity estimates. For the second disadvantage, instead of using point estimates of velocity in the spatiotemporal plane, I hypothesized that

averaging estimates along the length of the blood vessel would reduce the effects of noise. These two hypotheses lead to the development of the novel weighted optical flow algorithm (OP algorithm) that is presented in this chapter. This algorithm is based on the 1D optical flow constraint equation. Using the parametric image representation of dynamic angiographic data, velocity estimates are obtained as a function of both distance along a vessel segment and of time. These initial estimates are then weighted according to the magnitude of the spatial derivative of contrast material concentration. Finally, the weighted estimates are averaged along the vessel length to obtain the weighted average velocity as a function of time. The mathematical detail of the weighted optical flow algorithm is described in the following section.

4.2 The Weighted Optical Flow Algorithm

The weighted optical flow algorithm operates on the parametric image representation of dynamic angiographic data. The parametric image consists of a temporal sequence of concentration-distance curves. Consider two consecutive curves, $\mathbf{C}(x,t)$ and $\mathbf{C}(x,t+1)$, separated in time by one sampling interval Δt. If the shape of the curves is not different then,

$$\mathbf{C}(x,t+1) = \mathbf{C}(x - v\Delta t, t) \tag{4.1}$$

where v is the contrast material bolus velocity. Using the first order Taylor series approximation,

$$\mathbf{C}(x - v\Delta t, t) \approx \mathbf{C}(x, t) - v\Delta t\mathbf{C}'(x,t). \tag{4.2}$$

Substituting Eq. 4.2 into Eq. 4.1 and rearranging,

$$v = -\frac{\frac{\mathbf{C}(x,t+1)-\mathbf{C}(x,t)}{\Delta t}}{\mathbf{C}'(x,t)}. \tag{4.3}$$

In the limit $\Delta t \to 0$,

$$v = -\frac{\frac{\partial \mathbf{C}(x,t)}{\partial t}}{\frac{\partial \mathbf{C}(x,t)}{\partial x}}. \tag{4.4}$$

Eq. 4.4 is the 1D form of the optical flow constraint equation. In this derivation, the assumption that consecutive concentration-distance time curves are the same shape is equivalent to the constant brightness constraint. Applying this equation to the parametric image, the initial velocity estimate, v_{tx}, for pixel (t,x) in the image is

$$v_{tx} = -FR\frac{\frac{\partial \mathbf{C}(x,t)}{\partial t}}{\frac{\partial \mathbf{C}(x,t)}{\partial x}} \tag{4.5}$$

where FR is the image acquisition rate, and $\frac{\partial \mathbf{C}(x,t)}{\partial t}$ and $\frac{\partial \mathbf{C}(x,t)}{\partial x}$ are the temporal and spatial derivatives respectively for pixel (t,x). The estimation of these derivatives is a key step in the determination of the blood flow velocity along the vessel. With typical temporal and spatial sampling intervals, the magnitude of the temporal changes in contrast material concentration is much greater than that of the spatial changes for the majority of points in the parametric image. Therefore, the estimation of the spatial derivative is more sensitive to noise in the image data than the estimation of the temporal derivative. Fourth order polynomials were fitted to the concentration-distance

profiles by the method of least squares (see also section 3.4.1). The spatial derivative was then estimated by differentiating these polynomials. The temporal derivative was estimated from the polynomial fitted curves by method of finite differences,

$$\frac{\partial \mathbf{C}(x,t)}{\partial t} = \frac{\mathbf{C}(x,t+1) - \mathbf{C}(x,t-1)}{2}. \tag{4.6}$$

In order to overcome errors that occur when the value of the spatial derivative is low, each initial velocity estimate is weighted according to the magnitude of the spatial derivative. The weighted velocity, $v_{tx}^{'}$, is

$$v_{tx}^{'} = w_{tx} v_{tx} \tag{4.7}$$

where $w_{tx} = \frac{1}{k}\left|\frac{\partial C_{tx}}{\partial x}\right|$ and k is the maximum value of the magnitude of the spatial derivative in the parametric image. Assuming that the vessel cross-sectional area remains constant as a function of distance along the vessel, the weighted velocities are then averaged along the length to yield an average velocity value, $\overline{v_t^{'}}$, for each frame in the image sequence. The average instantaneous velocity is given by

$$\overline{v_t^{'}} = \frac{\sum_{x=0}^{x=L-1} v_{tx}^{'}}{\sum_{x=0}^{x=L-1} w_{tx}} \tag{4.8}$$

where L is the vessel segment length in mm. The volumetric flow waveform can then be calculated by multiplying the estimated velocity values by the cross-sectional area of the vessel.

4.3 Discussion

The weighted optical flow algorithm presented in this chapter is related to the approaches of Efron *et al.* [Efron 1978] and Huang *et al.* [Huang 1997a]. It differs from these techniques in the following ways:

1. Efron *et al.* used only 4 points covering a distance of 16 mm along the length of the target vessel to obtain 4 estimates of velocity for each angiographic image. My approach uses all points along the vessel length to compute velocity. Moreover, the algorithm combines the velocities using weighting based on the magnitude of the spatial derivative. Both of these features are likely to make the algorithm more robust to image noise.
2. Like the technique of Efron *et al.*, the approach of Huang *et al.* produced point estimates for velocity as a function of distance along the target vessel for each angiographic image. Moreover, the method was only valid for measurements made along the leading edge of the bolus, thereby applicable to a very limited part of the angiographic sequence. My algorithm can be used for all the images of the angiographic sequence that contain contrast material in the vessel lumen.

It is important to consider the assumptions made by the weighted optical flow algorithm:

1. The weighted optical flow algorithm makes the assumption that the shape of the concentration-distance curve does not change within one sampling interval. This is equivalent to the constant brightness constraint of optical flow. For angiographic images, this will occur if the bolus moves with the same velocity in all parts of the vessel, i.e. in conditions of plug flow, and if there is zero diffusion of contrast

material. In physiological flow conditions, there is variation between the conditions of plug and laminar flow. Under conditions of laminar flow, convective dispersion will cause the bolus shape to change over time, predominating over the effects of diffusion.

2. In averaging velocity estimates along the length of the target vessel, the weighted optical flow algorithm assumes that vessel cross-sectional area is constant. This means that this algorithm is not suitable for velocity measurements on arteries with significant taper or for a vessel segment that includes a region of stenosis.

4.4 Summary

The previously reported 1D optical flow algorithms for measurement of blood flow from angiographic data suffer from two main limitations. They fail when the temporal and spatial derivatives of contrast material are small, and they are sensitive to image noise. I have developed a weighted optical flow algorithm that addresses these limitations in two ways. Firstly, it uses the magnitude of the spatial derivative as a weighting factor for measured velocities. Secondly, it averages velocities along the length of the target vessel. The differences of this algorithm from related previous approaches have been discussed as have the assumptions made by the new approach.

The weighted optical flow algorithm was validated by two methods. Firstly, in chapter 5 of this thesis, I detail the initial validation using a computer simulation of pulsatile flow. Secondly, in chapter 6, I detail the further validation using a pulsatile blood flow circuit and comparison to the concentration-distance curve correlation approaches described in chapter 3.

Chapter 5

Validation of the Weighted Optical Flow Algorithm using Synthetic Parametric Images

5.1 Introduction

This chapter details the validation of the weighted optical flow algorithm using a computer simulation of pulsatile blood flow. The output of the simulation were synthetic parametric images. The theory of the underlying flow model and the method to generate the parametric images is given in section 5.2. The performance of the weighted optical flow algorithm was tested by two simulation experiments. The first experiment investigated the variation of measured flow velocity with changing vessel length, changing distance from the contrast material injection site, and added noise in the synthetic parametric images. The second experiment investigated the ability of the weighted optical flow algorithm to measure a range of physiological velocities. The details of the simulation studies are given in section 5.3.

5.2 Generation of Synthetic Parametric Images

The computer simulation used a model of blood flow through a straight vessel of constant circular cross-section. The simulation allowed for injection of contrast material into the vessel and calculated the total mass of contrast medium present in the vessel as a function of distance from the injection site and of time from the start of the injection. The output from the simulation was a parametric image. Table 5.1 shows the parameters used for the computer simulation and the definitions of the symbols used in this section.

Parameter	Symbol	Units
Length of the vessel segment	L	mm
Radius of the vessel segment	R	mm
Number of cylindrical laminae	N	
Blood flow waveform	$Q_b(t)$	ml/min
Contrast medium injection waveform	$Q_c(t)$	ml/min
Contrast medium concentration	c	mg/ml
Spatial sampling interval	Δx	mm
Temporal sampling interval	Δt	s
Total length of time after start of flow	T	s
Heart rate	f	/min

Table 5.1: Parameters used in the computer flow simulation.

The assumptions made by the flow model were:

1. The blood flow is laminar.
2. The vessel is straight, of constant circular cross-section, does not have any branches, and has rigid walls.
3. There is zero diffusion of contrast material.
4. The contrast material mixes uniformly with the blood at the injection site.
5. The flow of contrast material is additive to the blood flow in the vessel.

Figure 5.1 illustrates that the simulated vessel was divided into N cylindrical laminae each of constant width $\frac{R}{N}$. For laminar flow, the maximum velocity of the blood flow is given by

$$v_{\max}(t) = \frac{2Q_b(t)}{\pi R^2}. \tag{5.1}$$

The fraction of the blood flow in lamina n where $0 \le n \le N-1$ is

$$qb_n(t) = \int_{r_n}^{r_{n+1}} 2\pi v_{\max}(t)(1-\frac{r^2}{R^2})rdr \tag{5.2}$$

where $r_n = \frac{nR}{N}$.

The fraction of the added flow due to contrast material injection in lamina n is

$$qc_n(t) = \frac{Q_c(t)(r_{n+1}^2 - r_n^2)}{R^2}. \tag{5.3}$$

Therefore the total flow in lamina n is

$$qt_n(t) = qb_n(t) + qc_n(t). \tag{5.4}$$

Now, the velocity as a function of time in lamina n is given by

$$v_n(t) = \frac{qt_n(t)}{\pi(r_{n+1}^{\ 2} - r_n^{\ 2})}. \tag{5.5}$$

Also, the injected mass of iodine as a function of time in lamina n is given by

$$m_n(t) = qc_n(t).c \tag{5.6}$$

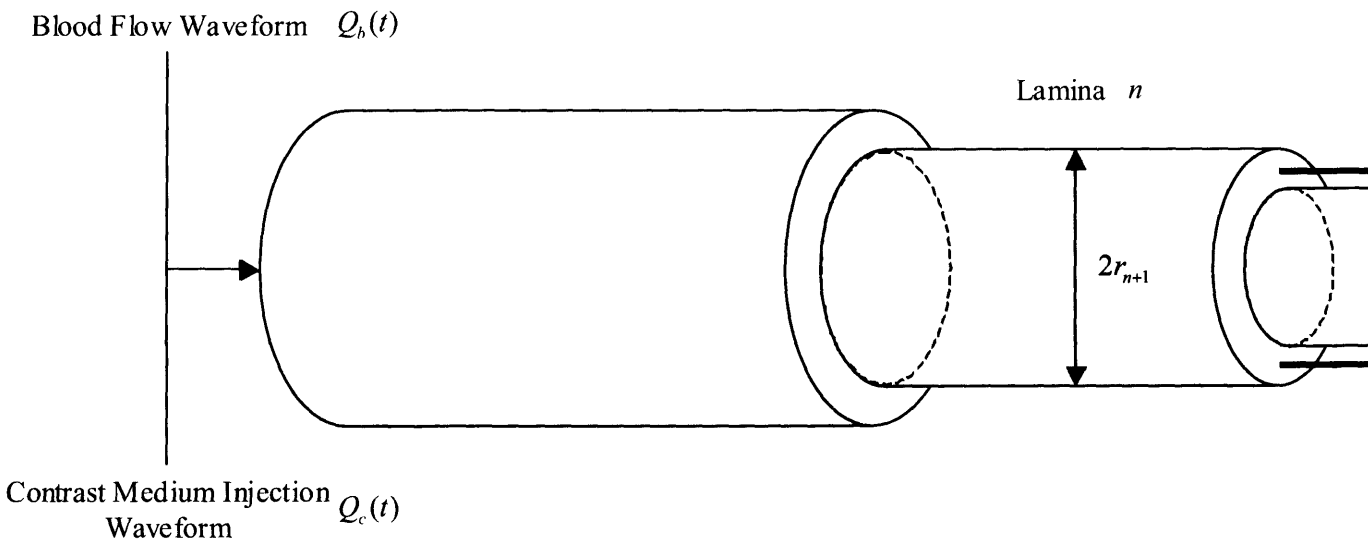

Figure 5.1: Division of the simulated blood vessel into concentric laminae by the computer flow model.

Therefore, for each lamina, both the velocity and mass of injected iodine are known as a function of time. The velocity-time curves and the mass-time curves for each lamina are then used to calculate the total mass of iodine as a function of time and distance along the vessel in discrete steps of Δt and Δx, respectively.

The output of the simulation program was a parametric image that was scaled in grey level so that it corresponded to 8 bits of information with the maximum value of 255 and the minimum value of 0. Zero mean Gaussian noise with standard deviation equal to a specified percentage of the maximum grey value could then be added to the images. This would simulate the additive effects of all sources of noise in the formation of the parametric image from an actual angiographic sequence.

5.3 Simulation Studies

Two simulation studies were performed, simulation study 1 and simulation study 2. The methodology and results for each study are now presented.

5.3.1 Simulation Study 1 Methodology

The first simulation study was carried out to assess the effect of the following parameters on the velocity measurement made by the weighted optical flow algorithm:

1. The distance from the contrast medium injection site.
2. The length of the vessel segment over which velocities were averaged.
3. The noise in the image data.

Parameter	Value	Units
Length of the vessel segment	500	mm
Radius of the vessel segment	3	mm
Number of cylindrical laminae	500	
Blood flow waveform	See figure 5.2	ml/min
Contrast medium injection waveform	Constant injection at 180 ml/min	ml/min
Contrast medium concentration	300	mg/ml
Spatial sampling interval	1	mm
Temporal sampling interval	0.04	s
Total length of time after start of flow	5	s
Heart rate	60	/min

Table 5.2: Parameters used for simulation study 1.

Table 5.2 shows the parameters that were used for simulation study 1. The input waveform used for this study was constructed from an EMF recording taken during one of the pulsatile flow circuit studies described in chapter 6. Figure 5.2a shows the EMF waveform. The mean flow rate for this waveform was 121 ml/min and the instantaneous flow values ranged from 0 to 433 ml/min. This corresponds to a mean velocity of 71.5 mm/sec and instantaneous velocities from 0 to 255 mm/sec in the 6 mm diameter simulated vessel. This waveform was repeated at 1 second intervals for 5 seconds and added to the contrast medium injection waveform to form the total flow waveform as shown in figure 5.2b. The parametric image generated by the computer simulation is shown in figure 5.3a. This parametric image was used to generate 3 other images with increasing levels of zero mean Gaussian noise of standard deviation 2, 5, and 10% of the maximum grey value. Figure 5.3b shows the parametric image with 5% added noise. The velocity waveforms for the 4 parametric images were calculated using the weighted optical flow algorithm. The vessel segment length over which velocities were averaged and the distance of measurements from the contrast medium injection site were varied by placing a moving window over the parametric images. Vessel segment lengths of 25,

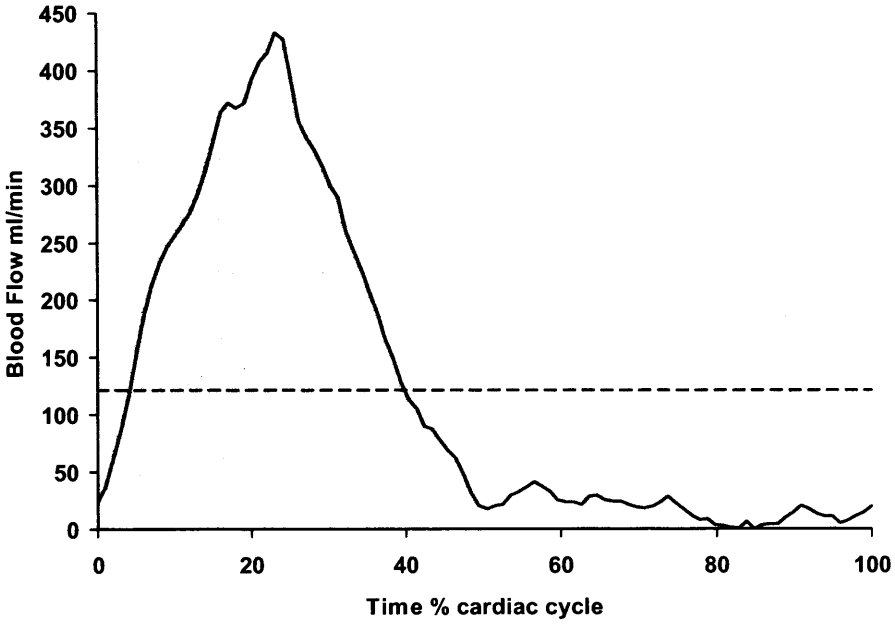

(a)

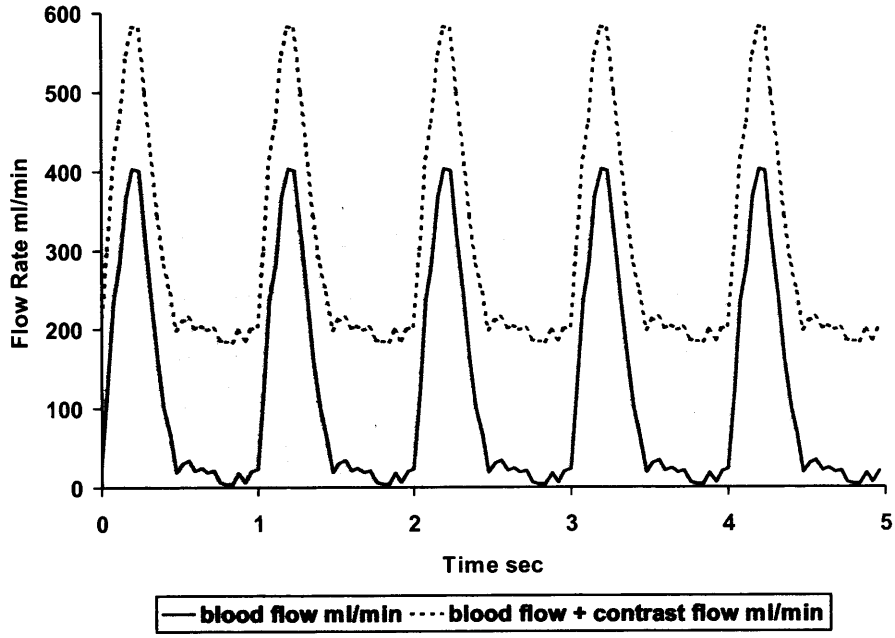

(b)

Figure 5.2: Simulation study 1: (a) The EMF recording that was used to construct the blood flow input waveform. The dotted line indicates the mean flow. (b) The solid line shows the blood flow input waveform. The dotted line is the total flow waveform that is equal to the sum of the blood flow waveform and the contrast material injection waveform. The contrast material injection rate was constant at 180 ml/min.

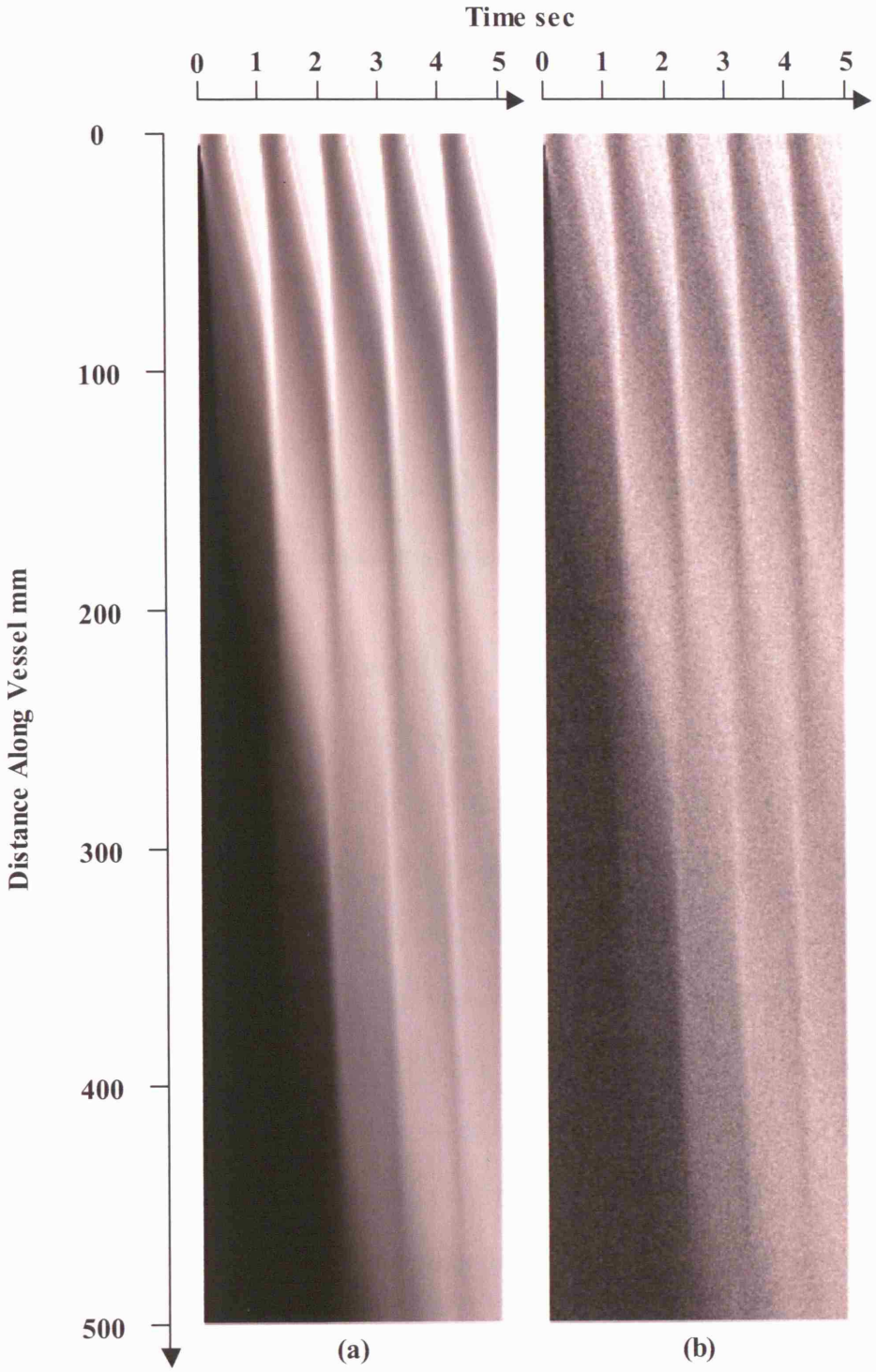

Figure 5.3: Simulation study 1: (a) Parametric image generated from the computer simulation using the input waveform shown in figure 5.2b. (b) Parametric image formed from (a) by adding zero mean Gaussian noise with standard deviation equal to 5% of the maximum grey value.

50, 75, 100, 125, and 150 mm were used. Also, for each length, the distance from the injection site at which measurements were started from was varied from 0 to 300 mm in steps of 5 mm. If l is the length of the vessel segment used for flow calculation and D is the distance from the injection site at which measurements were started, then the location of the average point used for measurements is

$$\overline{D} = D + \frac{l}{2}. \tag{5.7}$$

The computed velocities were compared to the known true velocities from the total flow waveform and the results are presented in section 5.3.3.

5.3.2 Simulation Study 2 Methodology

For the second simulation study, the ability of the weighted optical flow algorithm to measure blood flow velocity for a range of different mean velocities was assessed. The input parameters used for simulation study 2 were identical to those shown in table 5.2. However, the input waveforms were derived from the waveform shape model that was based on principal component analysis of many EMF recordings as described in section 6.3. 31 input waveforms were generated using the shape model by adding a variable amount of the first mode of variation to the mean waveform shape. –1.0 to +3.0 standard deviations of the first eigenvector where added to the mean shape to generate the waveforms shown in figure 5.4. The mean flow rate ranged from 119 to 294 ml/min and the instantaneous flow values ranged from –70.6 to 891 ml/min. This corresponds to mean velocities from 70.3 to 173 mm/sec and instantaneous velocities from -41.6 to 525 mm/sec in the 6 mm diameter simulated vessel. The parametric images generated from the computer flow model were corrupted by 2% added noise. Velocities were

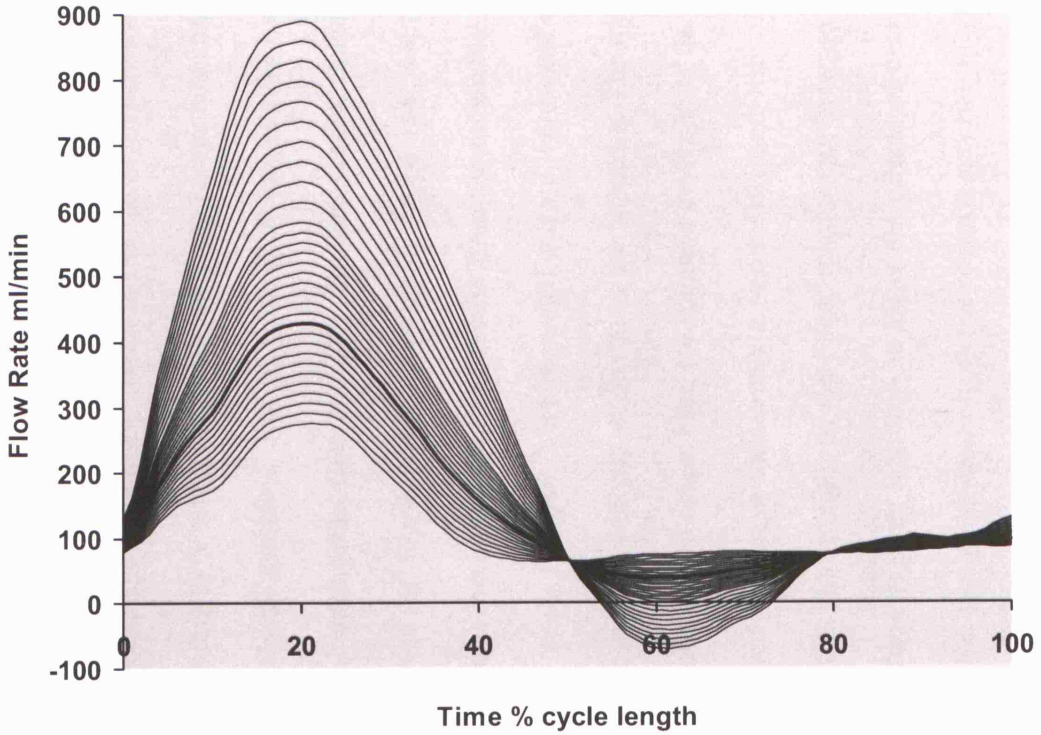

Figure 5.4: Simulation study 2: The 31 input waveforms used. These were derived from the PCA based waveform shape model of EMF recordings detailed in section 6.3. The waveforms were formed by adding –1.0 to +3.0 standard deviations of the first mode of variation to the mean waveform shape.

estimated for a segment length of 100 mm and at a starting distance of 75 mm from the injection site, which corresponds to an average measurement distance of 125 mm. The computed velocities were compared to the known true velocities from the total flow waveforms and the results are presented in section 5.3.4.

5.3.3 Simulation Study 1 Results

Application of the weighted optical flow algorithm to the synthetic parametric images produced waveforms consisting of 5 complete cycles. Each cycle was composed of 25 equally spaced temporal velocity estimates. Not all parts of the target vessel segments contained contrast material during the first 2 cycles. In these cases, modeling the concentration-distance curves by fourth order polynomials failed (see section 4.2). Therefore, the first two cycles were not used. The results from the remaining 3 cycles were almost identical. The results for cycle 3 are presented and are representative of the data. The methods used for the data analysis are given in the appendix. The mean error of velocity measurements was used to assess bias, the standard deviation of the velocity measurement error was used to assess measurement variability, and the correlation coefficient was used to assess the strength of the linear relationship between velocity measurements and true values. Figures 5.5a to 5.5c show the effects of changing the vessel segment length and the average distance from the contrast material injection site. Figures 5.6 a to 5.6c show the effects of added noise and average distance from the injection site for a fixed vessel segment length of 100 mm.

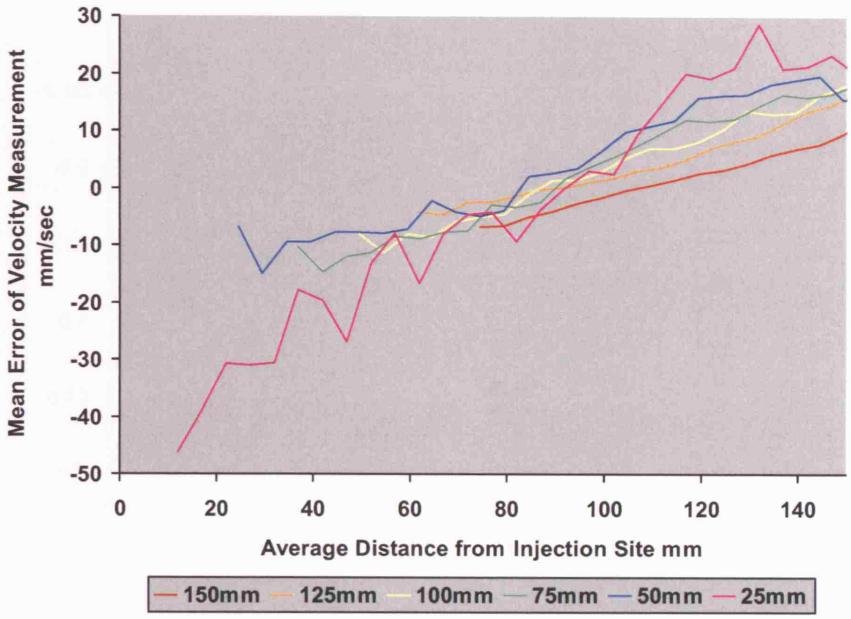

Figure 5.5a: Simulation study 1: The variation of mean error of velocity measurement with average distance from the injection site. Results were computed using vessel segment lengths of 25-150 mm and are shown as the different coloured lines.

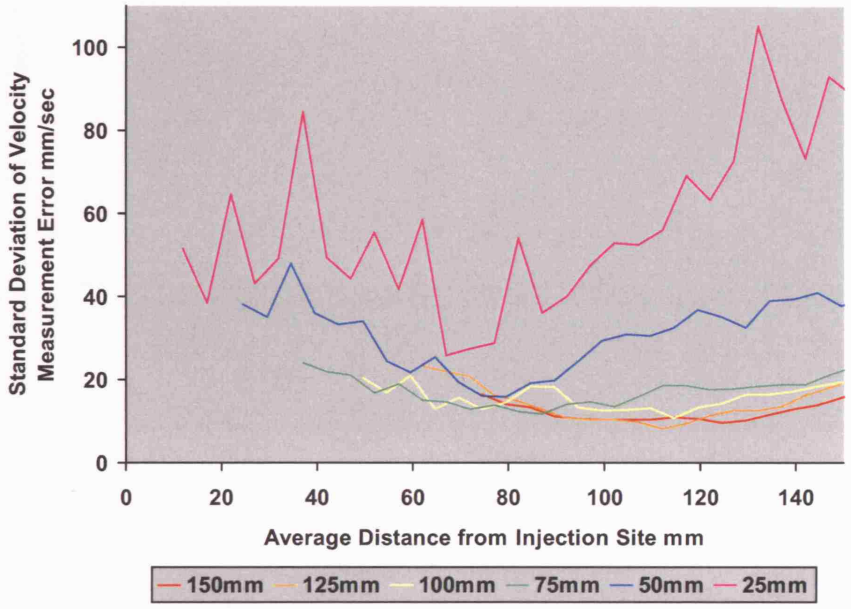

Figure 5.5b: Simulation study 1: The variation of standard deviation of velocity measurement error with average distance from the injection site. Results were computed using vessel segment lengths of 25-150 mm and are shown as the different coloured lines.

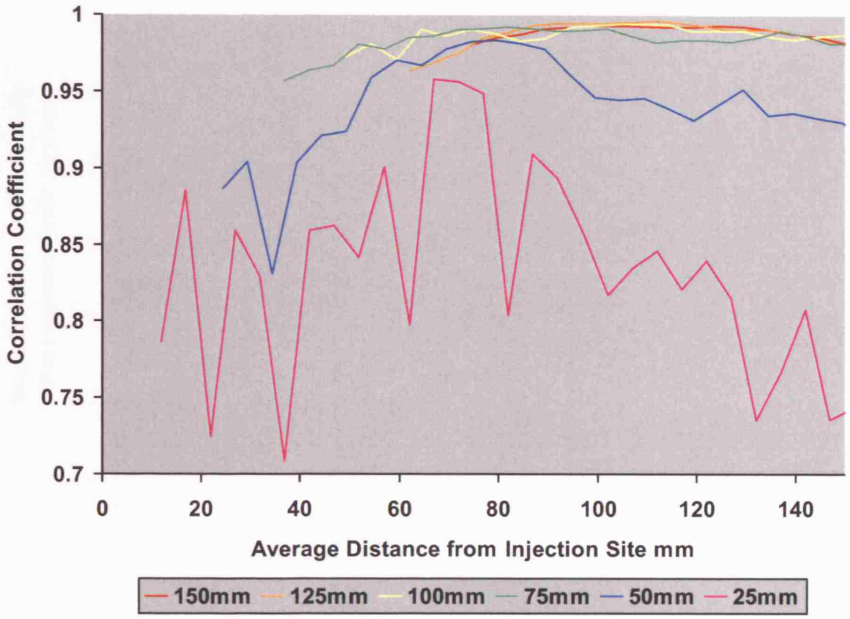

Figure 5.5c: Simulation study 1: The variation of correlation coefficient with average distance from the injection site. Results were computed using vessel segment lengths of 25-150 mm and are shown as the different coloured lines.

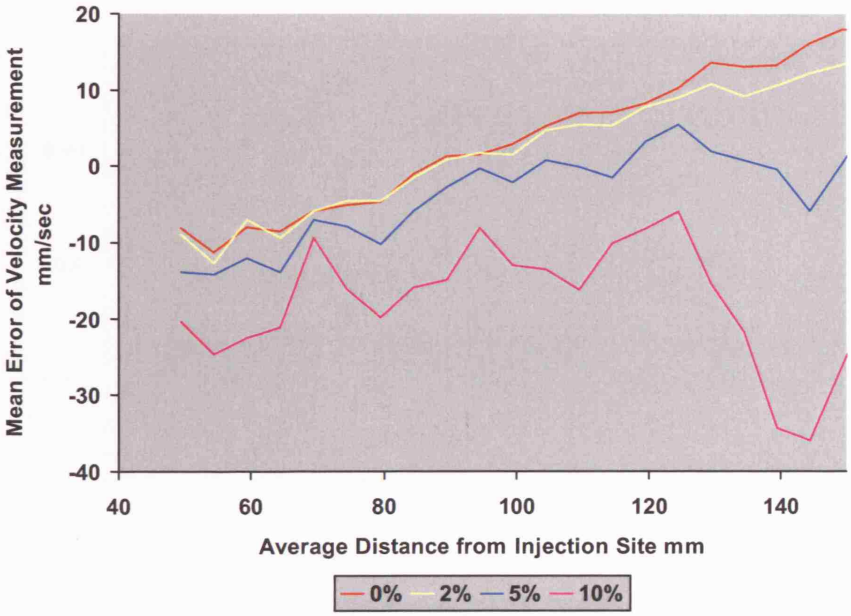

Figure 5.6a: Simulation study 1: The variation of mean error of velocity measurement with average distance from the injection site. The vessel segment length was 100 mm. Results were computed using 0 to 10% added noise and are shown as the different coloured lines.

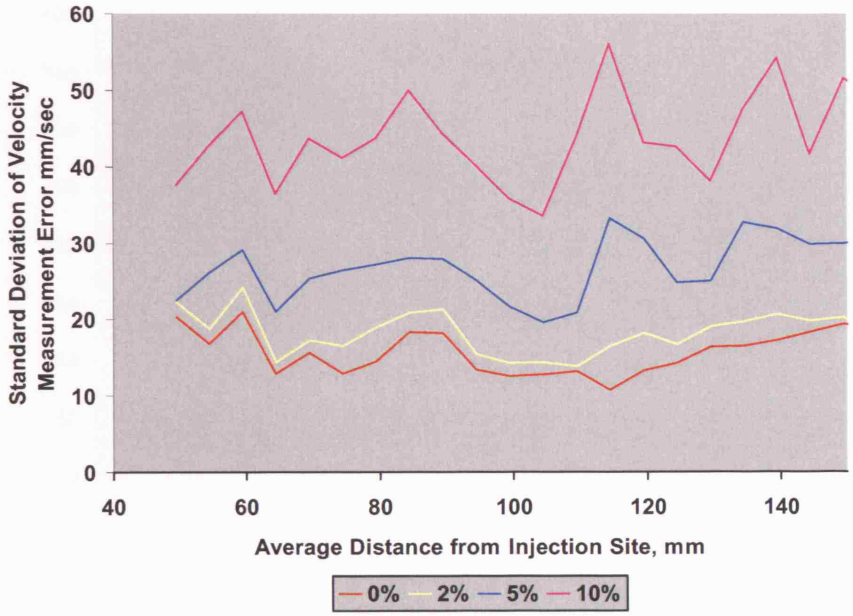

Figure 5.6b: Simulation study 1: The variation of standard deviation of velocity measurement error with average distance from the injection site. The vessel segment length was 100 mm. Results were computed using 0 to 10% added noise and are shown as the different coloured lines.

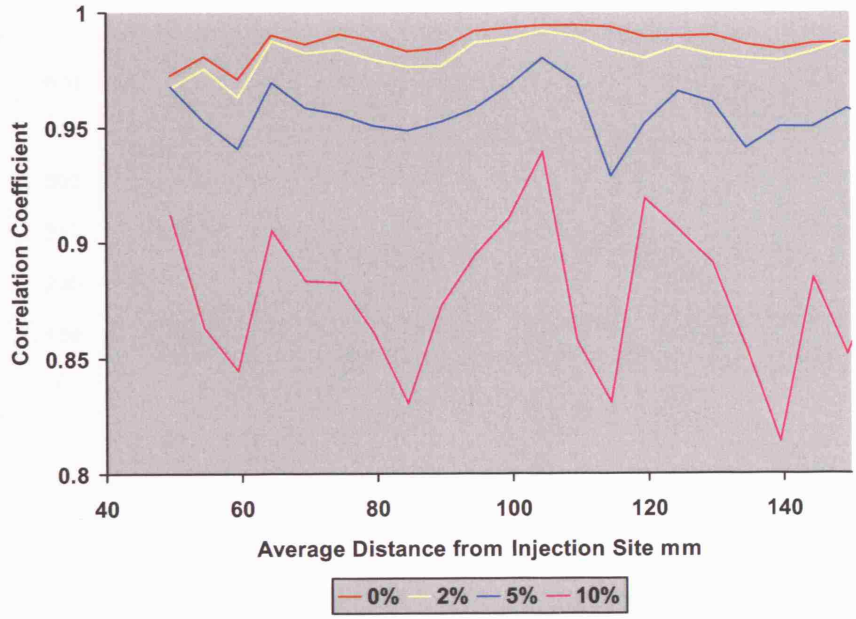

Figure 5.6c: Simulation study 1: The variation of correlation coefficient with average distance from the injection site. The vessel segment length was 100 mm. Results were computed using 0 to 10% added noise and are shown as the different coloured lines.

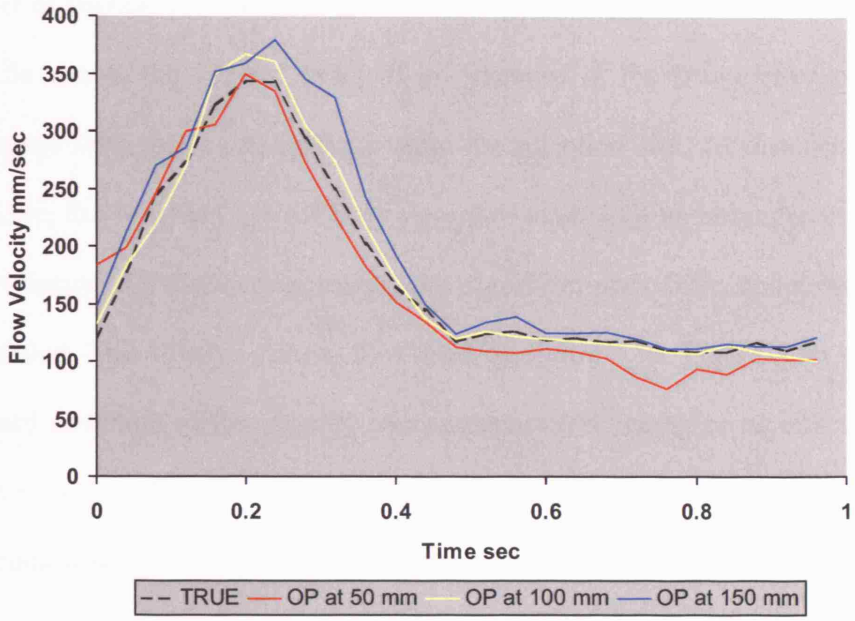

Figure 5.7a: Simulation study 1: Computed velocity waveforms for cycle 3. The vessel segment length was 100 mm. The solid lines show waveforms computed at average distances of 50, 100, and 150 mm from the injection site and the dotted line shows the true velocity waveform for comparison.

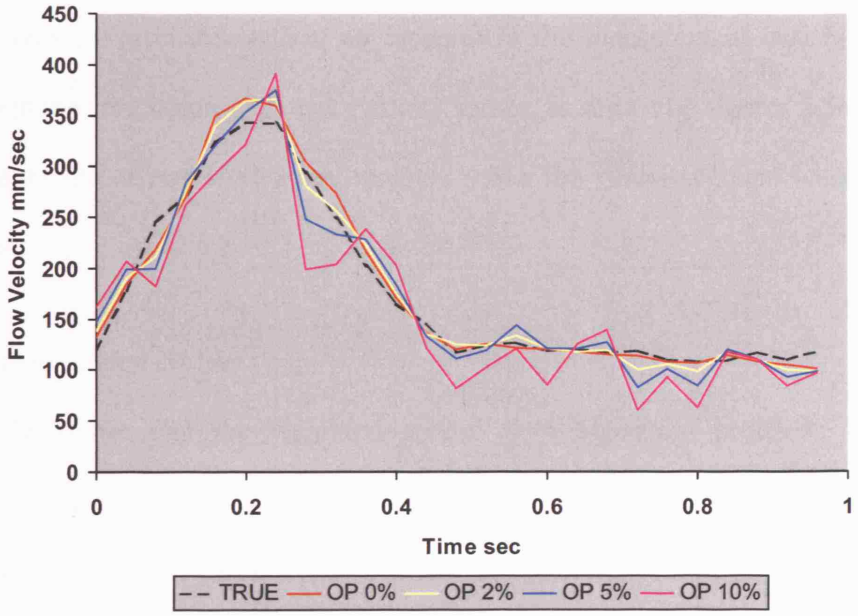

Figure 5.7b: Simulation study 1: Computed velocity waveforms for cycle 3. The vessel segment length was 100 mm. The solid lines show waveforms computed for added noise levels of 0, 2, 5, and 10% and the dotted line shows the true velocity waveform for comparison.

The Effect of Distance from the Injection Site:

Figure 5.5a shows the general trend of an increase in the mean error of velocity measurements with increasing distance from the injection site. At distances near the injection site, the weighted optical flow algorithm tends to give an underestimation of the true velocity. As distance increases, the algorithm goes from underestimation to overestimation. This trend is further illustrated by figure 5.7a. Figure 5.5b shows that the standard deviation of the velocity measurement error increases on either side of a minimum value as a function of distance from the injection site. Figure 5.5c illustrates that correlation with true velocity decreases on either side of a maximum value as a function of distance.

The Effect of Vessel Segment Length:

Reducing the vessel segment length over which the weighted optical flow algorithm averages velocity estimates caused an increase in the measurement variability and a reduction in the correlation with true velocity values, as shown by figures 5.5b and 5.5c, respectively. The effects were most apparent when the vessel segment length was 50 mm or less.

The Effect of Added Noise:

Figure 5.6a shows that the weighted optical flow algorithm produced increasing underestimation of true velocity as the noise the parametric images was increased. The variability of measurements increased with increasing noise, as illustrated in figure 5.6b. Figure 5.6c shows that correlation with true velocity values decreased with increasing noise. These effects are further illustrated by figure 5.7b.

5.3.4 Simulation Study 2 Results

The weighted optical flow algorithm was used to extract the velocity waveform for each of the 31 input waveforms used in simulation study 2. For the same reasons as mentioned in section 5.3.3, only the last 3 cycles out of 5 were used in the data analysis. For each waveform, the instantaneous velocity estimates were compared to the true velocities. Also, the mean velocity over the entire waveform was compared to the true mean velocity. The statistical methods used were the correlation coefficient and Bland-Altman analysis (see appendix).

Figure 5.8 illustrates an example velocity waveform calculated using the weighted optical flow algorithm and the true velocity waveform with a mean velocity of 211 mm/sec. It can be seen that the calculated waveform follows the true waveform closely. There is greater velocity measurement variability during the diastolic parts of the flow cycles when the flow rate is slowly changing.

	Instantaneous Velocity	**Mean Velocity**
Range of calculated velocity values	-28.5 to 1040 mm/sec (-48.3 to 1770 ml/min)	178 to 271 mm/sec (302 to 460 ml/min)
Range of true velocity values	65.6 to 630 mm/sec (111 to 1070 ml/min)	176 to 278 mm/sec (299 to 471 ml/min)
Correlation coefficient	0.931 (n=2294, $p<0.0001$)	0.997 (n=31, $p<0.0001$)
Mean error (calculated – true)	2.11 mm/sec (3.57 ml/min)	2.12 mm/sec (3.60 ml/min)
95% Limits of agreement	-97.1 to 101 mm/sec (-165 to 172 ml/min)	-4.01 to 8.25 mm/sec (-6.80 to 14.0 ml/min)

Table 5.3: Summary of statistical results for simulation study 2.

Table 5.3 shows the statistical results for simulation study 2. There were a total of 2294 instantaneous velocity estimates that were compared to the true velocity values.

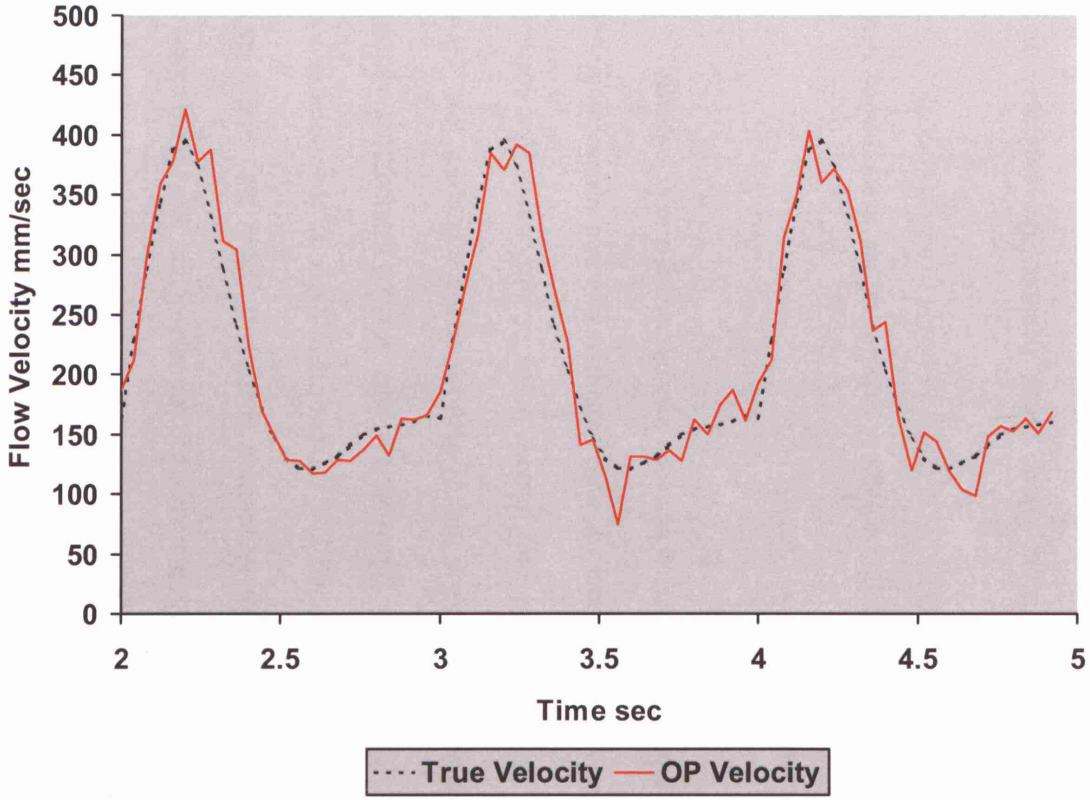

Figure 5.8: Simulation study 2: Example of a velocity waveform calculated using the weighted optical flow algorithm and the true velocity waveform for comparison. The true mean velocity was 211 mm/sec.

Figure 5.9 shows a scatter plot of this data and figure 5.10 is the Bland-Altman plot. It can be seen that the data points are distributed symmetrically about the line of identity or the zero error line for velocities up to approximately 450 mm/sec. However, for higher velocities there was overestimation. The overall bias was a very small overestimation of 2.11 mm/sec and the 95% limits of agreement were narrow when compared to the range of velocities that were measured. The patterning of points that is visible in figures 5.9 and 5.10 resulted from the use of the waveform shape model to derive the input waveforms for simulation study 2. Figures 5.11 and 5.12 show the scatter plot and the Bland-Altman plot for the mean velocity measurements computed by averaging the instantaneous velocities for each of the 31 calculated waveforms. The data points were very close to the line of identity or the zero error line, giving a very small bias of 2.12 mm/sec and very narrow limits of agreement. The correlation with true velocity was very significant for both instantaneous and mean calculated velocity showing a strong linear relationship between measured and true velocities.

5.4 Discussion

It is important to consider the physiological validity of the assumptions made by the flow model in section 5.2:

1. Under physiological conditions, flow varies between the extremes of plug and laminar flow.
2. Arterial vessels can be tortuous. They usually show a gradual tapering of cross-sectional area with distance. Long, unbranched segments are uncommon in the human arterial tree. Finally, arteries are elastic and will undergo cross-sectional area changes due to the pulsatile pressure variations within their lumens.

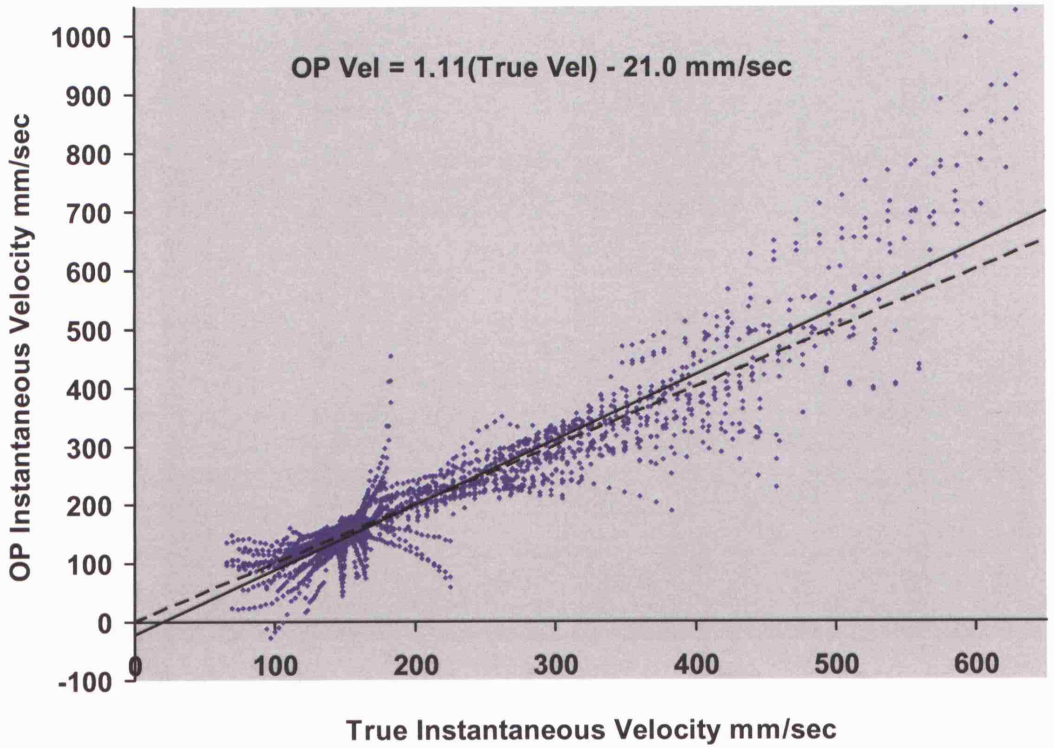

Figure 5.9: Simulation study 2: Scatter graph showing the instantaneous velocity computed using the weighted optical flow algorithm against the true instantaneous velocity. The solid line is the regression line with equation given. The dotted line is the line of identity. PMCC = 0.931, n=2294.

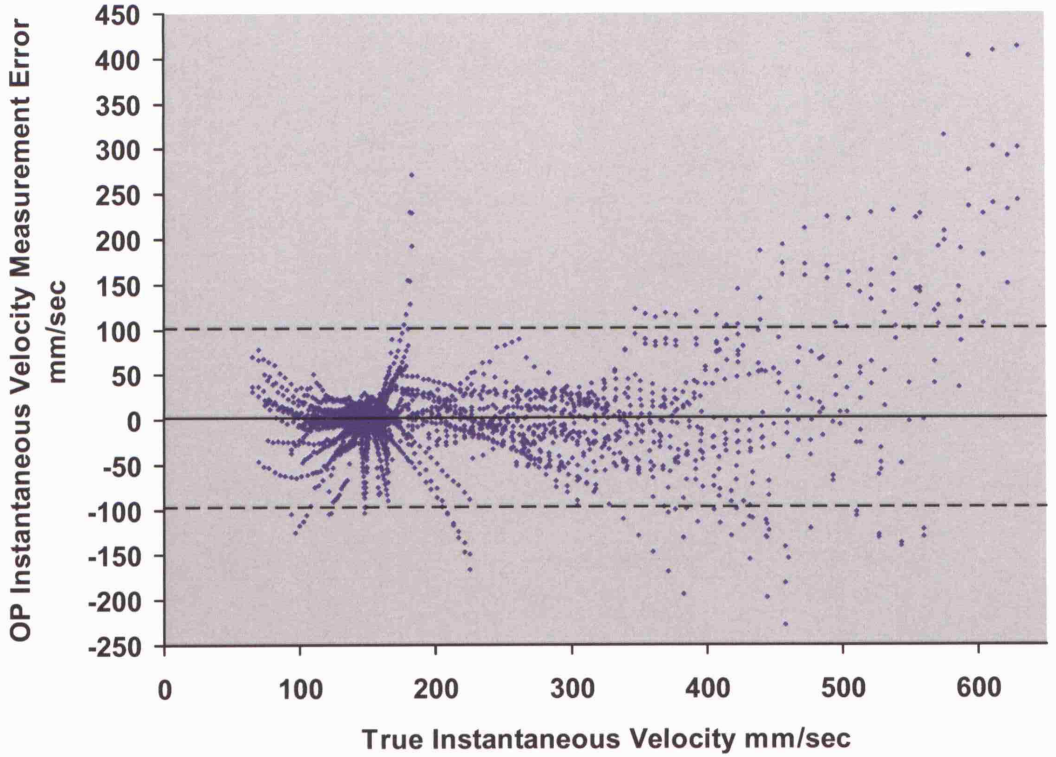

Figure 5.10: Simulation study 2: Plot of instantaneous velocity measurement error against true instantaneous velocity for velocities determined using the weighted optical flow algorithm. The mean measurement error is shown as the solid line and the dotted lines show the 95% limits of agreement.

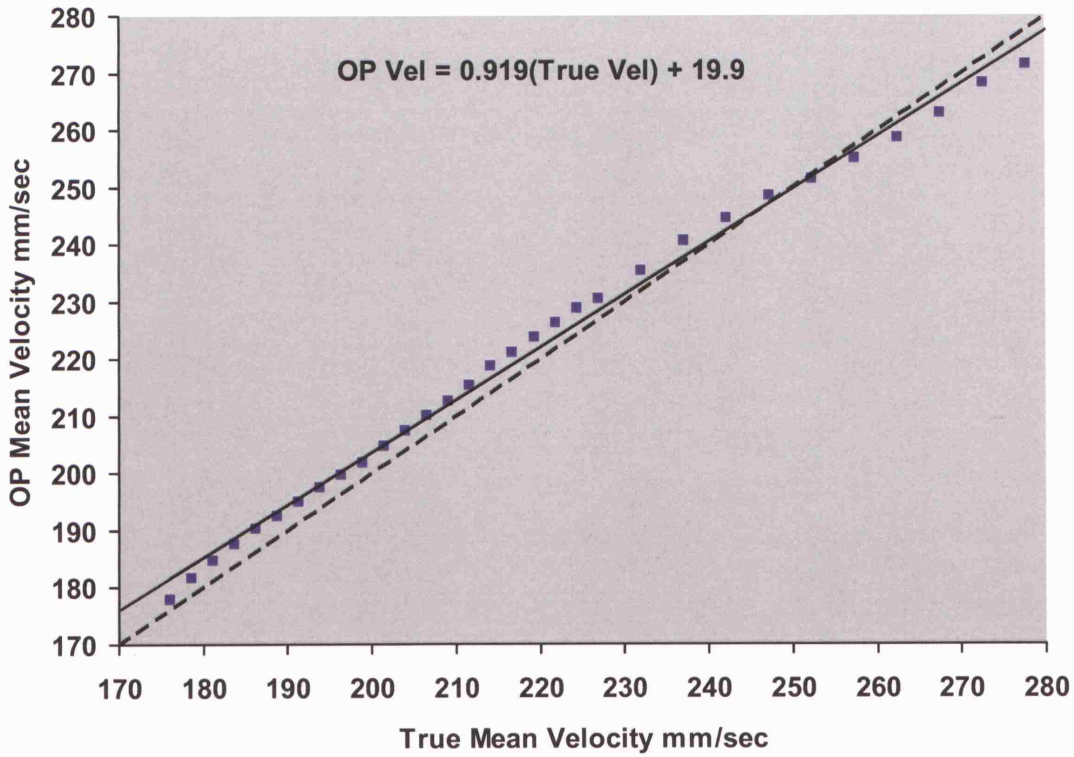

Figure 5.11: Simulation study 2: Scatter graph showing the mean velocity computed using the weighted optical flow algorithm against the true mean velocity. The solid line is the regression line with equation given. The dotted line is the line of identity. PMCC = 0.997, n=31.

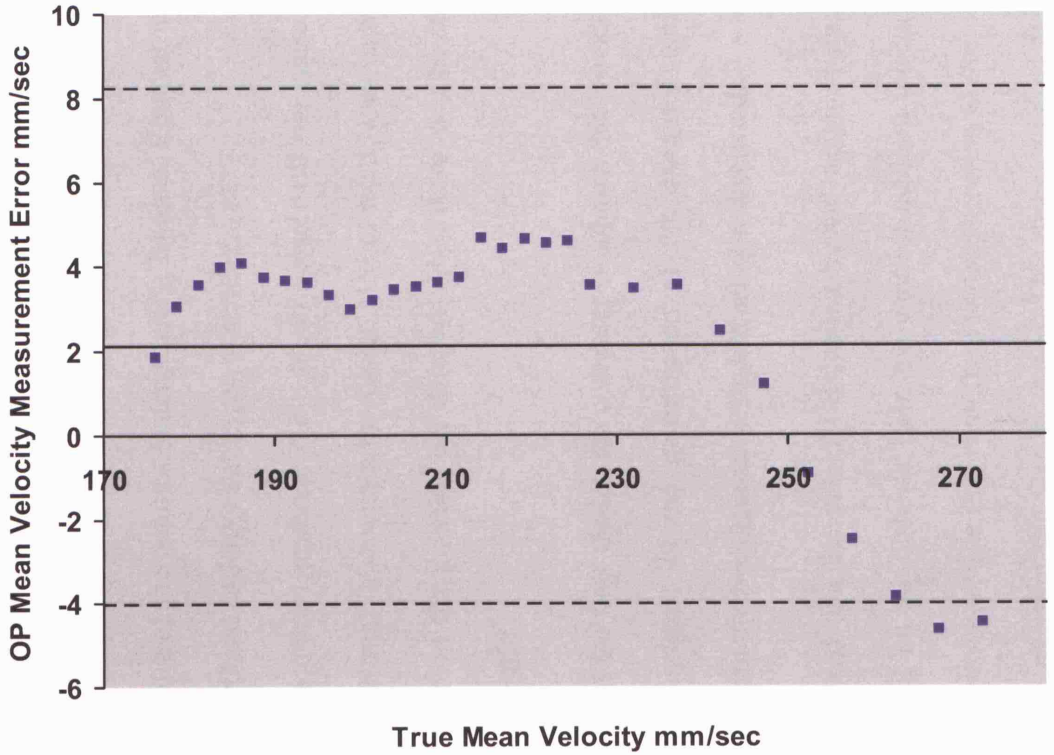

Figure 5.12: Simulation study 2: Plot of mean velocity measurement error against true mean velocity for velocities determined using the weighted optical flow algorithm. The mean measurement error is shown as the solid line and the dotted lines show the 95% limits of agreement.

3. Contrast material undergoes diffusion as it propagates along a vessel. However, the effects of diffusion are minimal over the time periods for which angiographic images are acquired (typically a few seconds).
4. Contrast material does not mix uniformly with blood. Since the diameter of injection catheters is typically much smaller than the vessel under investigation, the contrast material is introduced into a small cross-sectional region of the blood vessel. This may produce streaming of the contrast material along laminae. Contrast material is also denser than blood and undergoes a degree of settling.
5. The introduction of contrast material into a blood vessel will not cause a purely additive effect on the total flow within the vessel. Due to the downstream vascular resistance, the effects of the injection are damped. Also, there may be some back flow of contrast material.

Despite the limitations of the flow model, the computer simulation did provide a useful initial tool for the assessment of the performance of the weighted optical flow algorithm. The results from the two simulation studies are now discussed.

Simulation study 1 showed that the velocity estimated by the weighted optical flow algorithm was dependent on the distance from the contrast medium injection site at which measurements were made. The bias went from underestimation to overestimation as the distance from the injection site was increased. This distance-based dependency was also reported by Huang *et al.* [Huang 1997a] for their optical flow based approach. In order to understand this effect, a distinction must be made between true fluid velocity and contrast material bolus velocity. Angiographic techniques can only measure the bolus velocity and use this as an estimate of the true fluid velocity. If the contrast

material mixes uniformly with the fluid and then undergoes no dispersion, the bolus velocity will exactly equal the fluid velocity. This will be the case if there is zero diffusion and plug flow. However, during the conditions of laminar flow, the effects of convective dispersion will predominate. The parts of the bolus traveling closer to the centre of the vessel are transported at a greater velocity. Therefore, as the bolus travels along the vessel, the leading edge of the bolus will have a velocity that is greater than the trailing edge. The velocity of the leading edge will be more than the average fluid velocity whereas the trailing edge will have a velocity that is lower. This explains the distance dependency observed in simulation study 1. It can be seen from figures 5.5a to 5.5c that there seems to be an optimal distance from the injection site at which velocity estimates made by the weighted optical flow algorithm produce least bias, least variability, and greatest correlation. This optimal distance lies in the range of 60 to 130 mm for the mean flow rate used in simulation study 1 but it is likely that this optimal distance will depend on the mean flow rate.

Simulation study 1 showed that decreasing the vessel segment length produced an increase in velocity measurement variability and a decrease in correlation. Since the weighted optical flow algorithm is carrying out a weighted average of velocities along the length of the vessel segment, for smaller vessel segments there will be less points along the vessel for which this can be done and therefore an increase in the statistical uncertainty. The performance of the algorithm was most affected when the vessel segment length was 50 mm or below. Velocity measurements can only be made if the contrast material bolus does not move entirely out of the vessel segment between successive temporal sampling intervals. The peak flow velocity was 343 mm/sec during simulation study 1. Therefore, the maximum displacement of the bolus in one sampling

interval (0.04 s) was approximately 14 mm. It is apparent that reliable velocity estimates were only achieved for vessel segments lengths that were much more than this minimum requirement.

With increasing image noise, simulation study 1 illustrated that the weighted optical flow algorithm produced velocity measurements that showed increasing underestimation, increasing variability, and decreasing correlation with the true velocity. Increasing the noise in the parametric images will increase the errors in the estimation of the temporal and spatial derivatives required to calculate velocity. In fact, Jahne [Jahne 1997] showed that differential based optical flow techniques will give underestimation of velocity in the presence of image noise.

Simulation study 2 showed that the weighted optical flow algorithm was able to measure a range of flow velocities with highly significant correlation, small bias and narrow limits of agreement for both instantaneous and mean flow rates. The instantaneous velocity results showed that there was greater measurement variability when the velocity was slowly changing in the diastolic part of the flow cycle. This is to be expected since both spatial and temporal gradients become small during this time. Furthermore, there was overestimation of the peak velocity for flow rates above 450 mm/sec. This can be explained by the effect of convective dispersion of the contrast medium bolus as discussed above.

5.5 Conclusion

The results from the simulation studies demonstrated the following properties of the weighted optical flow algorithm:

1. Velocity measurement was dependent on the distance from the injection site of the target vessel segment.
2. The performance of the algorithm increased as the vessel segment length was increased.
3. The algorithm showed decreasing performance with increasing noise in the synthetic parametric images.
4. When the distance from the injection site was fixed, the algorithm produced velocity estimates that were linear and showed low variability over a range of physiological flow rates.

These properties will have the following implications on the application of the weighted optical flow algorithm to clinical flow measurement:

1. The measurement of absolute blood flow may be limited because of the dependency on the distance from the contrast material injection site.
2. The requirement of relatively long vessel lengths may limit clinical application.
3. The algorithm may not be suitable for low dose fluoroscopy imaging due to sensitivity to noise.
4. The measurement of relative blood flow, e.g. to assess coronary flow reserve or to monitor serial changes during an intervention, may be practical since the algorithm demonstrates linearity and low variability if the distance from the contrast material injection site is kept constant.

The validation of the algorithm was taken forward using dynamic angiographic images of vessels in a pulsatile flow circuit and is detailed in chapter 6.

Chapter 6

Algorithm Validation using a Pulsatile Blood Flow Circuit

6.1 Introduction

This chapter describes the validation of the polynomial approximation (PA), weighted optical flow (OP) and model based (MB) algorithms using a pulsatile blood flow circuit. Section 6.2 details the flow circuit that was developed to simulate blood flow in arteries. The flow circuit included an EMF that was used as the gold standard for volumetric flow measurement. Section 6.2 also gives the details of the three different types of simulated vessel used:

1. Silicone tubing -
    a. stationary tubing of 3, 4, and 6 mm internal diameter.
    b. a moving section of tubing of 6 mm internal diameter.
2. Prosthetic vascular grafts -
    a. polytetrafluoroethene (PTFE)
    b. compliant polyurethane (CPU).

3. An anthropomorphic cerebral vascular phantom made from silicone.

The simulated vessels provided a progression of more challenging conditions for the x-ray determination of blood flow. Section 6.3 describes how a waveform shape model was formed from sample EMF waveforms collected from the pulsatile flow circuit. This shape model was a prerequisite for application of the model based algorithm. Dynamic x-ray images were acquired of the simulated vessels during injection of iodine based contrast material for a range of volumetric flow rates. The experimental protocol is detailed in section 6.4. The angiographic image data were analysed using an integrated software package called *"System for Angiographic Reconstruction and Analysis 2000"* (SARA 2000) as described in section 6.5. The PA, OP, and MB algorithms were applied to the resulting parametric images and the computed volumetric flow waveforms were compared to the simultaneously acquired EMF waveforms. The new algorithms were further compared to the original concentration-distance curve correlation (ORG) algorithm. Section 6.6 describes how one of the parametric images was used to assess the effects of varying the vessel segment length and of adding image noise. The results of all the experiments are presented in section 6.7.

Throughout the experimental studies, utmost care was taken to ensure that safety procedures were adhered to as stipulated by the place of work where experiments were carried out. This was particularly important with respect to the handling of blood products, since date-expired blood was used as the circulated fluid in the flow circuit, and with respect to exposure to x-ray radiation. All researchers present during x-ray imaging were monitored using film badges.

6.2 The Pulsatile Blood Flow Circuit

A pulsatile blood flow circuit was constructed to simulate blood flow in arteries and to allow the validation of the flow extraction algorithms using angiographic image data. The flow circuit had the following characteristics:

1. The flow was pulsatile and the mean flow rate, mean pressure, and waveform shape could be altered.
2. There was monitoring and recording of instantaneous/mean flow rate and pressure.
3. Date-expired blood was used as the circulating fluid.
4. The type of simulated vessel could be changed and different diameter vessels could be used.
5. The injection of contrast material was possible using a syringe connected to a catheter.
6. It was possible to set up and dismantle the flow circuit in the catheter laboratory safely, without the risk of spillage of blood products.

6.2.1 Components of the Flow Circuit

Figure 6.1 shows a schematic of the blood flow circuit and figure 6.2 shows the actual circuit in the catheter laboratory at the Royal Free Hospital, London, UK. A pulsatile pump (Pulsatile Blood Pump 1405, Harvard Apparatus, Massachusetts, USA) provided the pulsatile flow in the circuit and is shown in figure 6.3. The pumping mechanism consisted of a syringe connected to two one-way ball bearing valves. One valve allowed entry of fluid into the cylinder of the syringe during the filling phase, and the other

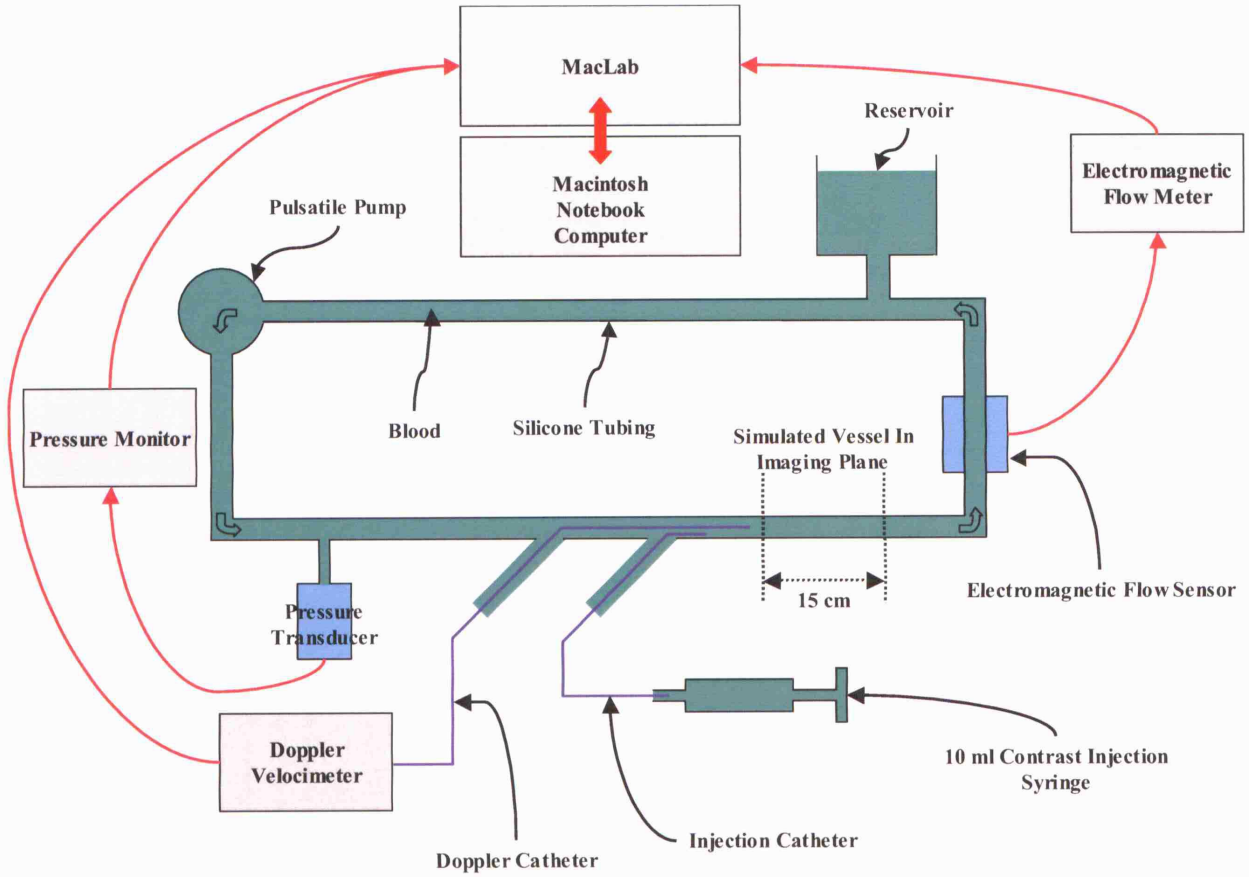

Figure 6.1: Schematic of the pulsatile blood flow.

Figure 6.2: The pulsatile blood flow circuit in the catheter laboratory at the Royal Free Hospital.

Figure 6.3: The pulsatile blood pump (Pulsatile Blood Pump 1405, Harvard Apparatus, Massachusetts, USA) that provided the pulsatile flow in the flow circuit.

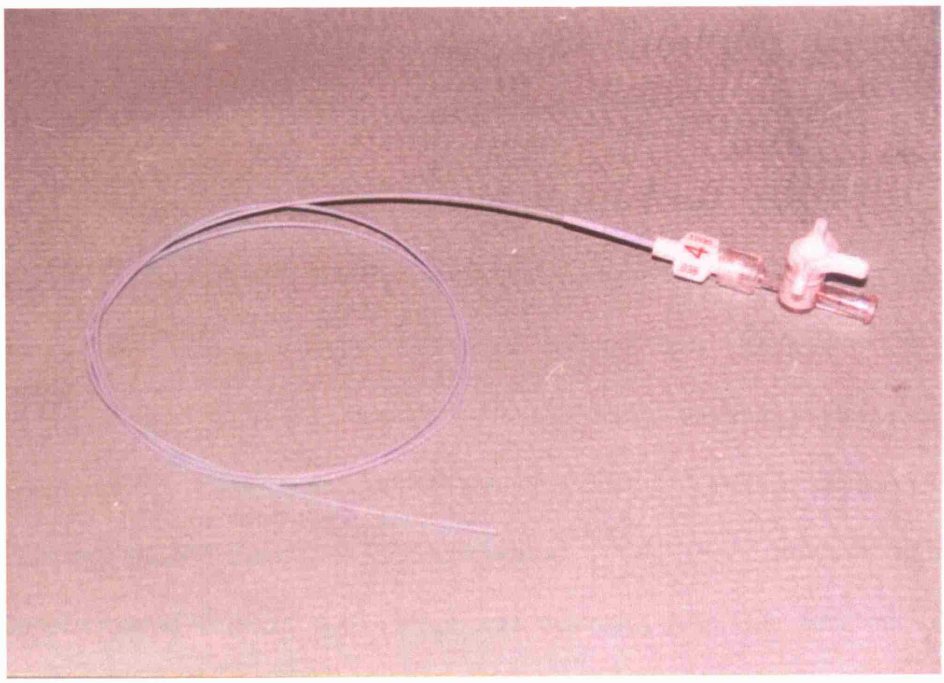

Figure 6.4: The 4-French catheter used for contrast material injection via a single end hole. The injection syringe was connected to the three-way valve shown in the picture.

permitted the fluid to exit during the emptying phase. Varying the pumping frequency and the stroke volume allowed control of the mean flow rate.

Date-expired whole blood was used as the circulating fluid. This was obtained from the blood bank at the Royal Free Hospital, London. The blood was placed in a fluid reservoir consisting of a conical flask that can be seen in figure 6.2. Between 250 and 500 ml of blood were required to fill the circuit. Silicone tubing (Portex division of Smiths Group, UK) of 6 mm internal diameter was used to connect the fluid reservoir to the pump and form a complete circuit. The tubing was interrupted in several locations to allow the insertion of other devices. Firstly, a T-connector was placed downstream from the pump. A pressure transducer, shown in figure 6.5, was connected to this via a two-way valve. The valve allowed the transducer to be connected either to the flow circuit or to the atmosphere for zeroing. The pressure transducer was in turn connected to a pressure monitor (Light Monitor, Datex-Ohmeda division of GE Healthcare, UK) shown in figure 6.6.

Further downstream were placed two Y-connectors. These allowed insertion of catheters into the flow circuit. The first Y-connector was used to insert a Doppler-tipped catheter (20 MHz Mikro-Tip Doppler Catheter, Millar, Texas, USA), shown in figure 6.7, and the second was used to insert a 4-French contrast medium injection catheter, shown in figure 6.4. The Doppler catheter was connected to a Doppler velocimeter (20 MHz Pulsed Doppler Velocimeter MDV-20, Millar, Texas, USA), shown in figure 6.8. The Doppler-tipped catheter was placed just upstream from the first part of the simulated vessel that was in the imaging plane. The injection catheter was connected to a 10 ml syringe via a three-way valve. This syringe was used for manual contrast

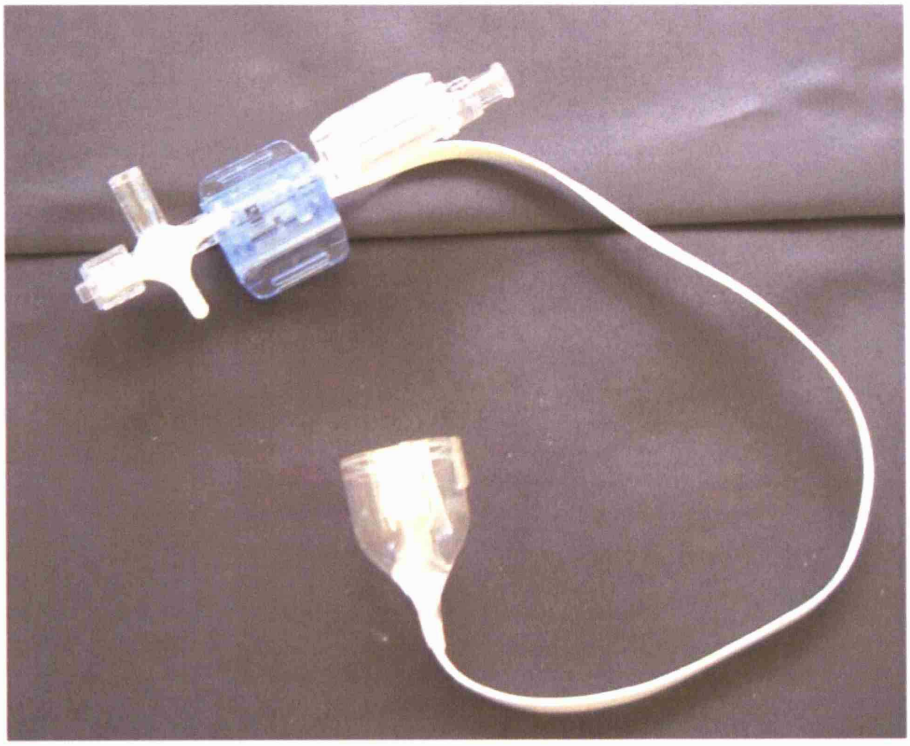

Figure 6.5: The pressure sensor. The two-way valve allowed connection to the flow circuit or to the atmosphere for zeroing.

Figure 6.6: The pressure monitor (Light Monitor, Datex-Ohmeda division of GE Healthcare, UK).

Figure 6.7: The 20 MHz Doppler-tipped catheter (20 MHz Mikro-Tip Doppler Catheter, Millar, Texas, USA).

Figure 6.8: The 20 MHz Doppler velocimeter (20 MHz Pulsed Doppler Velocimeter MDV-20, Millar, Texas, USA).

material injection. The injection catheter had a single end hole and was placed approximately 10 cm upstream from the first part of the simulated vessel that was in the imaging plane.

Downstream to the Y-connectors was the portion of circuit that was placed in the x-ray imaging plane. Two self-sealing connectors were used in this part of the circuit to allow the insertion of one of the different types of simulated vessels. The electromagnetic flow sensor (Electromagnetic Blood Flow Sensor, Skalar Medical BV, The Netherlands), shown in figure 6.9, was placed in-line with the circuit either upstream of the simulated vessel or downstream depending on the type of vessel used. For non-branching vessels such as straight silicone tubes, the sensor was placed downstream. For branching vessels such as the anthropomorphic cerebral phantom, the sensor was placed upstream. The sensor was connected to the electromagnetic flow meter (Electromagnetic Blood Flow and Velocity Meter, Skalar Medical BV, The Netherlands), shown in figure 6.10. This device provided the gold standard measurement of volumetric flow rate. The Doppler velocimeter was used to provide a fallback gold standard method of flow measurement in case of failure of the EMF. The pressure monitor, the EMF, and the Doppler velocimeter provided analog output signals. These were digitally recorded using a recording system consisting of an eight channel analog-to-digital converter (MacLab 8s, ADInstruments, UK) and associated software running on a Macintosh notebook computer.

The shape of the flow waveform could be altered by:

1. altering the pump frequency and stroke volume;

Figure 6.9: The electromagnetic blood flow sensor (Electromagnetic Blood Flow Sensor, Skalar Medical BV, The Netherlands).

Figure 6.10: The electromagnetic blood flow meter (Electromagnetic Blood Flow and Velocity Meter, Skalar Medical BV, The Netherlands).

2. altering the mean pressure by adjusting the height of the fluid reservoir using a retort stand;
3. and changing the diameter of the tubing connected to the pump using adjustable metal clips.

6.2.2 Calibration of the Electromagnetic Flow Meter

Calibration of the EMF was carried out using timed fluid collection under conditions of constant flow. Steady flow was achieved using a constant head reservoir. Calibration was carried out using 11 flow rates ranging from 55.9 to 828 ml/min. The calibration results are shown in figures 6.11 and 6.12. It can be seen from figure 6.11 that the device was highly linear (PMCC = 0.999, n = 11). However, figure 6.12 shows that the device tended to underestimate the true flow rate. The mean measurement error was -18.9 ml/min and the 95% limits of agreement were -48.3 to 10.4 ml/min. The underestimation generally increased as the mean flow rate increased.

6.2.3 Details of the Different Types of Simulated Vessel

6.2.3.1 Silicone Tubing

For the first series of experiments, silicone tubing was used to simulate an arterial vessel. The tubing had a circular cross-section and internal diameters of 3, 4, and 6 mm were used. These diameters are those of medium-sized to large arteries in the human circulation such the renal, femoral, and carotid vessels. The wall thickness was 1 mm for the two smaller sizes and 1.5 mm for the larger vessel. This tubing was more rigid than a real artery and underwent no noticeable diameter changes during the pumping cycle. This meant that the cross-sectional area would be known accurately and errors in

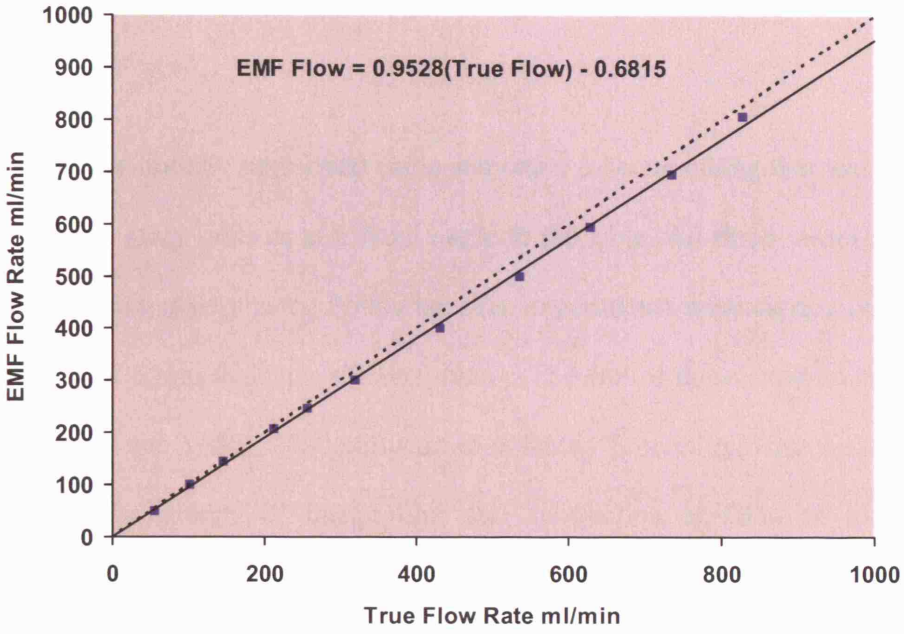

Figure 6.11: EMF calibration: Scatter plot showing EMF flow rate against true flow rate as determined by fluid collection. The solid line is the regression line with equation given. The dotted line is the line of identity. PMCC = 0.999, n = 11.

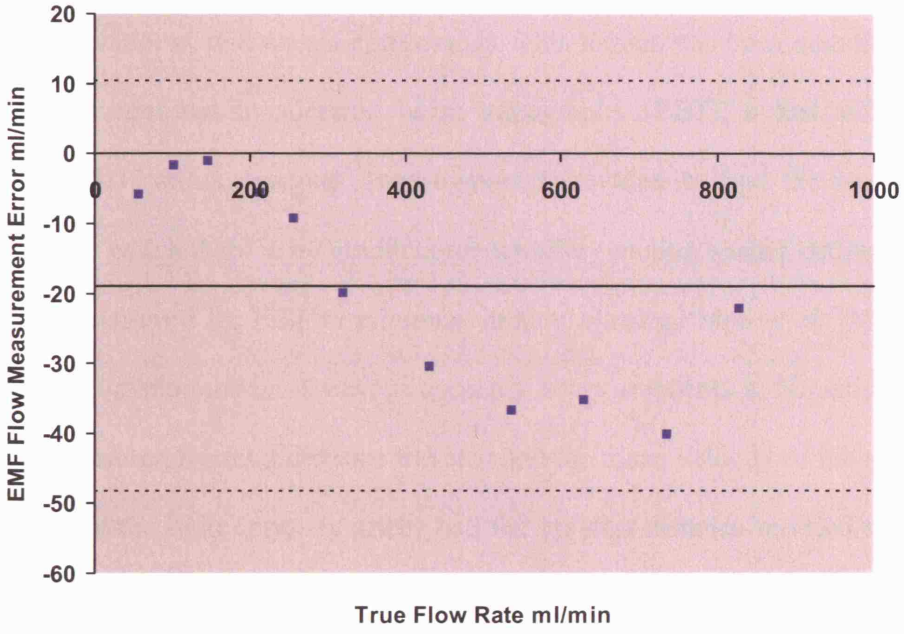

Figure 6.12: EMF calibration: Plot of EMF flow measurement error against true flow rate. The mean measurement error is shown as the solid line and the dotted lines show the 95% limits of agreement.

flow measurement incurred due to diameter change during the pumping cycle would be minimal.

Experiments were initially performed using stationary silicone tubing that was mounted either flat on the x-ray table or at a fixed angle to the table. All three vessel diameters were used for these experiments. Following this, experiments were carried out using a moving length of 6 mm diameter silicone tubing. The aim of these experiments was to test the ability of the SARA 2000 software to correctly process moving vessel images and to assess the effects of image blur and subtraction artifacts on x-ray flow measurement error.

A programmable vessel manipulator was constructed to allow cyclic motion of a length of silicone tubing. The intention was to simulate the motion of coronary arteries during the cardiac cycle. The motion of the coronary arteries is complicated, consisting of translational, rotational, and elastic components. This motion has been quantified from cardiac images acquired by electron beam tomography (EBT), a fast x-ray based technique for 3D cardiac imaging. Investigators have tried to find the parts of the cardiac cycle in which there is minimum coronary artery motion so that optimal cardiac gating can be achieved for EBT to minimize motion blurring. Mao *et al.* [Mao 2000] measured the in-plane motion of various coronary artery segments in 20 patients using EBT. They measured the total distance traveled and the mean velocity of the segments. They found that the right coronary artery had the greatest distance traveled and mean velocity during the cardiac cycle. This was followed by the left circumflex, the left main, and the left anterior descending arteries. The mean distance traveled for all coronary arteries was 42.5 mm and the mean velocity was 55.5 mm/sec for patients at

rest. Achenbach *et al.* [Achenbach 2000] reported similar finding from EBT images of 25 patients. They found the mean velocity of the right coronary artery to be 69.5 mm/sec, the left circumflex artery to be 48.4 mm/sec, and the left anterior descending artery to be 22.4 mm/sec. The overall average velocity was 46.6 mm/sec. The findings of these two studies were taken into account when designing the vessel manipulator.

Modeling the complicated motion of the coronary arteries would be difficult in a phantom and a simplified approach was adopted. Figure 6.13 shows a schematic of the vessel manipulator and figure 6.14 shows a photograph of the device. The manipulator had a single axis of motion. The vessel was placed with one end fixed to the acrylic base of the manipulator and the other end fixed to a moveable caddy. The caddy was placed on a linear drive axis consisting of a screw driven by a geared d.c. motor. A guide rail was used to prevent rotation of the caddy about the screw. The d.c. motor was controlled using a pulse-width modulated control circuit. This enabled both speed and directional control of the motor. The control circuit was in turn connected to the parallel port of a laptop computer that could be programmed to control the motion of the caddy. The limits of motion of the caddy were set using two moveable microswitches placed on the guide rail. These were connected to the laptop computer making it possible to detect when the caddy had reached the limits of its motion. The switches were placed to give a total lateral travel of 40 mm, based on the findings of Mao *et al.*. The motion was programmed to give the velocity profile shown in figure 6.15, based on the findings of Achenbach *et al.*. The frequency of motion was 43 cycles per minute, which is lower than the normal human heart rate at rest. However, this was the maximum frequency that could be achieved with this manipulator due to the gearing needed to allow the rapid reversal of the motor without causing slipping. During the flow experiments, the

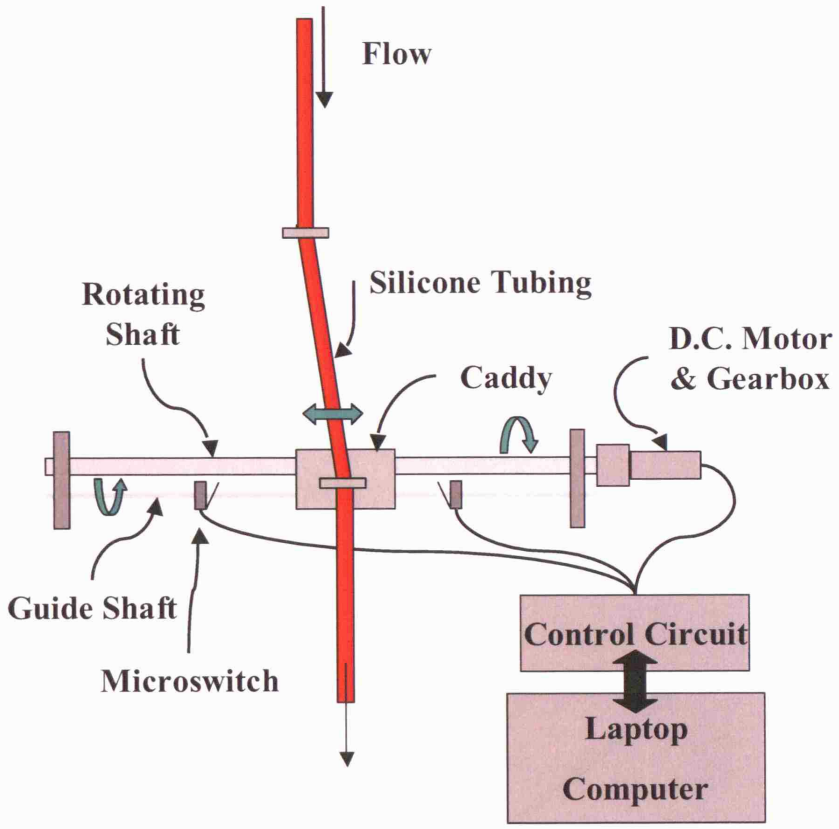

Figure 6.13: Schematic of the vessel manipulator used for the moving silicone tubing experiments.

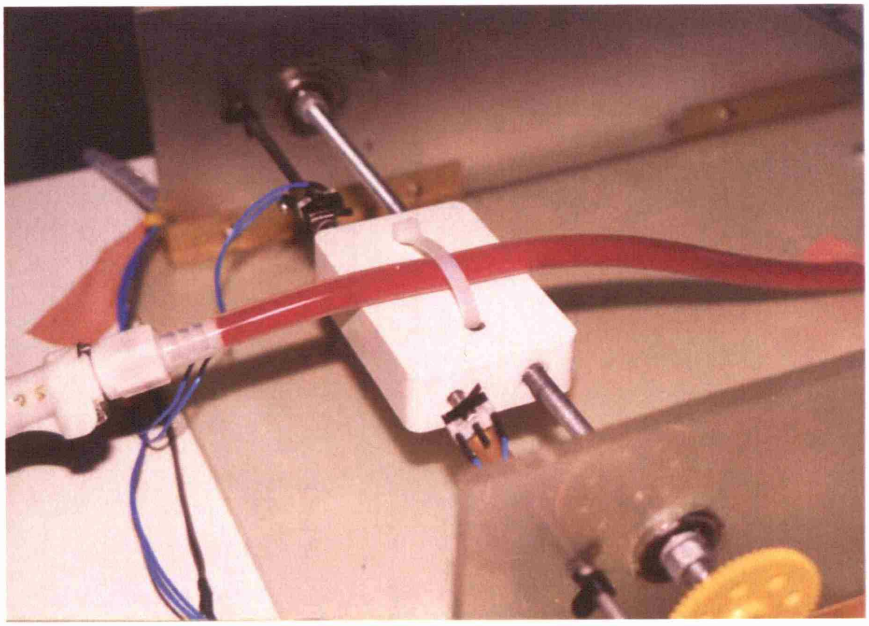

Figure 6.14: Photograph of the vessel manipulator.

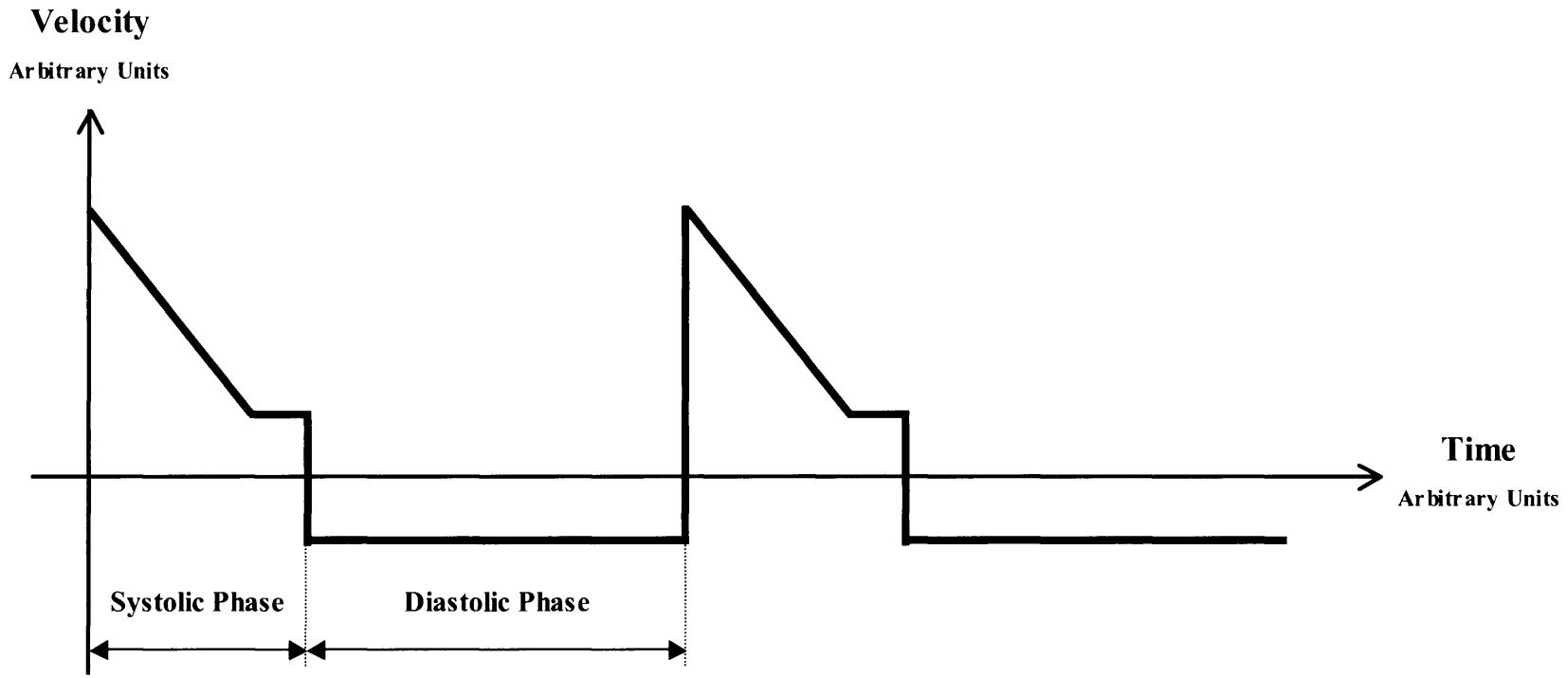

Figure 6.15: Velocity-time graph for the vessel manipulator.

pump was also set to the same frequency. The average velocity of the vessel was 28.7 mm/sec, which is less than the mean value for all coronary arteries reported by Mao *et al.* and Achenbach *et al.* but comparable to the reported mean value for the left anterior descending artery.

6.2.3.2 Prosthetic Vascular Grafts

Figure 6.16 shows three examples of prosthetic vascular grafts that can be used to replace or by-pass vessels during vascular surgery. The most commonly used types of graft are polytetrfluoroethene (PTFE) and Dacron. Newer grafts made from compliant polyurethane (CPU) are also being developed. For the third series of experiments, PTFE and CPU grafts were used as simulated arteries. These have physical properties that are more similar to real arteries than the silicone tubing used for the first two series of experiments. The grafts were thin-walled and more compliant than the silicone tubes. Therefore, they underwent more diameter change during the pumping cycle. The CPU graft has been specially developed to have similar compliance to real arteries, more so than PTFE or Dacron grafts [Tai 2000]. Therefore, the error incurred due to changes in the vessel diameter during the pumping cycle would be included in this series of experiments. The CPU graft is porous. Therefore, this graft had to be pre-clotted before the flow experiments were started. One end of the graft was sealed by clamping and the other end was infused with fresh blood taken from a volunteer. The blood passed through the pores in the graft wall and was allowed to clot. This sealed the pores and the graft was then inserted into the flow circuit. Dacron grafts are also porous but were excluded from this series of experiments due to difficulty in adequately pre-clotting

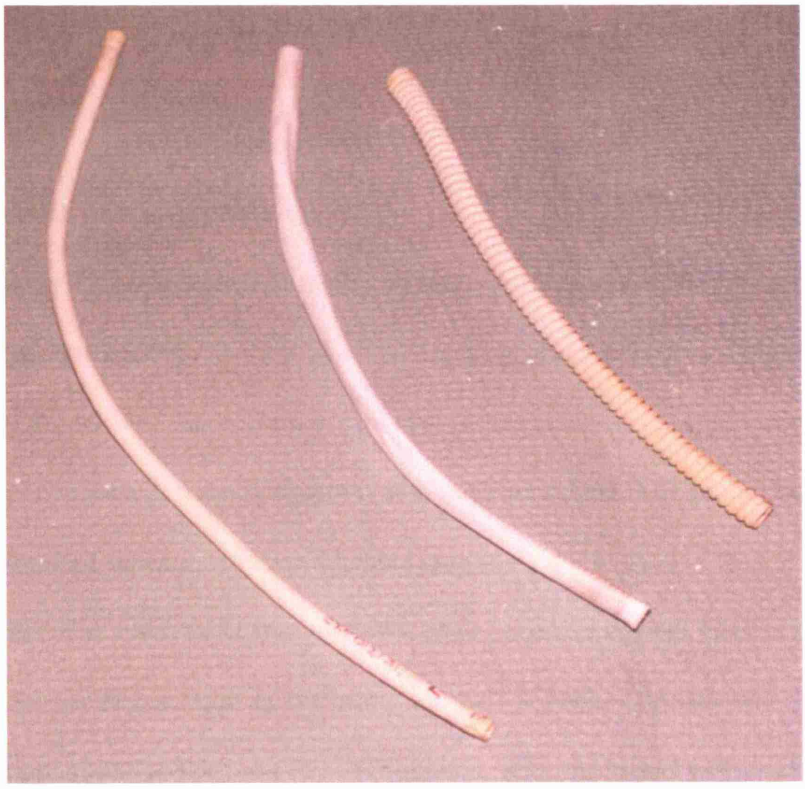

Figure 6.16: Examples of the different types of prosthetic vascular grafts used during vascular surgery. From left to right: PTFE, CPU, and Dacron.

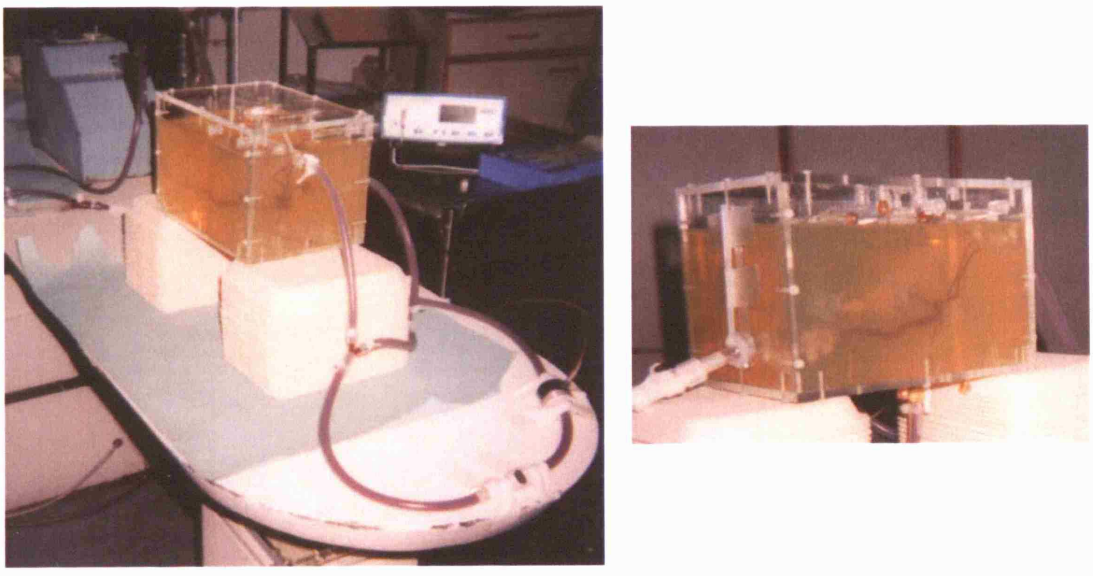

Figure 6.17: Two views of the anthropomorphic cerebral vascular phantom.

these grafts. The PTFE and CPU grafts were placed flat on the x-ray table for the flow experiments.

6.2.3.3 Cerebral Vascular Phantom

For the final series of flow experiments, an anthropomorphic cerebral vascular model was used (Elastrat Model, Shelley Medical Imaging Technologies, Ontario, Canada). This silicone model was made from a wax cast of the cerebral vessels of a pathological human brain specimen and contained two cerebral aneurysms. The model had one input vessel, the internal carotid artery, and three output vessels, modeling one half of the circle of Willis. The model was mounted in a clear acrylic box with three-way valves on the outside connecting to each of the entry and exit vessels. The box was filled with a gelatin solution and allowed to set in a refrigerator. This simulated surrounding tissue to give realistic x-ray scatter. The cerebral phantom is shown in figure 6.17. The phantom was placed in-line with the flow circuit with flow entering via the internal carotid artery. Flow from the three exit vessels was directed to a common outflow tube that was connected to the flow circuit. The internal carotid artery was used as the target vessel for x-ray flow measurements.

6.3 Construction of the Waveform Shape Model

Blood flow waveforms extraction by the MB algorithm required a pre-existing waveform shape model describing the likely flow waveforms encountered in the target vessel. This shape model was constructed by collecting sample waveforms from the pulsatile blood flow circuit and applying principal component analysis, as detailed in section 3.3. Instantaneous volumetric flow waveforms were recorded from the EMF during varying conditions of flow. The sampling rate for data collection was between 40 and 100 samples per second. A variety of flow waveforms were produced by altering the following parameters:

1. the stroke volume of the pump;
2. the frequency of the pump;
3. the mean pressure;
4. the output impedance;
5. the target vessel size;
6. and the rate of contrast material injection.

For each flow condition approximately 10 seconds of the flow signal was captured. Figure 6.18 shows a typical blood flow signal recording from the EMF. For each recording the individual cycles were isolated. This was performed automatically by identifying the systolic upstroke, or foot, of each cycle. The systolic foot was found by searching for 5 consecutive positive gradients that exceeded a predefined threshold. The foot was then marked as the first point in this series of gradients. This method was adapted from the technique used by Kontis *et al.* [Kontis 1989] to find the systolic foot of Doppler ultrasound blood flow sonograms. Alternative methods have been suggested

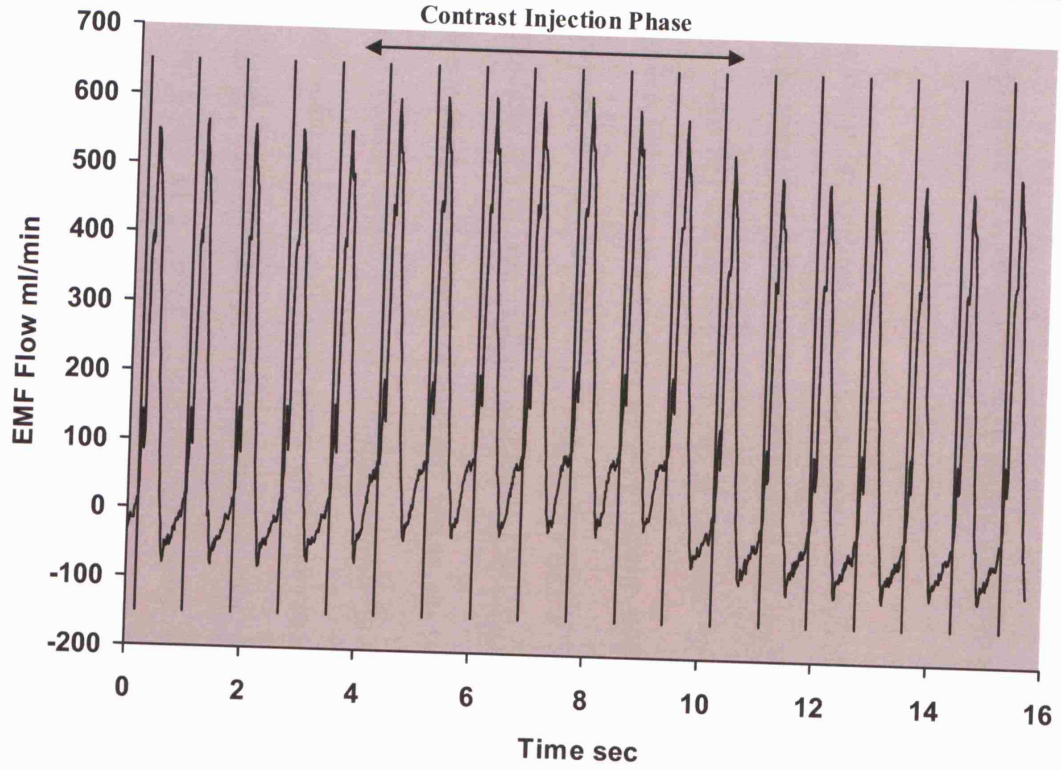

Figure 6.18: Example of an instantaneous flow recording from the electromagnetic flow meter. The systolic foot of each cycle has been marked with a vertical line. Notice the increase in flow rate during contrast material injection.

by Evans [Evans 1988] and by Wright *et al.* [Wright 1997] for the same application. The value of the threshold was altered interactively until the feet where correctly identified. In some waveforms that contained more than one rising edge per cycle, more than one systolic foot was marked for each cycle. This was overcome by setting a refractory period during which further systolic feet could not be marked in the cycle. For a small number of waveforms, the automated foot identification method failed. In these cases the systolic feet were marked manually. Figure 6.18 shows the identified positions of the systolic feet for an example waveform. For each recording approximately 10 cycles were identified. Since x-ray flow measurements were to be made during the injection of contrast material, only the cycles identified during the injection phase where used for further analysis. In order to overcome the effects of different cycle lengths, each cycle was normalized over time to 100 sample points by resampling using linear interpolation. In total, 434 cycles were isolated under the varying conditions in the flow circuit and these were used as the input waveforms for PCA. Figure 6.19 shows 20 examples of the input waveforms. The mean flow rates ranged from 43 to 375 ml/min. The instantaneous flow rates ranged from –247 to 1060 ml/min. This range of flow rates covered the values for which x-ray determination of flow was to be carried out in the flow circuit.

Since the input waveforms derived from the EMF recordings were sampled using 100 points, the PCA yielded 100 eigenvectors with corresponding eigenvalues. Table 6.1 shows the eigenvalues of the first 20 eigenvectors. The percentage variation contributed by each eigenvector has been calculated (Eq. 3.7) and also the cumulative percentage variation. It can be seen from table 6.1 that only the first 3 eigenvectors are needed to explain over 90% of the total variation in the waveform shape.

Eigenvector Number	Eigenvalue (3 s.f.)	% Variation (2 d.p.)	Cumulative % Variation (2 d.p.)
1	1080000	73.50	73.50
2	179000	12.17	85.67
3	98800	6.71	92.38
4	50100	3.40	95.78
5	20900	1.42	97.20
6	14000	0.95	98.15
7	7430	0.50	98.65
8	5760	0.39	99.04
9	3820	0.26	99.30
10	2700	0.18	99.49
11	1910	0.13	99.62
12	1010	0.07	99.69
13	839	0.06	99.74
14	652	0.04	99.79
15	461	0.03	99.82
16	390	0.03	99.84
17	333	0.02	99.87
18	281	0.02	99.89
19	196	0.01	99.90
20	154	0.01	99.91

Table 6.1: Eigenvalues of the first 20 eigenvectors with corresponding attributed percentage variation and cumulative percentage variation.

Each input waveform was described by 100 principal component scores and these were calculated using Eq. 3.8. Visualisation of this high dimensionality data is difficult, however, it is possible to view the relationship between any two given PCSs. Figure 6.20 show a plot of the second PCS against the first PCS for the input waveforms. It can be seen that the data points are spread largely in the direction of the first principal component axis. This is to be expected since the first eigenvector or mode of variation has the largest eigenvalue or variance. The spread in the direction of the second principal component axis is less since the second mode of variation has a lower

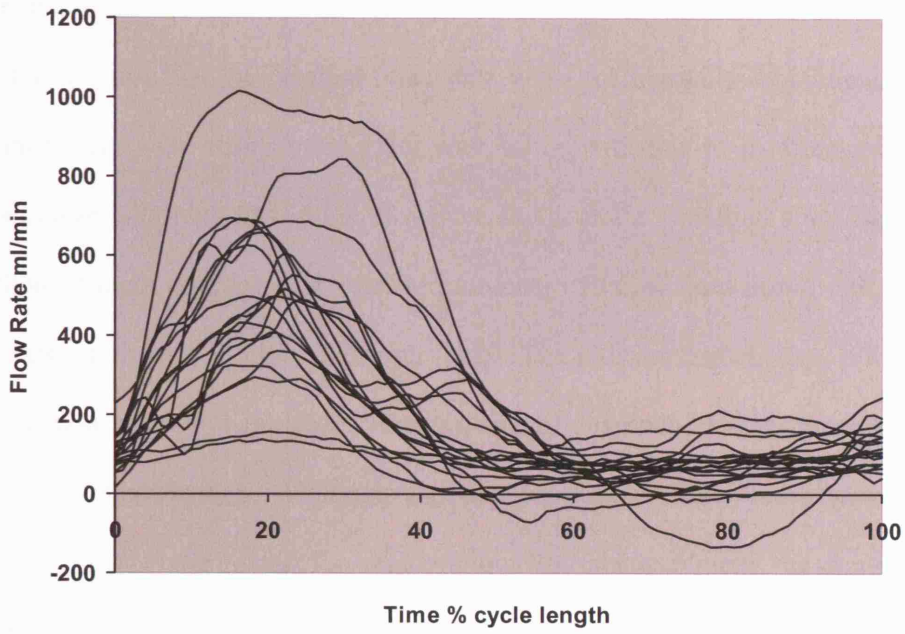

Figure 6.19: 20 examples from the 434 flow cycles that were analysed using principal component analysis. This illustrates the different waveform shapes that were produced by altering the parameters of the flow circuit.

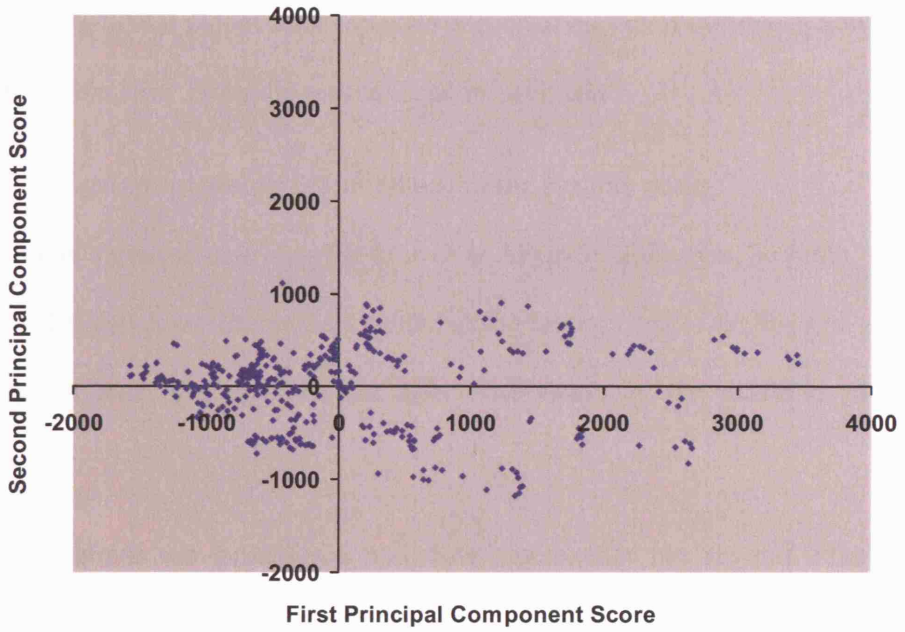

Figure 6.20: Graph to show second principal component score against first principal component score for the 434 input waveforms analysed by PCA.

variance. It can also be seen that the distribution of the first PCSs is positively skewed. This would suggest that the original input data were not normally distributed. This is likely since there were many more input waveforms with low to medium mean flow rates than those with high flow rates. However, this is not a limitation since the normal distribution of input data is not a strict requirement of PCA. Data points can often be seen to exist in clusters in plots like figure 6.20. The clusters contain data points from waveforms with similar shape characteristics. Identifying such clusters forms the basis of waveform classification. Although the use of PCA in this thesis was not for classification of waveforms but for angiographic flow measurement, the possibility to classify waveforms is a useful feature of PCA.

Figures 6.21a to 6.21e show the effect of adding ±1 and ±2 standard deviations of the first 5 eigenvectors to the mean waveform shape (using Eq. 3.9). It is possible with PCA to see that a particular eigenvector affects a particular aspect of the shape, however, this is not always the case. From the results it can be seen that:

1. the first eigenvector affects the amplitude of the systolic peak;
2. the second eigenvector affects the time of occurrence of the systolic peak;
3. the third eigenvector affects the gradient of the falling edge of the systolic peak;
4. the fourth and fifth eigenvectors affect the shape of the diastolic part of the waveform.

These observations are generalized and each eigenvector has several effects on the waveform shape. Figures 6.22a and 6.22b show plots of the mean and peak flow rates, respectively, calculated for each input waveform against the first PCS. It can be seen that there is a very good linear relationship between the mean and peak flow rates and

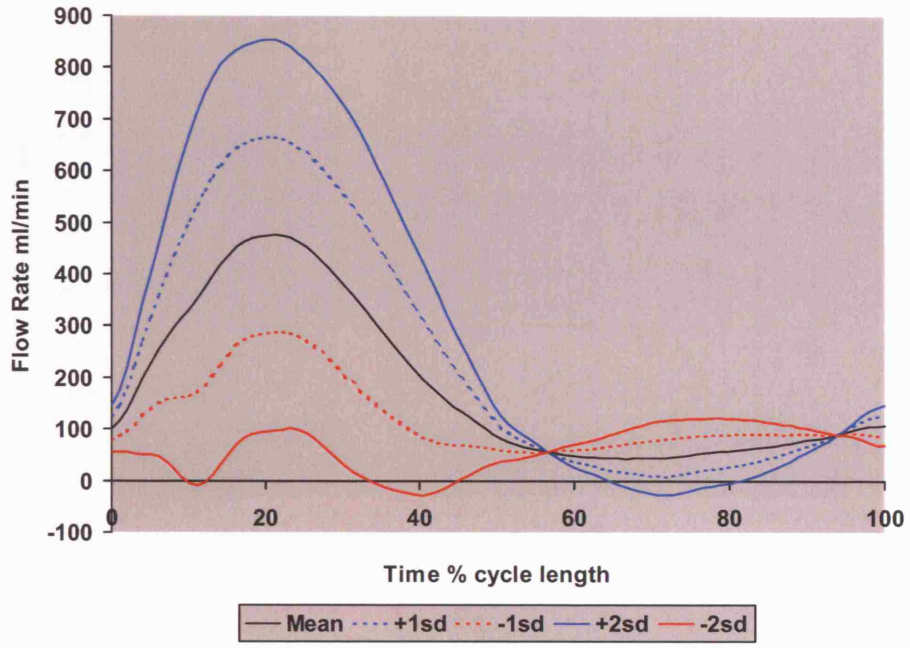

Figure 6.21a: Effect of the first mode of variation on the mean waveform shape.

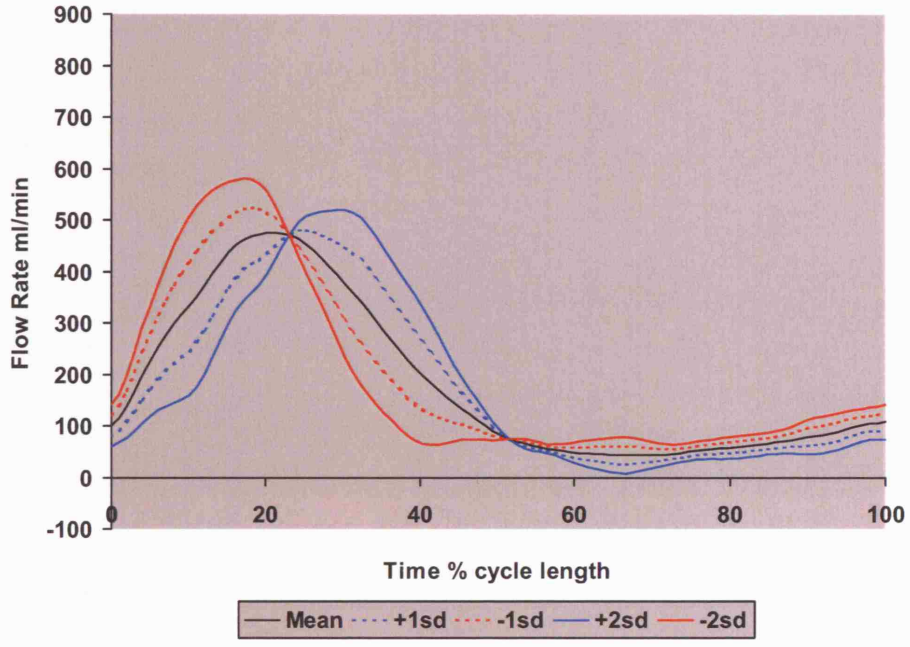

Figure 6.21b: Effect of the second mode of variation on the mean waveform shape.

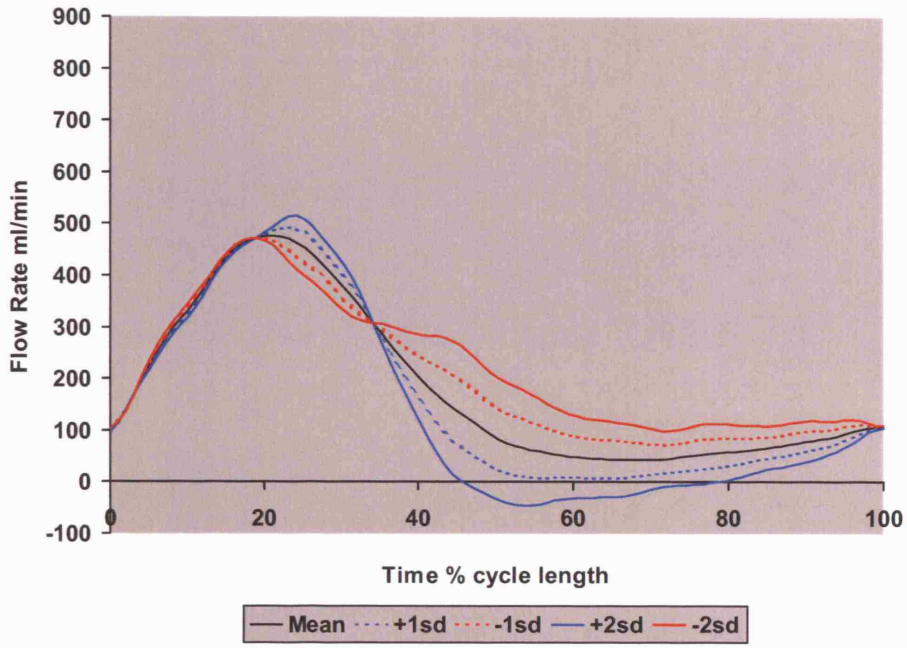

Figure 6.21c: Effect of the third mode of variation on the mean waveform shape.

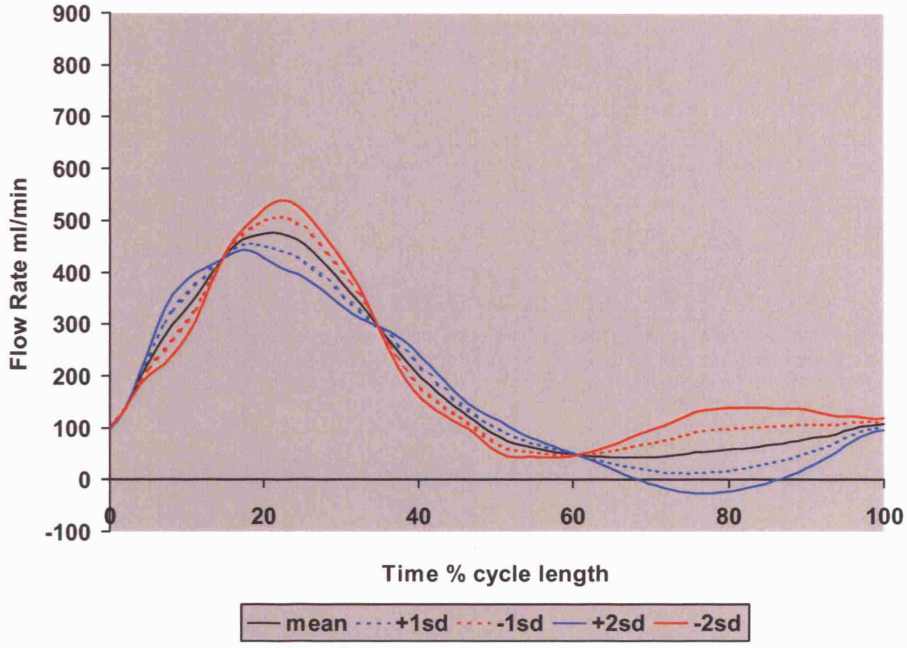

Figure 6.21d: Effect of the fourth mode of variation on the mean waveform shape.

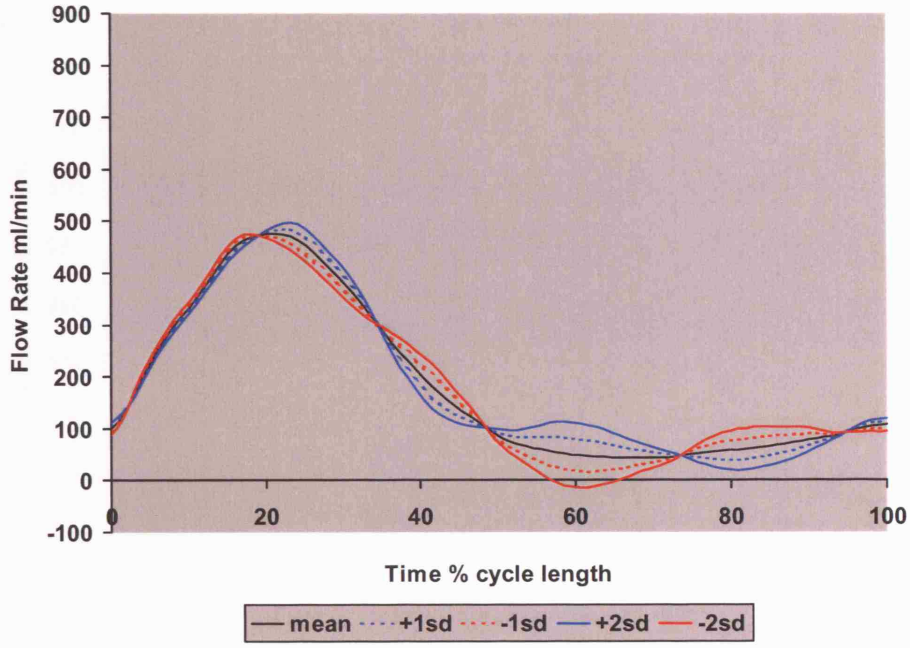

Figure 6.21e: Effect of the fifth mode of variation on the mean waveform shape.

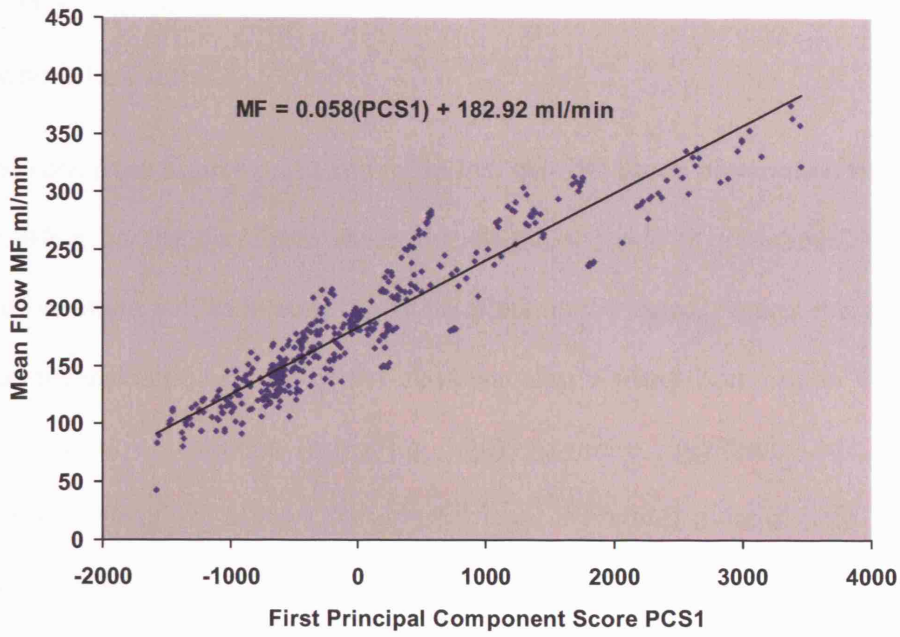

Figure 6.22a: Graph to show mean flow rate for each input waveform against the first principal component score. The linear regression line and equation are shown. PMCC = 0.937, n=434.

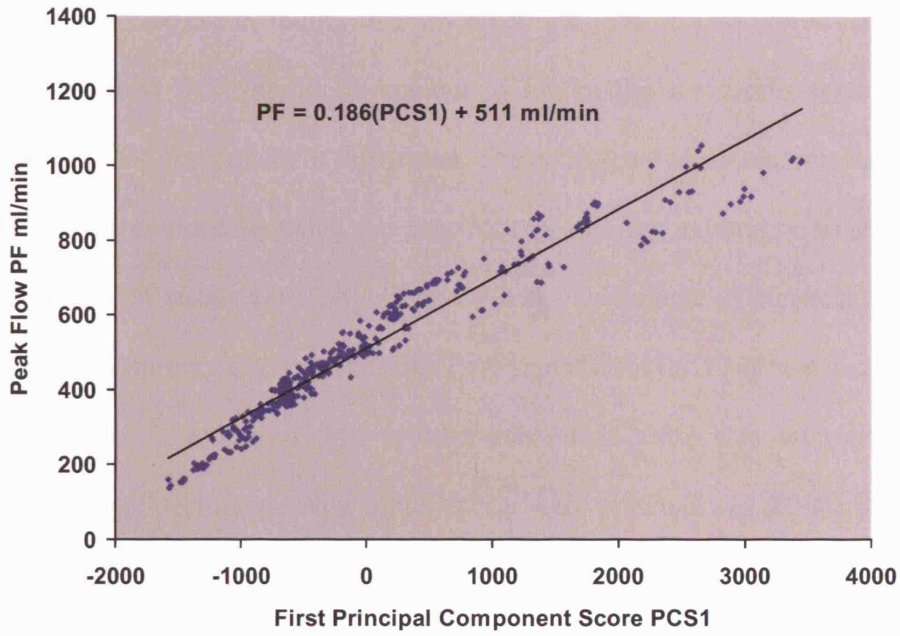

Figure 6.22b: Graph to show peak flow rate for each input waveform against the first principal component score. The linear regression line and equation are shown. PMCC = 0.967, n =434.

the first PCS. This suggests that the value of the first PCS could be used to estimate the mean or peak flow rates.

It can be seen from figures 6.21a and 6.21e that the fifth mode of variation has a much smaller effect on the waveform shape than the first mode of variation. Subsequent modes of variation will have even less of an effect on the shape. Figures 6.23a to 6.23d show the reconstruction of one of the input waveforms using from one to four of the first four modes of variation (using Eq. 3.10). As more eigenvectors are used, the reconstructed waveform follows the original input waveform more closely. It can be seen that there is little to be gained by using more than the first three eigenvectors in this case. Figure 6.24 shows a plot of the average percentage error (calculated using Eq. 3.16) against the number of PCs retained for the first 20 PCs. With only one retained PC the average percentage error was found to be 30.7%. This decreased rapidly as more PCs were retained, falling to 2.1% when the first 20 PCs were retained. The number of retained PCs should be enough to model the waveform signal without modelling the noise component of this signal. The noise level of measurements made by the EMF was determined by using the data collected during calibration of this device under conditions of steady flow (see section 6.2.2). For a range of constant flow rates from 55.9 to 828 ml/min, the instantaneous flow signal from the EMF was recorded and the percentage noise estimated. The average percentage noise was determined to be 4.9%. The average percentage error when 9 PCs were retained was 5.39% and 4.68% when 10 PCs were retained. Therefore, it was decided that 10 PCs would be sufficient to represent the waveform shape information without modelling the noise component.

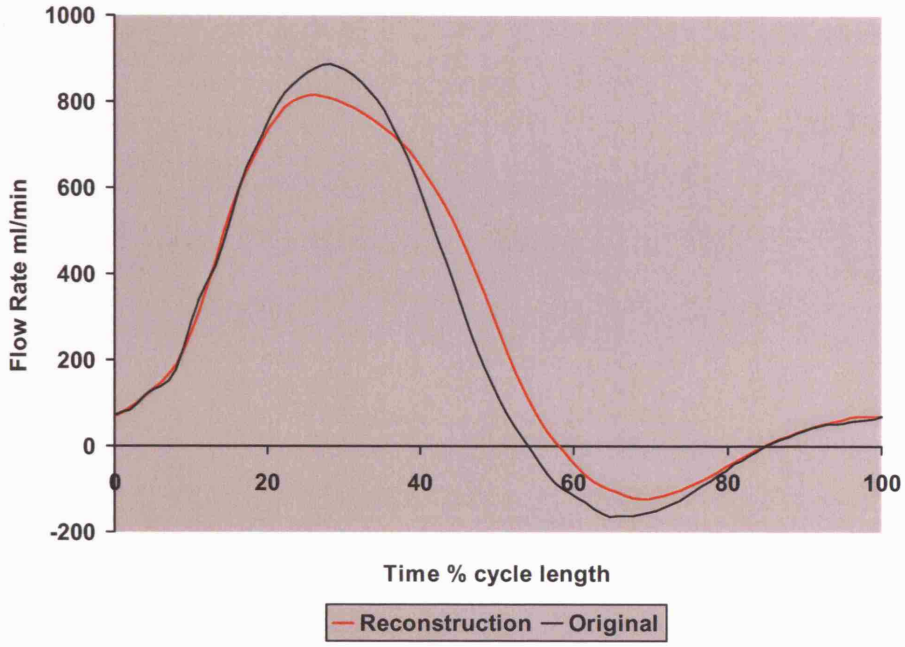

Figure 6.23a: Reconstruction of an example input waveform using only the first mode of variation.

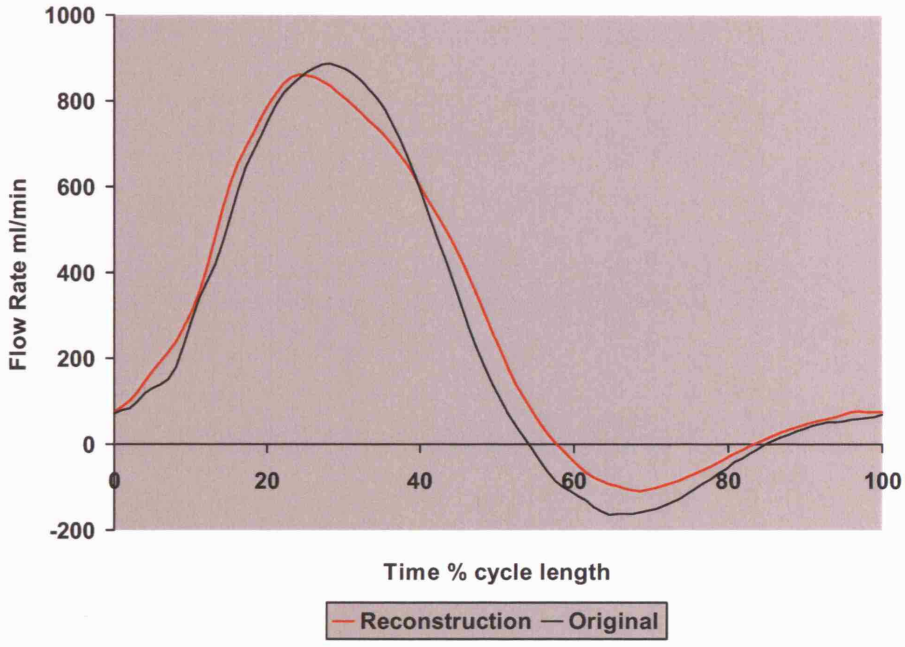

Figure 6.23b: Reconstruction of an example input waveform using only the first two modes of variation.

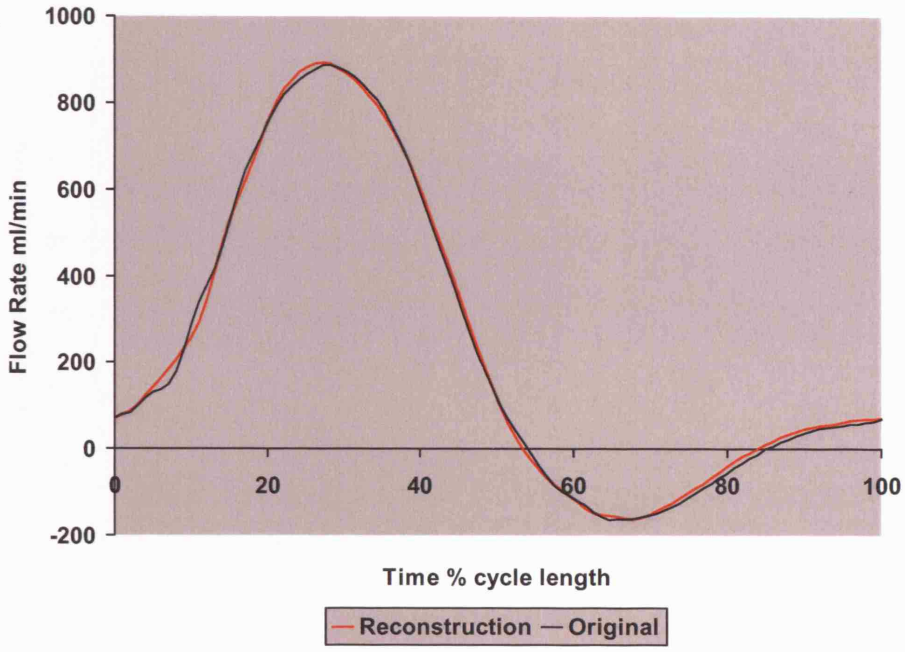

Figure 6.23c: Reconstruction of an example input waveform using only the first three modes of variation.

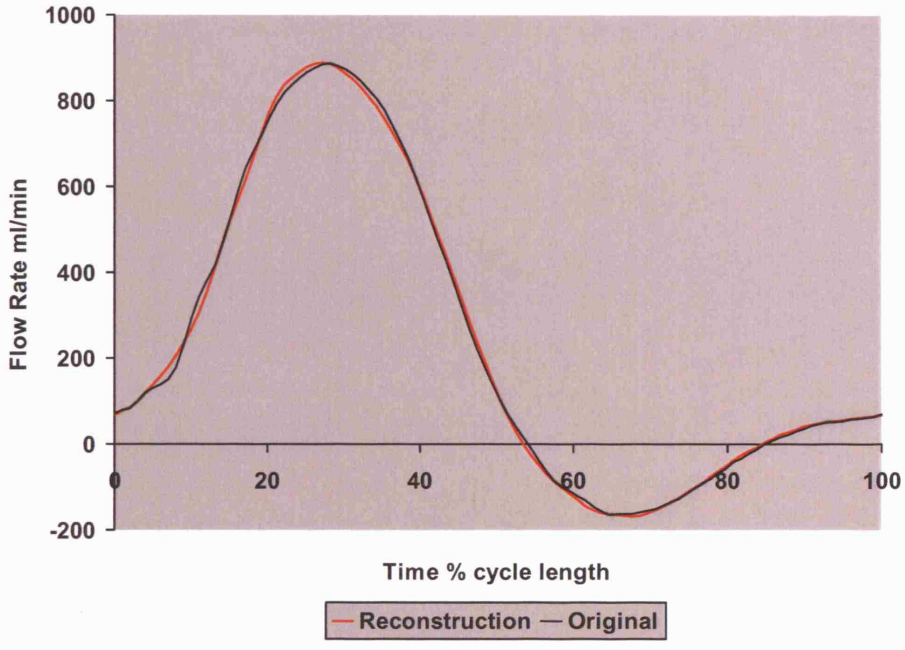

Figure 6.23d: Reconstruction of an example input waveform using only the first four modes of variation.

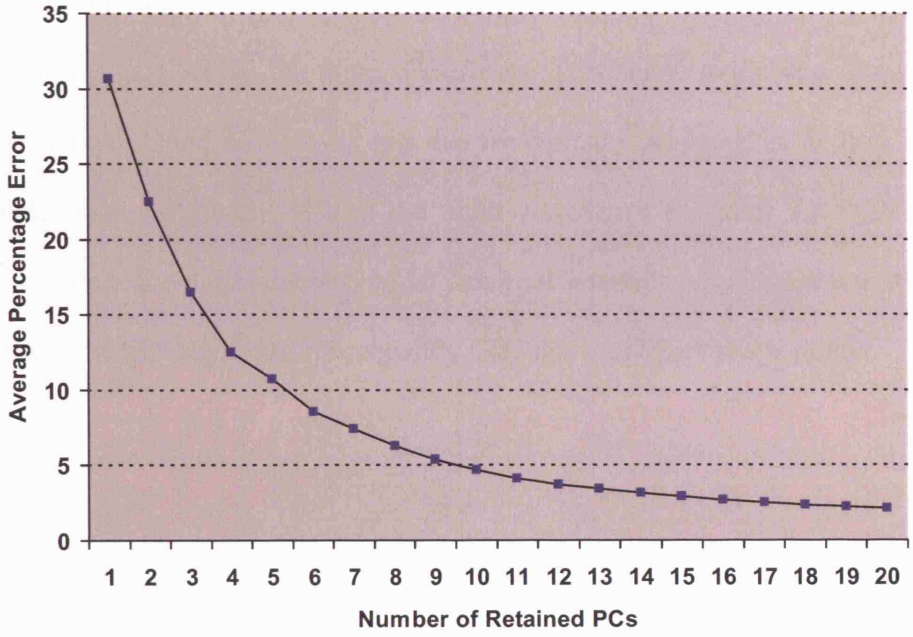

Figure 6.24: Plot of average percentage error against the number of principal components retained to reconstruct the input waveforms.

Therefore, by the use of PCA, a blood flow waveform shape model was produced using recording from the EMF as the input waveforms. This shape model has allowed the characterization of blood flow waveforms that are typically produced in the flow circuit. 100 sample points originally defined the input waveforms but after the PCA it was possible to reduce the dimensionality to 10 parameters without significant loss of shape information. The MB algorithm subsequently used this waveform shape model.

6.4 Experimental Protocol for Flow Circuit Experiments

All experiments with the blood flow circuit were carried out in the catheterisation laboratory at the Royal Free Hospital, London, UK. The installed x-ray system was a GE Advantx DX x-ray system (GE Healthcare, UK). This was a single plane system consisting of an image intensifier with a 20 cm field of view connected to an analogue video camera. X-ray image data was internally stored in the x-ray control unit by logarithmic amplification and then digitization of the video camera signal. The x-ray system dated back to the early nineties and therefore did not represent the state-of-the-art in digital x-ray systems. One of the problems encountered with this system was the difficultly in exporting the digital image data. Eventhough the system allowed digital storage to 8 mm magnetic tapes, it was not possible to read the image data due to the proprietary image format used. An image capture solution was devised to address this problem. This consisted of a frame grabber card installed in a personal computer and specially developed software. X-ray images were then acquired from the x-ray system by digitisation of the composite video signal that is normally available for recording of images to a video tape recorder or for display on a monitor. This signal is almost universally available in all x-ray systems. Therefore, the image capture solution provided a versatile method to obtain digital x-ray data.

The frame grabber used was the Pulsar (Matrox Imaging, Canada). This allowed the input of a variety of video signal formats, e.g. PAL and NTSC. The card was supplied with a C++ software library (MIL-Lite) that was used for software development. The software was developed using Microsoft Visual C++ and ran under the Microsoft Windows operating system. It allowed the user to acquire and review images from the

x-ray system using the familiar Microsoft Windows interface. The frame grabber allowed a maximum acquisition frame rate of 25 frames per second. Therefore, the x-ray system was set for pulsed mode (5 ms pulses) at this frame rate to give the best possible temporal resolution. At this high frame rate it was not possible to simultaneously acquire and save images to the computer's hard disk. Therefore, the acquired images were initially transferred to the computer's random access memory (RAM) and then transferred to hard disk after acquisition. The images were digitised on a 512 x 512 pixel matrix at 8 bits grey level depth. Each image was 256 kilobytes in size and the maximum time for a dynamic acquisition was limited by the amount of RAM available. The computer used had 128 megabytes (Mb) of RAM but only 20 Mb were available for image storage. This allowed a maximum acquisition time of 3.2 seconds at 25 frames per second. This length of time was adequate to capture the passage of injected contrast material through a target vessel for all the flow rates and vessel lengths used. In fact, all sequences consisted of 3-second dynamic acquisitions giving 75 individual images per sequence.

One advantage of the image capture solution is its versatility in allowing image acquisition from nearly all x-ray systems. A further advantage is that it can provide real-time image acquisition, a feature that could be important if flow measurements are to be made during vascular interventions. However, a disadvantage of the image capture solution is that the frame grabbed x-ray images will contain additional noise added by the digitization process. Direct digital data export of image data is a normal feature of modern x-ray systems and will provide better quality images than the image capture solution. However, the export is invariably slow and not suitable if real-time image data are required.

Once the blood flow circuit had been set up in the catheterisation laboratory, dynamic biplane x-ray images were acquired of the simulated vessel during injection of contrast material for a range of mean flow rates. Since the x-ray system was single plane, each view of the biplane acquisition was acquired separately. There was simultaneous recording of flow from the EMF. Following each set of experiments, a calibration cube was imaged to subsequently determine the perspective projection parameters of the x-ray system and a distortion correction grid was imaged for subsequent correction of image intensifier distortion (detailed in section 6.5). The following experimental protocol was used for each of the different simulated vessels:

1. The x-ray system was set to the required acquisition mode (80 kV tube voltage, 25 frames per second acquisition rate, 5 ms pulsed mode, automatic gain control turned off).
2. The simulated vessel was placed at the iso-centre of the x-ray system under fluoroscopic guidance.
3. The EMF, Doppler velocimeter, and the pressure monitor were zeroed with the pump switched off.
4. The circuit was adjusted to achieve the required waveform shape, mean flow rate, and mean pressure. The circuit was allowed to equilibrate for approximately one minute.
5. The x-ray system C-arm was rotated to between the right anterior oblique (RAO) 30° and RAO 45° positions.

6. The contrast material injection syringe was filled with either 6 ml of contrast for mean flow rates of 150 ml/min or below, or 9 ml of contrast for mean flow rates above 150 ml/min.
7. A 3-second sequence of x-ray images was acquired prior to contrast medium injection. This was used to form a pre-contrast or mask image for image subtraction.
8. The recording of signals from the EMF, the Doppler velocimeter, and the pressure monitor was started. Also the *"x-ray on"* signal from the x-ray system was recorded, which allowed synchronisation of the acquired flow signals with x-ray image acquisition.
9. X-ray imaging was started.
10. Contrast material injection was started.
11. X-ray image frame capture was started when the contrast material was seen to enter the simulated vessel.
12. After 3 seconds of image capture, x-ray imaging and data logging was stopped.
13. The x-ray system C-arm was rotated to between the left anterior oblique (LAO) 30° and LAO 45° positions.
14. Steps 6 to 12 were repeated.
15. Steps 3 – 14 were repeated for different mean flow rates. Typically 5 different mean flow rates were used for each type of simulated vessel.
16. The calibration cube was positioned as close as possible to the simulated vessel and orientated to give a clear view of all markers in the x-ray images. X-ray images were acquired of the cube using the same two views used for the simulated vessel.

17. The distortion correction grid was attached to the face of the image intensifier. X-ray images of the grid were acquired using the same two views used for the simulated vessel.

Due to accumulation of contrast medium in the circuit, it was necessary to renew the circulating blood during the course of each experiment. This was typically performed twice.

6.5. X-ray Angiographic Image Analysis to Extract Flow Waveforms

The dynamic x-ray angiographic images acquired of the simulated vessels in the pulsatile flow circuit were analysed with a newly developed software package to extract the flow waveforms using the ORG, PA, OP, and MB algorithms. This software package, called *"System for Angiographic Reconstruction and Analysis 2000"* (SARA 2000), was a re-implementation and enhancement of a previously developed software package (SARA). The limitations of the old software and the features of the new software are discussed in section 6.5.1. The stages involved in the extraction of volumetric flow waveforms from the pulsatile flow circuit image data are described in section 6.5.2 using an example data set.

6.5.1 Development of the Integrated Angiographic Image Analysis Software – SARA 2000

The SARA software package was originally developed at the Computational Imaging Sciences Group (CISG), Guy's Hospital, London [Seifalian 1993, Seifalian 1995 &

Seifalian 1996]. This software allowed the formation of parametric images from biplane dynamic angiographic image data. Initially this software was used to analyze some of the first image data from the flow circuit experiments. This highlighted several limitations of the software:

1. The software was only able to run on an outdated Unix platform consisting of an IPX Workstation (Sun Microsystems, California, USA) and the SunOS 4.2/SunView operating system (Sun Microsystems). The software could not be run on newer workstations because of incompatibility with the new operating systems. Therefore, image analysis was time-consuming, being limited by the speed of the outdated hardware.
2. The angiographic image data had to be transferred to the IPX Workstation using either a local area network connection or optical disk. This was a time-consuming process.
3. The angiographic image data had to be pre-processed before the SARA software could be used. The pre-processing included image file format conversion since the software only accepted a single format known as *"ALVEY"* (created by the CISG but now obsolete). Other pre-processing stages included image averaging and image subtraction. These pre-processing tasks had to be carried out using non-intuitive command line tools.
4. There were several problems with the user interface. For example, the image grey values were rescaled for display using only the first image in a dynamic angiographic series. This often meant that subsequent images in the series were not correctly visualized. Also, the perspective projection calibration from the cube images had to be repeated for every angiographic series since the calibration

parameters could not be saved and recalled. In fact, it was not possible to save and recall any of the intermediate stages in the analysis of an angiographic series, so that if an error was made then the analysis would have to be restarted from the beginning.

5. Memory management was a problem that often resulted in the software crashing.

Overall, the analysis of image data using SARA was very time-consuming and inflexible. This software was fully re-implementation, as part of the work carried out for this thesis, to produce the SARA 2000 software. SARA 2000 was subsequently used to analyse all the flow circuit image data. The advantages and improvements offered by the new software were:

1. SARA was programmed using the C language whereas SARA 2000 was implemented using the C++ language, an object orientated extension to the C language. This meant that the new software was modular and better structured, allowing for easier future development. SARA 2000 was designed to run using the Microsoft Windows operating system, the most widespread operating system in use. Therefore, SARA 2000 had the familiar user interface of this operating system and could be run on the latest personal computer hardware.
2. SARA 2000 was installed on the same personal computer that was used for image acquisition using the frame grabber card. Therefore, image transfer was not required.
3. All image preprocessing, such as averaging and subtraction, could be carried out within the new software environment. Several image formats were supported, including the old ALVEY format and the native BITMAP format of the Microsoft

Windows operating system. Further formats could easily be incorporated into the software due to the modular programming style used.

4. The results of each processing stage could be saved and recalled so that the image analysis could be restarted from any stage. Furthermore, the results from stages that were common to many data sets could be reused, such as the perspective projection parameters.
5. The new software was more stable through efficient memory management and a user interface that prevented the user from carrying out operations in the incorrect sequence.
6. Further enhancements included the ability to carry out geometric distortion correction of the images, a feature that was not previously available. Also, the flow extraction algorithms were integrated into the software as well as the ability to compute the vessel cross-sectional area. Therefore, the volumetric flow waveforms could be extracted within the software environment.

The enhancements incorporated into SARA 2000 meant that the extraction of a volumetric flow waveform from an angiographic data set could be performed in several minutes as opposed to more than half an hour as was the case with the SARA software.

6.5.2 Angiographic Image Analysis using SARA 2000

Each biplane angiographic data set from the pulsatile flow circuit experiments consisted of:

1. a pair of image sequences prior to the injection of contrast material, known as the *"mask sequences"* (75 images per sequence);

2. a pair of image sequences during contrast material injection, known as the *"contrast sequences"* (75 images per sequence);
3. a pair of distortion correction grid images;
4. and a pair of calibration cube images.

The paired data corresponded to the RAO and LAO x-ray views acquired. All the image data from the pulsatile flow circuit experiments were analysed using the SARA 2000 software and figure 6.25 shows a schematic of the analysis stages. These stages will be described and illustrated using an example data set taken from the cerebral vascular phantom experiments.

Stage 1: Image Pre-Processing

Image pre-processing consisted of geometric distortion correction, image averaging, image subtraction, and maximum intensity image calculation.

X-ray image distortion correction was carried out by using the scheme proposed by Haaker *et al.* [Haaker 1990]. The transformation that maps points from corrected image space to distorted image space was modeled using third order polynomials,

$$x' = f_0 + f_1 y + f_2 x + f_3 y^2 + f_4 xy + f_5 x^2 + f_6 y^3 + f_7 y^2 x + f_8 y x^2 + f_9 x^3$$

$$y' = g_0 + g_1 y + g_2 x + g_3 y^2 + g_4 xy + g_5 x^2 + g_6 y^3 + g_7 y^2 x + g_8 y x^2 + g_9 x^3 . \qquad (6.1)$$

where (x, y) is a point in corrected image space, (x', y') is a point in distorted image space, and f_j, g_j $(0 \le j \le 9)$ are the coefficients of the correcting polynomials. Given a set of N corresponding points in distorted and corrected image spaces, it is possible to compute the coefficients f_j, g_j by separate least squares minimisation of the terms

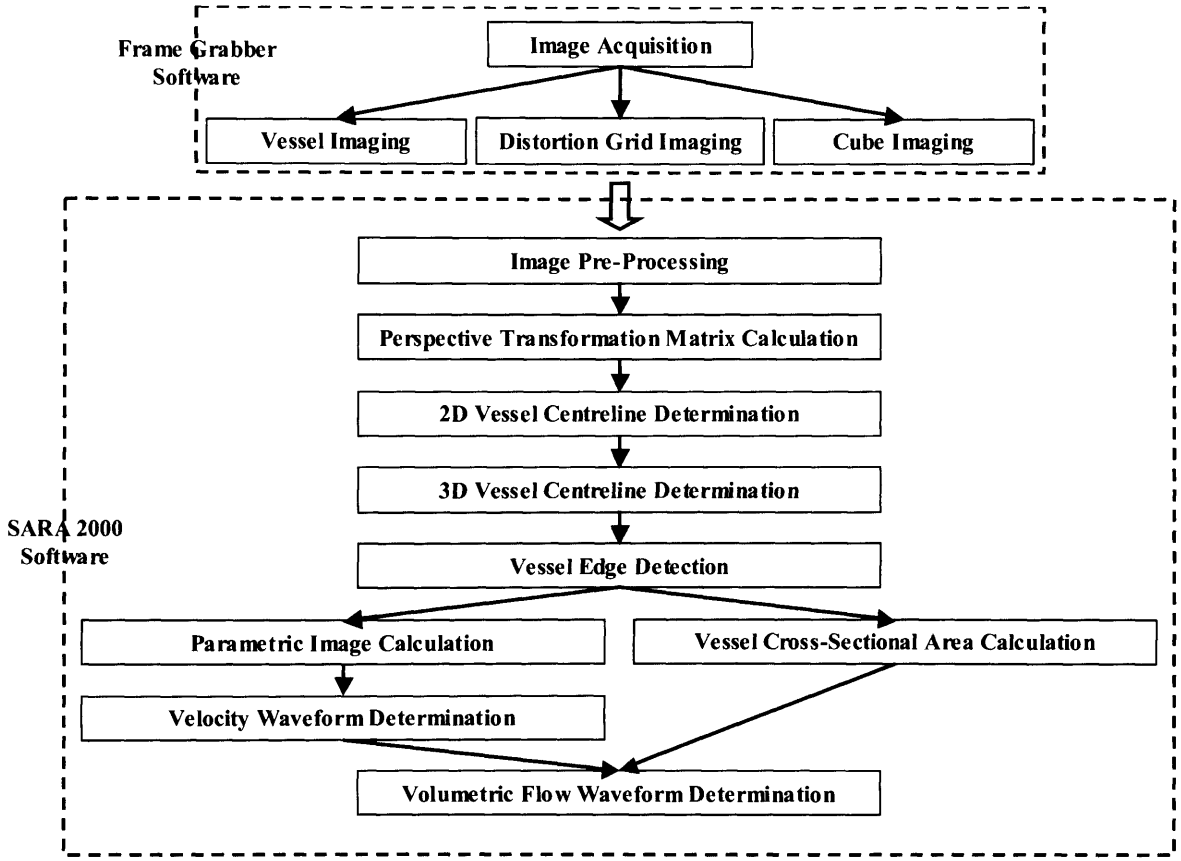

Figure 6.25: A schematic diagram showing the image processing stages carried out in the SARA 2000 software package to generate volumetric flow waveforms from input image data acquired in the pulsatile flow circuit experiments.

$$S_X = \sum_{i=1}^{i=N} (x_i - x'_i)^2$$

$$S_Y = \sum_{i=1}^{i=N} (y_i - y'_i)^2 \,. \tag{6.2}$$

A distortion correction grid was used to find the coefficients of the correcting polynomials. This was a 400 mm diameter acrylic plate with embedded 1 mm diameter steel ball bearings positioned to form a grid with 15 mm spacing. The grid was fixed to the input surface of the image intensifier and imaged with the x-ray system gantry orientated at the same positions used for vessel imaging. The LAO x-ray image of the distortion correction grid for the example data set is shown in the left image of figure 6.26a. The positions of all the visible ball bearings were determined by manual marking. The marked positions can be seen as the purple crosses in the left image of figure 6.26a. These positions formed the set of points in distorted image space, (x'_i, y'_i). The corresponding set of points in corrected image space, (x_i, y_i), was generated using the centre ball bearing (marked with the red cross in the left image of figure 6.26a) and the two horizontally adjacent ball bearings, assuming that there is no distortion at the centre of the image. The calculated positions of the ball bearings in the undistorted image are shown in the right image of figure 6.26a. After calculation of the correcting polynomials, any x-ray image acquired in the same view as the grid image could be corrected for geometric distortion by applying the correcting polynomials and bilinear interpolation. Figure 6.26b shows the grid image itself after correction. Correction was applied to the mask sequence, the contrast sequence, and the cube image for each of the two biplane views.

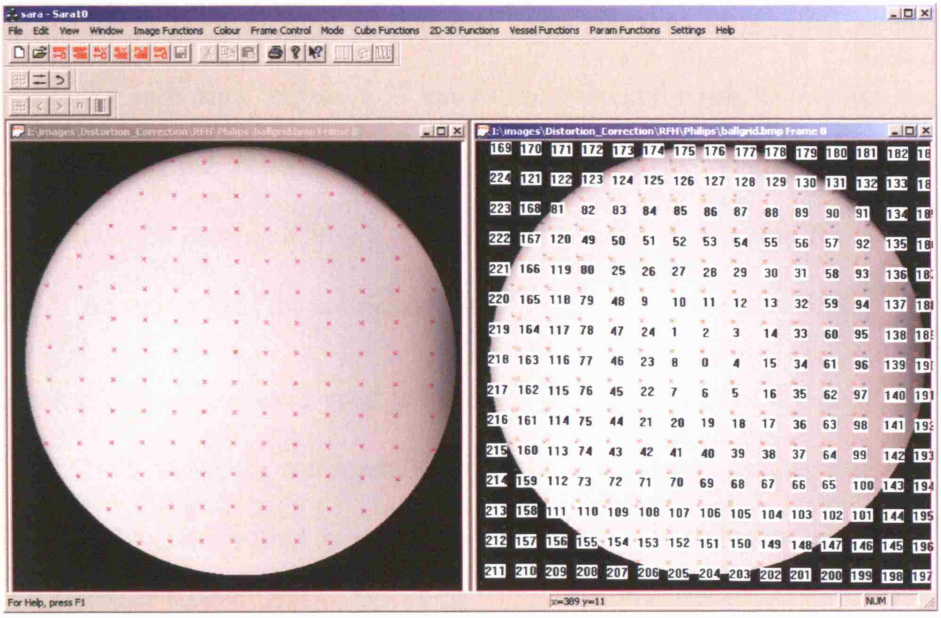

(a)

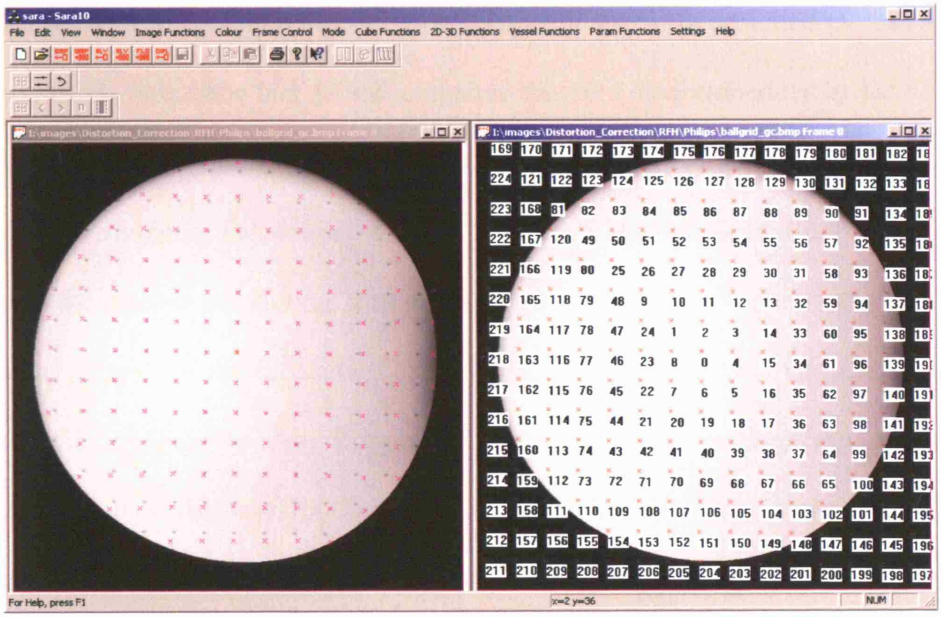

(b)

Figure 6.26: SARA 2000 software: Stage 1: Geometric Distortion Correction: (a) The LAO x-ray view of the distortion correction grid for the example data set is shown on the left. The purple crosses show the marked positions of the ball bearings and the red cross indicates the centre ball bearing. In the right image the numbered red crosses show the undistorted position of the ball bearings calculated using ball bearing numbers 0,4, and 8. (b) The grid image after correction.

The first 5 images from each mask sequence were averaged to produce an averaged mask image for each view. Figure 6.27 shows the averaged mask images for the LAO and RAO views of the example data set. Each image in the contrast sequences was subtracted from the corresponding averaged mask image to generate the *"subtracted sequences"*. An example of the subtracted images can be seen in figure 6.28.

The subtracted sequences were used to generate a maximum intensity image for each view. Figure 6.29 shows the maximum intensity images for the example data set. These images were subsequently used to determine the target vessel centreline and edges.

Stage 2: Perspective Transformation Matrix Calculation

For calibration of the geometry of the x-ray system, a specially designed 60 mm acrylic cube was used. This cube had 14 radio-opaque markers, one embedded at each vertex and one in the centre of each face. Images of the cube were acquired in the same two views used for imaging the simulated vessels. Figure 6.30a shows an x-ray image of the cube with the marker numbering scheme illustrated. Figure 6.30b shows the LAO and RAO x-ray images of the calibration cube for the example data set. The markers were manually identified in the x-ray images and a minimum of 6 markers was required to generate the perspective transformation matrix for each view. This matrix described the mapping of points in 3D cube space, with millimetre dimensions, to 2D image space, with pixel dimensions. Using the perspective transformation matrices for the two views, it was possible to project the location of a point in one view to a line in the other view. This line is called the *"epipolar line"* and figure 6.31 illustrates this feature of the SARA 2000 software.

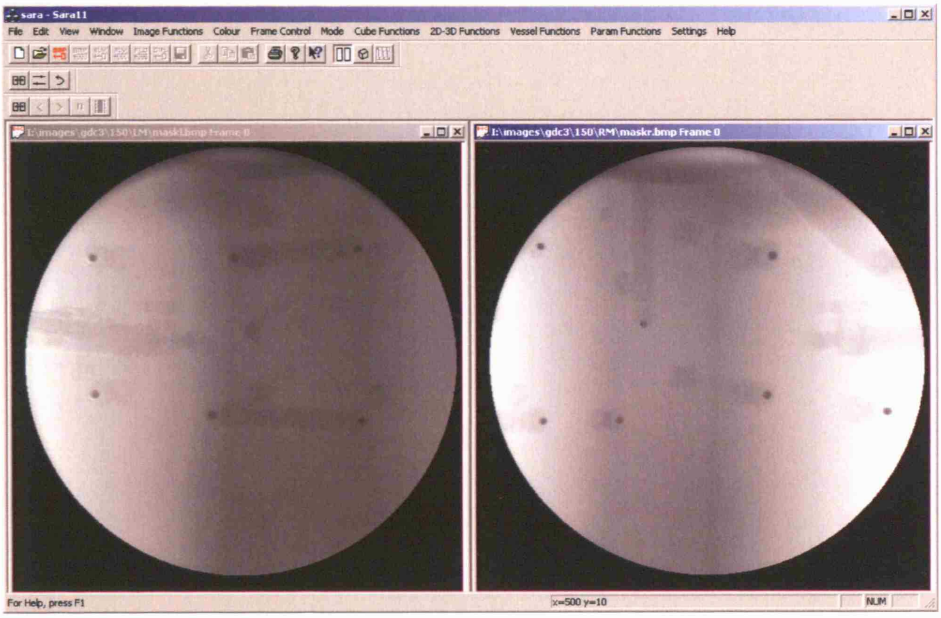

Figure 6.27: SARA 2000 software: Stage 1: Averaged Mask Image Generation: An averaged mask image was generated from the mask sequences by averaging the first 5 images in each sequence. The LAO and RAO averaged mask images for the example data set are shown on the left and right, respectively.

Figure 6.28: SARA 2000 software: Stage 1: Image Subtraction: Mask subtracted x-ray images of the cerebral vascular phantom. One frame from the subtracted sequences is shown for LAO and RAO views.

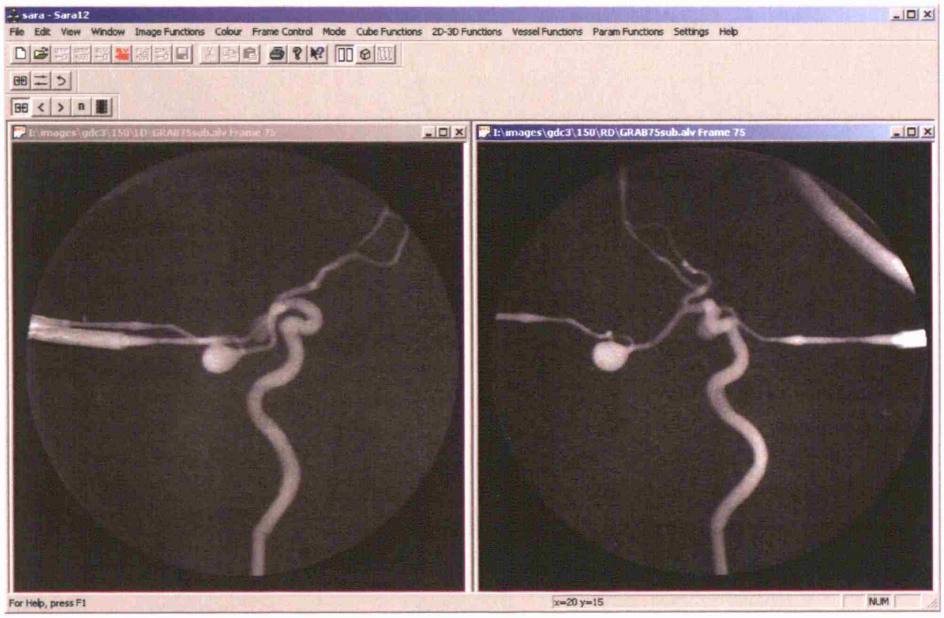

Figure 6.29: SARA 2000 software: Stage 1: Maximum Intensity Image Generation: The subtracted sequences were used to generate maximum intensity images. These are shown for the example data set. These images were used to define the target vessel centreline and edges.

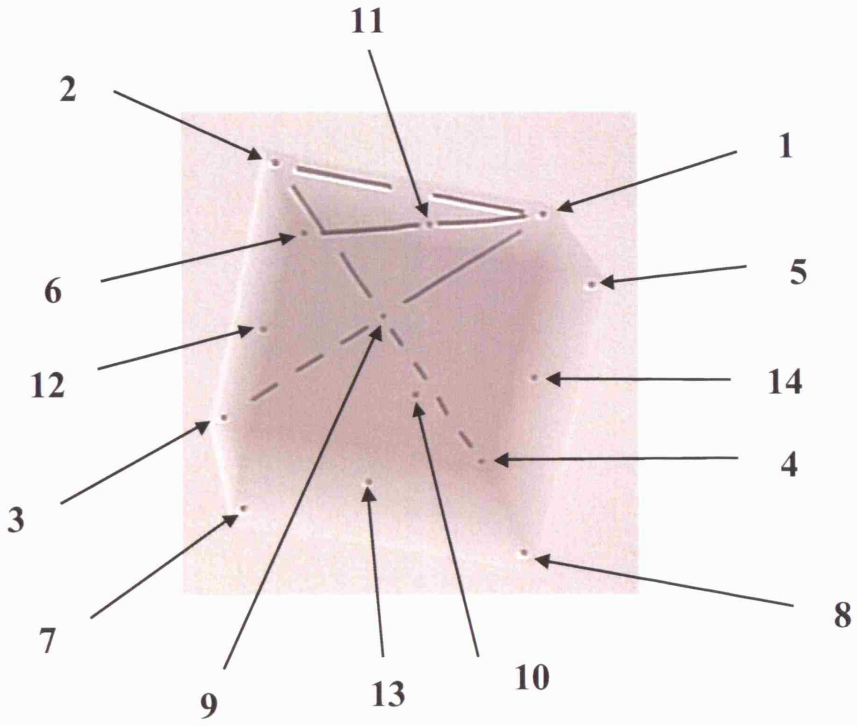

(a)

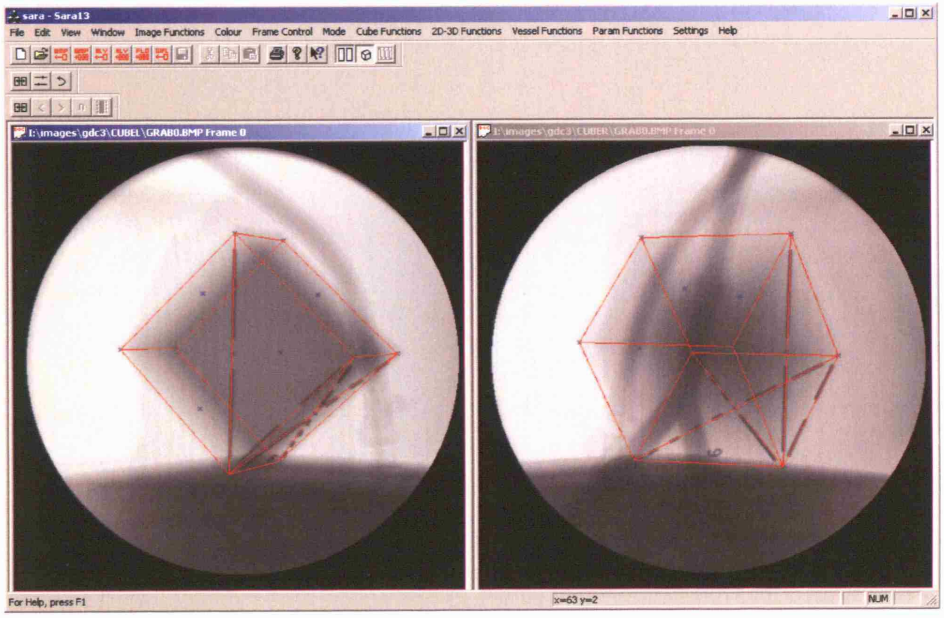

(b)

Figure 6.30: SARA 2000 software: Stage 2: Perspective Transformation Matrix Calculation: (a) An x-ray image of the calibration cube illustrating the marker numbering scheme. (b) LAO and RAO view of the cube for the example data set. The marked positions of the markers are shown as blue crosses.

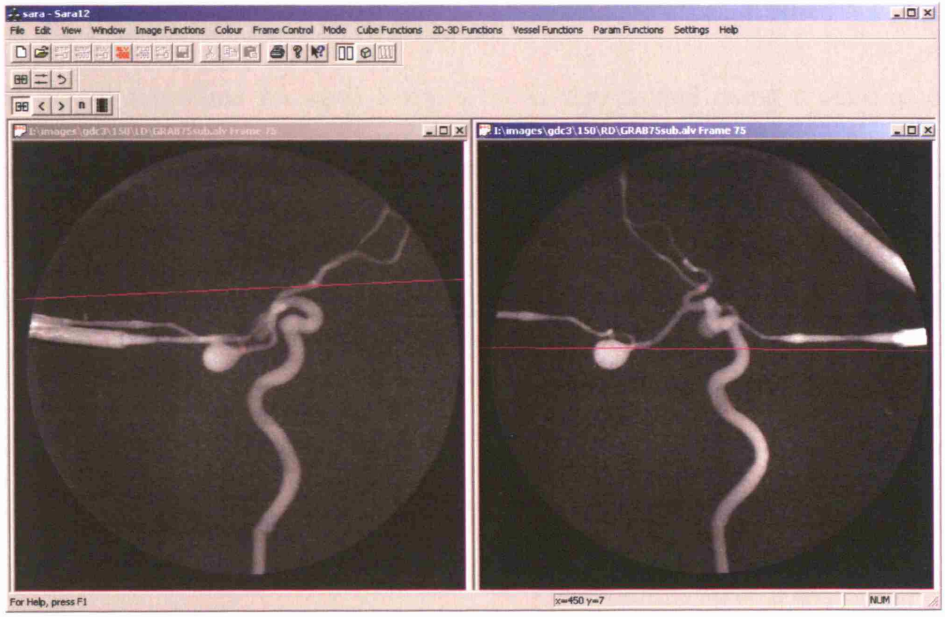

Figure 6.31: SARA 2000 software: Stage 2: Epipolar Line Calculation: Once the perspective transformation matrices have been determined for the two views, it is possible to project epipolar lines. The purple epipolar line shown in each of the two images corresponds to the point marked with the purple cross in the other image.

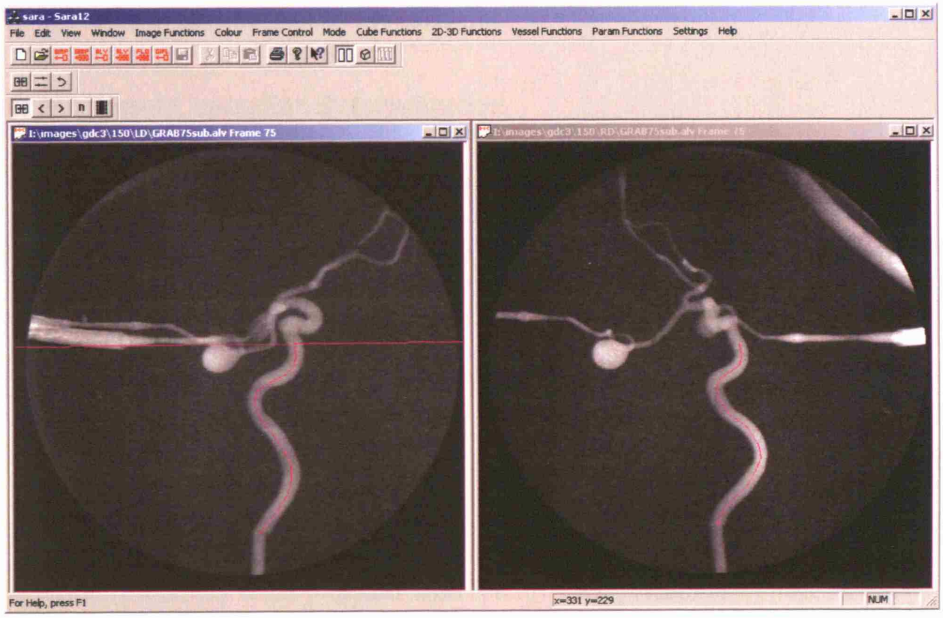

Figure 6.32: SARA 2000 software: Stage 3: 2D Vessel Centreline Determination: The rough centreline, shown in purple, is defined using the epipolar constraint.

Stage 3: 2D Vessel Centreline Determination

The 2D vessel centreline for each x-ray view is determined using a semi-automatic approach. Initially, the user identifies a point at the start of the target vessel segment, approximately at the centre, in one of the two views. The epipolar line will be shown in the other view. The user then selects a point along this epipolar line that is approximately at the centre of the target vessel segment. This procedure is repeated for several points along the length of the target vessel segment. These points are joined by straight lines to define a rough centreline for each view, as illustrated by figure 6.32. Two lines parallel to this can be adjusted to the approximate vessel edges. The intensity profile perpendicular to the centreline is called the *"transverse density profile"* (TDP). The centreline definition is automatically refined by placing the centreline at the centre of gravity of the TDPs. The refined centreline and an example TDP are illustrated by figure 6.33.

Stage 4: 3D Vessel Centreline Determination

The refined 2D centreline definitions are used along with the perspective transformation matrices to calculate the path of the target vessel segment in 3D. Since the transformations matrices map from millimetre dimensions to pixel dimensions, the 3D centreline definition is in millimetre units. For each point in the 3D definition, the angle of the vessel centreline to the x-ray beam is calculated and the geometric magnification factor. The methods for x-ray system perspective calibration and 2D/3D vessel centerline determination were adapted from [Kim 1982, MacKay 1982, Hawkes 1987, & Seifalian 1993].

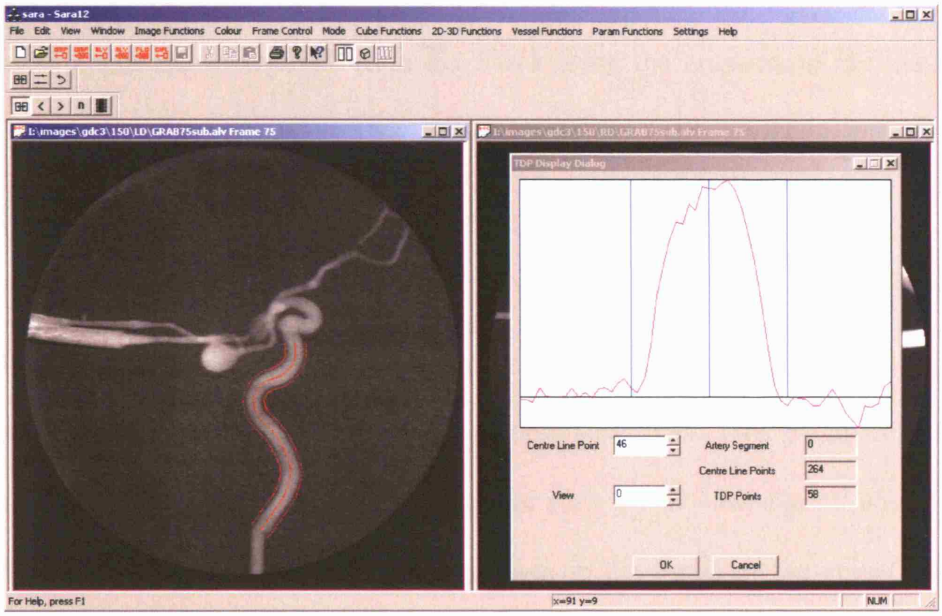

Figure 6.33: SARA 2000 software: Stage 3: 2D Vessel Centreline Determination: The refined centreline, shown as the middle red line on the x-ray image, is calculated using the centre of gravity of the TDP, an example of which is shown on the right.

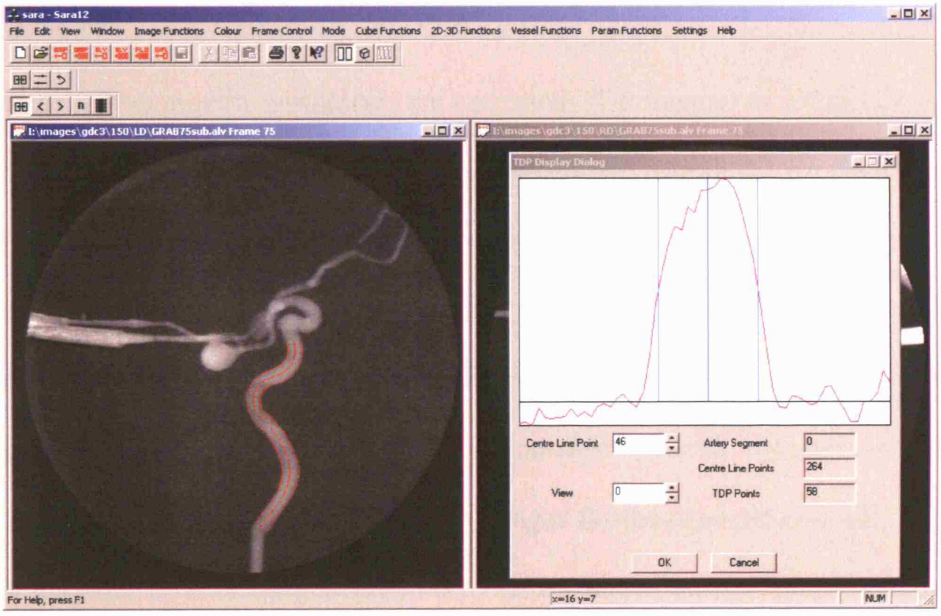

Figure 6.34: SARA 2000 software: Stage 5: Vessel Edge Detection: The detected vessel edges are shown as the two outer red lines in the x-ray image. The vertical blue lines marked on the TDP show the position of the vessel edges and centreline for one point along the vessel.

Stage 5: Vessel Edge Detection

The vessel edges are determined from the TDPs using the criterion of the maximum sum of moduli of the first and second derivatives of the TDP [Seifalian 1993]. Figure 6.34 illustrates the detection of the vessel edges.

Stage 6: Parametric Image Calculation

The 2D and 3D centreline definitions and the detected vessel edges are used to generate the parametric image representation of the angiographic data. Two parametric images were generated for each biplane data set, one for each x-ray view. For all points along the 2D centreline, the integral of the TDPs between the limits of the vessel edges is computed. This integral is then corrected for angulation of the 3D centreline to the x-ray beam and the magnification factor. The corrected TDP integral as a function of distance along the target vessel segment is computed for all 75 images in the subtracted sequence to form the *"raw parametric image"*. The raw parametric image is then *"row normalized"*. This process normalizes the corrected TDP integral as a function of time for each point along the 2D centreline to the maximum value in the parametric image. Row normalization removes the effects of non-uniformities in the x-ray images, caused for example by beam hardening and the anode heal effect, and allows for variation in the vessel cross-sectional area [Hawkes 1992 & Seifalian 1993]. The intensity value in the parametric image is now proportional to contrast material concentration. Figure 6.35a shows the row normalized parametric images for the example data set. The final stage in the parametric image generation is to convert the distance dimension from pixel units to millimetre units by using the 3D centerline definition. Figure 6.35b shows the final parametric image output for the example data set. It can be seen that the images are shorter in the distance axis when compared to those shown in figure 6.35a. This is

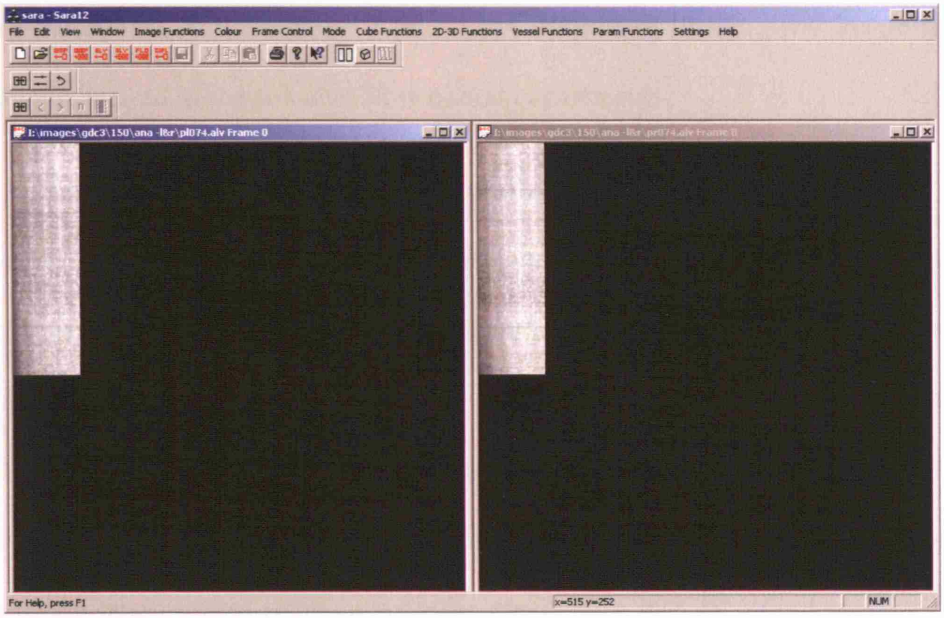

(a)

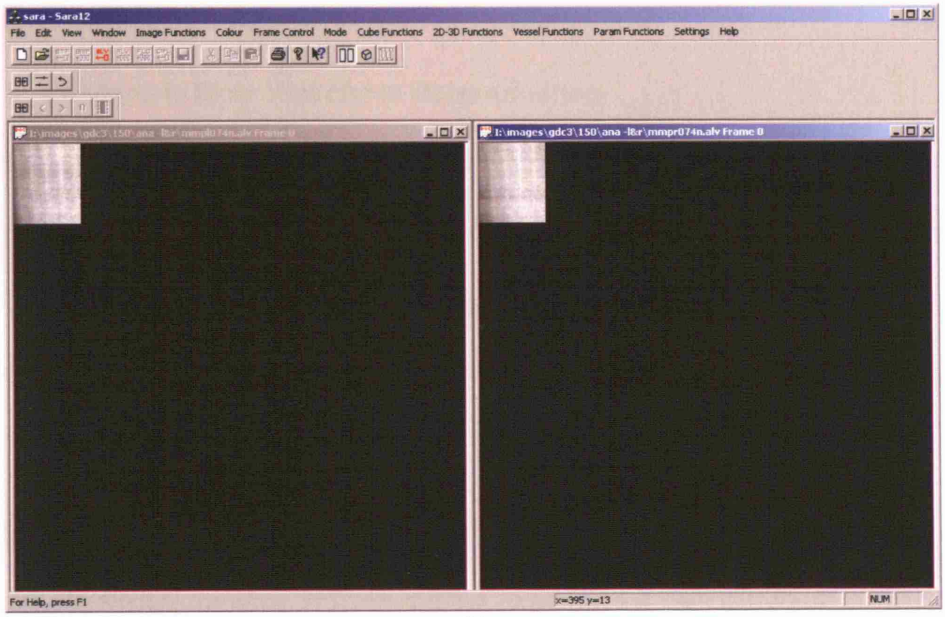

(b)

Figure 6.35: SARA 2000 software: Stage 6: Parametric Image Calculation: (a) The row normalised parametric images for the example data set. Pixel intensity represents contrast material concentration. The vertical axis is distance along the vessel (top is proximal part and bottom is distal part) and the horizontal axis is time. The units of distance are pixels along the 2D centreline. (b) The final parametric image output of the SARA 2000 software for the example data set. The distance axis is now such that 1 pixel represents 1 mm along the target vessel.

because there were approximately 3 pixels per millimetre in the x-ray image for the magnifications used in the pulsatile flow circuit experiments.

Stage 7: Vessel Cross-Sectional Area Calculation

The vessel cross-sectional area was determined from the know diameters for the stationary and moving silicone tubing experiments. The densitometric method described by Hawkes *et al.* [Hawkes 1992] was used to determine the average vessel cross-sectional area for the prosthetic vascular graft and cerebral vascular phantom experiments using the maximum intensity images. Averaging was performed along the length of the target vessel segment with the assumption that the vessel cross-sectional area was constant.

Stage 8: Volumetric Flow Waveform Determination

The ORG, PA, OP, and MB algorithms were applied to the parametric images to extract the velocity waveforms. The volumetric flow waveforms were calculated by multiplying the velocity waveforms by the vessel cross-sectional area. Each flow waveform typically contained between 2 and 4 complete cycles depending on the pump frequency.

Modified Analysis for Moving Silicone Tubing Experiments

The analysis for the moving silicone tubing experiments was different to that of the other experiments because the vessel centreline position was continually changing during the x-ray image acquisition. The subtracted sequences were generated by matching each image in the contrast sequence with the corresponding phase matched image in the mask sequence. This is known as *"phase matched subtraction"*. The vessel centreline definition was performed for each image in the subtracted sequence.

Therefore, for each subtracted sequence there were 75 2D and 3D vessel centreline definitions. The parametric image was then generated using these centreline definitions and the image intensity from the subtracted sequence.

6.6 Investigation of the Effects of Varying Image Noise and Vessel Segment Length

A parametric image was selected from the pulsatile flow circuit image data analysis to study the effects of varying the image noise and the vessel segment length on x-ray flow measurements. The chosen image is shown in figure 6.36a. This was taken from the analysis of the moving silicone tubing experiment image data. The vessel diameter was 6 mm, the mean EMF flow rate was 468 ml/min (minimum = 150 and maximum = 1330 ml/min) and the mean velocity was 276 mm/sec (minimum = 88.4 and maximum = 784 mm/sec).

To study the effects of image noise, different amounts of zero mean Gaussian distributed random noise were added to this parametric image. The amounts chosen were of standard deviations of 0, 1, 2, 5, 10, 20, and 30% of the maximum grey value in this parametric image. Figure 6.36b shows the generated parametric image with 30% added noise. The flow waveforms were calculated using each of the four flow extraction algorithms for each of the parametric images, including the original parametric image with no added noise. The vessel segment length was 125 mm.

In order to study the effect of changing the vessel segment length, different sized windows were placed over the parametric image with no added noise. The windows spanned the parametric image in the time axis and varied in their extent in the distance

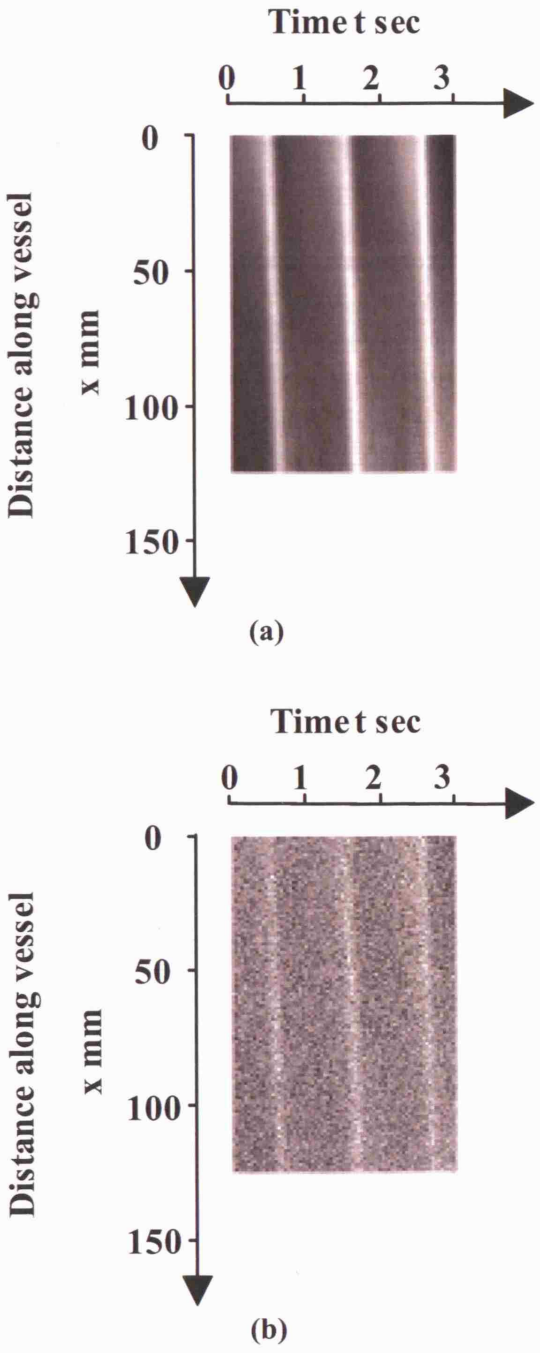

Figure 6.36: (a) The parametric image used for investigating the effects of varying image noise and vessel segment length. (b) The parametric image after adding zero mean Gaussian distributed random noise with standard deviation equal to 30% of the maximum pixel intensity.

axis, starting from the most proximal part of the vessel. The vessel segment lengths chosen varied from 25 to 125 mm in steps of 5 mm. The flow waveforms were calculated using the four flow extraction algorithms for each of the different vessel segment lengths.

For the ORG, PA, and MB algorithms, the maximum distance that the contrast bolus was allowed to travel in one frame interval was restricted to 75% of the total vessel segment length.

6.7 Results for Pulsatile Flow Circuit Experiments

6.7.1 Data Analysis Methods

The pulsatile flow circuit experiments were divided into categories depending on the simulated vessel used in the flow circuit. The categories were: stationary silicone tubing, moving silicone tubing, prosthetic vascular grafts, and cerebral vascular phantom experiments. The flow waveforms extracted using the ORG, PA, OP and MB algorithms from the parametric images were compared to the gold standard EMF waveforms using the statistical methods of correlation analysis and Bland-Altman analysis (see appendix). Both instantaneous flow estimates and mean flow estimates calculated over complete cycles were compared to EMF values. Each calculated flow waveform contained up to 75 instantaneous flow estimates and one or more complete flow cycles. For each experimental category, the following results are presented:

1. Two tables summarizing the experimental results for both instantaneous and mean flow rates calculated using all four algorithms.

2. One or more examples of the flow waveforms extracted using the four algorithms, showing the EMF waveform for comparison.
3. Scatter plots showing the MB and OP algorithm calculated mean flow rate against the EMF flow rate. The ORG algorithm data is shown on these graphs for comparison.
4. Bland-Altman plots showing the MB and OP algorithm mean error of flow rate measurement against the mean EMF flow rate. The ORG algorithm data is shown on these graphs for comparison.

The scatter plots and Bland-Altman plots have not been shown for the PA algorithm data but the results are presented in the summary tables.

6.7.2 Results for Stationary Silicone Tubing Experiments

Tables 6.2a and 6.2b present a summary of the results for the stationary silicone tubing experiments for instantaneous and mean flow values, respectively. The results have been divided into the three vessel sizes (3, 4, and 6 mm diameters) and then grouped together for all vessel sizes. The range of vessel lengths used was from 132 to 167 mm. For instantaneous flow values, a total of 2025 x-ray measurements were compared to EMF values. The instantaneous flow rates ranged from –245 to 1051 ml/min. For mean flow values, a total of 94 x-ray measurements were compared to EMF values. The range of mean flow values was from 68 to 354 ml/min. Three typical examples of x-ray waveforms and corresponding EMF waveforms are shown in figures 6.37a, 6.37b and 6.37c, one for each of the three different vessel diameters. Figures 6.38a and 6.38b show scatter plots of the mean flow values obtained using the MB and OP algorithms, respectively, against the mean EMF flow. The ORG algorithm data is shown on these

graphs for comparison. The error between the mean x-ray measurements and the mean EMF measurements as a function of mean EMF flow is shown in figures 6.39a and 6.39b for the MB and OP algorithms, respectively. The ORG algorithm data is shown on these graphs for comparison. Figure 6.40 shows the mean EMF flow rate plotted against the first principal component score computed by the MB algorithm.

Internal Tube Diameter (mm)	Range of Vessel Lengths (mm)		Number of Data Points	Range of EMF Flow Values (ml/min)		Algorithm	Correlation Coefficient	Mean Error (ml/min)	SD of Error (ml/min)	95% Limits of Agreement (ml/min)	
	Min	Max		Min	Max					Lower Limit	Upper Limit
3	151	165	815	10	516	ORG	0.880	32	70	-106	170
						PA	0.914	32	57	-80	145
						OP	0.892	13	53	-92	117
						MB	0.946	34	46	-56	124
4	140	167	701	-28	610	ORG	0.929	32	80	-124	189
						PA	0.950	52	60	-65	170
						OP	0.935	32	51	-69	132
						MB	0.963	50	57	-62	162
6	132	132	509	-245	1051	ORG	0.770	-5	219	-434	424
						PA	0.784	10	207	-395	416
						OP	0.857	-3	149	-295	288
						MB	0.903	41	124	-202	283
Combined Results	132	167	2025	-245	1051	ORG	0.821	23	128	-229	275
						PA	0.839	34	116	-195	262
						OP	0.877	15	88	-158	188
						MB	0.916	41	77	-109	191

Table 6.2a: Stationary silicone tubing experiments: Summary of instantaneous flow rate results.

Internal Tube Diameter (mm)	Range of Vessel Lengths (mm)		Number of Data Points	Range of EMF Flow Values (ml/min)		Algorithm	Correlation Coefficient	Mean Error (ml/min)	SD of Error (ml/min)	95% Limits of Agreement (ml/min)	
	Min	Max		Min	Max					Lower Limit	Upper Limit
3	151	165	39	103	214	ORG	0.847	32	19	-5	68
						PA	0.882	32	17	-1	65
						OP	0.758	12	22	-30	55
						MB	0.872	34	19	-2	71
4	140	167	33	104	213	ORG	0.878	32	23	-12	77
						PA	0.845	52	23	8	97
						OP	0.783	31	21	-11	74
						MB	0.867	50	22	7	93
6	132	132	22	68	354	ORG	0.872	-6	60	-123	112
						PA	0.838	11	61	-108	130
						OP	0.865	-3	49	-98	92
						MB	0.890	40	50	-57	138
Combined Results	132	167	94	68	354	ORG	0.824	23	37	-50	96
						PA	0.811	34	37	-38	107
						OP	0.819	16	32	-48	79
						MB	0.887	41	30	-18	100

Table 6.2b: Stationary silicone tubing experiments: Summary of mean flow rate results.

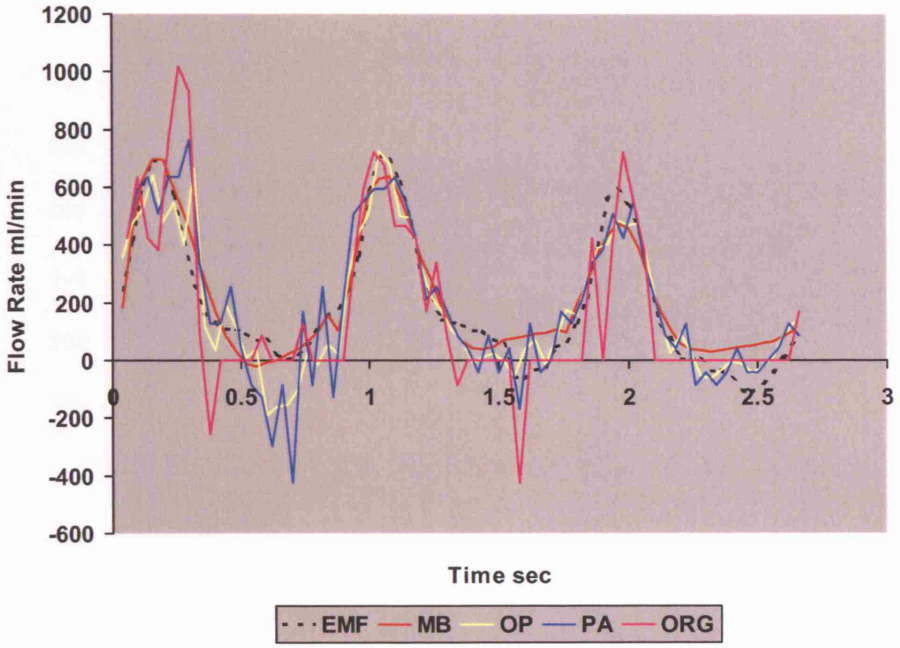

Figure 6.37a: Stationary silicone tubing experiments: An example of x-ray calculated and EMF waveforms for the 6 mm diameter vessel. The mean EMF flow rate was 198 ml/min.

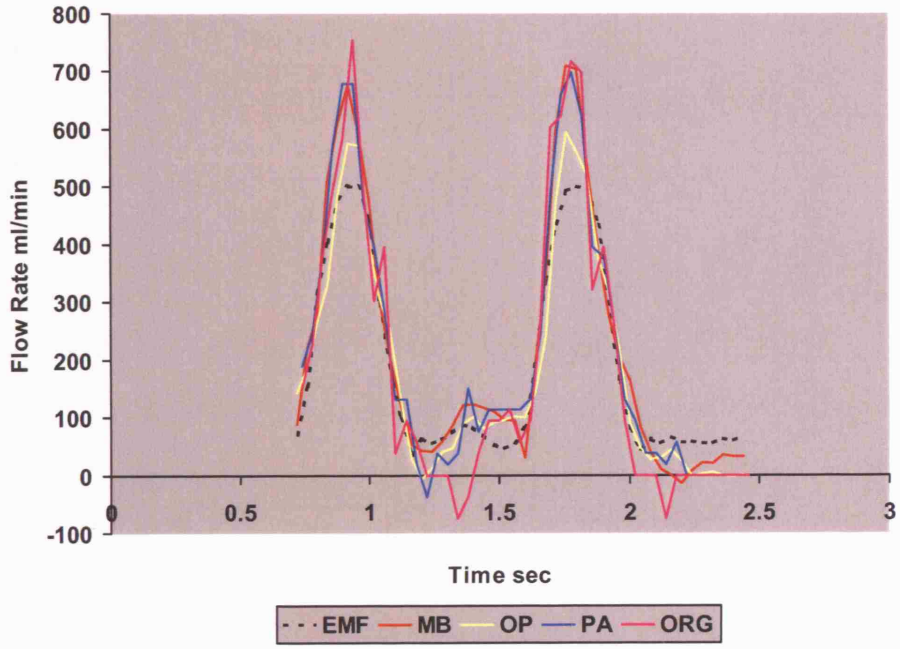

Figure 6.37b: Stationary silicone tubing experiments: An example of x-ray calculated and EMF waveforms for the 4 mm diameter vessel. The mean EMF flow rate was 186 ml/min.

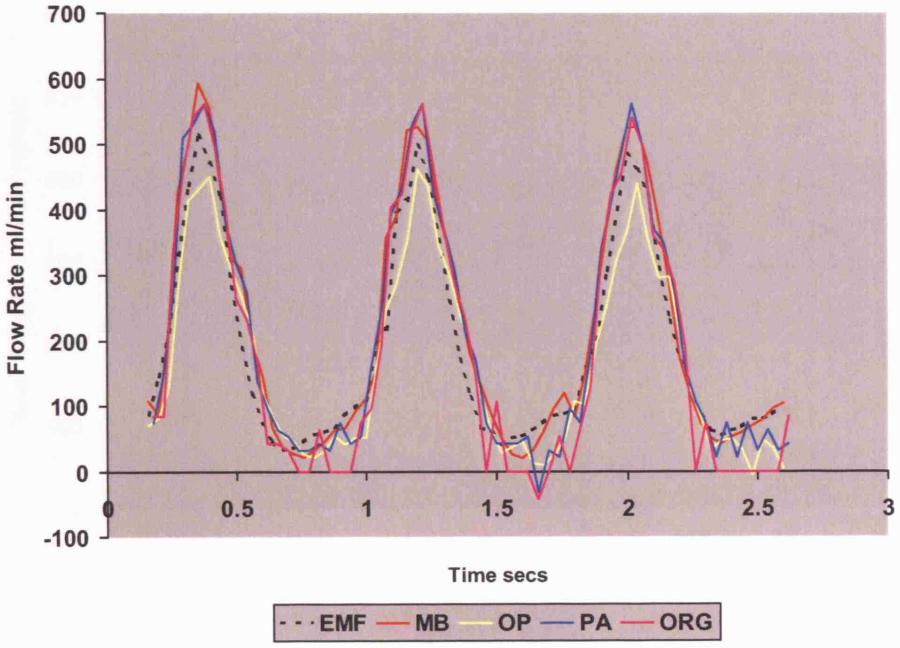

Figure 6.37c: Stationary silicone tubing experiments: An example of x-ray calculated and EMF waveforms for the 3 mm diameter vessel. The mean EMF flow rate was 187 ml/min.

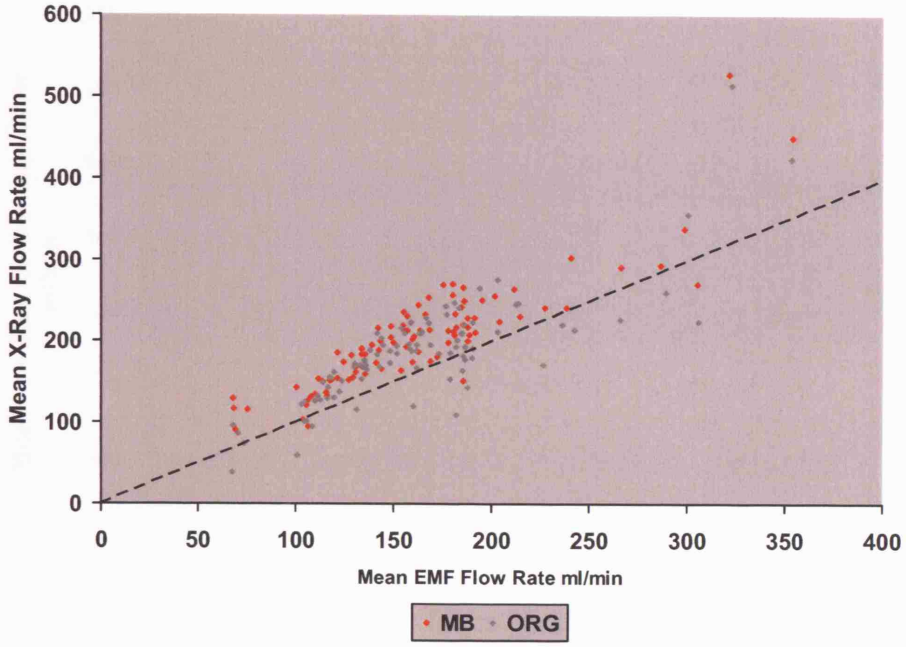

Figure 6.38a: Stationary silicone tubing experiments: Scatter graph to show mean MB & ORG algorithm calculated flow rate against mean EMF flow rate. The dotted line is the line of identity.

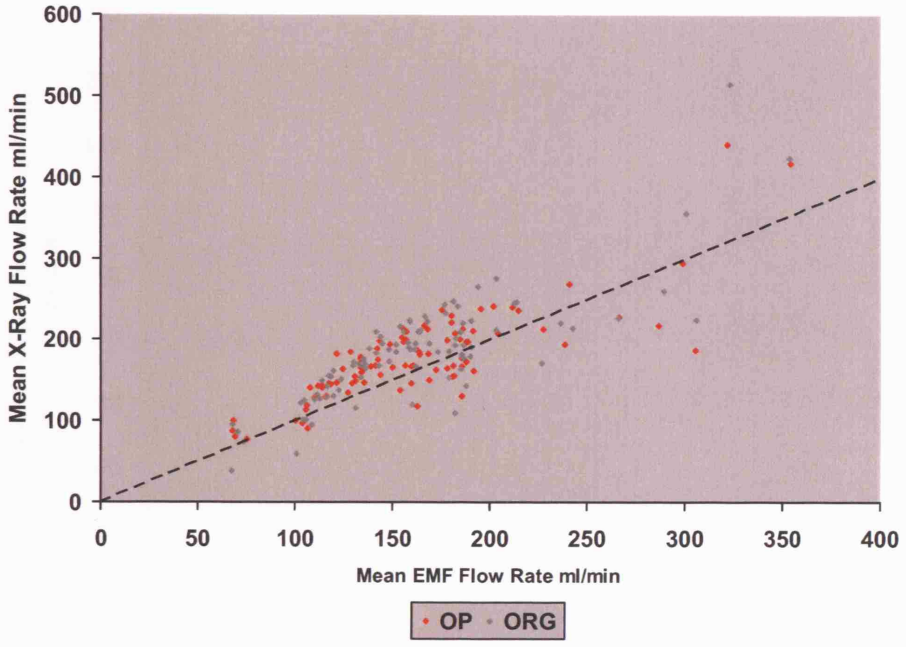

Figure 6.38b: Stationary silicone tubing experiments: Scatter graph to show mean OP & ORG algorithm calculated flow rate against mean EMF flow rate. The dotted line is the line of identity.

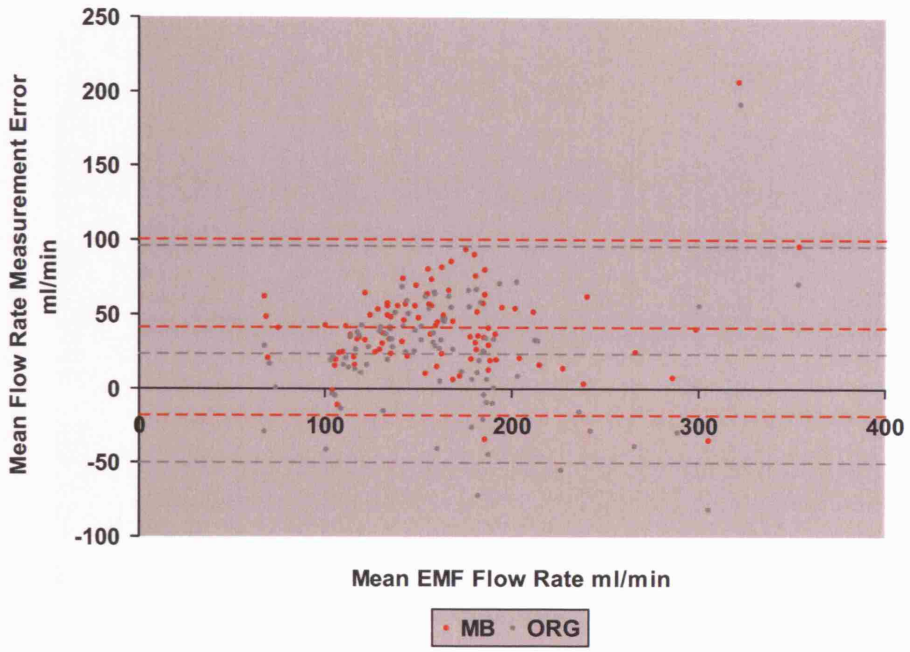

Figure 6.39a: Stationary silicone tubing experiments: Scatter plot to show error in mean flow rate measurement for the MB & ORG algorithms against mean EMF flow rate. The dotted lines show the mean error and the 95% limits of agreement.

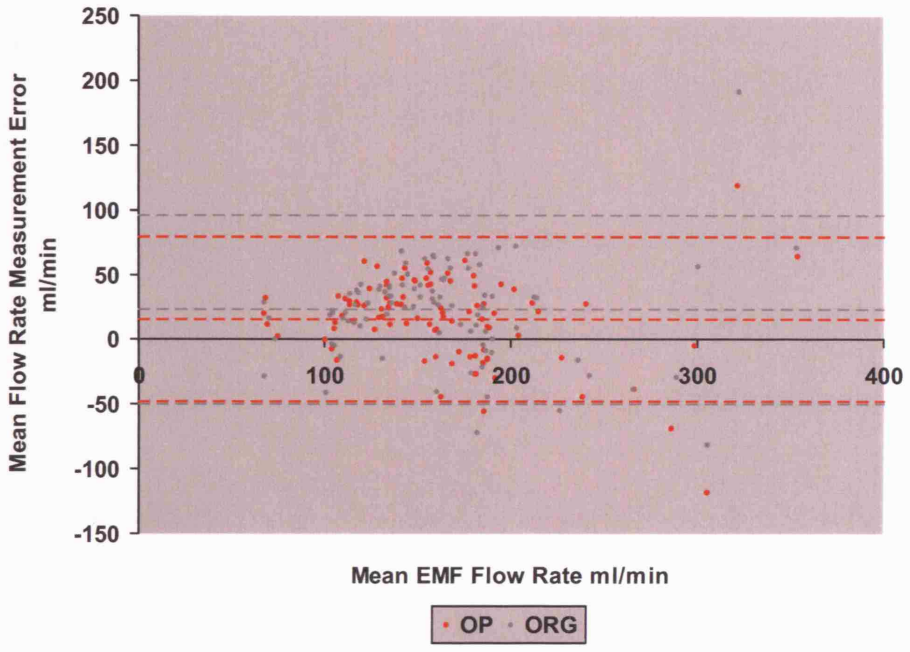

Figure 6.39b: Stationary silicone tubing experiments: Scatter plot to show error in mean flow rate measurement for the OP & ORG algorithms against mean EMF flow rate. The dotted lines show the mean error and the 95% limits of agreement.

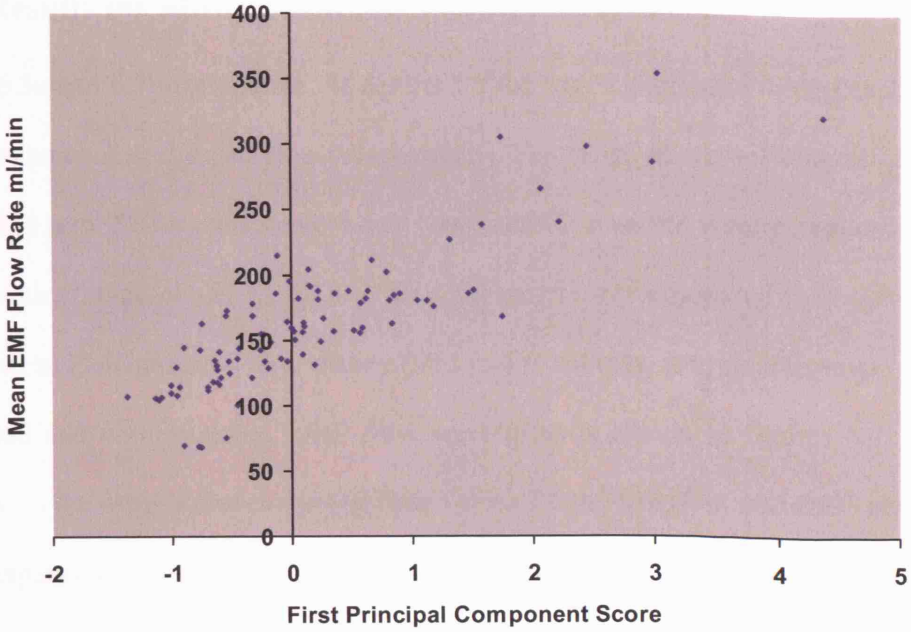

Figure 6.40: Stationary silicone tubing experiments: MB algorithm: Scatter plot to show mean EMF flow rate against first principal component score. PMCC = 0.868, n = 94.

6.7.3 Results for Moving Silicone Tubing Experiments

Tables 6.3a and 6.3b summarize the results for the moving silicone tubing experiments for instantaneous and mean flow, respectively. The range of vessel lengths used was 133 to 136 mm. 520 instantaneous x-ray computed flow values were compared to EMF values with a range of –81 to 1414 ml/min. 20 mean x-ray computed flow values were compared to EMF values with a range of 255 to 534 ml/min. A typical example of x-ray calculated and corresponding EMF flow waveforms is shown in figures 6.41. Figure 6.42 shows the mean x-ray computed flow values for the MB, OP, and ORG algorithms plotted against the mean EMF flow rate. Figure 6.43 shows the error in x-ray measured mean flow values as a function of mean EMF flow rate for the MB, OP, and ORG algorithms.

Internal Tube Diameter (mm)	Range of Vessel Lengths (mm)		Number of Data Points	Range of EMF Flow Values (ml/min)		Algorithm	Correlation Coefficient	Mean Error (ml/min)	SD of Error (ml/min)	95% Limits of Agreement (ml/min)	
	Min	Max		Min	Max					Lower Limit	Upper Limit
6	133	136	520	-81	1414	ORG	0.914	25	175	-318	368
						PA	0.927	41	155	-263	345
						OP	0.931	1	134	-262	264
						MB	0.957	21	119	-212	254

Table 6.3a: Moving silicone tubing experiments: Summary of instantaneous flow rate results.

Internal Tube Diameter (mm)	Range of Vessel Lengths (mm)		Number of Data Points	Range of EMF Flow Values (ml/min)		Algorithm	Correlation Coefficient	Mean Error (ml/min)	SD of Error (ml/min)	95% Limits of Agreement (ml/min)	
	Min	Max		Min	Max					Lower Limit	Upper Limit
6	133	136	20	255	534	ORG	0.920	26	46	-63	116
						PA	0.912	42	48	-51	136
						OP	0.895	2	44	-84	87
						MB	0.874	22	45	-67	110

Table 6.3b: Moving silicone tubing experiments: Summary of mean flow rate results.

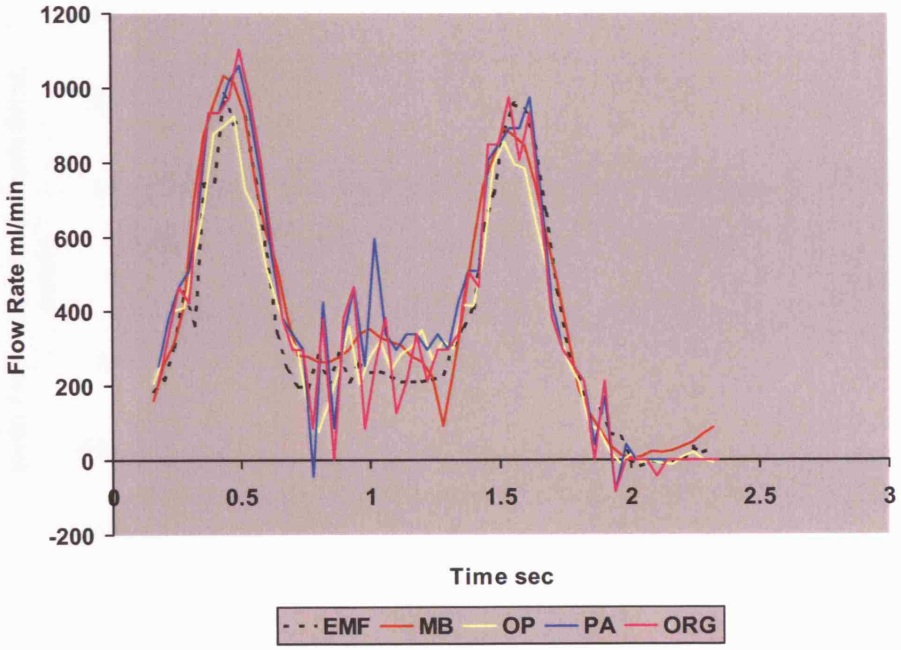

Figure 6.41: Moving silicone tubing experiments: An example of x-ray calculated and EMF waveforms. The mean EMF flow rate was 347 ml/min.

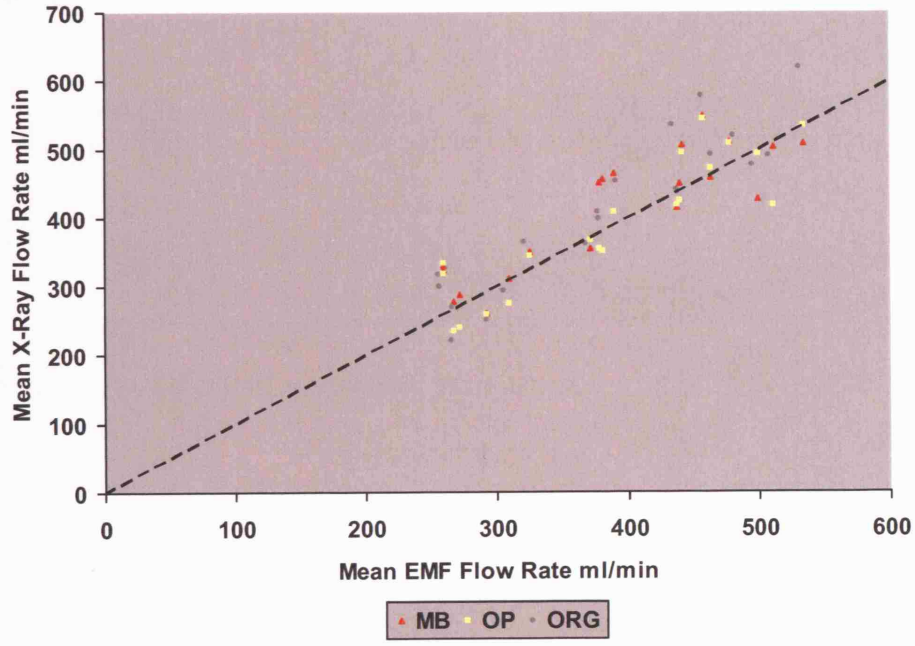

Figure 6.42: Moving silicone tubing experiments: Scatter graph to show mean MB, OP, & ORG algorithm calculated flow rate against mean EMF flow rate. The dotted line is the line of identity.

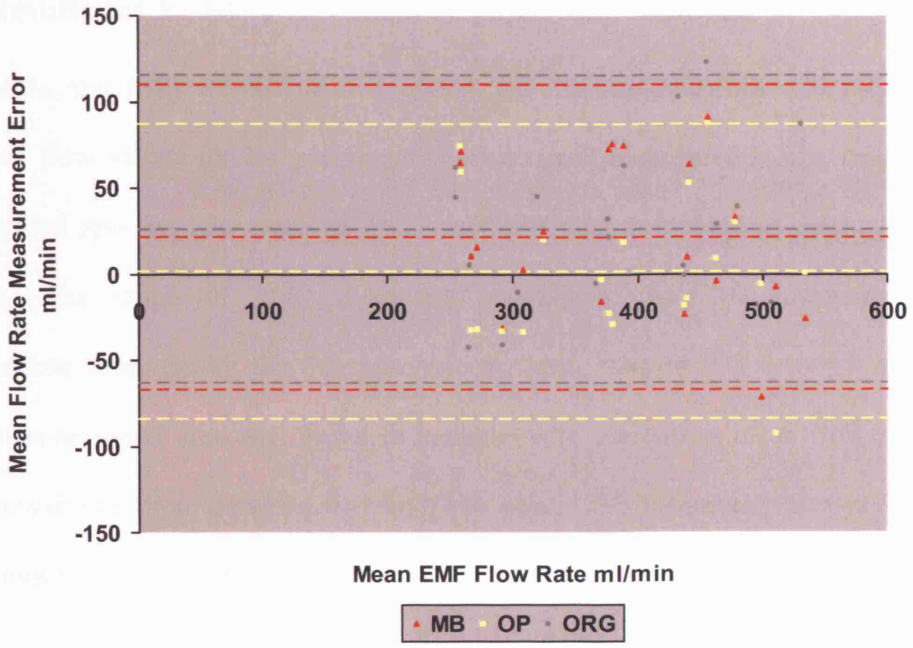

Figure 6.43: Moving silicone tubing experiments: Scatter plot to show error in mean flow rate measurement for the MB, OP, & ORG algorithms against mean EMF flow rate. The dotted lines show the mean error and the 95% limits of agreement.

6.7.4 Results for Prosthetic Vascular Graft Experiments

Tables 6.4a and 6.4b summarize the results for the instantaneous and mean x-ray calculated flow values for the prosthetic vascular graft experiments. The results have been divided into the two types of graft used and then combined to produce overall statistics. The range of graft diameters, calculated from the measured mean cross-sectional area (using the densitometric method), was from 3.8 to 4.9 mm. The mean cross-sectional area was found to increase with increasing mean flow rate. The vessel length used was between 114 and 126 mm. 1533 instantaneous x-ray derived flow values were compared to EMF values ranging from –144 to 875 ml/min. 70 x-ray derived mean flow values were compared to mean EMF values ranging from 59 to 313 ml/min. Figure 6.44a shows a typical example of x-ray calculated waveforms and the corresponding EMF waveform for the CPU vascular graft with a mean flow rate of 107 ml/min. Figure 6.44b is a similar plot showing a typical example for the PTFE vascular graft with a mean flow rate of 308 ml/min. Figures 6.45a and 6.45b show the MB and OP algorithm calculated mean flow against the mean EMF flow, respectively, with the ORG data for comparison. Figures 6.46a and 6.46b show the error in x-ray calculated mean flow as a function of EMF mean flow for the MB and OP algorithms, respectively, with the ORG data for comparison.

Graft Type	Range of Internal Diameters (mm)		Range of Vessel Lengths (mm)		Number of Data Points	Range of EMF Flow Values (ml/min)		Algorithm	Correlation Coefficient	Mean Error (ml/min)	SD of Error (ml/min)	95% Limits of Agreement (ml/min)	
	Min	Max	Min	Max		Min	Max					Lower Limit	Upper Limit
PTFE	4.0	4.9	126	126	561	-13	875	ORG	0.853	-11	127	-260	237
								PA	0.899	5	98	-187	197
								OP	0.923	-17	82	-178	145
								MB	0.958	-4	62	-125	116
CPU	3.8	4.8	114	114	972	-144	807	ORG	0.734	-18	205	-420	385
								PA	0.778	-6	170	-340	327
								OP	0.848	-40	109	-254	174
								MB	0.904	-1	91	-180	179
Combined Results	3.8	4.9	114	126	1533	-144	875	ORG	0.768	-15	181	-369	339
								PA	0.813	-2	148	-292	288
								OP	0.875	-32	101	-229	166
								MB	0.924	-2	82	-162	158

Table 6.4a: Prosthetic vascular graft experiments: Summary of instantaneous flow rate results.

Graft Type	Range of Internal Diameters (mm)		Range of Vessel Lengths (mm)		Number of Data Points	Range of EMF Flow Values (ml/min)		Algorithm	Correlation Coefficient	Mean Error (ml/min)	SD of Error (ml/min)	95% Limits of Agreement (ml/min)	
	Min	Max	Min	Max		Min	Max					Lower Limit	Upper Limit
PTFE	4.0	4.9	126	126	27	59	320	ORG	0.952	-11	32	-74	52
								PA	0.980	5	25	-43	53
								OP	0.980	-17	18	-53	20
								MB	0.971	-4	24	-52	43
CPU	3.8	4.8	114	114	43	59	293	ORG	0.725	-19	59	-135	97
								PA	0.801	-7	41	-87	73
								OP	0.781	-39	41	-119	41
								MB	0.914	-1	27	-54	52
Combined Results	3.8	4.9	114	126	70	59	320	ORG	0.843	-16	50	-114	82
								PA	0.907	-2	36	-72	67
								OP	0.884	-30	35	-100	39
								MB	0.947	-2	26	-53	48

Table 6.4b: Prosthetic vascular graft experiments: Summary of mean flow rate results.

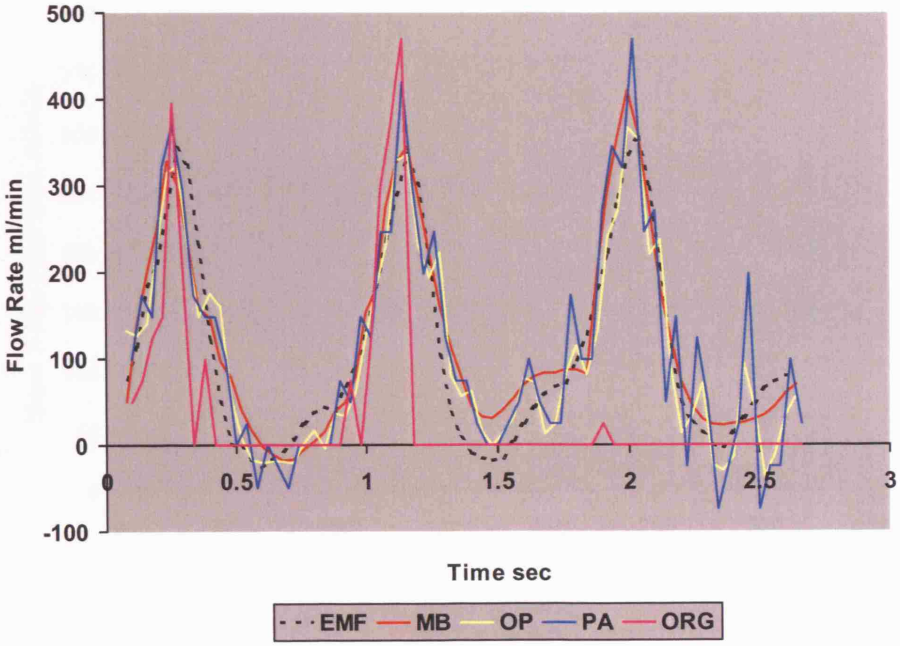

Figure 6.44a: Prosthetic vascular graft experiments: An example of x-ray calculated and EMF waveforms for the CPU graft. The mean EMF flow rate was 107 ml/min.

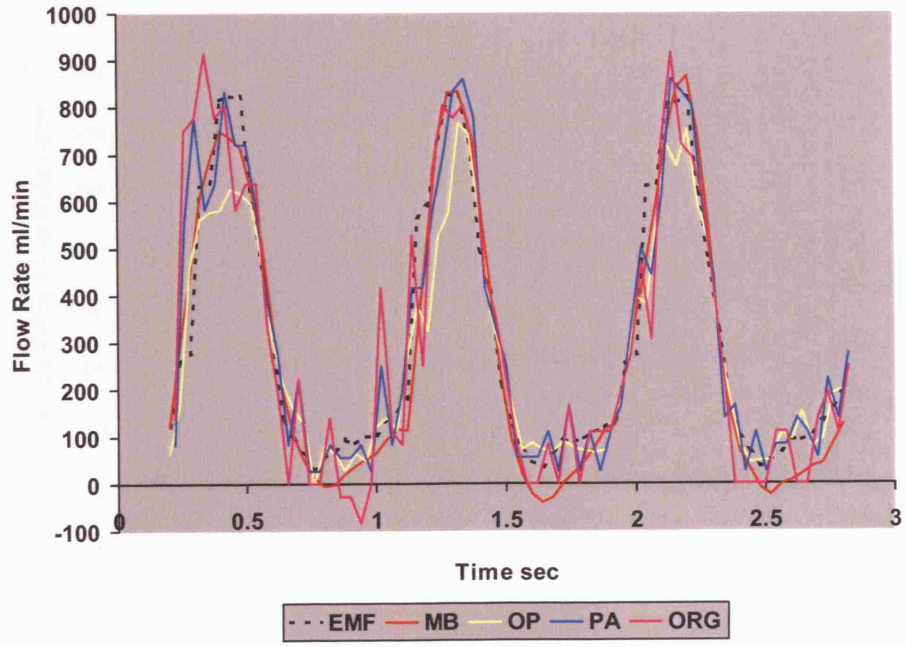

Figure 6.44b: Prosthetic vascular graft experiments: An example of x-ray calculated and EMF waveforms for the PTFE graft. The mean EMF flow rate was 308 ml/min.

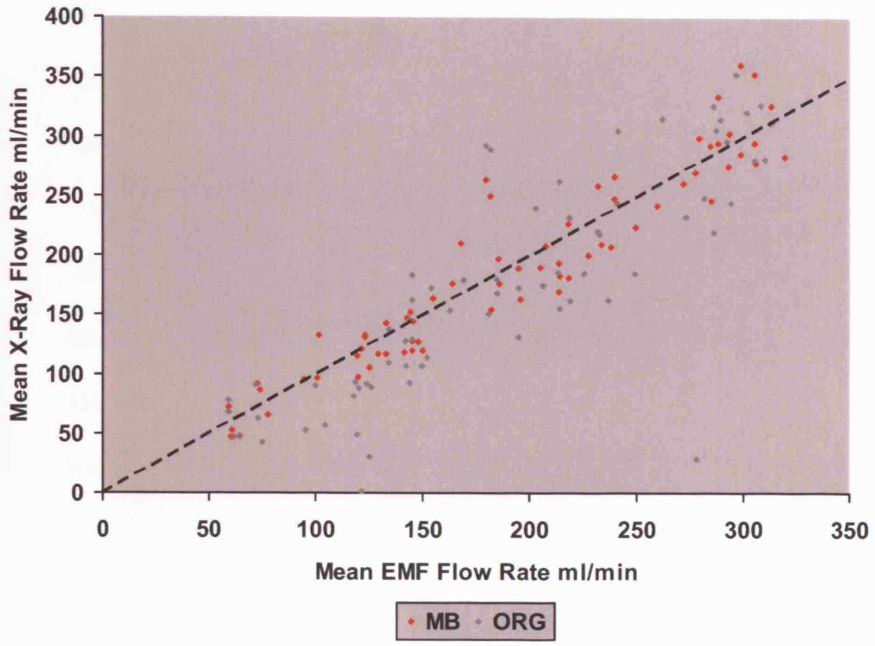

Figure 6.45a: Prosthetic vascular graft experiments: Scatter graph to show mean MB & ORG algorithm calculated flow rate against mean EMF flow rate. The dotted line is the line of identity.

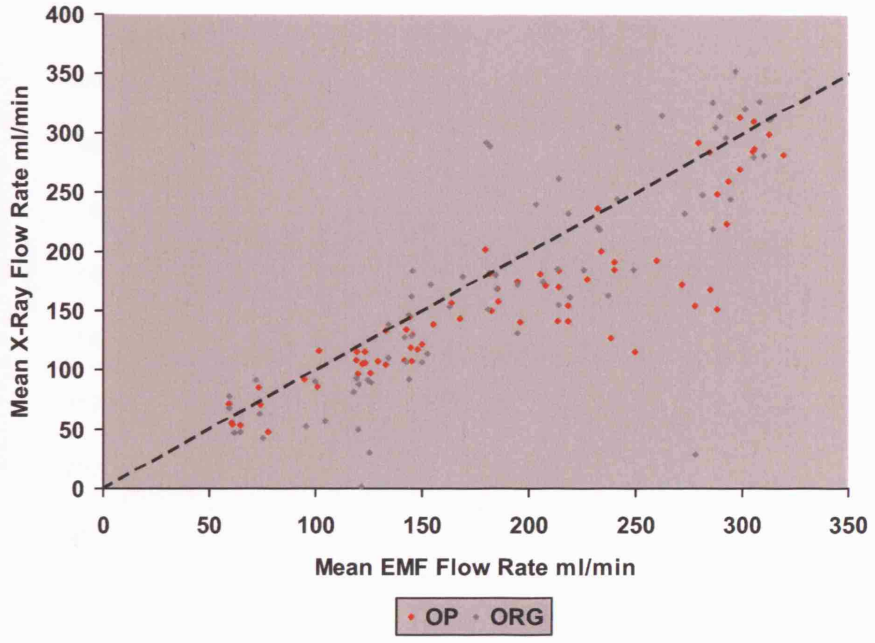

Figure 6.45b: Prosthetic vascular graft experiments: Scatter graph to show mean OP & ORG algorithm calculated flow rate against mean EMF flow rate. The dotted line is the line of identity.

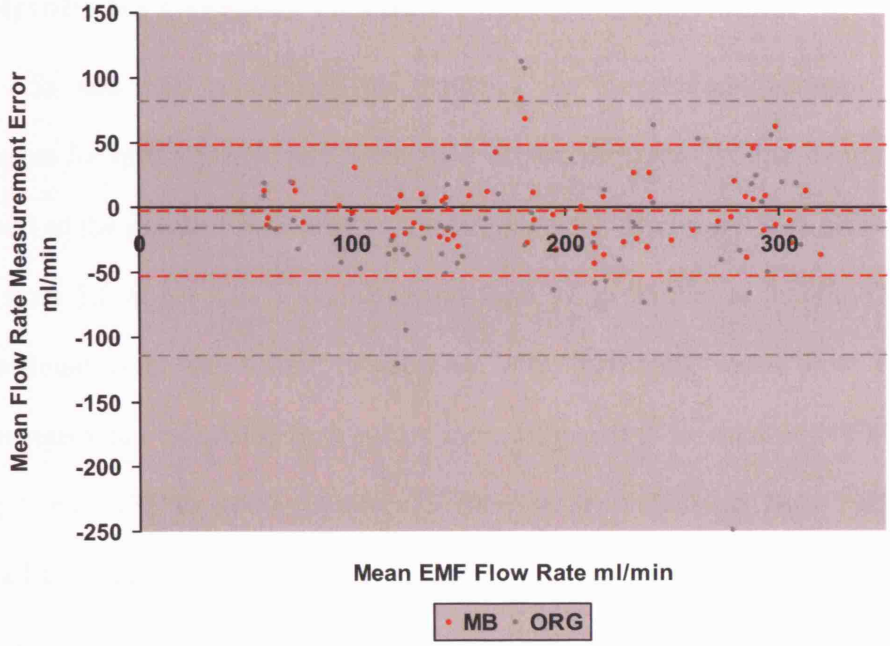

Figure 6.46a: Prosthetic vascular graft experiments: Scatter plot to show error in mean flow rate measurement for the MB & ORG algorithms against mean EMF flow rate. The dotted lines show the mean error and the 95% limits of agreement.

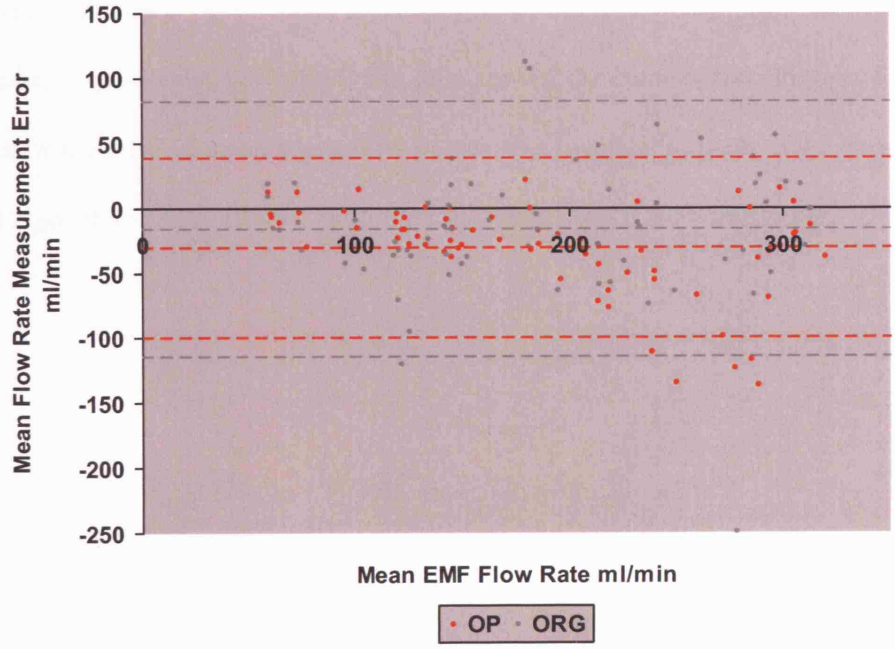

Figure 6.46b: Prosthetic vascular graft experiments: Scatter plot to show error in mean flow rate measurement for the OP & ORG algorithms against mean EMF flow rate. The dotted lines show the mean error and the 95% limits of agreement.

6.7.5 Results for Cerebral Vascular Phantom Experiments

Tables 6.5a and 6.5b summarize the statistics for the cerebral vascular phantom experiments for instantaneous and mean flow values, respectively. The internal carotid artery part of the phantom was used as the target vessel. The vessel size measurements ranged from 5.1 to 5.5 mm in diameter and from 92 to 96 mm in length. The vessel cross-sectional area was found to increase with increasing mean flow rate. 857 instantaneous x-ray calculated flow values were compared to instantaneous EMF values ranging from –172 to 1000 ml/min. 43 mean x-ray calculated flow values were compared to mean EMF values ranging from 31 to 380 ml/min. Typical examples of x-ray calculated and corresponding EMF waveforms are shown in figures 6.47a and 6.47b. Figure 6.47a is an example for a lower mean flow rate of 129 ml/min and figure 6.47b is for a higher mean flow rate of 306 ml/min. Figures 6.48a and 6.48b show the mean x-ray calculated flow values as a function of the mean EMF flow for MB and OP algorithms, respectively, with the ORG data shown for comparison. Figures 6.49a and 6.49b show the error in mean x-ray flow values as a function of mean EMF flow for MB and OP algorithms, respectively, with the ORG data shown for comparison.

Range of Internal Diameters (mm)		Range of Vessel Lengths (mm)		Number of Data Points	Range of EMF Flow Values (ml/min)		Algorithm	Correlation Coefficient	Mean Error (ml/min)	SD of Error (ml/min)	95% Limits of Agreement (ml/min)	
Min	Max	Min	Max		Min	Max					Lower Limit	Upper Limit
5.1	5.5	92	96	857	-172	1000	ORG	0.540	-86	324	-721	550
							PA	0.684	-33	234	-492	426
							OP	0.741	-103	194	-484	279
							MB	0.885	-33	133	-294	228

Table 6.5a: Cerebral vascular phantom experiments: Summary of instantaneous flow rate results.

Range of Internal Diameters (mm)		Range of Vessel Lengths (mm)		Number of Data Points	Range of EMF Flow Values (ml/min)		Algorithm	Correlation Coefficient	Mean Error (ml/min)	SD of Error (ml/min)	95% Limits of Agreement (ml/min)	
Min	Max	Min	Max		Min	Max					Lower Limit	Upper Limit
5.1	5.5	92	96	43	31	380	ORG	0.610	-89	92	-270	93
							PA	0.741	-31	63	-154	92
							OP	0.754	-102	66	-231	26
							MB	0.870	-33	48	-127	61

Table 6.5b: Cerebral vascular phantom experiments: Summary of mean flow rate results.

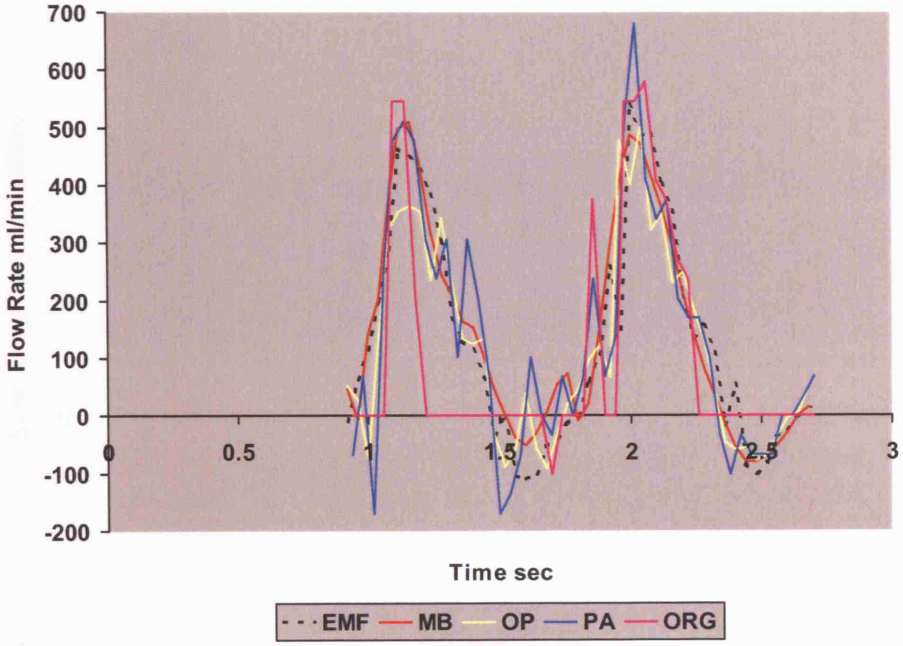

Figure 6.47a: Cerebral vascular phantom experiments: An example of x-ray calculated and EMF waveforms. The mean EMF flow rate was 129 ml/min.

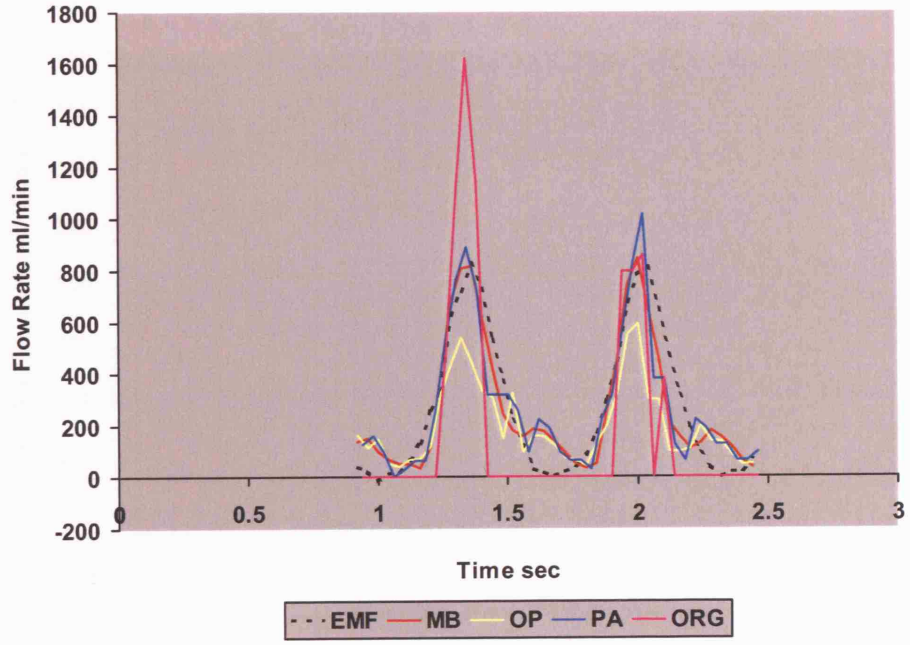

Figure 6.47b: Cerebral vascular phantom experiments: An example of x-ray calculated and EMF waveforms. The mean EMF flow rate was 306 ml/min.

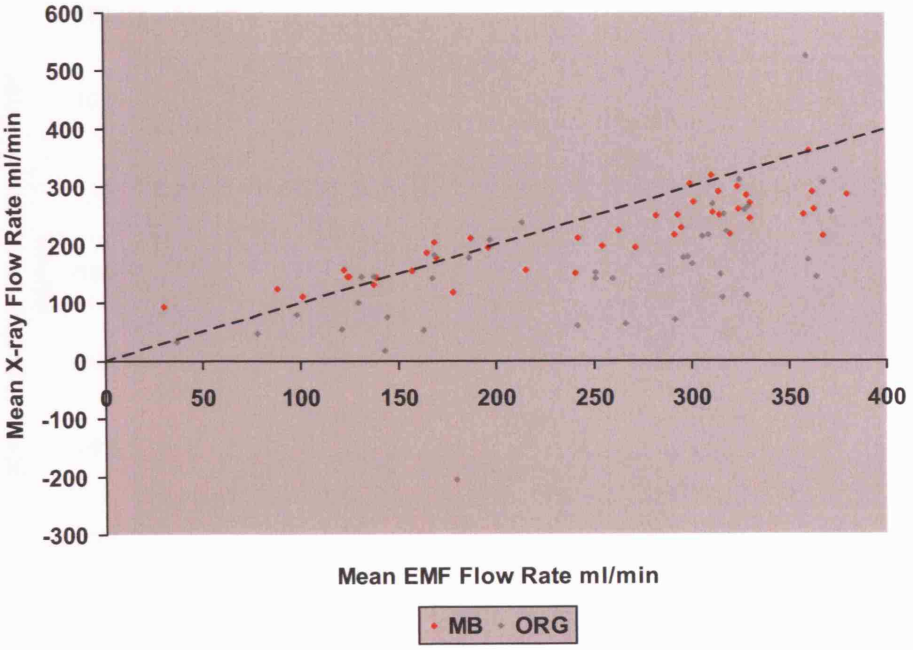

Figure 6.48a: Cerebral vascular phantom experiments: Scatter graph to show mean MB & ORG algorithm calculated flow rate against mean EMF flow rate. The dotted line is the line of identity.

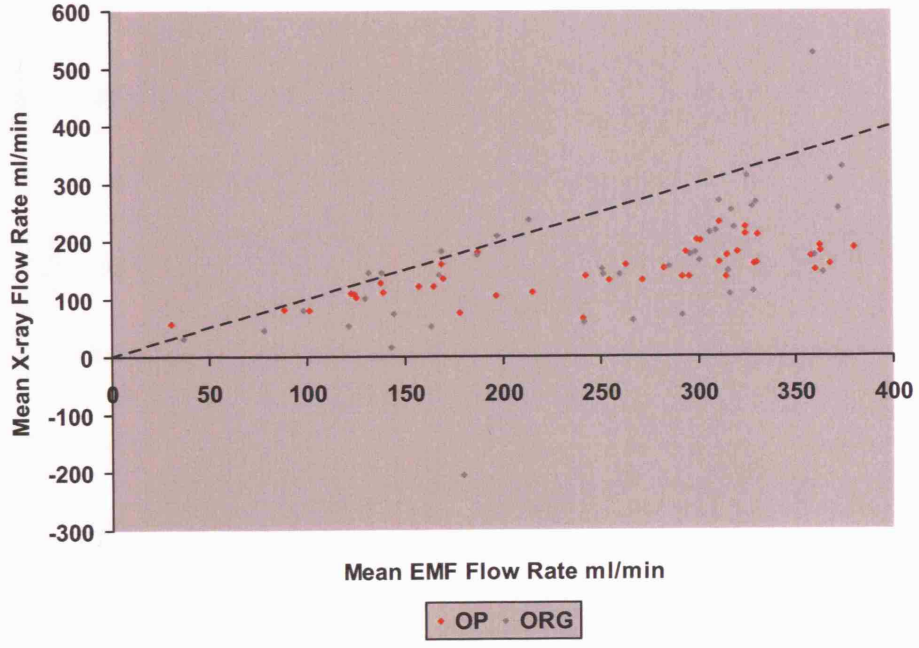

Figure 6.48b: Cerebral vascular phantom experiments: Scatter graph to show mean OP & ORG algorithm calculated flow rate against mean EMF flow rate. The dotted line is the line of identity.

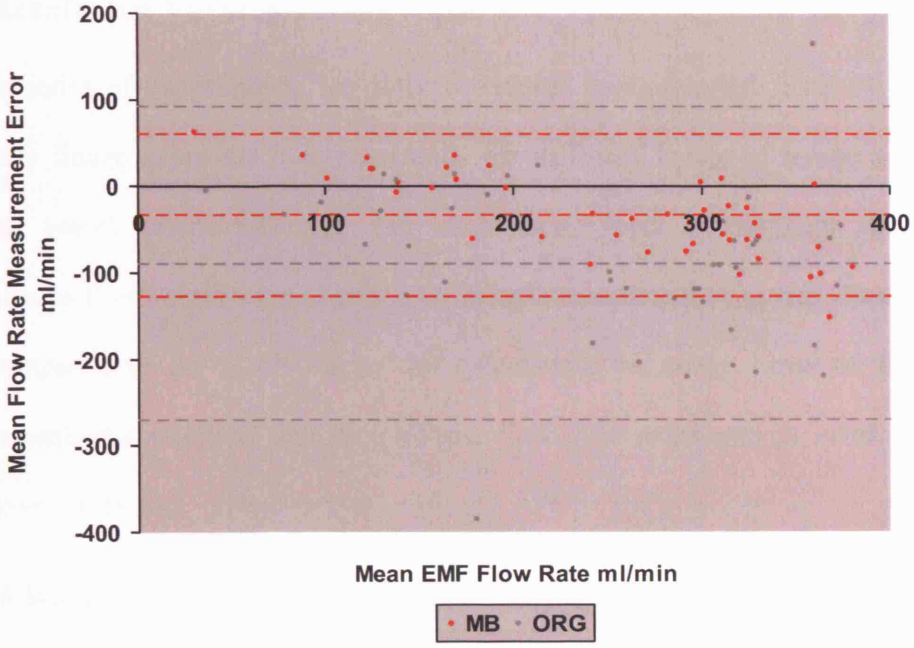

Figure 6.49a: Cerebral vascular phantom experiments: Scatter plot to show error in mean flow rate measurement for the MB & ORG algorithms against mean EMF flow rate. The dotted lines show the mean error and the 95% limits of agreement.

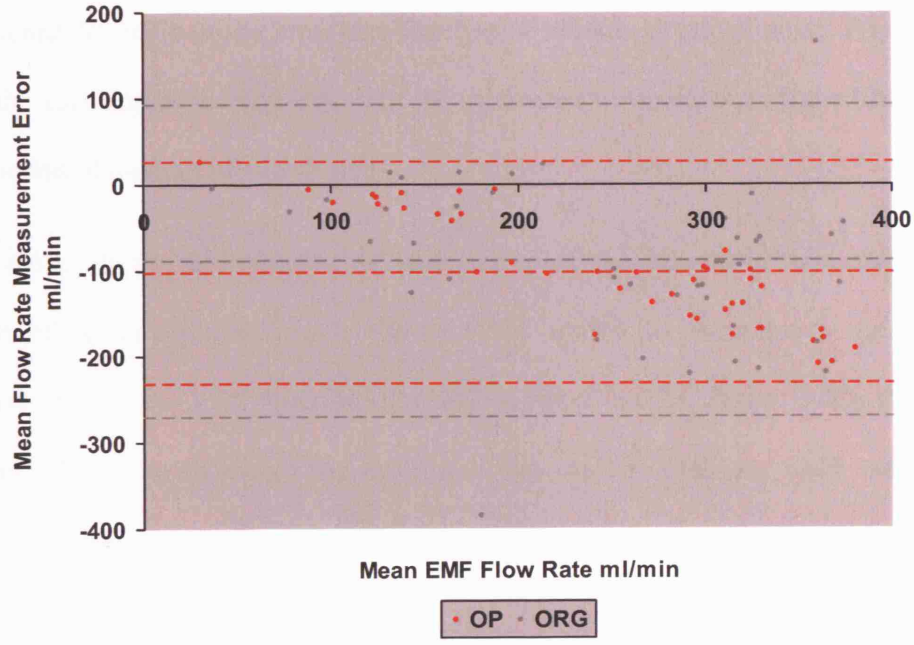

Figure 6.49b: Cerebral vascular phantom experiments: Scatter plot to show error in mean flow rate measurement for the OP & ORG algorithms against mean EMF flow rate. The dotted lines show the mean error and the 95% limits of agreement.

6.7.6 Results for Varying Image Noise and Vessel Segment Length

For this series of experiments, the flow waveform was extracted from the selected parametric image using all four algorithms for different levels of image noise and changing vessel segment length. For each noise level or segment length, 50 instantaneous flow values were obtained covering 2 complete flow cycles. These values were compared to the EMF values by calculating the mean error of flow rate measurement, the standard deviation of the flow rate measurement error, and the correlation coefficient.

Figure 6.50a to 6.50d show the flow waveforms extracted using the MB, OP, PA, and ORG algorithms, with the EMF waveform for comparison, for different amounts of added image noise. Figure 6.51a shows the variation of the mean error of the calculated flow values as a function of amount of added noise. Figure 6.51b shows the variation in the standard deviation of the error as a function of amount of added noise. Figure 6.51c shows the variation of the correlation of the calculated flow values with the EMF values as a function of amount of added noise.

Figure 6.52a shows the variation of mean error of the calculated flow values as a function of vessel segment length. Figure 6.52b shows the variation in the standard deviation of the error as a function of vessel segment length. Figure 6.52c shows the variation of the correlation of the calculated flow values with the EMF values as a function of vessel segment length.

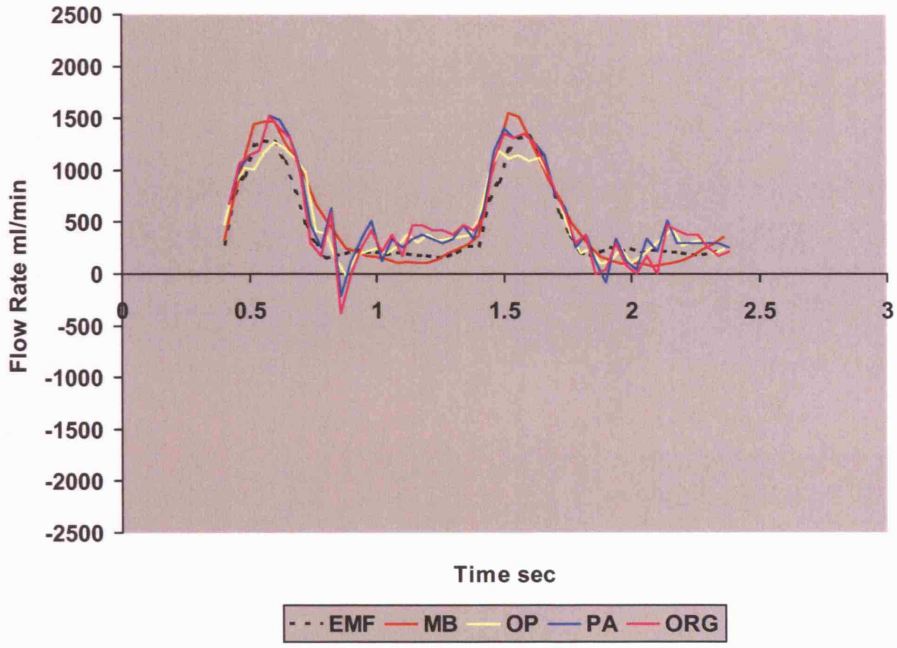

Figure 6.50a: Effect of image noise: X-ray calculated and EMF waveforms for the parametric image with 0% added noise.

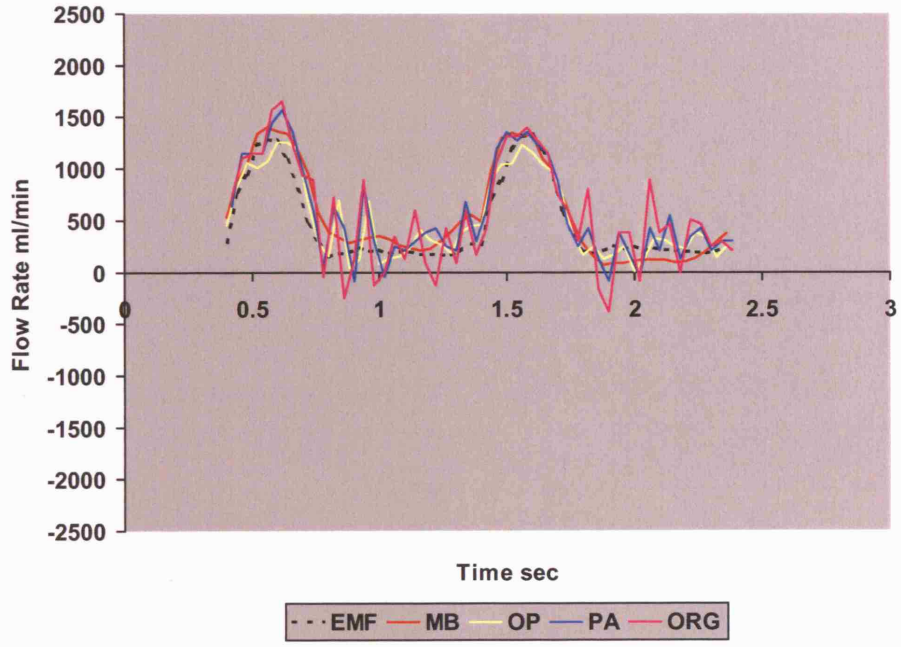

Figure 6.50b: Effect of image noise: X-ray calculated and EMF waveforms for the parametric image with 5% added noise.

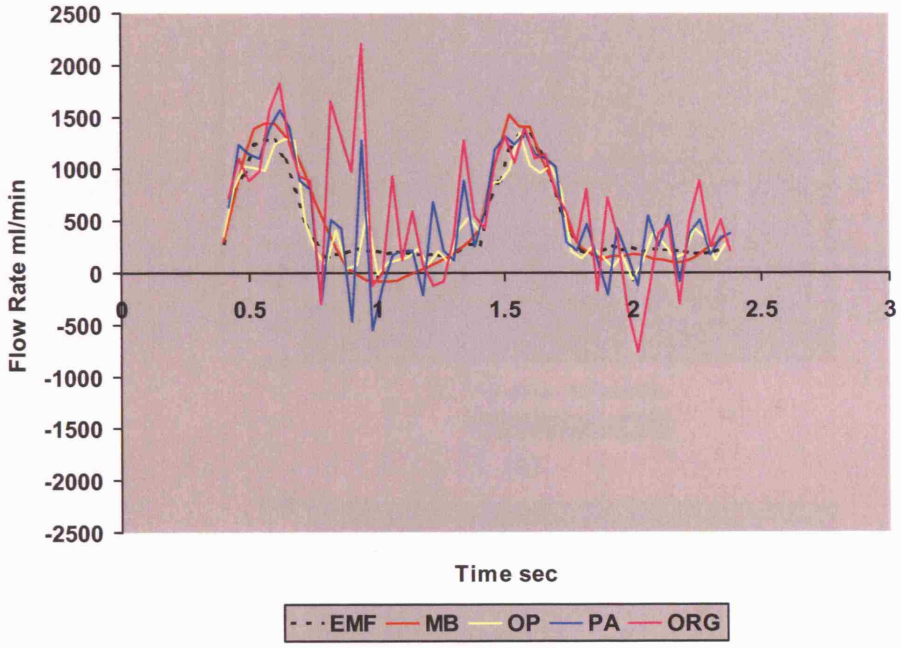

Figure 6.50c: Effect of image noise: X-ray calculated and EMF waveforms for the parametric image with 10% added noise.

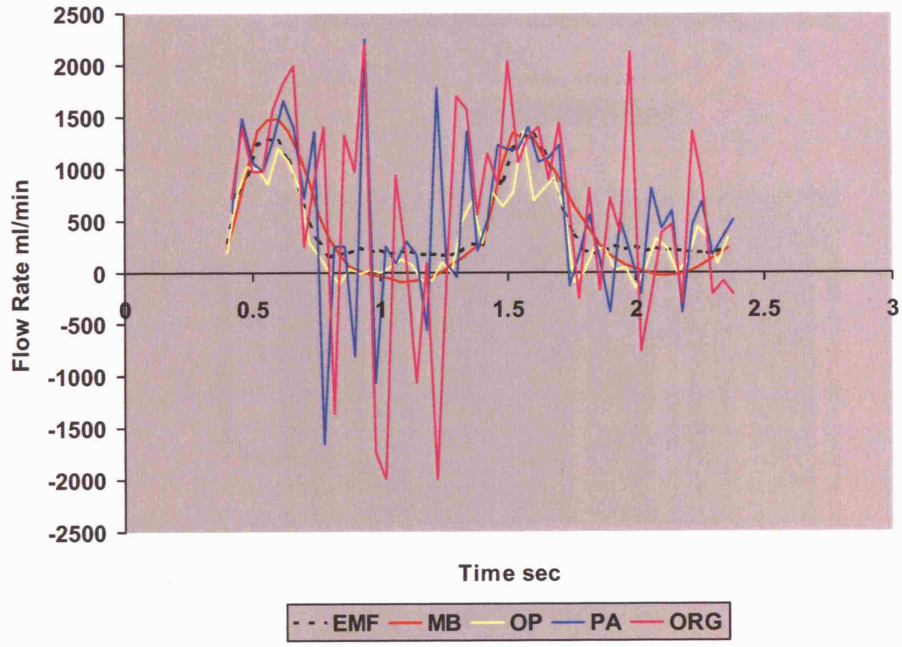

Figure 6.50d: Effect of image noise: X-ray calculated and EMF waveforms for the parametric image with 20% added noise.

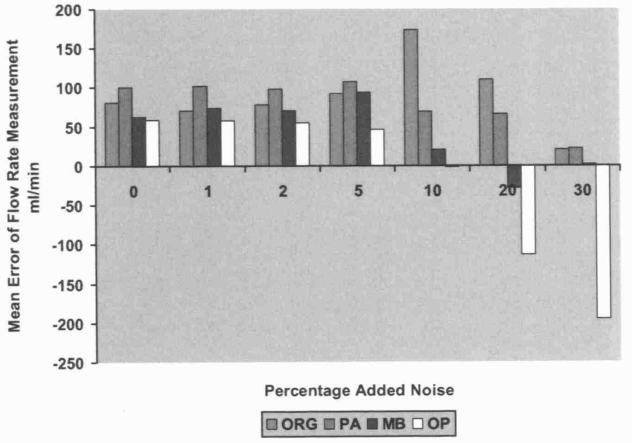

(a)

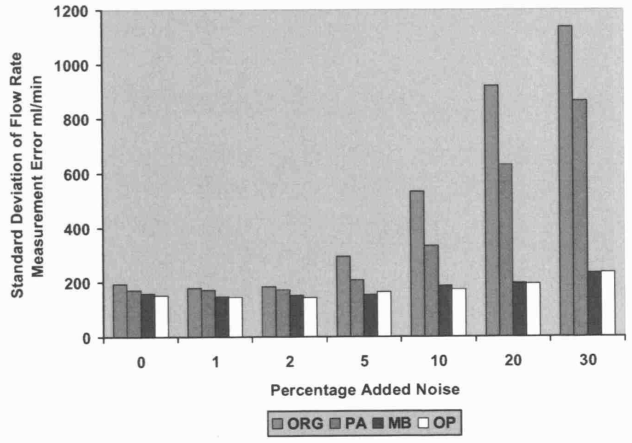

(b)

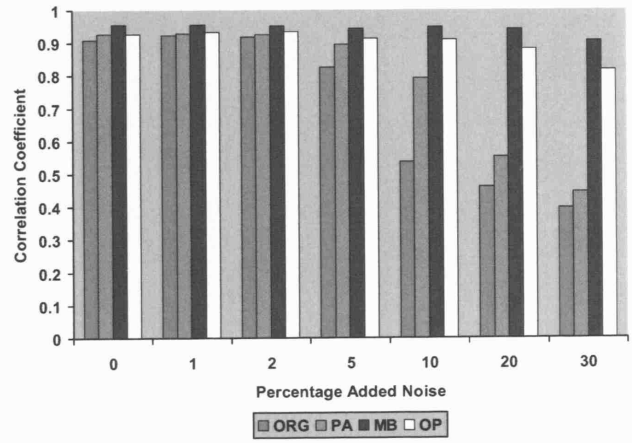

(c)

Figure 6.51: Effect of image noise: (a)Variation of mean error of flow rate measurement,(b) standard deviation of flow rate measurement error, and (c) correlation with EMF flow rate with the amount of added noise.

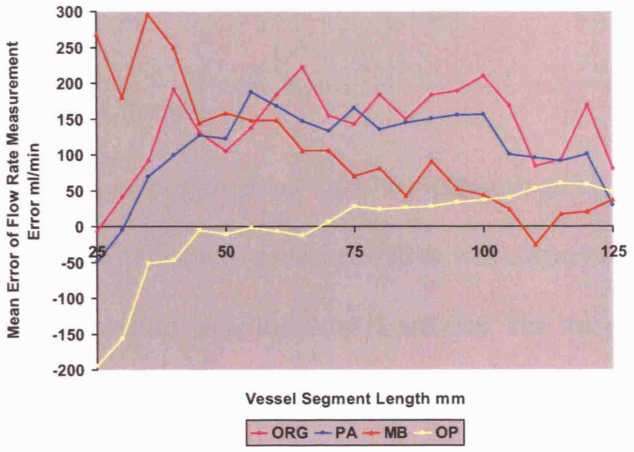

(a)

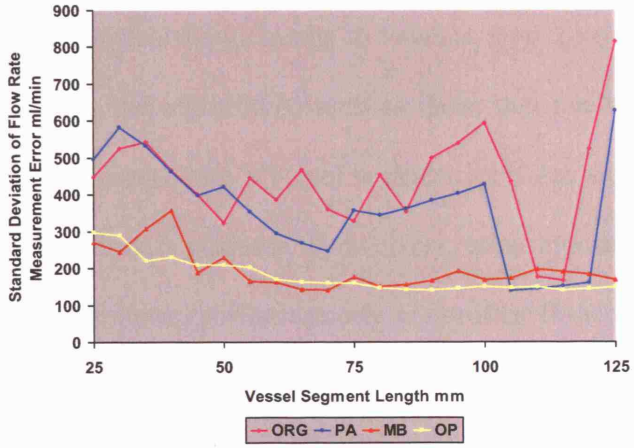

(b)

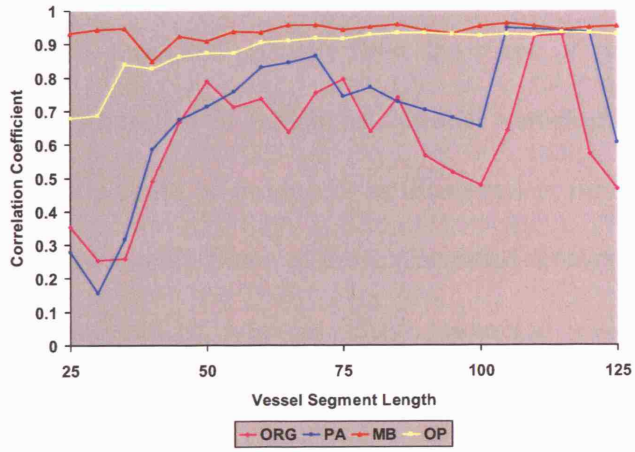

(c)

Figure 6.52: Effect of vessel segment length: (a) Variation of mean error of flow rate measurement, (b) standard deviation of flow rate measurement error, and (c) correlation with EMF flow rate with the vessel segment length.

6.8 Discussion

6.8.1 The Blood Flow Circuit

The blood flow circuit was designed to simulate physiological flow conditions in arteries for the validation of the newly developed flow waveform extraction algorithms. The simulated flow was pulsatile, as is the flow in arteries. The use of pulsatile flow for algorithm validation is very important if the results are to be interpreted with respect to the clinical suitability of an algorithm. It was reported in chapter 2 that many investigators have used constant flow circuits to validate their x-ray flow measurement methods. It is clear that some algorithms, such as those that use the measurement of bolus arrival time at two sites along a vessel segment, perform well in constant flow conditions but fail when flow is pulsatile. Conversely, other algorithms, such as those based on optical flow techniques, perform poorly in constant flow conditions but show promising results in pulsatile conditions where there is more temporal and spatial variation of contrast material concentration.

Although the flow circuit simulated pulsatile flow, the shape of simulated waveforms could not be precisely controlled to match real arterial waveforms. However, many different waveform shapes could be produced, as illustrated in figure 6.19, by altering the parameters of the flow circuit. Some of these resembled femoral artery waveforms, having a distinct biphasic pattern, whereas others resembled waveforms seen in the cerebral circulation, showing a more damped pattern with no reverse flow component.

The use of date-expired whole blood as the circulated fluid had several advantages over using saline. Two devices were used to provide the gold standard measurement of flow during the experiments. The primary device was the EMF and the secondary, back-up

device was the Doppler velocimeter. The EMF was factory calibrated for use with blood and the red blood cells provided the scattering signal required for the operation of the Doppler velocimeter. Furthermore, the use of blood meant that the circulated fluid had realistic haemodynamic properties and realistic interaction with the injected contrast material.

The way in which injected contrast material interacts with the blood flow in real arteries depends partly on the downstream vascular resistance caused by the branching of the arterial tree. If the injection rate is above the underlying flow rate, contrast material will replace blood, achieving a high concentration at the injection site. If the injection rate is below the underlying flow rate, then the contrast material will mix with the blood and achieve a lower concentration. A higher concentration at the injection site is preferable since this will result in greater temporal and spatial variations of contrast material concentration. This will improve the performance of all four of the x-ray flow measurement algorithms used. However, high rate injections will cause greater alteration of the underlying flow. The downstream resistance was simulated to an extent in the flow circuit by applying a metal clip to the tubing distal to the simulated vessel. It was found that the underlying flow rate was increased during the injection of contrast material, as shown by the example EMF recording in figure 6.18. The increase was typically 50 ml/min for the injection rates (120ml/min and 180 ml/min) used during the flow circuit experiments. Therefore, by simulating the downstream vascular resistance, the effects of contrast material injection were not purely additive to the underlying flow rate.

The EMF was used as the gold standard device for measurement of flow rate. Calibration of the EMF under constant flow conditions using timed fluid collection showed that the device was highly linear for measurement of volumetric flow (PMCC = 0.999, n = 11). However, the EMF showed underestimation of true flow that increased with flow rate. Furthermore, the dynamic performance of the EMF for measurement of rapidly changing flow rates was not known and could not be measured since a more accurate flow measurement device was not available. Therefore, it was assumed that the performance of the EMF for flow measurement was the same during pulsatile flow conditions as for constant flow conditions. The calibration of the EMF was performed using date-expired whole blood. The EMF flow values used for comparison to those measured by the x-ray flow extraction algorithms were recorded during the injection of contrast material. The presence of the contrast material will affect the conductivity of the blood, a property that is assumed to be constant for the EMF calibration. The effect of this on the accuracy of EMF flow measurements will be unpredictable due to the variable mixing of the contrast material with the blood. Therefore, the uncertain accuracy of the EMF during pulsatile flow conditions and with the injection of contrast material has to be taken into account when assessing the results of the flow circuit experiments since all x-ray flow measurements were compared to the EMF values.

Overall, the blood flow circuit provided a versatile method to validate the x-ray flow measurement algorithms. The use of the different types of simulated vessel allowed testing in progressively more challenging conditions.

6.8.2 Stationary Silicone Tubing Experiments

For the stationary silicone tubing experiments the simulated vessels (3, 4, and 6 mm diameter) were either fixed flat on the x-ray table or supported at an angle to the table. Since the vessels were surrounded by air, the effects of x-ray scatter were minimal. Also, the thick-walled silicone tubing was rigid so that there was no noticeable change in vessel diameter with the pulsatile pressure changes in the flow circuit and the vessel cross-sectional area was computed from the known vessel diameters. Therefore, in this series of experiments, the flow extraction algorithms were being tested for their ability to measure flow velocity from high quality dynamic angiographic images for a range of mean flow rates and different vessel diameters.

The flow measurement bias was assessed using the mean measurement error. The measurement linearity was assessed using the correlation with EMF flow values. Finally, the measurement variability was assessed using the standard deviation of the measurement error and the 95% limits of agreement. The measurement linearity and variability are important when assessing the ability of an algorithm to measure changes in flow but the bias is only important if single isolated measurements are to be made. For typical clinical applications, such as measurement of coronary flow reserve, the ability to measure changes in flow is more important. Therefore, the interpretation of results has focused on measurement linearity and variability. Furthermore, the interpretation is based on the instantaneous flow results rather than the mean flow results. This was for two reasons. Firstly, the instantaneous flow values were the direct output of the flow extraction algorithms whereas the mean flow values were derived quantities. Secondly, there were approximately 20 times more instantaneous flow values

than mean flow values. Therefore, the instantaneous flow values have greater statistical significance.

It can be seen from the examples of x-ray measured flow waveforms in figures 6.37a to 6.37c that these waveforms were in good agreement with the EMF waveforms. The agreement was better during the systolic part of the flow cycles than the diastolic part. This was especially the case for the ORG algorithm that showed much greater error and variability during the diastolic part of the flow cycles. In fact, the ORG algorithm occasionally recorded zero flow when incorrect shifts in adjacent concentration-distance curves were identified, as can be seen in cycles 2 and 3 in figure 6.37a. During the diastolic part of the flow cycles the flow rate is slowly changing. Therefore, the temporal and spatial variations of contrast material concentration are small. This leads to the increased error and variability of flow rate measurement by the flow extraction algorithms that all depend on these variations for good performance. Figures 6.37a to 6.37c also show that the algorithms performed better for the 3 and 4 mm diameter vessels than the 6 mm vessel. This is further illustrated by the summary of the instantaneous flow measurement results given in table 6.2a. All four algorithms showed lower correlation and greater variability of flow measurements for the 6 mm diameter vessel than the 3 and 4 mm diameter vessels. The dilution of contrast material was greater in the 6 mm diameter vessel due to the increased vessel cross-sectional area into which the contrast material was introduced. Contrast material dilution was also greater because of the higher mean flow rates used for this larger vessel size. Therefore, the temporal and spatial gradients of contrast material were less for the larger vessel, reducing the performance of the flow extraction algorithms.

The combined results for the three vessel diameters produced 2025 instantaneous flow measurements that were compared to the EMF values. The MB algorithm showed the greatest correlation with EMF flow values, followed by the OP, PA, and ORG algorithms (PMCC = 0.916 for MB, 0.877 for OP, 0.839 for PA, 0.821 for ORG). The variability of measurements was lowest for the MB algorithm, followed by the OP, PA, and ORG algorithms (SD = 77 for MB, 88 for OP, 116 for PA, 128 ml/min for ORG). The 95% limits of agreement for the MB algorithm (-109 to 191 ml/min) were narrow when compared to the range of flow rates measured (-245 to 1051 ml/min). The 95% limits of agreement were substantially wider for the ORG algorithm (-229 to 275 ml/min). All four algorithms had a positive bias as shown by the mean error of instantaneous flow measurement. Figures 6.39a and 6.39b show that there was no trend in the measurement bias with mean flow rate. For the MB algorithm a strong linear relationship was demonstrated between the value of the first principal component score and the mean EMF flow rate (see figure 6.40). This suggests that the value of the first principal component score alone could be used to estimate the mean flow rate in the target vessel.

The results from the stationary silicone tubing experiments suggest that even for high quality angiographic images, the use of the waveform shape model constrained method (MB algorithm) can improve the measurement of flow when compared to the basic concentration-distance curve correlation method (ORG algorithm). However, modeling the concentration-distance curves by polynomials (PA algorithm) shows only a marginal improvement over using the original concentration-distance curve data (ORG algorithm). Furthermore, the weighted optical flow method has similar performance to the model based method.

6.8.3 Moving Silicone Tubing Experiments

For the moving silicone tubing experiments 520 instantaneous flow measurements were computed using the four algorithms and compared to the EMF values. The results for the different algorithms showed the same trends as for the stationary silicone tubing experiments. The MB algorithm showed the best correlation with EMF recordings, followed by the OP, PA, and ORG algorithms (PMCC = 0.957 for MB, 0.931 for OP, 0.927 for PA, 0.914 for ORG). The variation in measurement was the least for the MB algorithm, followed by the OP, PA, and ORG algorithms (SD = 119 for MB, 134 for OP, 155 for PA, 175 ml/min for ORG). When compared to the results for the 6 mm diameter stationary silicone tubing, the moving silicone tubing results were surprisingly better in terms of measurement linearity and variation. Also the difference between the four algorithms was not as marked. This was surprising since it was expected that the presence of motion blur and subtraction artifacts in the image data would reduce algorithm performance. The results suggest that the effects of motion blur and subtraction artifacts in the image data were not significant enough to cause deterioration of algorithm performance. The repeatability of the motion simulated by the vessel manipulator resulted in minimal artifacts after phase matched subtraction. Therefore, although the moving silicone tubing experiments effectively tested the ability of the SARA 2000 software to generate parametric images from moving vessel image data, the performance of the flow extraction algorithms was similar to that in the stationary vessel experiments. This can be explained by the limitations of the vessel manipulator that provided only a simplified model of coronary artery motion. Algorithm performance would certainly be expected to be worse for actual dynamic coronary angiographic images when compared to images from arteries that are stationary, such as

the carotid vessels. Firstly, the stretching of the coronary arteries during the cardiac cycle would be a potential source of error. Secondly, for coronary angiographic images, subtraction artifacts occur after phase matched subtraction due to the beat-to-beat variation of the cardiac cycle. Finally, variable vessel overlap during the cardiac cycle would present a further challenge. For a stationary vessel, the presence of an overlapping vessel can be accommodated by the flow extraction algorithms by excluding the overlapping region in the parametric image. This would be more difficult if this region was continually changing during the cardiac cycle.

6.8.4 Prosthetic Vascular Graft Experiments

The PTFE and CPU prosthetic vascular grafts were thin-walled and had similar compliance properties to arterial vessels. These underwent visible diameter changes due to the pulsatile pressure variations in the flow circuit. For each of the prosthetic vascular graft experiments an average value for cross-sectional area was estimated using the densitometric method. For the PTFE graft, the computed diameter varied from 4.0 mm for a mean flow rate of 59 ml/min to 4.9 mm for a mean flow rate of 320 ml/min. For the CPU graft, the diameter varied from 3.8 mm for a mean flow rate of 59 ml/min to 4.8 mm for a mean flow rate of 293 ml/min. It was likely that the actual variation of diameter with the pulsatile flow was greater since the instantaneous flow variations were much greater for each experiment than the mean flow variation between experiments. The variation of the vessel cross-sectional area during the pumping cycle would introduce error into the volumetric flow measurement since all four of the flow extraction algorithms assume a constant cross-sectional area.

A total of 1533 instantaneous flow measurements were made using the four algorithms and compared to EMF values. The MB algorithm showed the best correlation with EMF recordings followed by the OP, PA, and ORG algorithms (PMCC = 0.924 for MB, 0.875 for OP, 0.813 for PA, 0.768 for ORG). Also, the MB algorithm showed the least variation in measurement followed by the OP, PA, and ORG algorithms (SD = 82 for MB, 101 for OP, 148 for PA, 181 ml/min for ORG). The difference in the results between the algorithms was more marked than with the results of the stationary silicon tubing experiments. The example extracted waveforms shown in figures 6.44a and 6.44b show that the MB and OP algorithm waveforms follow the EMF waveform closely and show small variation in measurement. However, the PA and ORG algorithm waveforms show greater variation. Figure 6.44a clearly illustrates the advantage of the MB, OP, and PA algorithms over the ORG algorithm. The ORG algorithm has failed in several instances during the extraction of this particular waveform, especially during cycle 3 where zero flow has been computed for nearly the entire cycle. All four algorithms had a negative bias, underestimating the true instantaneous flow on average. Figure 6.46a shows that there was no trend in the measurement bias with mean flow rate for the MB algorithm. Figure 6.46b would suggest that the OP algorithm showed a tendency to increasingly underestimate flow as the mean flow rate was increased.

6.8.5 Cerebral Vascular Phantom Experiments

The final series of experiments using the pulsatile blood flow circuit were those with the cerebral vascular phantom. These experiments were the most challenging test for the flow extraction algorithms. The vascular structures in the phantom were made from thin-walled silicone so that they underwent diameter changes with the pulsatile pressure

variations. Also, the vessels were embedded in gelatin to produce realistic x-ray attenuation and scatter. The image quality of the x-ray sequences obtained from this series of experiments was noticeably worse than the other experiments involving tubing placed in air alone. Furthermore, the length of the target vessel, the internal carotid artery part of the phantom, was approximately 95 mm. This was shorter than the vessel lengths used for the other experiments.

In total 857 instantaneous flow measurements were made using the four algorithms and compared to EMF values. The MB algorithm showed the best correlation with the EMF recordings followed by the OP, PA, and ORG algorithms (PMCC = 0.885 for MB, 0.741 for OP, 0.684 for PA, 0.540 for ORG). The MB algorithm also showed the least variation in measurement followed by the OP, PA, and ORG algorithms (SD = 133 for MB, 194 for OP, 234 for PA, 324 ml/min for ORG). The difference in the results between the algorithms was most marked of all the experimental categories. In fact, there was a striking difference between the MB and ORG algorithms. The example extracted waveforms shown in figure 6.47a show that the MB, OP, and PA algorithm waveforms follow the EMF waveform closely with the PA waveform showing the greater variation. However, the ORG algorithm has failed in many instances and measured zero flow. The waveforms shown in figure 6.47b were for a higher mean flow rate. The OP waveform can be seen to underestimate the EMF flow at nearly all instances. This was a consistent feature of the OP algorithm for the cerebral vascular phantom data. All four of the algorithms showed a negative measurement bias. Figure 6.49a shows that the MB algorithm bias went from overestimation at low mean flow rates to underestimation at high mean flow rates. As seen in figure 6.49b, the trend was more marked for the OP algorithm that went from a small bias at low mean flow to

increasing underestimation at higher mean flow rates. However, both MB and OP algorithm computed flow rates showed a high degree of linear relationship with EMF values as seen in figures 6.48a and 6.48b.

6.8.6 Effects of Varying Image Noise and Vessel Segment Length

Assessing the effects of varying image noise on the performance of the flow extraction algorithms was important in the interpretation of the differences seen between the algorithms for the different types of simulated vessel. The parametric image quality was best for the silicone tubing experiments followed by the prosthetic vascular graft experiments and then the cerebral vascular phantom experiments. In fact, the best parametric images were obtained from the moving silicon tubing experiments and this is the reason why one of these parametric images was chosen to investigate the effects of adding noise. Figures 6.51a to 6.51c show very similar performance for all four algorithms when up to 2% zero mean Gaussian distributed noise was added to the selected parametric image. However, going from 5% to 30% added noise, the ORG and PA algorithms showed a marked increase in measurement variability and a marked decrease in correlation with EMF values. However, the MB and OP algorithms maintained low measurement variability and high correlation. This suggests that the MB and OP algorithms are more robust to image noise than the ORG and PA algorithms in terms of measurement variability and correlation. This was reflected by the results of the pulsatile flow circuit experiments that showed that the MB and OP algorithms maintained low measurement variability and high correlation for the different types of simulated vessel. The ORG and PA algorithms showed a marked increase in measurement variability and a decrease in correlation when going from the high quality

images in the silicone tubing experiments to the low quality images in the cerebral vascular phantom experiments.

Figure 6.51a shows that the MB and OP algorithms produced flow measurements with a positive measurement bias (overestimation) at low levels of noise and a negative bias (underestimation) at higher levels of noise. The trend was more marked with the OP algorithm than the MB algorithm. These results can explain the variation in measurement bias as a function mean flow rate seen especially with the cerebral vascular phantom results. For higher mean flow rates there was increasing underestimation by the MB and OP algorithms. The contrast material concentration achieved in the target vessel is likely to be lower for higher flow rates due to increased dilution. Therefore, the signal to noise ratio is less. Even though a trend in measurement bias with mean flow rate was observed in the cerebral vascular phantom experiments, both the MB and OP algorithm showed a strong linear relationship with the EMF flow values. This was confirmed by the results of the image noise experiment, where the MB and OP algorithm maintained high correlation as noise level was increased. Therefore, these algorithms would be suitable for measuring changes in flow even when image quality was poor.

The vessel segment lengths used for the pulsatile flow circuit experiments varied from 92 to 167 mm. It was important to investigate the effects of reducing the vessel segment length since long lengths of unbranched artery are seldom encountered in the human circulation. The same parametric image used for the image noise experiments was used for the investigation of varying vessel segment length. Figure 6.52a shows the variation of measurement bias as the segment length was decreased from 125 to 25 mm. The OP

algorithm went from overestimation to underestimation, whereas the MB, ORG, and PA algorithms generally showed increasing overestimation as segment length was reduced. Figures 6.52b and 6.52c show that the MB and OP algorithms maintained low measurement variability and high correlation as the segment length was decreased. Measurement variability showed a gradual increase and the correlation showed a gradual decrease. For the ORG and PA algorithms, the measurement variability was greater and the correlation was lower than for the MB and OP algorithms for almost all vessel segment lengths. All four algorithms showed a marked decrease in performance when the segment length was reduced to below 50 mm. The maximum velocity for this data set was 784 mm/sec. This corresponds to a distance shift of 31 mm between consecutive concentration-distance curves. Since the maximum shift allowed was 75% of the vessel segment length, this meant that when the segment length was below 42 mm the peak velocity could not be measured by the ORG and PA algorithms. This explains why the performance of these algorithms became reduced below segment lengths of 50 mm. The MB algorithm is also based on the concentration-distance curve correlation method. However, the performance of this algorithm was better than the ORG and PA algorithms for segment lengths below 50 mm. Although the peak velocity could not be measured directly due to the limit of the maximum shift allowed, the MB algorithm used the remaining part of the flow waveform for the waveform shape model fitting procedure. Therefore, the peak velocity was being effectively extrapolated by the model. Since the OP algorithm uses a weighted average of velocity measurements along the length of the vessel, reducing the vessel segment length means that there are fewer velocity estimates available for averaging. This explains the decrease in the performance of the OP algorithm as vessel segment length was reduced.

6.9 Conclusion

A pulsatile blood flow circuit has been used to validate the newly developed blood flow extraction algorithms. The flow circuit design was versatile and allowed testing of the algorithms using progressively more challenging simulated vessels. Dynamic biplane x-ray images of the vessels were acquired during the injection of iodine-based contrast material for a range of different pulsatile flow rates. The x-ray image data were transferred from the x-ray system using a flexible image capture solution consisting of a frame grabber and specially developed software. The image data were analysed to generate the parametric image representation of the motion of contrast material along the target vessel segments using the newly developed SARA 2000 software package. All the required tools for image analysis were integrated into this software package so that blood flow waveforms could be extracted from the image data in only a few minutes. The waveform shape model required for the MB algorithm was constructed using principal component analysis of sample EMF recordings from the blood flow circuit for a range of different flow conditions. It was found that only 10 parameters were needed to characterize the waveforms produced by the flow circuit. Both the newly developed MB, OP, and PA algorithms and the existing ORG algorithm were used to extract the flow waveforms from the angiographic data and these were compared to simultaneous flow measurements made using the EMF. For all four different types of simulated vessel the MB algorithm demonstrated the best performance in terms of low measurement variability and high linearity with EMF flow values. This was followed by the OP algorithm and then the PA algorithm. The ORG algorithm showed the worst performance. The difference in performance between the algorithms was less marked for the stationary silicone tubing experiments and the moving silicone

tubing experiment where image quality was best. However, the difference was more apparent for the prosthetic vascular graft experiments and most apparent for the cerebral vascular phantom experiments where image quality was worst. A low-noise parametric image was selected to test the effects of varying image noise and vessel segment length on the flow extraction algorithms. The MB and OP algorithms were found to be more robust to image noise than the PA and ORG algorithms. Furthermore, the MB and OP algorithms were found to be more robust when reducing the vessel segment length.

The results from the pulsatile flow circuit experiments suggest that the use of the waveform shape model to constrain flow measurement improves the measurement of blood flow when compared to the use of the concentration-distance curve correlation method alone. The model based approach was more robust to image noise and could successfully extrapolate flow values when the vessel segment length was below the minimum required to measure the peak flow velocity directly using the concentration-distance curve correlation method. Although the weighted optical flow algorithm did not perform as well as the model based approach, it showed better robustness to image noise and reducing vessel length than the concentration-distance curve correlation method. Replacing the concentration-distance curve data with polynomial functions prior to determining the optimum shift between successive curves also improved flow measurement when compared to using the original concentration-distance curve data. Therefore, the newly developed MB, OP, and PA algorithms all demonstrated improved performance when compared to the ORG algorithm. The implications of the findings to clinical flow measurement and the modifications required to extend the use of the newly developed algorithms to clinical flow measurement are discussed in chapter 7.

Chapter 7

Conclusions and Future Work

The main objective of the work described in this thesis was to design an algorithm to measure volumetric arterial blood flow from dynamic x-ray images of a target arterial vessel segment during the injection of iodine-based contrast material. The clinical motivation behind this work was to be able to provide an objective measure of the haemodynamic impact of catheter based cardiovascular interventional procedures, such as those involving the coronary arteries and the cerebral circulation, by monitoring pre-, intra-, and post-procedure blood flow. There was a specific requirement to address the main limitation of image noise sensitivity of the leading existing approaches for x-ray angiographic blood flow measurement. In this chapter, I will summarise the ways in which the main objective has been achieved, describe the novel contributions of the work, and suggest future work.

7.1 The Novel Algorithms for the Measurement of Pulsatile Blood Flow Waveforms

As a result of the literature review (chapter 2), it was decided to extend two of the leading existing approaches for the measurement of blood flow from dynamic x-ray angiographic images. The approaches chosen were the concentration-distance curve correlation method suggested by Seifalian *et al.* and the optical flow approach suggested by Efron *et al.*. Three novel algorithms were developed, two of these extended the concentration-distance curve correlation approach and the other extended the optical flow approach.

Chapter 3 describes the first algorithm that was based on the concentration-distance curve correlation approach. The novel contribution in this algorithm was to use a blood flow waveform shape model to constrain the determination of the optimal shifts between successive concentration-distance curves for calculation of the contrast material bolus velocity. This algorithm was called the *"model based algorithm"* (MB algorithm). A review of methods that have been previously used to model blood flow waveform shape was presented in chapter 3. As a result of this, the method of principal component analysis was chosen to construct the waveform shape model used by the MB algorithm. It was shown that the analysis of residuals could be used to determine the number of model parameters required to describe the waveform shape.

The second algorithm is also described in chapter 3. This was a small variation of the concentration-distance curve correlation method that arose from the pre-processing stages of the MB algorithm. The novel contribution in this algorithm was to use polynomial functions to model the concentration-distance curves prior to determining

the optimal shift between successive curves for calculation of the contrast material bolus velocity. This algorithm was called the *"polynomial approximation algorithm"* (PA algorithm).

Finally, chapter 4 describes the third algorithm that was based on an optical flow method. Blood flow velocity was determined as the ratio of the temporal and spatial derivatives of contrast material concentration. The novel contribution in this algorithm was to perform a weighted average of the velocity estimates along the length of the target vessel segment with the weighting based on the magnitude of the spatial derivative. This algorithm was called the *"weighted optical flow algorithm"* (OP algorithm).

7.2 Validation of the Novel Algorithms

Chapter 5 describes the validation of the OP algorithm using a computer simulation of pulsatile blood flow in arteries. Even though the flow model used for the simulation had several limitations, the computer simulation did provide a useful tool for the initial validation of the OP algorithm. Two simulation studies were performed each providing a novel contribution to the understanding of the operation of the OP algorithm. The first simulation study demonstrated the effects of varying (1) the distance of flow measurements from the contrast material injection site; (2) the length of the vessel segment over which velocities were averaged; and (3) the noise in the synthetic parametric images generated by the computer simulation. It was found that (1) flow measurement was dependent of the distance from the injection site; (2) the algorithm performed better when the vessel segment length was greater; and (3) the algorithm performed worse as image noise was increased. The second simulation study

investigated the ability of the OP algorithm to measure a range of flow rates. The algorithm demonstrated very high linear correlation with true flow rates and low measurement variability over the range of flow rates measured. The findings of the simulation studies suggested that the OP algorithm would be useful for monitoring changes in blood flow during an interventional procedure if the contrast material injection site was fixed relative to the target vessel segment.

Chapter 6 describes the validation of the MB, OP, and PA algorithms using a pulsatile blood flow circuit. There were several important contributions presented in this chapter. A versatile flow circuit was developed to simulate pulsatile flow in arteries that allowed different types of simulated vessel to be used to progressively test the algorithms in more challenging conditions. A vessel manipulator was constructed to simulate coronary artery motion. An x-ray image capture solution was devised to allow real-time acquisition of the angiographic image data. An integrated software package was developed that resulted in a significant decrease in the time taken to analyse the angiographic data from almost half an hour per data set using the previously available software tools to only a few minutes using the new SARA 200 software. Finally, the MB, OP, and PA algorithms were used to extract volumetric flow waveforms from the dynamic angiographic images of each of the different types of simulated vessel for a range of flow rates. The waveforms were compared to simultaneous measurements made using an EMF. Waveforms were also extracted using the ORG algorithm for comparison. The MB algorithm demonstrated the best performance for volumetric blood flow measurement in terms of low measurement variability and high linear correlation with true flow values. This was followed by the OP algorithm and then the PA algorithm. The ORG algorithm was out-performed by the new algorithms in all

experimental categories with the difference in performance being more marked when going from the high image quality seen in the silicone tubing experiments to the low image quality seen in the cerebral vascular phantom experiments. Experiments using a single parametric image confirmed that the MB and OP algorithms were more robust to increasing image noise and reducing vessel segment length than the PA and ORG algorithms.

7.3 Extension to Clinical Flow Measurement

Although the novel algorithms developed in this thesis were not tested on clinical angiographic images, it is important to discuss the suitability of the algorithms for clinical flow measurement. An x-ray angiographic flow extraction method should satisfy the following criteria to be suitable for clinical flow measurement:

1. It should make use of the angiographic images that are routinely acquired during procedures so as to impose a minimal radiation dose penalty and prevent extension of procedure duration.
2. It should show high measurement linearity and low measurement variability so that changes in blood flow can be assessed during the course of a procedure.
3. It should operate on short vessel segment lengths in the order of a few centimetres.

The extents to which these criteria are satisfied by the algorithms developed in this thesis are as follows:

1. The novel algorithms will perform best if the x-ray images have both high temporal resolution and high radiation dose per image. However, during catheter based cardiovascular interventional procedures there is a compromise between temporal

resolution and dose per image. There are two types of image sequence that are routinely used during procedures. The first type is the fluoroscopy sequence. For this type of sequence, x-ray images are acquired at a high frame rate, usually 25 frames per second, but the radiation dose per image is kept low. Therefore, the image quality is low. The second type of sequence is the radiographic sequence. For this type of sequence, x-ray images are acquired at a low frame rate, usually in the order of 6 frames per second, but the dose per image is relatively high. Therefore, the image quality is high. The MB and OP algorithms are likely to perform well with fluoroscopy sequences since these algorithms have demonstrated robustness to image noise whereas the PA algorithm is likely to perform not as well due to sensitivity to image noise. For radiographic sequences, the reduced temporal resolution will affect the performance of the OP and PA algorithms. For the OP algorithm, there will be increased errors in the determination of the temporal gradients of contrast material concentration. For the PA algorithm, the lower temporal resolution will limit the maximum velocity that can be measured and could lead to the incorrect measurement of high velocities due to aliasing. However, the MB algorithm is likely to perform well for radiographic sequences since it is able to extrapolate high velocities and prevent aliasing artifacts due to the constraints of the waveform shape model. Therefore, both the MB and OP algorithms could be used on commonly acquired x-ray image sequences whereas the PA algorithm is likely to require a modified sequence that has both high temporal resolution and high dose per image.

2. The requirements of high measurement linearity and low measurement variability are important for clinical application of the flow extraction algorithms. The results

of the pulsatile flow circuit experiments demonstrated that the flow measurements made by the MB and OP algorithms were highly linearly correlated with true flow values with narrow limits of agreement. Furthermore, these properties were maintained even when image quality was progressively reduced by adding synthetic image noise. However, the PA algorithm demonstrated wide limits of agreement and the measurement linearity and variability were affected significantly when image quality was reduced.

3. The ability of the algorithms to measure flow successfully for small vessel lengths may be the limiting factor in the application of these algorithms for clinical flow measurement. The MB and OP algorithms maintained high measurement linearity and low measurement variability as vessel segment length was progressively reduced suggesting that these approaches may be most suitable for the relatively small lengths of unbranched vessel encountered in the arterial circulation. However, the PA algorithm demonstrated a marked decrease in performance for small vessel segment lengths.

The OP and PA algorithms can be applied directly to x-ray angiographic images. However, the MB algorithm requires a waveform shape model. It was described in chapter 3 how investigators have formed such models using Doppler ultrasound signals recorded from various arteries. Such shape models can be formed by collecting sample waveforms from both healthy volunteers and patients with vascular pathology. Transcutaneous Doppler ultrasound probes could be used for arteries such as the carotid and cerebral vessels or intra-arterial probes could be used for the coronary vessels.

7.4 Future Work

Future work should focus both on clinical validation and technical developments. The acquisition of calibrated biplane x-ray angiographic sequences during catheter based cardiovascular interventions could allow clinical validation. X-ray measured flow rates could be compared to flow rates measured simultaneously with a calibrated intra-arterial Doppler catheter. The application of the MB algorithm will require the construction of a blood flow waveform shape model and this could be performed by the collection of Doppler ultrasound waveforms as outlined in the previous section.

Technical developments could include the automation of several of the image analysis stages that are presently carried out semi-automatically or manually as part of the SARA 2000 software package. The determination of the 2D and 3D target vessel centrelines from biplane images was carried out semi-automatically using the epipolar constraint. This could be fully automated [Hoffmann 2000] and would present a significant timesaving especially in the case of coronary artery image analysis. The identification of the calibration cube markers and the geometric distortion grid markers could also be fully automated by application of standard image processing morphological operators. Since the OP algorithm performed almost as well as the MB algorithm during the pulsatile flow experiments, the application of the waveform shape model to the weighted optical flow method would possibly result in an algorithm with better performance than both the MB and OP algorithms. The investigation of a suitable method to incorporate the waveform shape model into the weighted optical flow approach could be a focus of future research. Another avenue of future work is the use of 2D-3D image registration to remove the requirement for biplane x-ray views. 3D

anatomical images of vasculature can be obtained using magnetic resonance, computerized tomography, or rotational angiography. If these images are registered to a single 2D x-ray view [Hipwell 2003] then the geometric parameters required for flow calculation could be determined by projecting the target vessel segment back to the 3D model.

Appendix

Statistical Methods

A combination of the product moment correlation coefficient (PMCC) and Bland-Altman analysis were the statistical methods used to compare the measured flow values to the true flow values. Let the computed flow values be $Vxray$ and the true flow values be $Vtrue$. Let the number of measurements be N.

A.1 The Product Moment Correlation Coefficient

The PMCC, $-1 \le r \le 1$, is used to assess the degree of linear relationship between two variables. As the degree of linear relationship increases, so does the magnitude of the PMCC. The PMCC was calculated by

$$r = \frac{\sum_{i=1}^{i=N} (Vxray_i - \overline{Vxray})(Vtrue_i - \overline{Vtrue})}{(N-1)s_{Vxray}s_{Vtrue}} \qquad \text{(A.1)}$$

where $\overline{Vxray}$, $\overline{Vtrue}$ are the average values, and s_{Vxray}, s_{Vtrue} are the standard deviations of the computed and true flow values, respectively.

A.2 Bland-Altman Analysis

The PMCC can only be used to assess the strength of the linear relationship between two variables but not the agreement. Bland-Altman analysis is an established method to assess the agreement between two methods of measurement [Bland 1986]. This method computes the measurement bias and variability of one method relative to another.

Measurement error was found by

$$e = Vxray - Vtrue . \tag{A.2}$$

Measurement bias is equal to the mean measurement error given by

$$\bar{e} = \frac{\sum_{i=1}^{i=N} e_i}{N} . \tag{A.3}$$

The standard deviation of the measurement error is

$$s_e = \sqrt{\frac{\sum_{i=1}^{i=N} \left(e_i - \bar{e}\right)^2}{N-1}} . \tag{A.4}$$

The measurement variability was assessed by calculating the 95% limits of agreement as given by

$$\bar{e} \pm 1.96 s_e . \tag{A.5}$$

If the mean measurement error (bias) is small and the 95% limits of agreement (variability) are narrow, then the two methods are in good agreement. A variation of the Bland-Altman plot was one of the graphical methods used to represent the measured flow data. The Bland-Altman plot shows the measurement error as a function of the mean value of the methods of measurement. However, since measured flow values were being compared to either known values from computer simulation input parameters or gold standard EMF recordings, the measurement error was shown as a function of these known values.

Bibliography

Achenbach S., Ropers D., Holle J., Muschiol G., Daniel W. G., and Moshage W., "In-plane coronary arterial motion velocity: measurement with electron-beam CT," Radiology, vol. 216(2), pp. 457-463, 2000.

Amini A.A., Egglin T.K., and Pollak J.S., "Physical models for measurement of blood velocity and flow from diagnostic images," in Proceeding of Computers in Cardiology, pp. 783-786, 1993.

Amini A.A., "Computational techniques for determining non-rigid motion of blood from medical images," in Proceeding of SPIE, Medical Imaging: Image Processing, vol. 2167, pp. 403-412, 1994.

Arjomand H., Turi Z. G., McCormick D., and Goldberg S., "Percutaneous coronary intervention: historical perspectives, current status, and future directions," Am. Heart J., vol. 146(5), pp. 787-796, 2003.

Baird R. N., Bird D. R., Clifford P. C., Lusby R. J., Skidmore R., and Woodcock J. P., "Upstream stenosis. Its diagnosis by Doppler signals from the femoral artery," Arch. Surg., vol. 115(11), pp. 1316-1322, 1980.

Bateman W. A. and Kruger R. A., "Blood flow measurement using digital angiography and parametric imaging," Med. Phys., vol. 11(2), pp. 153-157, 1984.

Beauchemin S.S. and Barron J.L., "The computation of optical flow," ACM Computing Surveys, vol. 27(3), 433-467. 1995.

Beldi G., Bosshard A., Hess O. M., Althaus U., and Walpoth B. H., "Transit time flow measurement: experimental validation and comparison of three different systems," Ann. Thorac. Surg., vol. 70(1), pp. 212-217, 2000.

Beutel J., Kundel H. L., van Metter R. L., "Handbook of medical imaging volume 1. physics and psychophysics," SPIE, Washington, USA, 2000.

Bland J. M. and Altman D. G., "Statistical methods for assessing agreement between two methods of clinical measurement," Lancet, vol. 1(8476), pp. 307-310, 1986.

Brackley K. J., Ramsay M. M., Pipkin F. B., and Rubin P. C., "A longitudinal study of umbilical artery Doppler waveforms in normal pregnancy: analysis using Laplace transform techniques," Br. J. Obstet. Gynaecol., vol. 105(1), pp. 78-82, 1998a.

Brackley K. J., Ramsay M. M., Pipkin F. B., and Rubin P. C., "A longitudinal study of maternal bloodflow in normal pregnancy and the puerperium: analysis of Doppler waveforms using Laplace transform techniques," Br. J. Obstet. Gynaecol., vol. 105(1), pp. 68-77, 1998b.

Brackley K. J., Ramsay M. M., Pipkin F. B., and Rubin P. C., "The maternal cerebral circulation in pre-eclampsia: investigations using Laplace transform analysis of Doppler waveforms," Br. J. Obstet. Gynaecol., vol. 107(4), pp. 492-500, 2000.

Brunt J. N., Wicks D. A., Hawkes D. J., Seifalian A. M., du Boulay G. H., Colchester A. F., and Wallis A., "The measurement of blood flow waveforms from X-ray angiography. Part 1: Principles of the method and preliminary validation," Proc. Inst. Mech. Eng. [H.], vol. 206(2), pp. 73-85, 1992a.

Brunt J. N., du Boulay G. H., and Wallis A., "The measurement of blood flow waveforms from X-ray angiography. Part 2: Application to video recordings of digital subtraction angiography," Proc. Inst. Mech. Eng [H.], vol. 206(2), pp. 87-91, 1992b.

Bursch J. H., Hahne H. J., Brennecke R., Gronemeier D., and Heintzen P. H., "Assessment of arterial blood flow measurements by digital angiography," Radiology, vol. 141(1), pp. 39-47, 1981.

Bursch J. H., "Use of digitized functional angiography to evaluate arterial blood flow," Cardiovasc. Intervent. Radiol., vol. 6(4-6), pp. 303-310, 1983.

Bursch J. H., Hahne H. J., and Heintzen P. H., "Functional imaging of blood flow," Ann. Radiol. (Paris), vol. 28(2), pp. 183-188, 1985.

Bushberg J. T., Seibert J. A., Leidholdt E. M. Jnr., Boone J. M., "The essential physics of medical imaging," 2nd Edition, Lippincot Williams & Wilkins, Philadelphia, USA, 2002.

Byrne J., "Review article: endovascular treatments for intracranial aneurysms," Br. J. Radiol., vol. 69(826), pp. 891-899, 1996.

Close R. A., Duckwiler G. R., and Vinuela F., "Fluid equations applied to blood flow measurement using digital videodensitometry," Invest. Radiol., vol. 27(7), pp. 504-509, 1992.

Colchester A.C.F. and Brunt J.N.H., "Measurement of vessel calibre and volume blood flow by dynamic quantitative digital angiography: an initial application showing variation of cerebral artery diameter with PaCO2," J. Cereb. Blood Flow Metabol., vol. 3[3], pp. S640-S641, 1983.

Colchester A.C.F., "The effect of changing PaC02 on cerebral artery calibre estimated by a new technique of dynamic quantitative digital angiography," PhD Thesis, University of London, 1984.

Colchester A.C.F., Hawkes D.J., Brunt J.N.H., du Bolay G.H., and Wallis A., "Pulsatile blood flow measurements with the aid of 3D reconstruction from dynamic angiographic recordings," in Information Processing In Medical Imaging, Dordrecht, Martinus Nijhoff, pp. 247-265, 1986..

Cornelius N and Kanade T., "Adapting optical flow to measure object motion in reflectance and x-ray image sequences," in Proc. ACM SIGGRAPH/SIGAART Interdisciplinary Worskshop on Motion: Representation and Control, pp. 50-58, 1986.

Crepeau R. L. and Silverman N. R., "Video-densitometric vascular flowrate measurement--some error considerations," Med. Biol. Eng, vol. 11(3), pp. 319-325, 1973.

Doriot P. A., Moore J. E. Jr., Guggenheim N., Dorsaz P. A., and Rutishauser W. J., "Computer simulation of the propagation of contrast medium in a coronary artery during one cardiac cycle," Int. J. Card Imaging, vol. 11(1), pp. 19-26, 1995.

Dorsaz P. A., Doriot P. A., Dorsaz L., Chatelain P., and Rutishauser W., "A new densitometric approach to the assessment of mean coronary flow," Invest. Radiol., vol. 32(4), pp. 198-204, 1997.

du Boulay G. H., Brunt J., Colchester A., Hawkes D., Wallis A., and Wicks D., "Volume flow measurement of pulsatile flow by digitised cine angiography," Acta Radiol. Suppl, vol. 369, pp. 59-62, 1986.

Efron U., Price R.R., Smith C.W., and Brill A.B., "A method to determine the instantaneous blood-flow using cine- or video-densitometric data," in Proc SPIE, Applications of Electronic Imaging Systems, vol.143, pp. 154-161, 1978.

Ersahin A., Molloi S. Y., and Hicks J. W., "Absolute phasic blood flow measurement in the brain using digital subtraction angiography," Invest. Radiol., vol. 30(4), pp. 244-253, 1995.

Evans D. H., Macpherson D. S., Bentley S., Asher M. J., and Bell P. R., "The effect of proximal stenosis on Doppler waveforms: a comparison of three methods of waveform analysis in an animal model," Clin. Phys. Physiol. Meas., vol. 2(1), pp. 17-25, 1981.

Evans D. H., "The interpretation of continuous wave ultrasonic Doppler blood velocity signals viewed as a problem in pattern recognition," J. Biomed. Eng, vol. 6(4), pp. 272-280, 1984.

Evans D.H., Archer L.N.J., and Levene M.I., "The detection of abnormal neonatal cerebral haemodynamics using principal component analysis of the Doppler ultrasound waveform," Ultrasound Med. Biol., vol. 11, pp. 441-449, 1985.

Evans D. H., "A pulse-foot-seeking algorithm for Doppler ultrasound waveforms," Clin. Phys. Physiol. Meas., vol. 9(3), pp. 267-271, 1988.

Evans D. H., McDicken W. N., Skidmore R., Woodcock J. P., "Doppler ultrasound: physics, instrumentation, and clinical applications," Wiley, UK, 1989.

Fitzpatrick J.M., "A method for calculating velocity in time dependent images based on the continuity equation," in Proc. IEEE Computer Society Conference on Computer Vision and Pattern Recognition, San Francisco, USA, pp. 78-81, 1985.

Forbes G., Gray J. E., and Felmlee J. P., "Phantom testing of peripheral artery. Absolute blood flow measurement with digital arteriography," Invest. Radiol., vol. 20(2), pp. 186-192, 1985.

Gatehouse P. D., Keegan J., Crowe L. A., Masood S., Mohiaddin R. H., Kreitner K. F., and Firmin D. N., "Applications of phase-contrast flow and velocity imaging in cardiovascular MRI," Eur. Radiol., vol. 15(10), pp. 2172-2184, 2005.

Guggenheim N., Chappuis F., Suilen C., Doriot P. A., Dorsaz P. A., Descouts P., and Rutishauser W., "3D-reconstruction of coronary arteries in view of flow measurement," Int. J. Card. Imaging, vol. 8(4), pp. 265-272, 1992.

Guggenheim N., Dorsaz P. A., Doriot P. A., Suilen C., Chappuis F., and Rutishauser W., "3D determination of the intravascular volume and flow of coronary arteries," Int. J. Biomed. Comput., vol. 35(1), pp. 13-23, 1994.

Haaker P., Klotz E., Koppe R., and Linde R., "Real-time distortion correction of digital X-ray II/TV-systems: an application example for digital flashing tomosynthesis (DFTS)," Int. J. Card. Imaging, vol. 6(1), pp. 39-45, 1990.

Hamilton W., Moore J., Kinsman J., and Spurlung R., "Simultaneous determination of pulmonary and systemic circulation times in man and of a figure related to cardiac output," Am. J. Physiol., vol. 84, pp. 338-344, 1928.

Hamilton W., Moore J., Kinsman J., and Spurlung R., "Studies on the circulation: IV. Further analysis of injection method and of changes in hemodynamics under physiological and pathological conditions," Am. J. Physiol., vol. 99, pp. 534-551, 1932.

Hangiandreou N. J., Folts J. D., Peppler W. W., and Mistretta C. A., "Coronary blood flow measurement using an angiographic first pass distribution technique: a feasibility study," Med. Phys., vol. 18(5), pp. 947-954, 1991.

Hawkes D.J., Colchester A.C.F., and Mol C.R., "The accurate 3-D reconstruction of the geometric configuration of vascular trees from x-ray recordings," in Physics and Engineering of Medical Imaging, Dordrecht, Martinus Nijhoff, 1985.

Hawkes D.J., Colchester A.C.F., Brunt J.N.H., Wicks D.A.G., du Bolay G.H., and Wallis A., "Development of a model to predict the potential accuracy of vessel blood flow measurements from dynamic angiographic recordings," in Mathematics and Computer Science in Medical Imaging , Berlin, Springer-Verlag, pp. 469-478, 1988.

Hawkes D.J., Colchester A.C.F., de Belder M.A., Norbury R.N., Camm A.J., and Davies M.J., "The measurement of absolute cross sectional area and lumen geometry in quantitative angiography," in Medical Images: Formation, Handling and Evaluation, Heidelburg, Springer-Verlag, pp. 607-624, 1992.

Hawkes D.J., Hardingham C.R., Seifalian A.M., Virdee M, and Colchester A.C.F., "Recent advances in extracting quantitative information from x-ray angiographic data," Innov. Tech. Biol. Med., vol. 13, pp. 100-107, 1992.

Hawkes D. J., Seifalian A. M., Colchester A. C., Iqbal N., Hardingham C. R., Bladin C. F., and Hobbs K. E., "Validation of volume blood flow measurements using three-dimensional distance-concentration functions derived from digital x-ray angiograms," Invest. Radiol., vol. 29(4), pp. 434-442, 1994.

Hilal S. K., "Determination of the blood flow by a radiographic technique. Physical considerations and experimental results," Am. J. Roentgenol. Radium. Ther. Nucl. Med., vol. 96(4), pp. 896-906, 1966a.

Hilal S. K., "Human carotid artery flow determination using a radiographic technique," Invest. Radiol., vol. 1(2), pp. 113-122, 1966b.

Hipwell J. H., Penney G. P., McLaughlin R. A., Rhode K., Summers P., Cox T. C., Byrne J. V., Noble J. A., and Hawkes D. J., "Intensity-based 2-D-3-D registration of cerebral angiograms," IEEE Trans. Med. Imaging, vol. 22(11), pp. 1417-1426, 2003.

Hoffmann K.R. and Doi K., "A new angiographic technique for measurement of instantaneous blood flow rates using distance-density curves," in Proc. SPIE, Medical Imaging IV: Image Processing, vol. 1233, pp. 240-243, 1990.

Hoffmann K. R., Doi K., and Fencil L. E., "Determination of instantaneous and average blood flow rates from digital angiograms of vessel phantoms using distance-density curves," Invest. Radiol., vol. 26(3), pp. 207-212, 1991.

Hoffmann K. R., Sen A., Lan L., Chua K. G., Esthappan J., and Mazzucco M., "A system for determination of 3D vessel tree centerlines from biplane images," Int. J. Card. Imaging, vol. 16(5), pp. 315-330, 2000.

Holdsworth D. W., Drangova M., and Fenster A., "Quantitative angiographic blood-flow measurement using pulsed intra-arterial injection," Med. Phys., vol. 26(10), pp. 2168-2175, 1999.

Horn K.P. and Schunck B.G., "Determining optical flow," Artificial Intelligence, vol. 17, pp. 185-203, 1981.

Huang S. P., Decker R. J., Goodrich K. C., Parker D. J., Muhlestein J. B., Blatter D. D., and Parker D. L., "Velocity measurement based on bolus tracking with the aid of three-dimensional reconstruction from digital subtraction angiography," Med. Phys., vol. 24(5), pp. 677-686, 1997a.

Huang S.P., Chapman B.E., Muhlestein J.B., Blatter D.D., and Parker D.L., "Computer simulation of convection and diffusion effects on velocity estimations from x-ray contrast density time curves," in Lecture Notes in Computer Science, vol. 1230, pp. 453-458, 1997b.

Imbert B., Meunier J., Mongrain R., Hudon G., and Bertrand M., "Blood flow assessment from optical flow in cineangiography," in Proc. Computers in Cardiology, pp. 537-540, 1995a.

Imbert B., Meunier J., Mongrain R., Hudon G., and Bertrand M., "Opitcal flow assessment of parabolic velocity profile in cineangiography: a simulation study," in Proc. Engineering in Medicine and Biology Society, pp. 419-420, 1995b.

Imbert B., Meunier J., Mongrain R., Hudon G., and Bertrand M., "Stenosis parameter assessment from contrast medium tracking in cineangiography with an optical flow method," in Proc. SPIE, Medical Imaging: Physiology and Function from Multidimensional Images, vol. 3034, pp. 631-640, 1997.

Jackson J.E., "A user's guide to principal components," Wiley, USA, 1991.

Jahne B., "Digital image processing concepts, algorithms, and scientific applications," Springer-Verlag, Germany, 1997.

Katzen B. T., "Current status of digital angiography in vascular imaging," Radiol. Clin. North Am., vol. 33(1), pp. 1-14, 1995.

Kim H.C., Min B.G., Lee T.S., Lee S.J., Lee C.W., Park J.H., and Han M.C., "Three-dimensional digital subtraction angiography," IEEE Trans. Med. Imaging vol. MI-1(2), pp. 152-158, 1982.

Kontis S. and Gosling R. G., "On-line Doppler ultrasound measurement of aortic compliance and its repeatability in normal subjects," Clin. Phys. Physiol. Meas., vol. 10(2), pp. 127-135, 1989.

Kruger R. A., Bateman W., Liu P. Y., and Nelson J. A., "Blood flow determination using recursive processing: a digital radiographic method," Radiology, vol. 149(1), pp. 293-298, 1983.

Kwan E. S., Hall A., and Enzmann D. R., "Quantitative analysis of intracranial circulation using rapid-sequence DSA," Am. J. Roentgenol., vol. 146(6), pp. 1239-1245, 1986.

MacKay S. A., Potel M. J., and Rubin J. M., "Graphics methods for tracking three-dimensional heart wall motion," Comput. Biomed. Res., vol. 15(5), pp. 455-473, 1982.

Macpherson D. S., Evans D. H., and Bell P. R., "Common femoral artery Doppler wave-forms: a comparison of three methods of objective analysis with direct pressure measurements," Br. J. Surg., vol. 71(1), pp. 46-49, 1984.

Mao S., Lu B., Oudiz R. J., Bakhsheshi H., Liu S. C., and Budoff M. J., "Coronary artery motion in electron beam tomography," J. Comput. Assist. Tomogr., vol. 24(2), pp. 253-258, 2000.

Marinus H., Buis B., and van Benthem A., "Pulsatile coronary flow determination by digital angiography," Int. J. Card. Imaging, vol. 5(2-3), pp. 173-182, 1990.

Martin T.R.P., Barber D.C., Sherriff S.B, and Prichard D.R., "Objective feature extraction applied to the diagnosis of carotid artery disease : a comparative study with angiography," Clin. Phys. Physiol. Meas., vol. 1[1], pp. 71-81, 1980.

Molloi S., Qian Y. J., and Ersahin A., "Absolute volumetric blood flow measurements using dual-energy digital subtraction angiography," Med. Phys., vol. 20(1), pp. 85-91, 1993.

Molloi S., Ersahin A., Tang J., Hicks J., and Leung C. Y., "Quantification of volumetric coronary blood flow with dual-energy digital subtraction angiography," Circulation, vol. 93(10), pp. 1919-1927, 1996.

Molloi S., Bednarz G., Tang J., Zhou Y., and Mathur T., "Absolute volumetric coronary blood flow measurement with digital subtraction angiography," Int. J. Card. Imaging, vol. 14(3), pp. 137-145, 1998.

Molloi S., Zhou Y., and Kassab G. S., "Regional volumetric coronary blood flow measurement by digital angiography: in vivo validation," Acad. Radiol., vol. 11(7), pp. 757-766, 2004.

Mongrain R., Bertrand M., Mailloux G.E., Meunier J., and Bourassa M.G., "Obtaining blood velocity profile from coronary arteriograms via optimally controlled optical flow," in Proc. Computers in Cardiology, pp. 13-16, 1991.

Mygind M., Engell L., and Mygind T., "Flow measurements with digital subtraction densitometry in a steady flow experimental model," Acta Radiol., vol. 36(4), pp. 402-409, 1995.

Nichols W. W. and O'Rouke M. F., "McDonald's Blood Flow in Arteries," 4th Edition, Oxford University Press, 1997.

Nissen S. E., "Shortcomings of coronary angiography and their implications in clinical practice," Cleve. Clin. J. Med., vol. 66(8), pp. 479-485, 1999.

Parker D., Pope D., van Bree R., and Marshall H., "Three-dimensional reconstruction of moving arterial beds from digital subtraction angiography," in Comput. Biomed. Res., vol. 20, pp. 166-185, 1985.

Press W. H., Teukolsky S. A., Vetterling W. T., and Flannery B. P., "Numerical recipes in C," Cambridge University Press, USA, 1997.

Prytherch D. R., Evans D. H., Smith M. J., and Macpherson D. S., "On-line classification of arterial stenosis severity using principal component analysis applied to Doppler ultrasound signals," Clin. Phys. Physiol. Meas., vol. 3(3), pp. 191-200, 1982.

Ramsay M. M., Broughton P. F., Rubin P. C., and Skidmore R., "Waveform shape analysis: extraction of physiologically relevant information from Doppler recordings," Clin. Sci.(Lond), vol. 86(5), pp. 557-565, 1994.

Razavi R., Hill D. L., Keevil S. F., Miquel M. E., Muthurangu V., Hegde S., Rhode K., Barnett M., van Vaals J., Hawkes D. J., and Baker E., "Cardiac catheterisation guided by MRI in children and adults with congenital heart disease," Lancet, vol. 362(9399), pp. 1877-1882, 2003.

Rosen L. and Silverman N. R., "Videodensitometric measurements of blood flow using crosscorrelation techniques," Radiology, vol. 109(2), pp. 305-310, 1973.

Rutishauser W., Simon H., Stucky J. P., Schad N., Noseda G., and Wellauer J., "Evaluation of Roentgen cinedensitometry for flow measurement in models and in the intact circulation," Circulation, vol. 36(6), pp. 951-963, 1967.

Satomura S., "Study of the flow patterns in peripheral arteries by ultrasonics," J. Acoust. Soc. Jpn., vol. 15, pp. 151-158, 1959 (in Japanese).

Sarry L., Boire J. Y., Zanca M., Lusson J. R., and Cassagnes J., "Assessment of stenosis severity using a novel method to estimate spatial and temporal variations of blood flow velocity in biplane coronarography," Phys. Med. Biol., vol. 42(8), pp. 1549-1564, 1997.

Sarry L., Peng Y. J., and Boire J. Y., "Blood flow velocity estimation from x-ray densitometric data: an efficient numerical scheme for the inverse advection problem," Phys. Med. Biol., vol. 47(1), pp. 149-162, 2002.

Seifalian A. M., Hawkes D. J., Colchester A. C., and Hobbs K. E., "A new algorithm for deriving pulsatile blood flow waveforms tested using stimulated dynamic angiographic data," Neuroradiology, vol. 31(3), pp. 263-269, 1989.

Seifalian A. M., Hawkes D. J., Hardingham C. R., Colchester A. C., and Reidy J. F., "Validation of a quantitative radiographic technique to estimate pulsatile blood flow waveforms using digital subtraction angiographic data," J. Biomed. Eng, vol. 13(3), pp. 225-233, 1991.

Seifalian A.M., Hawkes D.J., Bladin C., Hardingham C.R., Iqbal N., Colchester A.C.F., and Hobbs K.E.F., "Volume blood flow waveforms measurements from quantitative x-ray angiographic data with aid of 3-dimensional reconstructions," in Proc. Engineering in Medicine and Biology Society, vol. 14, pp. 1946-1947, 1992.

Seifalian A.M., "The computation of blood flow waveforms from digital x-ray angiographic data," PhD Thesis, University of London, 1993.

Seifalian A.M., Hawkes D.J., Guidiceandrea J, McNeil J., Colchester, A., and Hamilton G., "A novel technique of blood flow and compliance measurement using digital subtraction angiography," in Vascular Imaging for Surgeons, W. B. Saunders Company Ltd., London, UK, pp. 51-70, 1995.

Seifalian A.M., Hawkes D.J., Bladin C., Colchester A.C.F., and Hobbs K.E.F., "Blood flow measurements using 3d distance-concentration functions derived from digital x-ray angiograms," in Cardiovascular Imaging, Kluwer Academic, The Netherlands, pp. 425-442, 1996.

Seldinger S. I., "Catheter replacement of the needle in percutaneous arteriography; a new technique," Acta Radiol., vol. 39(5), pp. 368-376, 1953.

Shaw C. G. and Plewes D. B., "Pulsed-injection method for blood flow velocity measurement in intraarterial digital subtraction angiography," Radiology, vol. 160(2), pp. 556-559, 1986.

Shpilfoygel S.D., Close R.A., Jahan R., Duckwiler G.R., and Valentino D.J., "A modified distance-density method for instantaneous angiographic blood flow measurement," in Proc. SPIE, Medical Imaging: Physiology and Function from Multidimensional Images, vol. 3337, pp. 242-252, 1998.

Shpilfoygel S. D., Jahan R., Close R. A., Duckwiler G. R., and Valentino D. J., "Comparison of methods for instantaneous angiographic blood flow measurement," Med. Phys., vol. 26(6), pp. 862-871, 1999.

Shpilfoygel S. D., Close R. A., Valentino D. J., and Duckwiler G. R., "X-ray videodensitometric methods for blood flow and velocity measurement: a critical review of literature," Med. Phys., vol. 27(9), pp. 2008-2023, 2000.

Silverman N. R. and Rosen L., "Arterial blood flow measurement: assessment of velocity estimation methods," Invest. Radiol., vol. 12(4), pp. 319-324, 1977.

Skidmore R. and Woodcock J. P., "Physiological significance of arterial models derived using transcutaneous ultrasonic flowmeters," J. Physiol, vol. 277, pp. 29P-30P, 1978.

Skidmore R. and Woodcock J. P., "Physiological interpretation of Doppler-shift waveforms--I. Theoretical considerations," Ultrasound Med. Biol., vol. 6(1), pp. 7-10, 1980a.

Skidmore R. and Woodcock J. P., "Physiological interpretation of Doppler-shift waveforms--II. Validation of the Laplace transform method for characterisation of the common femoral blood-velocity/time waveform," Ultrasound Med. Biol., vol. 6(3), pp. 219-225, 1980b.

Skidmore R., Woodcock J. P., and Wells P. N., "Physiological interpretation of Doppler-shift waveforms--III. Clinical results," Ultrasound Med. Biol., vol. 6(3), pp. 227-231, 1980c.

Starmer C. F. and Clark D. O., "Computer computations of cardiac output using the gamma function," J. Appl. Physiol., vol. 28(2), pp. 219-220, 1970.

Stewart G., "Researches on the circulation time in organs and on the influences which affect it. Parts I-III," J. Physiol., vol. 15, pp. 1-89, 1894.

Stewart G., "Researches on the circulation time in organs and on the influences which affect it. IV. The output of the heart," J. Physiol., vol. 22, pp. 159-183, 1897.

Stone P. R., Macphail S., Bull S. B., and Morrow R. J., "Use of Laplace transform analysis to describe the effect of placental embolisation on umbilical arterial Doppler waveforms in fetal sheep," Ultrasound Med. Biol., vol. 20(6), pp. 551-558, 1994.

Stone P. R., Wiesender C. C. T., and Murakami N., "Maternal brachial arterial waveforms in gestational hypertension: analysis using a Laplace transform technique," Journal of Maternal-Fetal Investigation, vol. 8(3), pp. 113-120, 1998.

Swanson D. K., Myerowitz P. D., Hegge J. O., and Watson K. M., "Arterial blood-flow waveform measurement in intact animals: new digital radiographic technique," Radiology, vol. 161(2), pp. 323-328, 1986.

Swanson D. K., Kress D. C., Pasaoglu I., Hegge J. O., and Kroncke G. M., "Quantitation of absolute flow in coronary artery bypass grafts using digital subtraction angiography," J. Surg. Res., vol. 44(4), pp. 326-335, 1988.

Tai N. R., Salacinski H. J., Edwards A., Hamilton G., and Seifalian A. M., "Compliance properties of conduits used in vascular reconstruction," Br. J. Surg., vol. 87(11), pp. 1516-1524, 2000.

Thompson H. K. Jr., Starmer C. F., Whalen R. E., and McIntosh H. D., "Indicator transit time considered as a gamma variate," Circ. Res., vol. 14, pp. 502-515, 1964.

Walton L., Martin T. R., Collins M., Sherriff S. B., and Barber D. C., "An objective feature extraction technique applied to the Doppler waveforms from the groin: a prospective study," Ultrasound Med. Biol., vol. Suppl 2, pp. 263-268, 1983.

Wicks D.A.G., "Intravascular blood flow measurement by quantitative cineangiography image analysis," PhD Thesis, University of Manchester, 1989.

Wilson R. F., Marcus M. L., and White C. W., "Prediction of the physiologic significance of coronary arterial lesions by quantitative lesion geometry in patients with limited coronary artery disease," Circulation, vol. 75(4), pp. 723-732, 1987.

Wright I. A., Gough N. A., Rakebrandt F., Wahab M., and Woodcock J. P., "Neural network analysis of Doppler ultrasound blood flow signals: a pilot study," Ultrasound Med. Biol., vol. 23(5), pp. 683-690, 1997.

Publications

Articles in Journals

- Rhode K. S., Lambrou T., Hawkes D. J., and Seifalian A. M., "Novel approaches to the measurement of arterial blood flow from dynamic digital x-ray images," IEEE Trans. Med. Imag., Special Issue on Vascular Imaging, vol. 24(4), pp. 500-513, 2005.

Articles in Conference Proceedings

- Rhode K. S., Seifalian A. M., McNeill J., Hamilton G., and Hawkes D. J., "Quantitative measurement of volume blood flow in the coronary circulation using digital subtraction angiography," in Proceedings of Medical Image Analysis And Understanding, Leeds, UK, pp. 117-120, 1998.

- Rhode K., Lambrou T., Hawkes D. J., Hamilton G., and Seifalian A. M., "Validation of an optical flow algorithm to measure blood flow waveforms in arteries using dynamic digital x-ray images," in Proceeding of SPIE, Medical Imaging, San Diego, California, USA, vol. 3979, pp. 1414-1425, 2000.

- Rhode K., Lambrou T., Hogarth K., Hawkes D. J., Hamilton G., and Seifalian A. M., "Improved measurement of blood flow in arteries from dynamic digital x-ray images using a waveform shape model," in Proceedings of Medical Image Analysis and Understanding, London, UK, pp. 79-82, 2000.

- Rhode K., Ennew G., Lambrou T., Hawkes D., and Seifalian A., "The measurement of blood flow from dynamic digital x-ray images using a weighted optical flow algorithm: validation in a moving-vessel flow phantom," in Proceedings of Medical Image Analysis and Understanding, Birmingham, UK, pp. 29-32, 2001.

- Rhode K., Ennew G., Lambrou T., Seifalian A., and Hawkes D., "In-vitro validation of a novel model-based approach to the measurement of arterial blood flow waveforms from dynamic digital x-ray images," in Proceeding of MICCAI, Utrecht, The Netherlands, vol. 2208, pp. 291-300, 2001.

- Rhode K., Lambrou T., Seifalian A. M., and Hawkes D. J., "In-vitro validation of a novel model-based approach to the measurement of arterial blood flow waveforms from dynamic digital x-ray images," in Proceeding of SPIE, Medical Imaging, San Diego, California, USA, vol. 4683, pp. 286-296, 2002.